OPTIMIZED FUEL INJECTOR DESIGN for MAXIMUM IN-FURNACE NO_X REDUCTION and MINIMUM UNBURNED CARBON

FINAL REPORT

October 1, 1997 - November 1, 2000

M. P. Heap, K. A. Davis, N. S. Harding, A. F. Sarofim, M. J. Bockelie, D. A. Swensen
Reaction Engineering International

E. G. Eddings, J. P. Klewicki
University of Utah

R. H. Hurt
Brown University

R. A. Lisauskas
D. B. Riley, Inc.

March 2001

DE-AC22-95PC95103

Reaction Engineering International
77 West 200 South Suite 210
Salt Lake City, UT 84101

University of Utah
College of Engineering
Merrill Engineering Building
Salt Lake City, UT 84112

Brown University
Division of Engineering
Box D
Providence, RI 02912

D. B. Riley, Inc.
Riley Research Center
45 McKeon Road
Worcester, MA 01610

DISCLAIMER

ABSTRACT

Reaction Engineering International teamed with the University of Utah, Brown University, D.B. Riley and the Electric Power Research Institute to complete a two-year study on "in-furnace" NO_X control with the following specific objectives:

- Conduct research to better understand the interaction of heterogeneous chemistry and two-phase mixing on NO reduction processes in pulverized coal combustion.
- Improve the ability to predict combusting coal jets by verifying two-phase mixing models under conditions that simulate the near field of low-NO_X burners.
- Determine the limits on NO control by in-furnace NO_X control technologies as a function of furnace design and coal type.
- Evaluate waterwall wastage measurement techniques and develop a program and a monitoring device for assessing corrosion in boilers.
- Improve the char burnout model in REI's coal combustion code to take into account the recently obtained fundamental data on char reactivity during the late stages of burnout.
- Develop a user-friendly boiler simulation tool for industry.

The successful completion of this program has provided two commercial products and a substantial improvement to the computational fluid dynamic codes used at REI for the boiler/furnace industry. The two commercial products, a pc-based "Configured Fireside Simulator (CFS)" and a real-time corrosion monitoring system, also have shown great benefit to the utility industry.

TABLE OF CONTENTS

1.0: EXECUTIVE SUMMARY 1-1
1.1: PROGRAM GOALS AND ORGANIZATION 1-1
1.2: BOILER MODELING – CONFIGURED FIRESIDE SIMULATOR 1-3
1.3: WATERWALL WASTAGE 1-4
1.4: CHAR REACTIVITY 1.7
1.5: COMBUSTION INVESTIGATIONS 1-8
1.5.1: BENCH-SCALE STUDIES 1-8
1.5.2: PILOT-SCALE STUDIES 1-9
1.6: TWO-PHASE MIXING STUDIES 1-10

2.0: INTRODUCTION 2-1
2.1: PROGRAM GOALS 2-1
2.2: PROGRAM ORGANIZATION 2-3
2.3: PHASE II REPORT ORGANIZATION 2-4
2.4: REFERENCES 2-4

3.0: CONFIGURED FIRESIDE SIMULATOR (CFS) 3-1
3.1: INTRODUCTION 3-1
3.2: BACKGROUND/MOTIVATION FOR CFS DEVELOPMENT 3-2
3.3: DESCRIPTION OF CFS 3-2
3.3.1: SOFTWARE DESIGN GOALS 3-2
3.3.2: SOFTWARE IMPLEMENTATION 3-3
3.4: EXAMPLE IMPLEMENTATION: 3-4
3.4.1: PROBLEM SET-UP 3-4
3.5: TARGETED FACILITIES AND APPLICATIONS 3-9
3.6: FUTURE DEVELOPMENT OF CFS 3-9
3.7: COMMERCIAL POTENTIAL OF CFS 3-9

4.0: WATERWALL WASTAGE 4-1
4.1: INTRODUCTION 4-1
4.2: AVAILABLE TECHNOLOGIES 4-3
4.2.1: ELECTROCHEMICAL SENSOR APPROACH 4-3
4.3: EN PROBE DESCRIPTION 4-5
4.3.1: RESULTS 4-7
4.4: REFERENCES 4-13

5.0: CHAR REACTIVITY 5-1
5.1: DEVELOPMENT AND TESTING OF CARBON BURNOUT MODELS 5-1
5.1.1: CBK8 DEVELOPMENT 5-1
5.1.2: BURNOUT PARAMETER STUDIES 5-15
5.1.3: SUBTASK 5.1 CONCLUSIONS 5-18
5.2: CHARACTERIZATION OF UNBURNED CARBON PROPERTIES 5-20
5.2.1: TECHNICAL INTRODUCTION TO SUBTASK 5.2 5-20
5.2.2: LABORATORY EXPERIMENTS 5-22
5.2.3: RESULTS AND DISCUSSION 5-23
5.2.4: SUBTASK 5.2 CONCLUSIONS 5-34
5.3: CHAR REACTIVITY IN NO AND OXYGEN 5-36
5.3.1: NO_X REDUCTION ON CHAR 5-36
5.3.2: OXYGEN REACTIVITIES OF DIVERSE SOLID FUELS 5-40
5.3.3: SUBTASK 5.3 CONCLUSTIONS 5-43
5.4: REFERENCES 5-44

6.0: COMBUSTION INVESTIGATIONS 6-1
6.1: BENCH-SCALE STUDIES 6-1
6.1.1: INTRODUCTION 6-1
6.1.2: METHODS 6-2
6.1.3: COMBUSTION EQUIPMENT 6-3
6.1.4: TEST CONDITIONS 6-5
6.1.5: SAMPLE COLLECTION 6-6
6.1.6: SAMPLE ANALYSIS 6-8
6.1.7: TESTING OF THERMAL OPTICAL REFLECTANCE CARBON 6-8
6.1.8: RESULTS 6-9
6.1.9: DISCUSSION 6-12
6.2: PILOT-SCALE STUDIES 6-13
6.2.1: INTRODUCTION 6-13
6.2.2: EXPERIMENTAL FACILITIES 6-13
6.2.3: RESULTS AND DISCUSSION 6-15
6.2.4: CONCLUSIONS 6-21
6.3: REFERENCES 6-22

7.0: TWO-PHASE MIXING STUDIES 7-1
7.1: INTRODUCTION 7-1
7.2: FUNDAMENTAL UNDERSTANDING & BETTER INJECTOR DESIGNS 7-1
7.3: SUMMARY OF PHASE I RESULTS 7-2
7.3.1: DEVELOPMENT OF THE EXPERIMENTAL FACILITY 7-2
7.3.2: PHASE I EXPERIMENT PARAMETERS 7-4

7.3.3: VELOCITY FIELD STATISTICAL PROFILES 7-4
7.3.4: PASSIVE SCALAR AND PARTICLE CONCENTERATIONS 7-6
7.3.5: SPATIAL VELOCITY CORRELATION MEASUREMENTS 7-9
7.3.6: SUMMARY AND RECOMMENDATIONS FROM PHASE I 7-12
7.4: PHASE II STUDIES 7-14
7.4.1: BRIEF RE-EXAMINATION OF COAXIAL JET LITERATURE 7-14
7.4.2: EXPERIMENTAL FACILITY AND PARAMETERS 7-18
7.4.3: MEASUREMENT TECHNIQUES 7-24
7.4.4: PARTICLE CONCENTRATION RESULTS 7-30
7.4.5: SUMMARY 7-32
7.5: REFERENCES 7-37
APPENDIX A: EXPERIMENTAL APPARATUS A-1

1. EXECUTIVE SUMMARY

1.1 PROGRAM GOALS AND ORGANIZATION

The study described in this Phase II final report is concerned with the primary NO_x control technology for pulverized coal fired boilers, "in-furnace NO_x control", which includes staged low-NO_x burners, reburning, selective non-catalytic reduction (SNCR) and hybrid approaches; e.g., reburning with SNCR. The program has two primary objectives:

1) To improve the performance of "in-furnace" NO_x control processes.

2) To devise new, or improve existing, approaches for maximum "in-furnace" NO_x control and minimum unburned carbon.

When the program was conceived it was thought that the major impact on boiler performance associated with in-furnace NO_x reduction technologies was the increase in unburned carbon in the fly ash. Recently, the utility industry has been made aware of another problem, increased rates of waterwall wastage in units fitted with low-NO_x firing systems, particularly supercritical units firing eastern bituminous coals. As a result a program initiative was developed to investigate corrosion and to develop a corrosion measuring probe for application to the utility industry.

To accomplish the above-mentioned overall goals, Reaction Engineering International teamed with the University of Utah, Brown University, D.B. Riley and the Electric Power Research Institute to complete a two-year study with the following specific objectives:

1) Conduct research to better understand the interaction of heterogeneous chemistry and two-phase mixing on NO reduction processes in pulverized coal combustion.

2) Improve the ability to predict combusting coal jets by verifying two-phase mixing models under conditions that simulate the near field of low-NO_x burners.

3) Determine the limits on NO control by in-furnace NO_x control technologies as a function of furnace design and coal type.

4) Evaluate waterwall wastage measurement techniques and develop a program and a monitoring device for assessing corrosion in boilers.

5) Improve the char burnout model in REI's coal combustion code to take into account the recently obtained fundamental data on char reactivity during the late stages of burnout. This will improve our ability to predict carbon burnout with low-NO_x firing systems.

6) Develop a user-friendly boiler simulation tool for the industry.

The commercial products resulting from this effort included an improved computational tool to help the utility boiler operator determine the optimum low-NO_x firing configuration, Configured Fireside Simulator (CFS), and a corrosion-monitoring device for evaluating waterwall wastage.

The task structure for this program is shown in Figure 1.1; not shown is the Program Management Task. Computer simulation is central to the whole program; it provides both data evaluation and generalization. The two-phase mixing studies carried out at the University of Utah were planned to develop data to validate the two-phase mixing models in *GLACIER*. Since it is impossible to get meaningful data in the near field of a pulverized coal flame, these studies are being carried out under isothermal conditions. Studies at Brown University concentrated on two aspects of char reactivity with respect to char oxidation and the reduction of NO. In this report the emphasis shifted from carbon burnout to NO reduction. In addition, Brown University studies clearly demonstrated ash properties that limit its commercial use. The combustion testing for low-NO_X operation was carried out at the University of Utah in bench- and pilot-scale facilities. Because of a shift in emphasis no full-scale testing at the DB Riley U-Furnace Test Facility occurred. The simulation task concentrated on development of a pc-based tool for utility engineers. This tool provided a method to evaluate combustion and boiler optimization as a function of boiler operation and fuel quality.

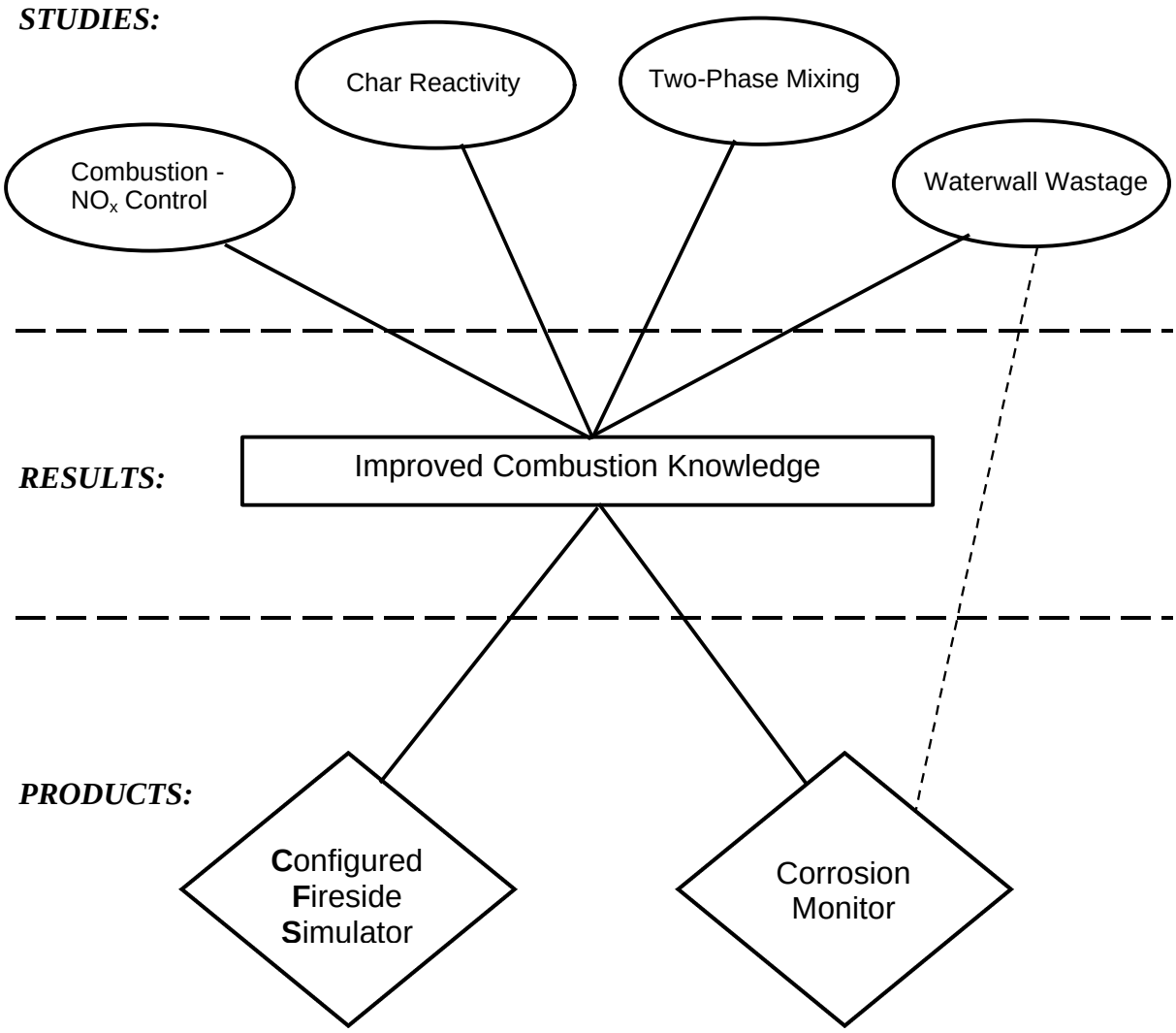

Figure 1.1 General program organization.

1.2 BOILER MODELING – CONFIGURED FIRESIDE SIMULATOR (CFS)

A major focus of the modeling efforts in Phase II of this program was the development of a proto-type combustion model for personal computers. This software utilizes the tremendous background of REI's more complex computational fluid dynamic codes, but allows for a user friendly, non-specialist approach to solving combustion problems. Reaction Engineering International's Configured Fireside Simulator (CFS) has been developed for the purpose of running pre-configured reacting CFD models of industrial furnaces. The CFS software is designed to be used by engineers who are not experts in computational fluid dynamics or advanced combustion concepts. CFS gives the real world engineer the tools needed to analyze and optimize complex combustion systems such as furnaces and boilers.

The CFS software utilizes a user-friendly, Microsoft Windows compatible graphical user interface (GUI) for specification of model inputs, control of model execution, monitoring of model execution status and all other required operations. Figure 1.2 shows the main splash window of the CFS software, which includes modeling results from a CFS simulation of an opposed, wall-fired boiler.

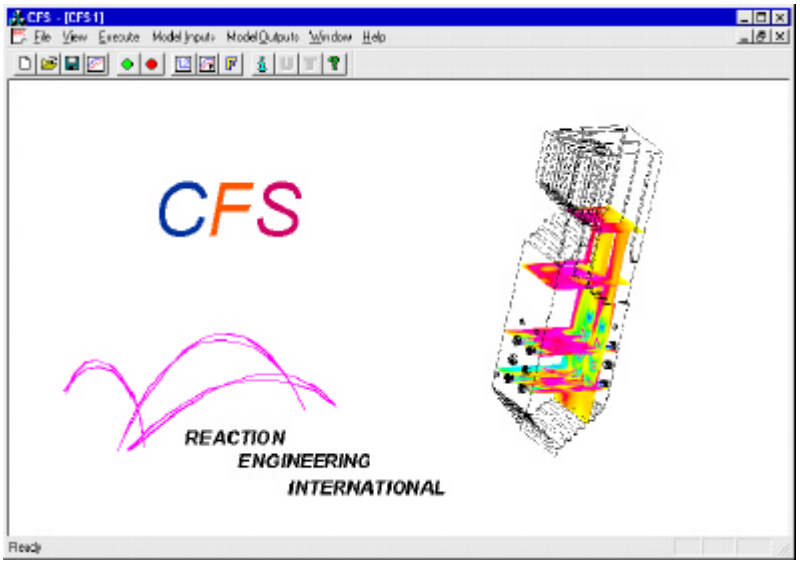

Figure 1.2 CFS Start-up screen.

The CFS software was designed to be adaptable to a variety of modeling applications. CFS models are available for utility and industrial boilers, chemical process and ethylene cracking furnaces, rotary kilns, blast furnaces, smelters, stokers, thermal oxidizers, incinerators and flares. CFS provides numerous capabilities for modeling these facilities. Typical applications include:

- Low-NO_X firing systems

- Cofiring of coal, gas, oil and biomass
- Fuel blending and fuel switching
- Burner balancing and zonal firing
- Staged air (OFA, UFA) and oxygen injection
- NO_X control strategies (SNCR, FGR, FLGR)
- Corrosion

Reaction Engineering has seen widespread interest in the CFS software concept. Several clients for whom REI has previously performed modeling jobs are interested in being able to run parametric modeling studies of their systems in-house. CFS models are routinely included as a standard option when REI provides cost proposals to potential clients. The positive, enthusiastic response REI has received from potential users of CFS clearly illustrates the need for this software tool. For the first time, non-experts have powerful combustion simulation tools at their disposal.

1.3 WATERWALL WASTAGE

Furnace corrosion problems can be difficult to diagnose and address. However, computational simulations can provide insight into the factors controlling the nature of the flow, temperature, and composition fields within a boiler. REI's in-house, two-phase, reacting, computational fluid dynamics software can simulate boilers fitted with advanced low-NO_X firing systems and provide a detailed description of conditions affecting waterwall corrosion such as local hydrogen sulfide concentration, heat flux, etc. Although the model cannot predict corrosion directly, empirical correlations relating corrosion rates to predicted properties are available. REI has performed computational simulations of several corner-, wall- and cyclone-fired units with the goal of understanding and addressing corrosion difficulties related to combustion modifications for the reduction of NO_X emissions.

CFD simulations provide a wealth of useful information related to the corrosion of waterwalls and can be used to develop strategies for modifying operating conditions, fuel selection, and maintenance approaches. However, the availability of actual measurements, in addition to the simulation results, would be most useful. A few examples of how real-time corrosion rate measurements would be useful in tandem with CFD results follow:

1. As precise model inputs are often unavailable, predictions of the location and magnitude of a potential corrosion problem can be uncertain. With a rough idea of the region provided by the model, a probe or group of probes can be used to verify the location and to insure that corrective measures suggested by the model have met their goal.

2. The relationship between actual corrosion rates and corrosion indicators, which can be provided through CFD predictions, is not well understood. The combination of CFD results and probe data can be used to refine and validate these empirical relationships.

3. Real time monitors can pick up perturbations in operating conditions or other upsets to detect problems before they cause serious damage.

4. Although the usefulness of CFD predictions is becoming more widely accepted throughout industry, actual measurements provide additional confidence and can be used to identify where improvements or additional detail in a model is required.

As a result of these issues, REI has been working with Corrosion Management from the U.K. to develop a corrosion probe utilizing electrochemical noise as the method of measurement. Electrochemical noise analysis techniques are used to analyze fluctuations in current and voltage occurring between nominally identical elements. These fluctuations can be used to characterize the electrochemical condition at a corroding interface. For linear polarization, $\Delta v/\Delta i = R_p$, in a manner similar to Ohm's law, where Δv and Δi are incremental changes in voltage and current respectively and R_p is a consequent polarization resistance. Similarly, it has been shown that the root-mean-square (RMS) value of the voltage noise divided by the RMS value of the current noise (defined as the "resistance noise") can be used to determine the rate of a corrosion process, the rate being inversely proportional to the resistance noise magnitude.

The following features make noise analysis particularly useful:

- Current and voltage transients indicative of high corrosion rates are detectable almost instantaneously and, more importantly, well before significant material loss occurs.
- The sensor array is very compact, with the potential to be small enough to insert in the webbing between boiler tubes.
- The nature of these transients provides quantitative and qualitative insight into the rates and mechanisms of the corrosion at the metal surface.

Figure 1.3 is a photograph of the corrosion probe used in the studies as part of this program.

Figure 1.3 Electrochemical noise corrosion probe.

Several bench- and pilot-scale studies were completed to verify the applicability of the corrosion measurement in combustion furnaces. Figure 1.4 is a summary of some of the pilot-scale tests measuring corrosion rate as a function of furnace stoichiometric ratio.

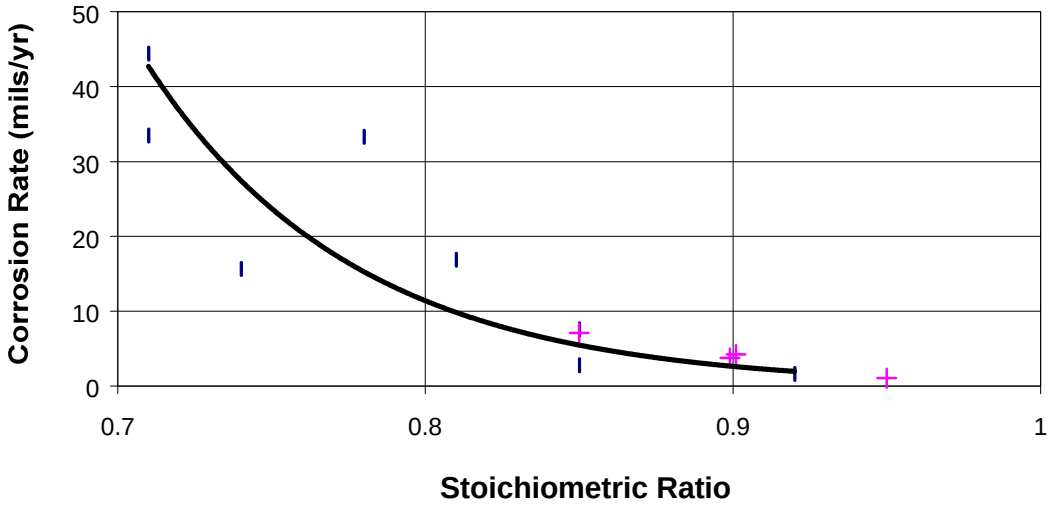

Figure 1.4. Pilot-scale results illustrating the effect of stoichiometry on corrosion rate.

Following the successful testing of the corrosion probe in the furnaces at the University of Utah, REI made preparations to install the probe in a 185 MW cyclone-fired boiler located in New Jersey. This concluded the studies with the corrosion probe on this program; additional testing is being done on other DOE and privately funded programs. Figures 1.5 and 1.6 show the response of the corrosion probe in the boiler during a start-up sequence and some steady-state operation.

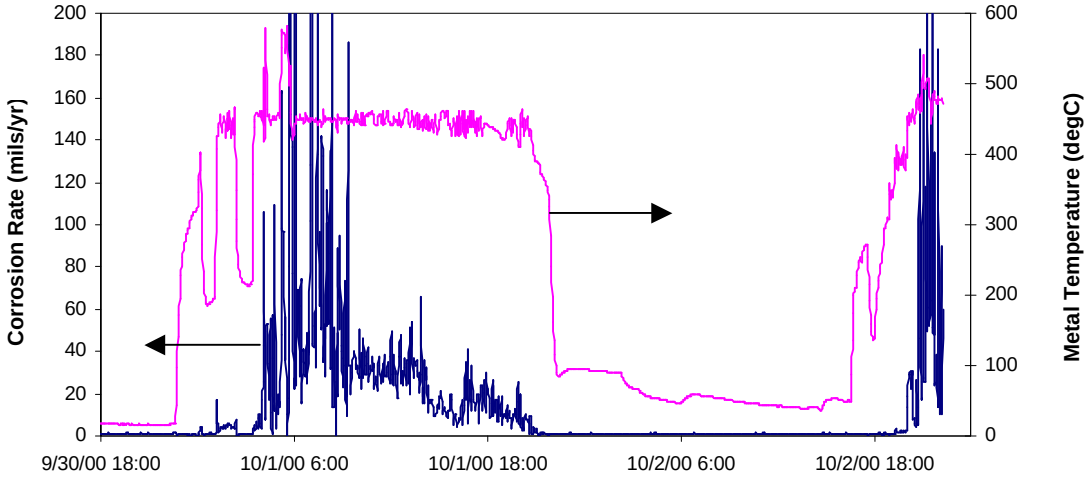

Figure 1.5 Corrosion probe response during start-up and shut down sequence.

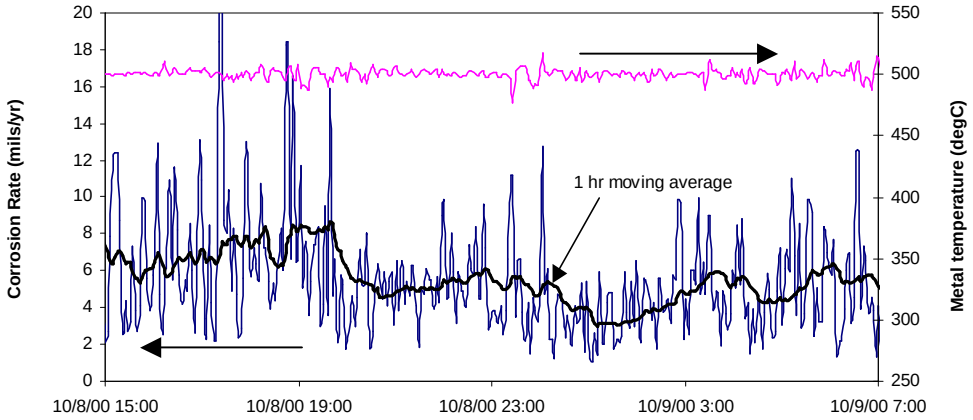

Figure 1.6 Corrosion probe response during steady-state operation.

The probe is now being further tested and calibrated against known corrosion rates. The current plans are then to install it in two different boilers, one a cyclone-fired unit and the other an opposed-wall-fired unit. Testing in each boiler will be approximately one month.

1.4 CHAR REACTIVITY

The char reactivity work was completed by Brown University. The work was divided into three subtasks:

1. The development and testing of carbon burnout submodels;

2. An experimental study of the effect of combustion conditions on unburned carbon *properties* (rather than *amount*), with emphasis on those properties critical to practical ash utilization markets;

3. An experimental study of the nitric oxide and oxygen reactivity of chars as a function of fuel type and heat treatment conditions.

This program successfully demonstrated that:

- Parameter studies with the validated model indicate that a number of coal-related factors exert a significant influence on carbon burnout and LOI. The burnout propensity of a fuel is not governed by a single dominant fuel property. LOI is particularly sensitive to the char yield (flame volatile loss), swelling factor, coal particle size distribution, and coal ash content. Despite the inclusion of a modest ash inhibition effect in the combustion model, *increases* in ash content are predicted always to lead to *decreases* in LOI by diluting of the unburned effect with inorganic matter. Lesser sensitivities are observed for intrinsic reactivity, gas temperature profiles, and the mode of burning parameter that describes the particle diameter evolution during combustion. The sensitivity to intrinsic reactivity increases with decreasing char reactivity.

- These first experiments under controlled combustion conditions confirm the conclusion from earlier studies that the adsorption of concrete surfactants on fly ash is a complex process that cannot be simply related to the *amount* of unburned carbon present. It also depends on the carbon surface area, its accessibility, and the chemical nature of the carbon surface.

- Partially combusted coal chars from well-characterized uniform combustion environments show large variations in specific surfactant adsorptivity over the course of conversion. The adsorptivity is low throughout most of devolatilization, rises sharply in the late stages of devolatilization, and then decreases sharply throughout char combustion.

- Analysis of pilot-scale samples suggests that carbon adsorptivity is less sensitive to flame structure (high vs. low NO_X) than to the absolute carbon burnout. Thus low-NO_X flames can produce high quality ash if the unburned carbon levels can be controlled.

- Two independent experimental techniques indicate that the reactivity of chars in NO reduction is quite sensitive to the extent of rapid heat treatment under flame-like conditions. The high reactivities of partially devolatilized coals and young chars suggests the importance of heterogeneous NO reduction routes in a variety of low-NO_X combustion systems, including those incorporating reburning.

- A first set of data has been acquired on the relative intrinsic combustion reactivities of chars from a diverse set of coals, biomass materials, and other alternative fuels. The alternative solid fuel chars have a wide range of intrinsic combustion reactivities that do not follow the simple trends observed for coal chars.

1.5 COMBUSTION INVESTIGATIONS

One area of major focus for Reaction Engineering International and the University of Utah was in continuing the combustion studies to determine the maximum possible NO_x reduction that might be achieved within a burner. This work combined the fundamental studies on bench-scale combustion testing and pilot-scale testing in the University of Utah's 5 MMBtu/hr L-1500 furnace. As a result of these combustion efforts, it was determined that there appeared little one could do from a burner retrofit scenario to reduce NO emissions to meet proposed EPA standards. However, from these low-NO_X studies, it became apparent that one of the potential problems that would be encountered by boiler operators would be the potential for waterwall wastage or corrosion. Therefore, an effort was undertaken to investigate waterwall wastage and to try and develop a "real-time" measurement technique.

1.5.1 Bench-Scale Studies

The bench-scale experiments completed for this program provide new data that confirms expectations regarding the variation of carbon in ash under staged pulverized coal combustion conditions. Previous work suggests that most of the carbon in ash is generated during excursions to low oxygen. These expected trends were confirmed and data are now

available on the magnitude of the variations. A summary plot of the carbon-in-ash as a function of stoichiometric ratio is shown in Figure 1.7.

1.5.2 Pilot-Scale Studies

In recent years, tighter restrictions on NO_X emissions have resulted in significant efforts to control NO_X levels in pulverized-coal-fired utility boilers. While low emissions can be achieved using expensive post-combustion control such as Selective Catalytic Reduction (SCR), the search continues for more effective in-furnace control techniques. REI did a series of tests to evaluate a potential new idea for in-furnace NO_X control: In-Situ Gas Reburning. The idea is straightforward: can selective amounts of natural gas be injected into the core of the pulverized coal flame to provide "in-situ" reburning of NO_X formed early in the flame?

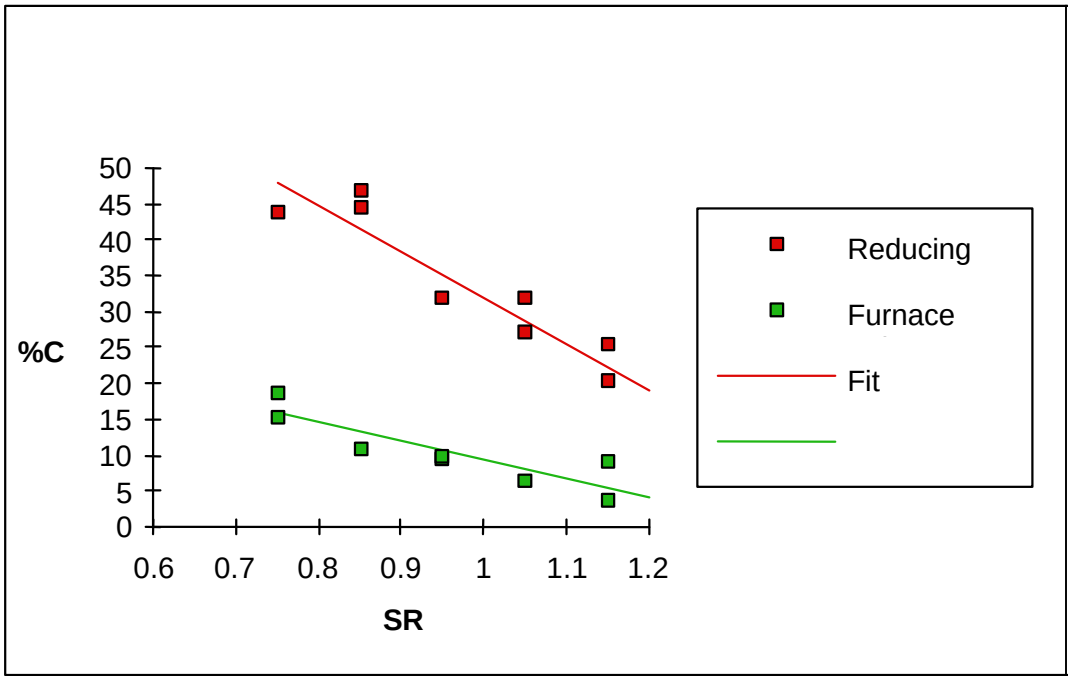

Figure 1.7. Percent carbon as measured upstream and downstream of burnout air injection as a function of burner Stoichiometric Ratio.

There were various parameters that required investigation including determination of the appropriate amount of gas, the most effective momentum for the gas jet, effect of initial NO level and the interplay with other burner operating parameters such as combustion air swirl. These parameters were systematically evaluated and the results of these evaluations will be described below. In addition, the effectiveness of in-situ gas reburning was contrasted with NO_X reduction obtained using conventional downstream gas reburning, to provide a comparison with an existing technology.

Figure 1.8 shows the compares the results of these experiments with those of conventional gas reburning. These tests concluded that conventional reburning would be the best option for utility applications. Other conclusions from this project include:

- The most effective use of in-situ gas reburning appears to be when applied under high initial NO_X conditions.

- Injection momentum has a clear effect on efficiency of internal gas addition, and higher jet momentums result in increased reduction efficiencies. Use of internal gas addition shows an effect not attributable to simple decrease in burner stoichiometry, as reductions were achieved in excess of those observed when simply staging the burner firing without internal gas addition.

- Comparison with a conventional reburning scenario indicated similar reduction efficiencies for an optimized in-situ gas injector and downstream gas addition indicating that either approach would be acceptable when applied under initially high NO_X conditions.

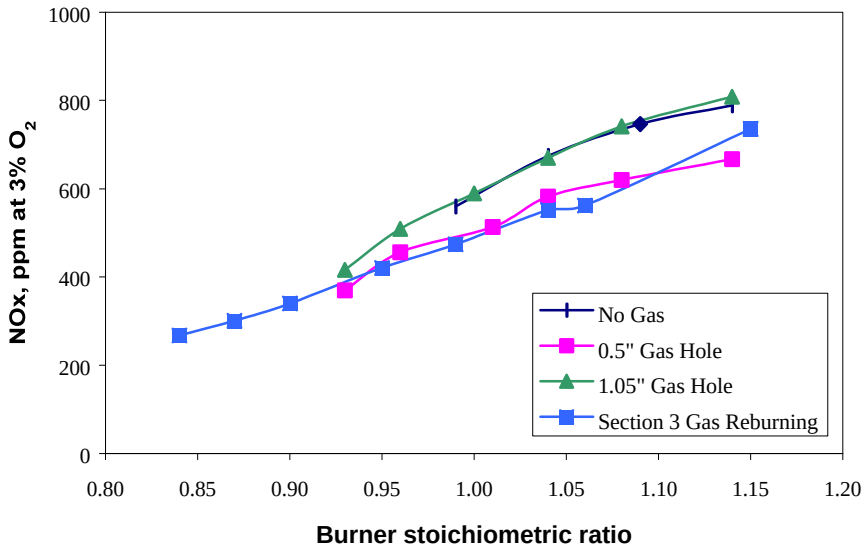

Figure 1.8. Internal gas addition vs. conventional reburning for high initial NO conditions with overfire air addition.

1.6 TWO-PHASE MIXING STUDIES

The goal of the two-phase mixing studies was to gain a better understanding of the flow field mechanisms underlying the dispersion of particles in the near-field of the injector jet flow. In the present experiments, the basic injector geometry was modeled as a coaxial jet, with the interior (primary) jet being loaded with particles. The particular objectives of the research focused on 1) obtaining accurate descriptions of the fluid velocity and velocity gradient field, and 2) correlating these descriptions with injector nozzle characteristics and the dispersion of the suspended phase. These studies were motivated by the broader PRDA goals of aiding in the validation and development of the computational models being employed to predict boiler performance and to provide data bases that quantify the

influences of injector geometry and operating parameters (e.g., secondary-to-primary jet velocity ratio).

From the data collected in this study, the effects of the flow field on particle dispersion are made evident by the changes in the particle density distribution at different primary/secondary air velocity ratios. This effect of the particles on the flow field is also implied by the change of normalized particle number density as the particle flow rate is varied.

A comparative example is shown in Figures 1.9 and 1.10 where contour plots are presented showing particle dispersion in a plane normal to the jet axis at a distance of x/d = 2.0 from the jet exit for two different volume flow ratios. The data are presented in the form of contour plots of normalized particle number densities. This is defined as the ratio of the local number density of the particles to the average particle number density. Therefore, a value of 1.0 corresponds to the average particle number density of the whole image.

These figures show that at a given velocity ratio, an increase in volume flow rate results in a more uniform particle distribution. Also, as the velocity ratio decreases, the extent of the particle cloud increases in the radial direction. This obviously indicates a larger particle diffusion, and is consistent our Phase I results. That is, as the velocity ratio decreases, the flow in this shear region loses its wake-type character and becomes more like a mixing layer type of flow. This can lead to a change in the turbulent characteristics in the intermediate mixing region and consequently greater particle mixing in the inner region.

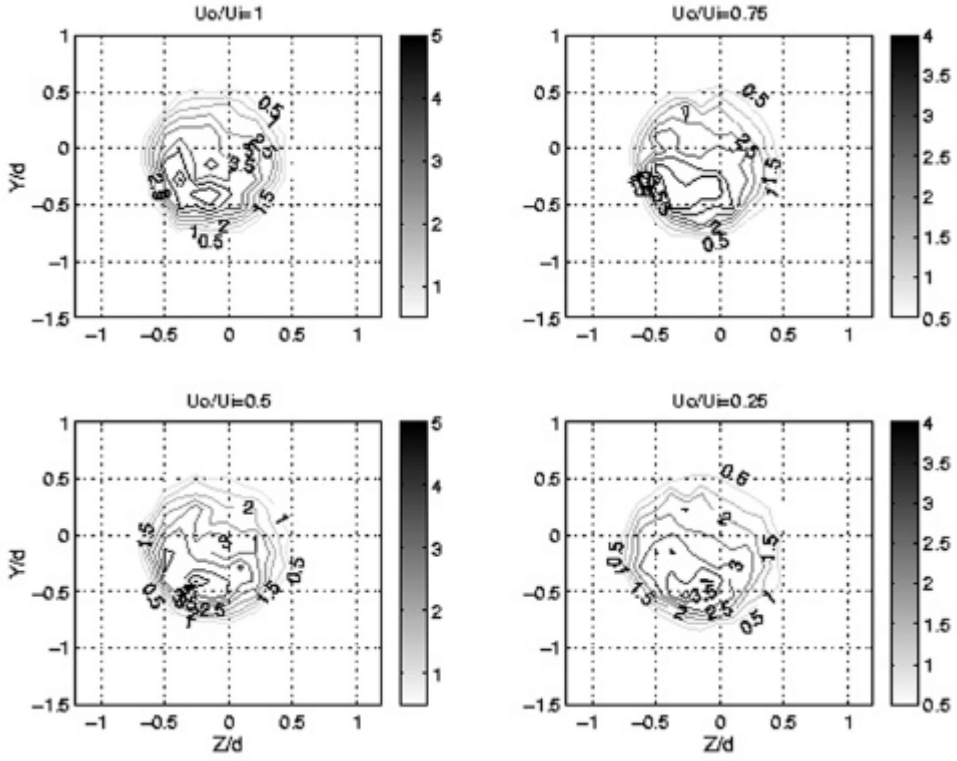

Figure 1.9. Particle dispersion results at x/d = 2, and volume flow rate of 0.024%.

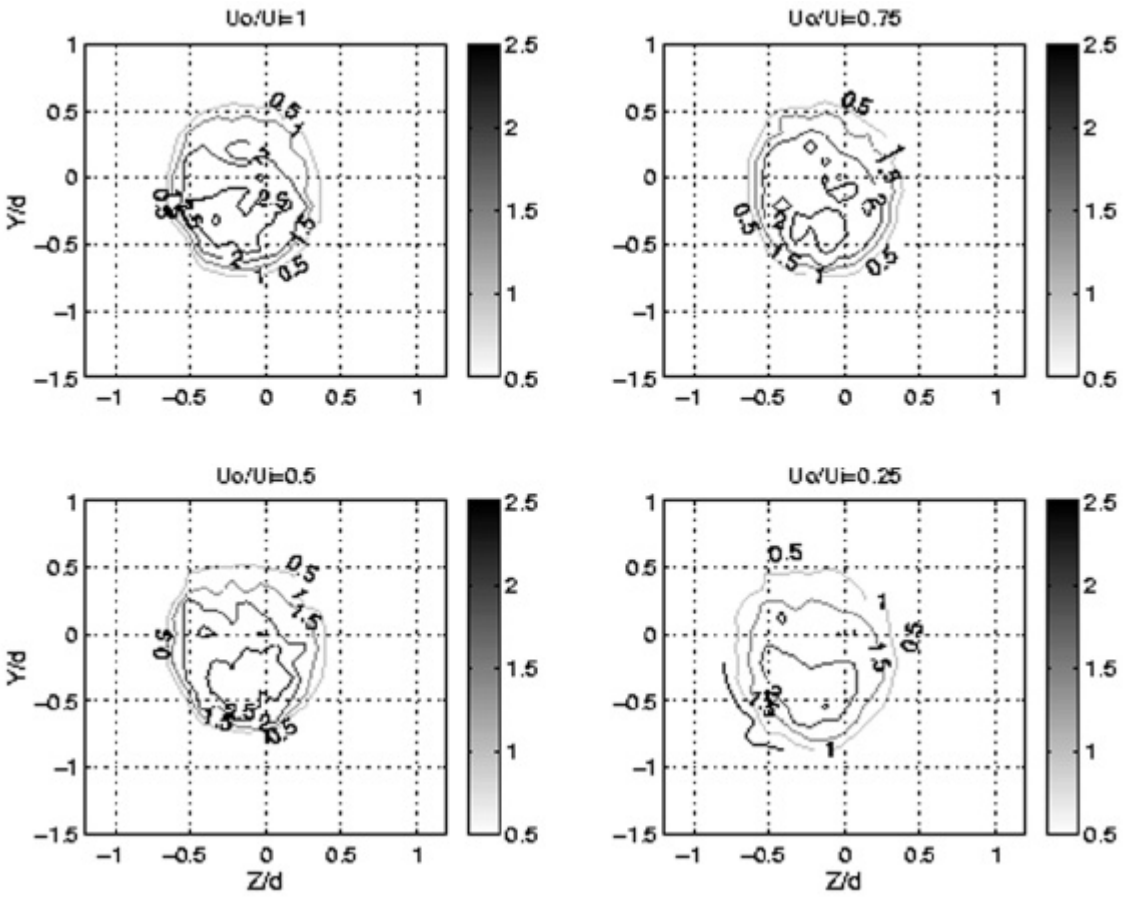

Figure 1.10. Particle dispersion results at x/d = 2, and volume flow rate of 0.075%.

2. INTRODUCTION

Coal is this country's most abundant energy source and one of the US Department of Energy's goals is to encourage and ensure the continual use of coal in an environmentally acceptable manner. Although coal is abundant, both mining and utilization can have serious environmental consequences if appropriate controls are not enforced. The presence of heteroatoms makes utilization through combustion a potential source of atmospheric pollutants. Species such as sulfur and nitrogen form gaseous pollutants, SO_2 and NO, and trace metals can form toxic aerosols. Coal is not a renewable energy source, thus CO_2 emissions contribute to global warming. However, coal is and will continue to be a major source of electrical energy well into the twenty-first century and probably beyond, until there is widespread acceptance of alternate energy. Also, consider the demand for energy in China and India, two counties with large populations and abundant supplies of coal. Coal will be the fuel of choice for new power plants, and considering economic realities, it will be used primarily in conventional pulverized coal fired steam generators. Thus, the problem of coal utilization is a global one and it is essential that reliable, cost effective environmental control technologies be developed not only for application in the US but also worldwide.

2.1 Program Goals

The study described in this Phase II final report is concerned with the primary NO_x control technology for pulverized coal fired boilers, "in-furnace NO_x control", which includes staged low-NO_x burners, reburning, selective non-catalytic reduction (SNCR) and hybrid approaches; e.g., reburning with SNCR. The program has two primary objectives:

1) To improve the performance of "in-furnace" NO_x control processes.

2) To devise new, or improve existing, approaches for maximum "in-furnace" NO_x control and minimum unburned carbon.

When the program was conceived it was thought that the major impact on boiler performance associated with in-furnace NO_x reduction technologies was the increase in unburned carbon in the fly ash. Recently, the utility industry has been made aware of another problem, increased rates of waterwall wastage in units fitted with low-NO_x firing systems, particularly supercritical units firing eastern bituminous coals.

For those units required to implement some form of NO_x control to meet Clean Air Act Amendment Phase I compliance limits, low-NO_x burners and/or combustion modification was the preferred option. Although many regarded low-NO_x burners the equivalent of "plug and play," field experience has been completely to the contrary [Jones, 1997]. Most plants that have installed low-NO_x burners report an increase in UBC (unburned carbon). An increase in 10% unburned carbon means a 1% loss in combustion efficiency. But the increased costs associated with ash disposal could dwarf the fuel replacement costs associated with this loss in efficiency. Some increase in LOI was expected; however, recently another problem has surfaced with units fitted with low-NO_x burners - waterwall tube wastage. Approximately ten percent of Phase I units are experiencing accelerated waterwall tube wastage associated with low-NO_x firing. The extent varies from noticeable but manageable to a significant increase and subsequent forced outages. Availability has a major impact on the cost of power produced by a particular plant. Thus the on-going

maintenance cost of low-NO_x firing systems may be significantly greater than the equipment/installation cost.
Waterwall corrosion is usually associated with reducing conditions on the wall. However, deposition of carbon-rich ash and sulfur on the walls can also accelerate corrosion rates. Thus, although the original program plan concentrated on the problem of increased LOI under low-NO_x firing conditions, much of the study is applicable to the corrosion problem.

Two in-furnace NO_x reduction techniques, reburning and staged low-NO_x burners involve similar processes that affect NO_x reduction and carbon conversion; thus the program plan was based on the following hypotheses:

1) NO destruction processes are key in both low-NO_x burners and coal reburning and there are indications that heterogeneous chemistry may play a role.

2) The current level of understanding of gas phase chemistry and coal pyrolysis far surpasses our ability to predict heterogeneous effects and two-phase mixing in the near field of pulverized coal flames.

3) The two-phase mixing taking place in the near field of the fuel injector/burner controls both NO emission level and unburned carbon in the fly ash. New insights on heterogeneous processes and two-phase mixing will enable us to design an improved firing system for simultaneously minimizing NO_x and unburned carbon.

4) NO reduction on char was always thought to be slow, but rates were measured with old char and, with the exception of De Soete [1979], concentrated on direct reduction. Little information is available on NO char reactions under rich conditions in the presence of NH_3 and HCN. These reactions might account for reburning performance with coal.

5) Char reactivity with respect to burnout depends on the age of the char. Old chars loose their reactivity and the late stages of burnout may require more time to complete carbon conversion than might be expected based on the extrapolation of rates measured on high carbon char. Perhaps the reactivity of char with respect to NO also varies with time.

The Phase II program involved:

1) Fundamental studies at laboratory- and bench-scales to define NO reduction mechanisms and to evaluate corrosion potential;

2) Laboratory experiments to improve our two-phase mixing predictive capability;

3) Evaluation of waterwall wastage measurement techniques; and

4) Development of a personal-computer-based boiler simulation tool for industry.

The specific objectives for the program were to:

1) Conduct research to better understand the interaction of heterogeneous chemistry and two-phase mixing on NO reduction processes in pulverized coal combustion.

2) Improve our ability to predict combusting coal jets by verifying two-phase mixing models under conditions that simulate the near field of low-NO_x burners.

3) Determine the limits on NO control by in-furnace NO_x control technologies as a function of furnace design and coal type.

4) Evaluate waterwall wastage measurement techniques and develop a program and a monitoring device for assessing corrosion in boilers.

5) Improve the char burnout model in REI's coal combustion code to take into account the recently obtained fundamental data on char reactivity during the late stages of burnout. This will improve our ability to predict carbon burnout with low-NO_x firing systems.

6) Develop a user-friendly boiler simulation tool for the industry.

The commercial products resulting from this effort included an improved computational tool to help the utility boiler operator determine the optimum low-NO_x firing configuration, Configured Fireside Simulator (CFS), and a corrosion-monitoring device for evaluating waterwall wastage.

2.2 Program Organization

The original task structure for Phases I and II of this program ensure maturity of the technology and maximize the opportunity for commercial deployment. In the intervening time outside influence suggested changes in emphasis (i.e., waterwall wastage evaluations), but the basic organizational structure remains applicable.

The Phase II program consists of:

1) Two fundamental studies, one concerned with char reactivity and the other with the development and application of a technique to study two-phase mixing close to the particle injector.

2) Combustion system testing at three scales: bench-, pilot- and full-scale.

3) Investigation of corrosion measurement techniques and an evaluation of the electrochemical potential method.

4) Development of a computer simulation tool for field operating boilers.

The task structure for the program is shown in Figure 2.1; not shown is the Program Management task. Computer simulation is central to the whole program; it provides both data evaluation and generalization. The two-phase mixing studies carried out at the University of Utah were planned to develop data to validate the two-phase mixing models in *GLACIER*. Since it is impossible to get meaningful data in the near field of a pulverized coal flame, these studies are being carried out under isothermal conditions. In Phase II, the two-phase experimental system was used to optimize particle mass distribution at the injector exit as a function of location and particle size.

Studies at Brown University concentrated on two aspects of char reactivity with respect to char oxidation and the reduction of NO. In Phase I the emphasis was placed on the development of an advanced burnout model that could be integrated with *GLACIER,* and the construction of an apparatus that will allow the hypothesis to be tested that young chars have a higher potential to reduce NO than old chars. In Phase II the emphasis shifted from carbon burnout to NO reduction. In addition, Brown University studies clearly demonstrated ash properties that limit its commercial use.

The combustion testing in Phase II was carried out at the University of Utah in bench- and pilot-scale facilities. Because of a shift in emphasis no full-scale testing at the DB Riley U-Furnace Test Facility occurred.

In Phase II the simulation task concentrated on development of a pc-based tool for utility engineers. This tool provided a method to evaluate combustion and boiler optimization as a function of boiler operation and fuel quality.

2.3 Phase II Report Organization

The major sections of this Final Report correspond to the major program tasks:

- Section 3 describes the development of the computer simulation tool, *Configured Fireside Simulator* (CFS);
- Section 4 highlights the development and initial testing of the corrosion assessment probe;
- Section 5 details the results of the char reactivity studies at Brown University;
- Section 6 presents the pilot-scale low-NO_x combustion tests; and
- Section 7 discusses the fundamental two-phase mixing studies.

2.4 References

De Soete, G.G., “Mechanism of Nitric Oxide Reduction on Solid Particles: Kinetic Study of NO Reduction on A1203 graphite and soot,” Report on EERC Subcontract No. 8318-6, IFP Report No. 27622, 1979.

Jones, C. “Maladies of Low-NO_x Firing Come Home to Roost” p.54, Power, February 1997.

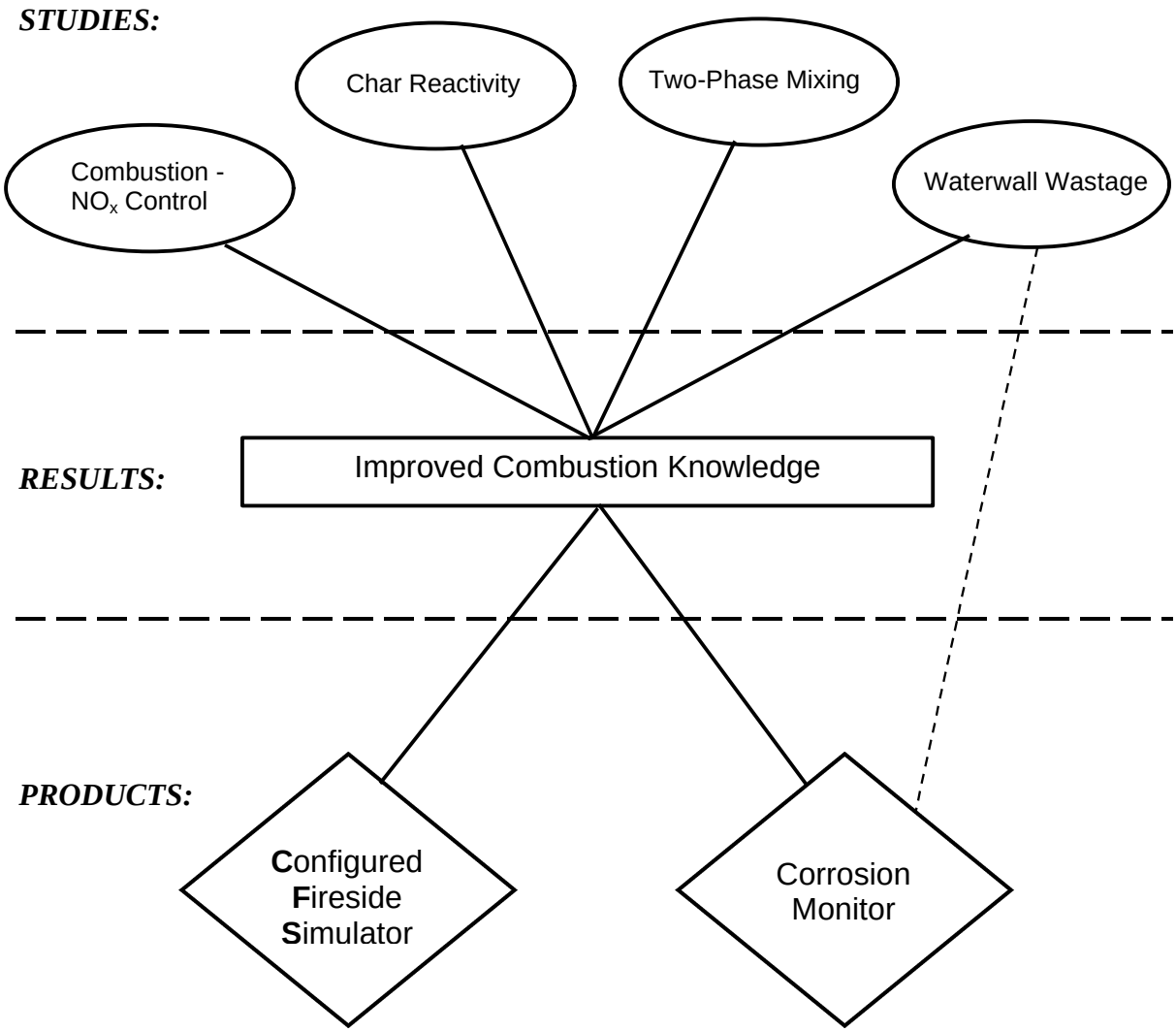

Figure 2.1 General program organization.

3. CONFIGURED FIRESIDE SIMULATOR (CFS)

3.1 Introduction

One focus of the modeling efforts in Phase II of this program was the development of a proto-type combustion model for personal computers. This software utilizes the tremendous background of REI's more complex computational fluid dynamic codes, but allows for a user friendly, non-specialist approach to solving combustion problems.

Reaction Engineering International's Configured Fireside Simulator (CFS) has been developed for the purpose of running pre-configured reacting CFD models of industrial furnaces. By design, CFS limits the number of input and output variables to allow the user to focus on the engineering analysis of the problem to be studied rather than the numerous details required to set up and run the computer programs on which the models are based.

The CFS software is designed to be used by engineers who are not experts in computational fluid dynamics or advanced combustion concepts. CFS gives the real world engineer the tools needed to analyze and optimize complex combustion systems such as furnaces and boilers.

The CFS software utilizes a user-friendly, Microsoft Windows compatible graphical user interface (GUI) for specification of model inputs, control of model execution, monitoring of model execution status and all other required operations. This sophisticated GUI keeps the user from having to work with arcane text files and complex command-line operations typically mandated by advanced scientific software applications.

The CFS software was written to be highly configurable and extensible. As a result, it can be custom tailored to meet customer's needs for a wide variety of combustion facilities. Figure 3.1 shows the main splash window of the CFS software, which includes modeling results from a CFS simulation of an opposed, wall-fired boiler.

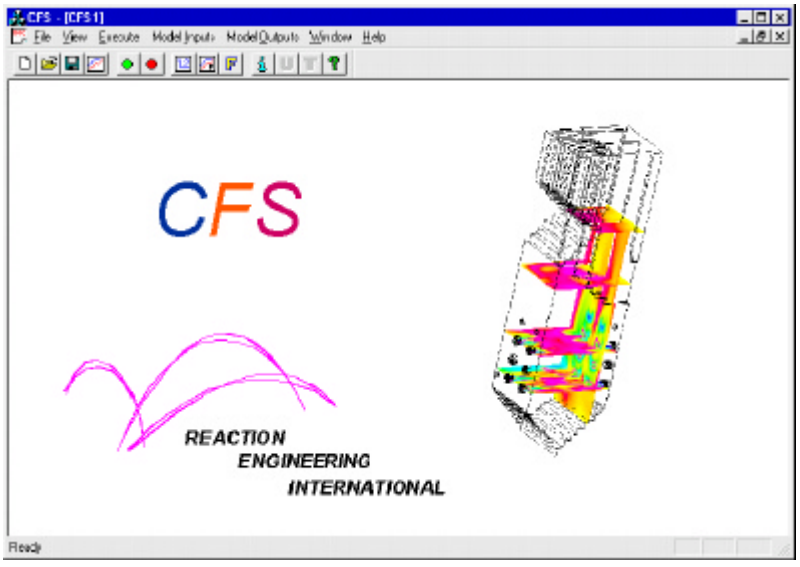

Figure 3.1 CFS Start-up screen.

3.2 Background/Motivation for CFS Development

The underlying computational models utilized by CFS include REI's 3D reacting CFD codes. These models represent the state-of-the-art in combustion modeling software. Reaction Engineering's computational models emphasize the coupling between turbulent fluid mechanics, gas and particle phase reactions, radiation, turbulent particle dispersion and NOx chemistry. Recent model additions include: advanced char burnout description, char nitrogen chemistry that includes the influence of the local free stream NO concentration, pyrite kinetics and deposition, kinetically limited gas phase sulfur chemistry, transient flow, and design optimization.

REI's computational models have seen extensive application to industrial problems and have a proven track record of successfully modeling disparate combustion systems. These codes are, however, very complicated and require a great deal of expertise to use successfully. In addition, setting up simulations can be very labor intensive due to the large number of input variables and complicated geometry information, which must be fed to the models. Such limitations make these powerful tools essentially inaccessible to the non-expert user.

Hence is the motivation for the CFS concept. Hidden from a user of CFS are the complexities of configuring and running sophisticated computational models. The encapsulation of these powerful tools by the CFS GUI makes the capabilities of these codes available to a wide audience of non-expert users.

3.3 Description of CFS

3.3.1. Pilot-Scale Studies

Ease of use

First and foremost, CFS was designed to be easy to use. This was given first priority since the very reason for developing CFS was to make sophisticated combustion modeling available to a wider audience of users.

Configurable and Extensible

CFS was designed using state-of-the-art object-oriented design principles to create a software infrastructure that could be modified and enhanced with relative ease. This design goal was a high priority since the CFS software is not a "one size fits all" tool. It is intended to be tailored to handle individual combustion simulation scenarios such that users are only required to navigate menus, dialog boxes, and configuration choices, which are directly applicable to their problem. This further enhances the ease of use design goal discussed above.

Consolidation of Tools

Having to deal with multiple software tools to traverse the spectrum of problem setup to post-processing is one of the most cumbersome and error prone aspects of performing advanced modeling. CFS addresses this problem by making all required tools directly accessible from within the GUI. This includes complete control capabilities for the underlying computational models (starting, stopping and monitoring). Even third-party post-processing and visualization tools can be set up and initiated using menu items and toolbars within the GUI.

Appropriate Coupling to Underlying Models

CFS was, by design, tightly coupled to the underlying computational models, enabling the user to observe the evolving results, and to allow user dynamic control of critical parameters. However, keeping the underlying models as separate processes (separate executables) was also an important design goal since this would allow the computational models to be altered and enhanced without the need to recompile or redistribute the software components that constitute the GUI.

To attain this tight coupling between the GUI and models, while allowing the models to exist as separate processes required the use of inter-process communication techniques. These methods allow the GUI process to communicate with the model processes in an efficient, robust manner.

Robustness

Another difficult aspect of using advanced modeling tools is the issue of robustness. Given the myriad inputs, geometric data and advanced mathematics used by the models, issues such as convergence problems can arise that require the user to "tweak" model parameters appropriately. To help alleviate this and other problems, CFS was designed to insulate the user from these details. This functionality is due, in part, to each CFS implementation being uniquely targeted to a specific boiler. Again, this design requirement further enhances the ease of use of the software.

3.3.2 Software Implementation

Graphical User Interface

The GUI for CFS was built using Microsoft Visual C++ and the MFC class libraries. This development package offers state-of-the-art tools for Windows development. The core language of this environment, C++, provides sophisticated object-oriented capabilities that contribute significantly towards the CFS design goals of being configurable and extensible.

Using the development tools, we have created a very user-friendly environment where model input and controls are specified with menu items, toolbar buttons and interactive graphics. Where possible, these interactive graphics are constructed to provide an accurate depiction of the physical elements in the simulation, such as burners. The graphics are programmed to be interactive such that a user can simply click on a given area of the screen and specify associated properties (such as specifying the mass flow rate of air through a particular annulus of a burner).

Control and Monitoring of Computational Models

As previously stated, the user has complete control over the computational processes running under CFS and the user is provided with information regarding the status of the model. Starting the underlying models is accomplished from the GUI code by using Win32 API library calls, which spawn separate operating system processes. Stopping the models is again accomplished with API calls, which are designed to terminate processes. A separate thread of execution monitors model status, watching all the processes in question to ensure they are "healthy" (i.e., they haven't terminate unexpectedly or quit responding). Any problems or abnormalities are reported immediately to the user.

Inter-process Communication between GUI and Computational Models

As stated in the CFS design goals, the GUI and the computational models exist as separate operating system processes. This necessitates the use of inter-process communication techniques to provide data transfer capabilities between the processes. For portability considerations, this communication link was designed and implemented using BSD-style sockets. The sockets connection allows the GUI to send commands in real-time to the computational processes, and also allows the models to send run-time information and current results back to the GUI for examination by the user.

Coupling to Third-Party Post-Processing Packages

The capabilities incorporated in CFS to interface with post-processing software packages vary greatly depending on the package in question. FieldView (by Intelligent Light) provides powerful visualization capabilities and is the package most often coupled with CFS. In this case, CFS creates a FieldView process using spawning API calls, with command-line arguments providing configuration information. CFS also allows the user to control which variables are output from the computational models to FieldView compatible binary database files.

3.4 Example Implementation: CFS for Opposed Wall-Fired Boiler

In this section, we discuss briefly a CFS implementation that was created to model a common Foster Wheeler opposed, wall-fired boiler facility. This facility includes both under-fire and over-fire air ports. In the following sections, we present, in detail, problem setup, running the combustion model, viewing evolving model results and post-processing using the CFS software.

3.4.1 Problem Set-up

Air Properties

Combustion air properties are specified within CFS using a menu item selection and a corresponding dialog box. This dialog contains input boxes for the mole fractions of O_2, N_2 and H_2O. Figure 3.2 shows the menu and dialog box used for this purpose.

Fuel Properties

Properties for solid and liquid fuels are specified using the menu items and dialog boxes shown in Figure 3.3. As seen in this figure, solid fuels are prescribed by an ultimate and proximate analysis, higher or lower heating value and, if the solid fuel is coal, by percent-through-mesh information. Liquid fuels are specified by an elemental analysis, higher or lower heating value, and size information (needed to model droplets). CFS allows the user to create a number of different fuels, which can then be chosen from when selecting fuels entering the facility.

Burner Settings

Figure 3.4 shows the dialog boxes, which are used to specify burner settings. The left-hand dialog shown in this figure contains a graphical depiction of the walls of the boiler. Visible are over-fire and under-fire air ports and the burners. To specify settings for a given burner (or group of burners simultaneously), the user can simply select the burners in the left-hand

dialog box (using the left mouse button) and right click to get burner "properties". At this point, the user is presented with the dialog box shown on the right-hand of Figure 3.4. This dialog contains a depiction of the burner, which is tailored for the type of burners in the facility being modeling. From this dialog, the user can double-click (using the mouse) on the different burner annuli to specify airflow rate, fuel types, fuel flow rates, etc.

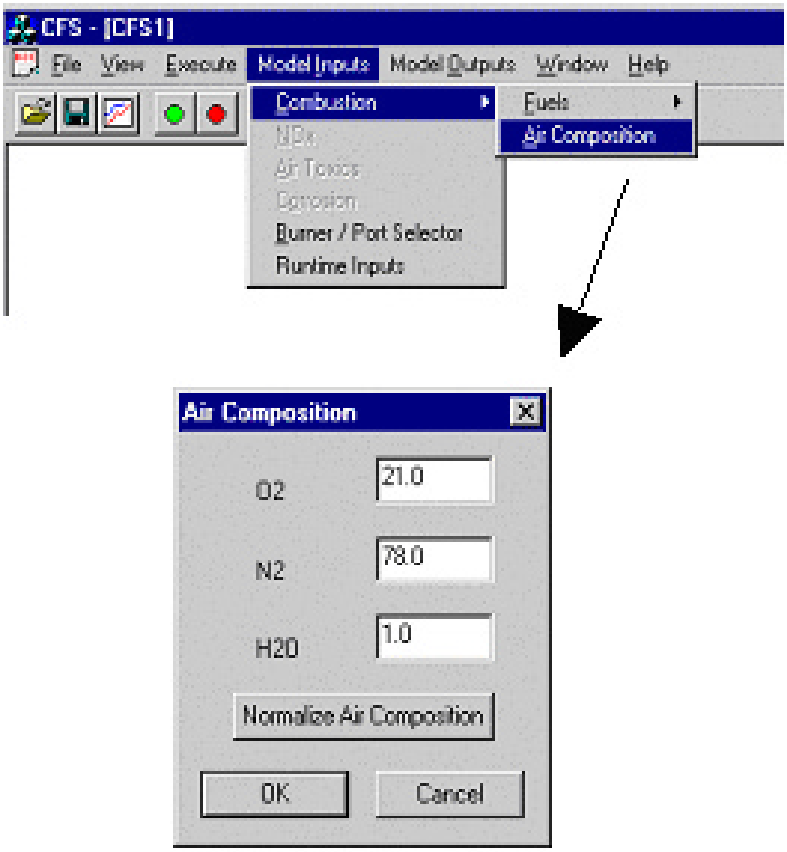

Figure 3.2 Specification of air properties.

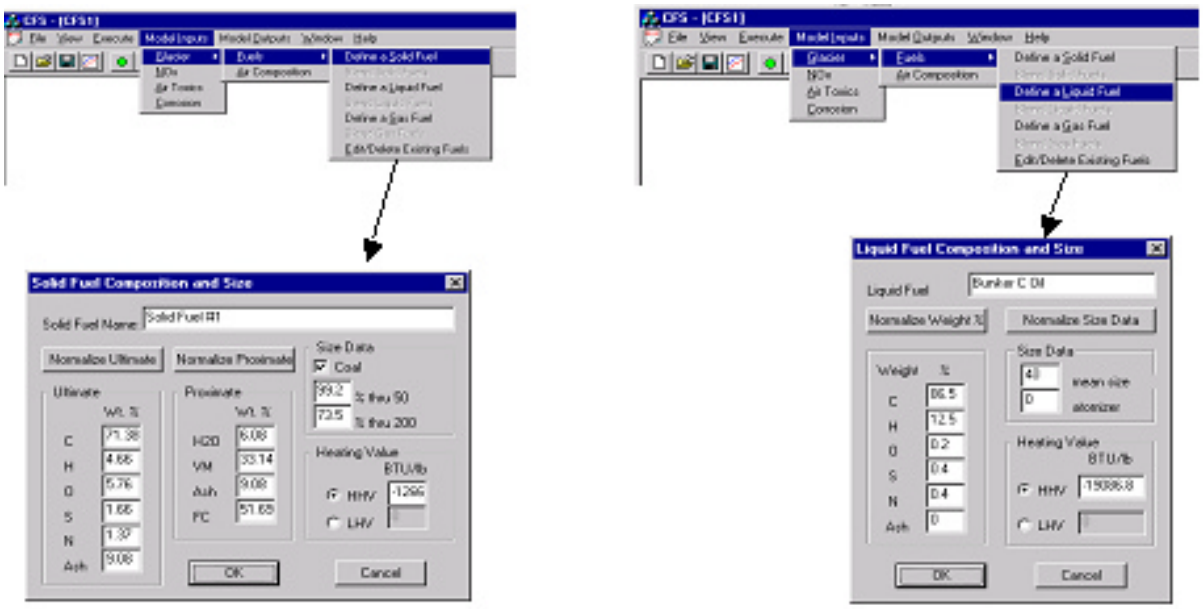

Figure 3.3 Specification of solid and liquid fuel properties.

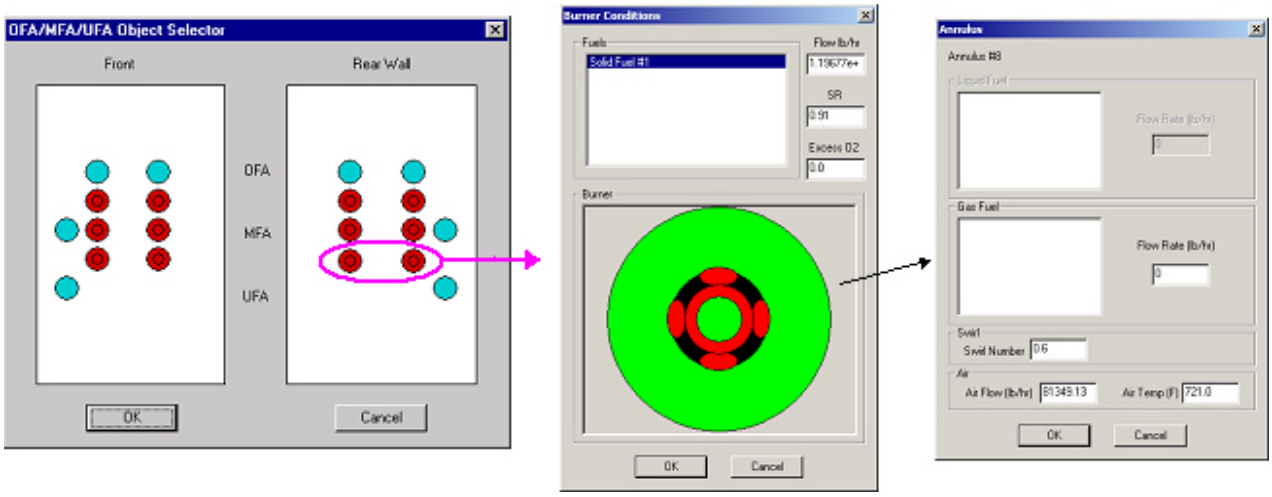

Figure 3.4 Specification of burner properties.

Over-fire and Under-fire Air Settings

Specifying settings for air ports is accomplished by using the left-hand dialog of Figure 3.5. The user chooses air ports with the mouse and is then presented with a dialog box for specifying temperature and mass flow rates. This dialog is shown on the right-hand side of Figure 3.5.

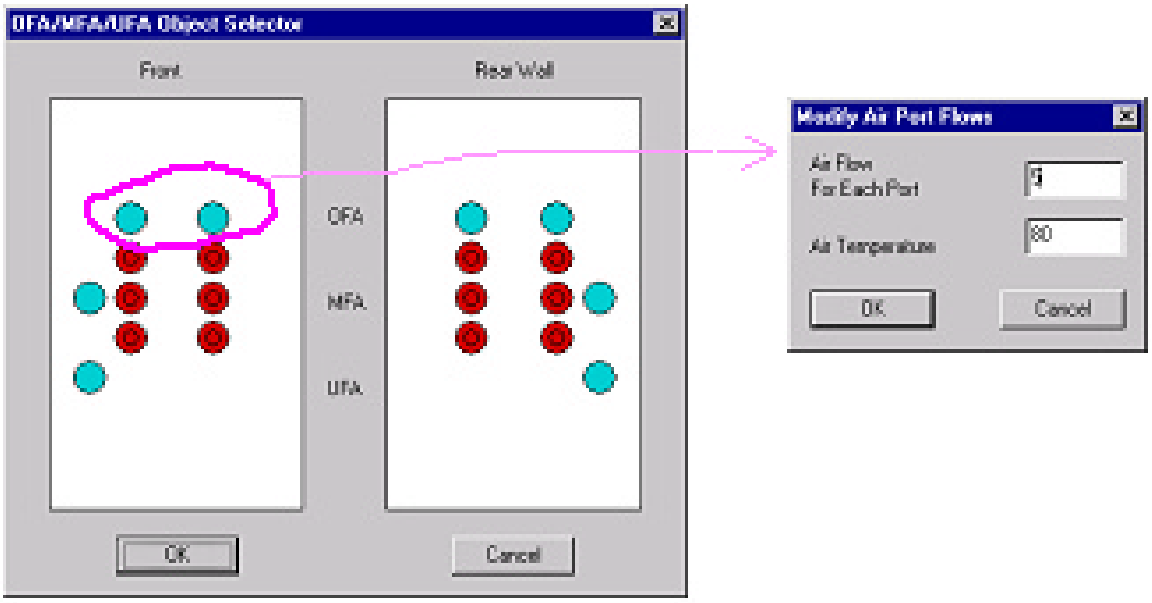

Figure 3.5 Over-fire and under-fire air settings.

Running the Model

When problem setup is complete, the model is ready to be executed. Figure 3.6 shows the main window of CFS. This figure details the main functionality provided by CFS to control model execution and to visualize results from the evolving solution.

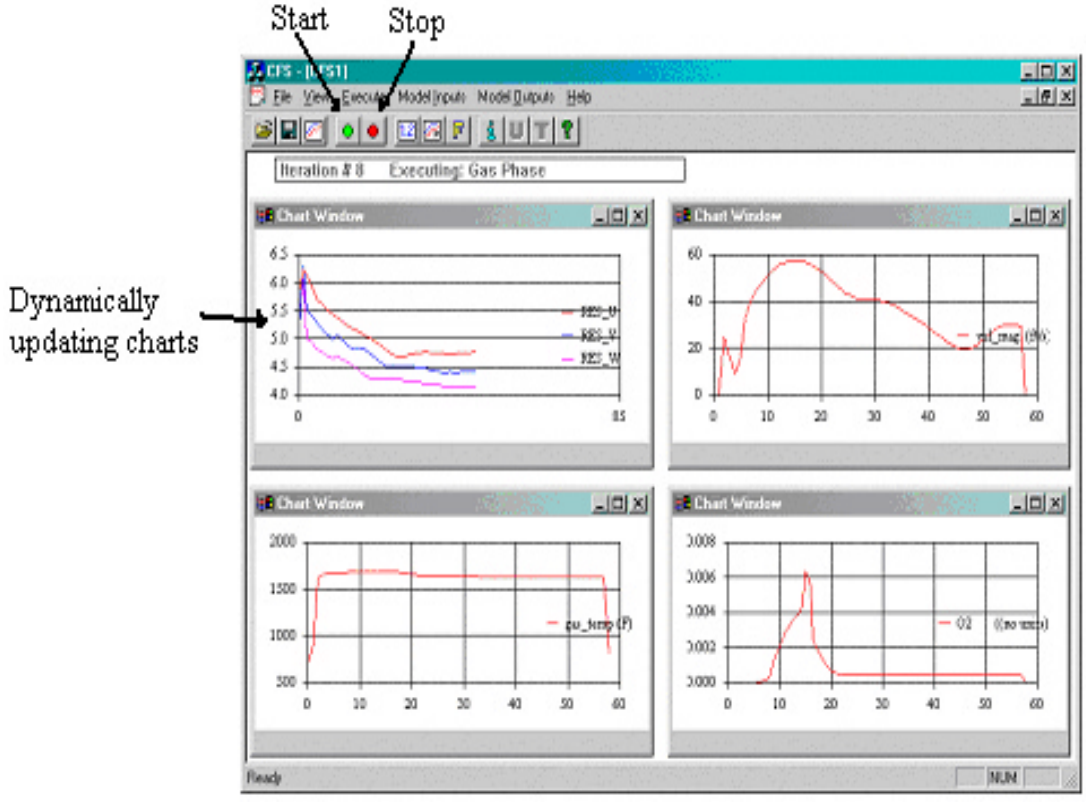

Figure 3.6 Model execution.

To begin execution of the combustion model, simply click on the toolbar button with the green circle (see Figure 3.6). The four charts that constitute the main window of CFS, after starting the model, will begin updating with evolving model results and convergence history. Note that by right-clicking on the bottom of each chart, the user can select which scalar quantity is plotted on the chart.

The combustion model will run for the specified number of iterations given in the run-time parameters dialog. If the user wishes to stop the case prior to this natural termination, the toolbar button with a red circle can be used. This will immediately terminate the combustion model.

Post-processing

Once the combustion model has completed successfully (or the user wishes to see the current detailed solution status), the FieldView (by Intelligent Light) post-processing package can be used for visualization of results. To start FieldView, the user can simply click on the toolbar button with the large "F" on it (see Figure 3.6). Once FieldView has started, the user can read in the output files from the combustion model, and visualize the solution using the detailed three-dimensional capabilities of the FieldView software. An example of using FieldView to visualize the temperature field inside the boiler is shown in Figure 3.7.

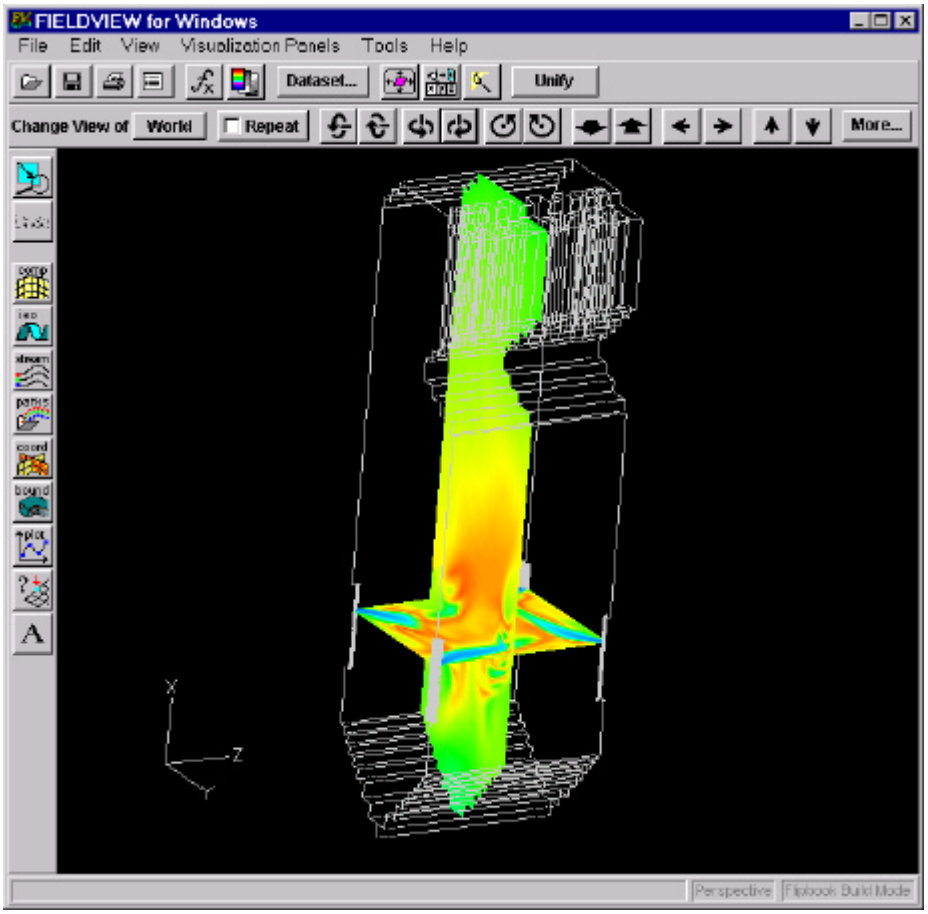

Figure 3.7. Example of FieldView cut-away of boiler.

3.5 Targeted Facilities and Applications

The CFS software was designed to be adaptable to a variety of modeling applications. CFS models are available for utility and industrial boilers, chemical process and ethylene cracking furnaces, rotary kilns, blast furnaces, smelters, stokers, thermal oxidizers, incinerators and flares. CFS provides numerous capabilities for modeling these facilities. Typical applications include:

- Low-NOx firing systems
- Cofiring of coal, gas, oil and biomass
- Fuel blending and fuel switching
- Burner balancing and zonal firing
- Staged air (OFA, UFA) and oxygen injection
- NO_x control strategies (SNCR, SCR, FGR, FLGR)
- Corrosion
- Air Toxics

3.6 Future Development of CFS

CFS functionality continues to be enhanced by the REI software team. Future developments include the addition of remote computing capabilities - allowing users the ability to execute the numerically intensive computational models on remote computer resources. This will allow users to run the CFS GUI on their desktop machines and control and monitor the progress of the simulations in the same user-friendly manner. Additional enhancements to the CFS software may also include porting to other operating systems, such as Linux.

3.7 Commercial Potential of CFS

Reaction Engineering has seen widespread interest in the CFS software concept. Several clients for whom REI has previously performed modeling jobs are interested in being able to run parametric modeling studies of their systems in-house. CFS models are routinely included as a standard option when REI provides cost proposals to potential clients.

The positive, enthusiastic response REI has received from potential users of CFS clearly illustrates the need for this software tool. For the first time, non-experts have powerful combustion simulation tools at their disposal.

4.0 WATERWALL WASTAGE

4.1 Introduction

Furnace corrosion problems can be difficult to diagnose and address. However, computational simulations can provide insight into the factors controlling the nature of the flow, temperature, and composition fields within a boiler. REI's in-house, two-phase, reacting, computational fluid dynamics software can simulate boilers fitted with advanced low-NO_X firing systems and provide a detailed description of conditions affecting waterwall corrosion such as local hydrogen sulfide concentration, heat flux, etc. Although the model cannot predict corrosion directly, empirical correlations relating corrosion rates to predicted properties are available. REI has performed computational simulations of several T-, wall- and cyclone-fired units with the goal of understanding and addressing corrosion difficulties related to combustion modifications for the reduction of NO_X emissions. Units evaluated include both subcritical and supercritical units.

The dominant mechanisms of corrosion at locations within a given boiler and from boiler to boiler can vary. Recent studies of corrosion in coal-fired boilers [Nava et al., 1997; EPRI, 1998; Bakker et al., 1999] indicate that corrosion rates can be dominated by the presence of rich gases (H_2S and CO) or by the deposition of coal/char/ash containing unreacted material (sulfide and carbon). In order to simplify our initial test efforts, the more straightforward gas-phase effects will be evaluated and are the focus of this research. Although it is thought that the highest corrosion rates (20 to 100 mils/yr) are caused by the deposition of unreacted coal [Davis et al., 1999; Bakker et al., 1999], gas-phase reactions can be important in a pulverized-coal-fired unit and could dominate in cyclone-fired boilers where deposition of unreacted material is small.

Figure 4.1 shows near-wall H_2S concentration contours along the front wall of a 480MW cyclone-fired boiler. As demonstrated in the first image, the only significant concentration of H_2S, prior to the use of fuel staging and overfire air, is in the fuel rich gases at the exit of the burners (the five circles near the bottom). After combustion modifications, the barrels are operated at a stoichiometry of 0.9 and the remainder of the combustion air is injected through overfire air (OFA) ports. The model indicates that the waterwall near and above the OFA will be exposed to rich gases that contain a much higher concentration of H_2S than before.

CFD simulations provide a wealth of useful information related to the corrosion of waterwalls and can be used to develop strategies for modifying operating conditions, fuel selection, and maintenance approaches. However, the availability of actual measurements, in addition to the simulation results, would be very useful. A few examples of how real-time corrosion rate measurements would be useful in tandem with CFD results follow:

1. As precise model inputs are often unavailable, predictions of the location and magnitude of a potential corrosion problem can be uncertain. With a rough idea of the region provided by the model, a probe or group of probes can be used to verify the location and to insure that corrective measures suggested by the model have met their goal.

2. The relationship between actual corrosion rates and corrosion indicators, which can be provided through CFD predictions, is not well understood. The combination of CFD results and probe data can be used to refine and validate these empirical relationships.
3. Real time monitors can pick up perturbations in operating conditions or other upsets to detect problems before they cause serious damage.
4. Although the usefulness of CFD predictions is becoming more widely accepted throughout industry, actual measurements provide additional confidence and can be used to identify where improvements or additional detail in a model is required.

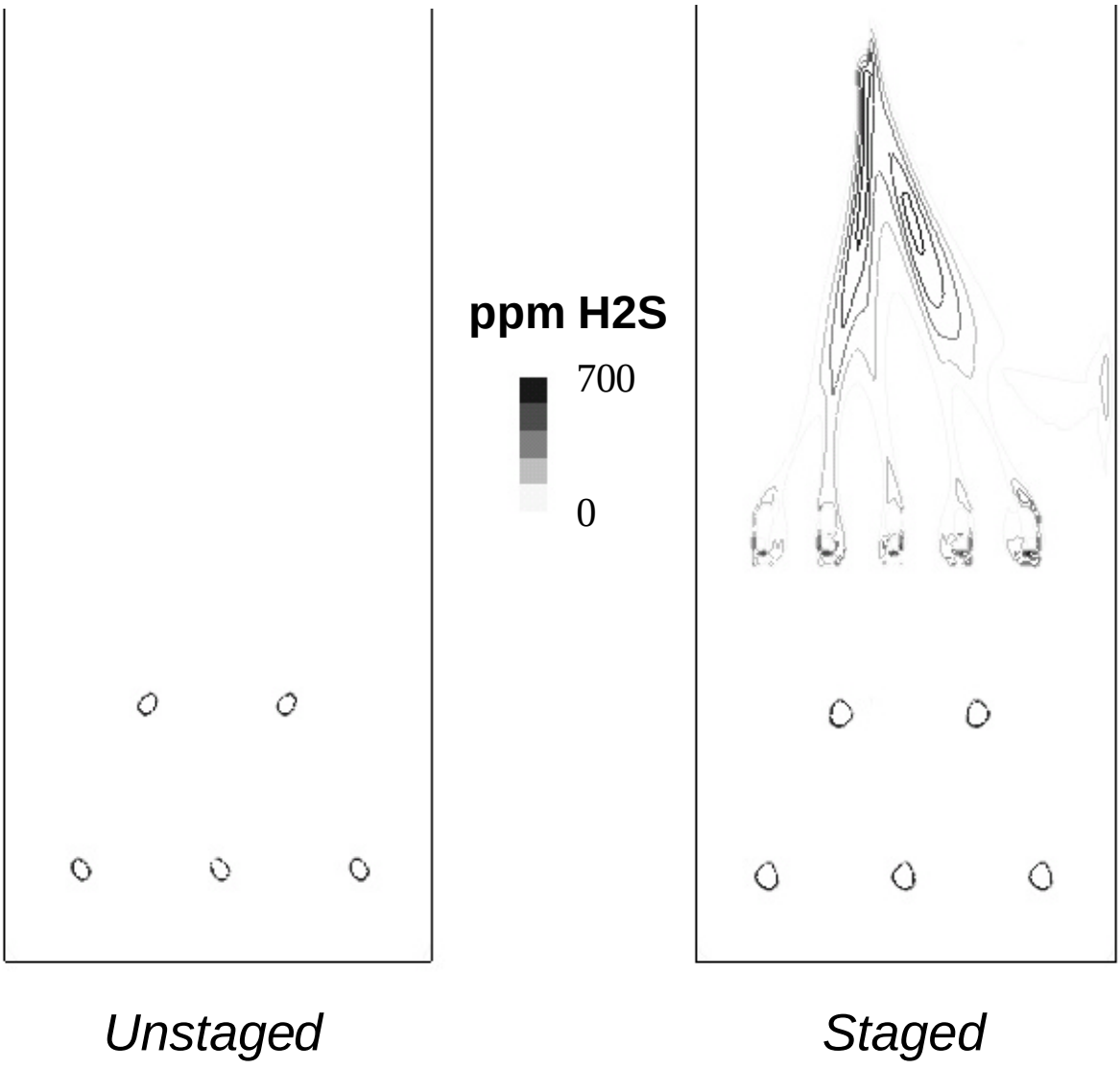

Figure 4.1. Near wall H_2S concentration in a 480-MW cyclone-fired boiler before and after combustion modifications for the reduction of NO_X emissions.

4.2 Available Technologies

Although estimates of cost savings vary, the advantages of using preventative and predictive maintenance approaches are well recognized. Application of this approach however requires effective diagnostics. Tools for retrospective monitoring of waterwall wastage have existed for many years. These techniques include ultrasonic wall-thickness measurements, radiography, and weight loss coupon determinations; unfortunately, such methods are difficult to implement on a time frame shorter than that between successive outages. The challenge therefore is to develop a technology capable of providing information on a time scale that will allow operators to determine when prevailing operating conditions, if allowed to continue unabated, would result in unacceptable rates of waterwall wastage - as opposed to knowing that damage has already been done.

The value of an improved diagnostic for this purpose is clear. Several efforts have been undertaken in recent years, but to date there is no widely used tool for on-line corrosion monitoring in boilers. The technologies that have been tested and that are, in most cases, still being developed include probes that measure electrical resistance, linear polarization resistance, activated thin layer radioactivity, electrochemical impedance and electrochemical noise. Although each of these technologies has shown sufficient promise to be considered for specific corrosion applications, none has been demonstrated by itself to be effective in the prediction of high temperature degradation in utility boilers. We believe however that recent improvements in commercially available capabilities to measure the small signals required in the electrochemical noise (EN) approach, combined with the application of modern CFD methodologies, could provide improved management of the furnace wall environment. Recent trials in a variety of challenging environments suggest that this approach would be cost-effective for application in large commercial coal-fired plants. The purpose of these initial trials was to verify the capability of an on-line electrochemical sensor to deliver the required sensitivity and speed of response to fault conditions, as a precursor to full-scale plant trials.

4.2.1 Electrochemical Sensor Approach

Fundamental Description

The sensor arrangement of the technology under consideration utilizes non-perturbative measurements to evaluate electrochemical activity associated with corrosion and degradation processes as they occur at the furnace wall. Electrochemical noise analysis techniques are used to analyze fluctuations in current and voltage occurring between nominally identical elements as illustrated in Figure 4.2. These fluctuations can be used to characterize the electrochemical condition at a corroding interface. For linear polarization, $\Delta v/\Delta i = R_p$, in a manner similar to Ohm's law, where Δv and Δi are incremental changes in voltage and current respectively and R_p is a consequent polarization resistance. Similarly, it has been shown that the RMS value of the voltage noise divided by the RMS value of the current noise (defined as the "resistance noise") can be used to determine the rate of a corrosion process, the rate being inversely proportional to the resistance noise magnitude [Eden et al., 1986; Mansfield and Xiao, 1986; Tan et al., 1996].

The following features make noise analysis particularly useful [Syrett and Cox, 1996]

- Current and voltage transients indicative of high corrosion rates are detectable almost instantaneously and, more importantly, well before significant material loss occurs.
- The sensor array is very compact, with the potential to be small enough to insert in the webbing between boiler tubes.
- The nature of these transients provides quantitative and qualitative insight into the rates and mechanisms of the corrosion at the metal surface.

Although these features make this technology very attractive, further development and testing is required to establish its use for application in the demanding environment encountered by the sensors and probe body in, and near, the furnace and the wiring and computer hardware outside the furnace of a coal-fired unit.

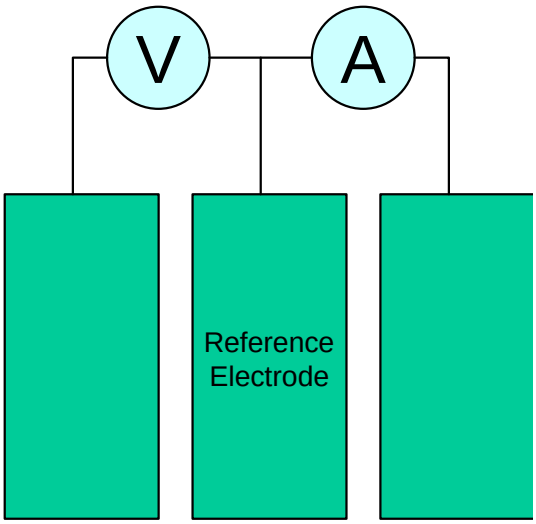

Figure 4.2. Conceptual diagram illustrating voltage and current noise measurements between "identical" electrodes.

Implementation

When a boiler that has been designed for conventional burners is fitted with low-NO_X burners and/or overfire air ports, the composition of the flame is altered to minimize oxygen-rich environments, particularly at the flame front. However, the fuel-rich flame of a low-NO_X burner is often longer and hence has a tendency to impinge on the waterwalls. The combined effects of reducing flame chemistry, reactive material deposition and higher tube metal temperatures increase the rate of metal degradation at particular locations within the furnace. Locations where fluctuations between oxidizing and reducing conditions occur are especially at risk. The effect is often unsteady and is affected by factors such as boiler load, burner configuration, fuel variability, slagging and soot-blowing conditions. These locations are often known to operations and maintenance personnel because they sustain the greatest damage. One response is to coat or overlay the tubes in problem areas. However, if the

problem is not addressed at the source, nearby unprotected areas can sustain attack and either the tubes have to be replaced or the expensive alloy cladding procedure progressively has to be extended.

An alternative approach is proposed in which a strategic plan is taken to the management of the combustion environment. Specific conditions of load, fuel and boiler design generate the combination of gas composition and tube metal temperature which place the boiler at risk of attack. These conditions cause oxidation, sulfidation, or (in some situations) high temperature chloride attack of the boiler tubes. It is possible for key locations, most at risk of attack, to be predicted by CFD modeling. Unfortunately, this alone is not sufficient to prevent attack because there is no visible indication of the risk to the operations personnel when the plant is in service. The purpose of the on-line electrochemical sensor is to provide continuous verification that the predicted boundary regime for the onset of tube damage has not been exceeded at key locations. If an electrochemical response is detected which indicates the onset of degradation, and an indication of the incipient risk is presented to operations personnel in a timely manner, small changes in burner configuration could be addressed so as to prevent tube damage. Controlling the fault condition, by the application of preventive measures at the most highly susceptible locations, ensures that degradation is lower in adjacent locations.

In some circumstances it may be decided for commercial reasons that water wall degradation will be tolerated. In this case, the combination of modern predictive risk management and on-line sensor technology can be used to provide an indication of the degree to which the service life of the wall tubes has been compromised. This enables precise costing and scheduling of remedial activities, thereby maximizing unit reliability, availability and operating profit.

4.3 EN Probe Description

The body of the current probe is approximately 3 feet in length and 3 inches in diameter; however, the design can be modified for deeper required penetrations or for placement between waterwall tubes. The main probe body contains a flush-mounted corrosion sensor housed in a water-cooled aluminum jacket. The sensor assembly is a multi-element sensor machined from carbon steel with a composition similar to that of a typical waterwall membrane. The operating temperature of the sensor assembly is precisely controlled with cooling air that enters down the central tube. The set-point temperature can be controlled locally or remotely. Data are output from the probe to the data acquisition unit, which is located in a nearby plant control room or instrument void. The computer monitors the current and potential noise, zero resistance ammetry current, conductivity of deposits, and polarization resistance of the corrosion cell.

The equipment, shown schematically in Figure 4.3, is comprised of:

- The probe with sensor array, mounting flange, and water and air connections,
- An air flow control valve with input from the temperature controller,
- The electrochemical signal evaluation unit (electrochemical interface, or corrosion monitor), where the noise, temperature and (possibly) other process signals (for example, pH, conductivity, ion analyses, etc.) are interfaced, and

- A data logging, display and control computer.

The computer contains an Ethernet network card, so that it can download process data from the plant computer, and it can upload corrosion results calculated from the electrochemical responses. The unit therefore is self-contained and can operate independently of the process control instrumentation, while downloading appropriate data from it. Also, where an appropriate network is available, the unit can be supervised remotely.

The face of the probe is positioned in line with the outermost curvature of the wall tubes. If the face sits too far back into the wall, the hot furnace gases do not blow past it in a representative manner. Alternately, if the face is too far forward, the surface temperature of the probe will not be representative of tube conditions and slagging will tend to occur. The sensor is inserted through an access port in the wall of the boiler or combustion rig. It is important that any gaps along the probe be sealed as air in-leakage alongside the probe can have a significant impact on corrosion conditions at the sidewall location.

It is possible to use this instrumentation to measure the cumulative rate of damage, as has been done by wall thickness inspection methods in the past. However, the objective now is to be able to take immediate remedial action to prevent continued damage, thereby ***managing*** the corrosion condition and preserving the fabric of the boiler.

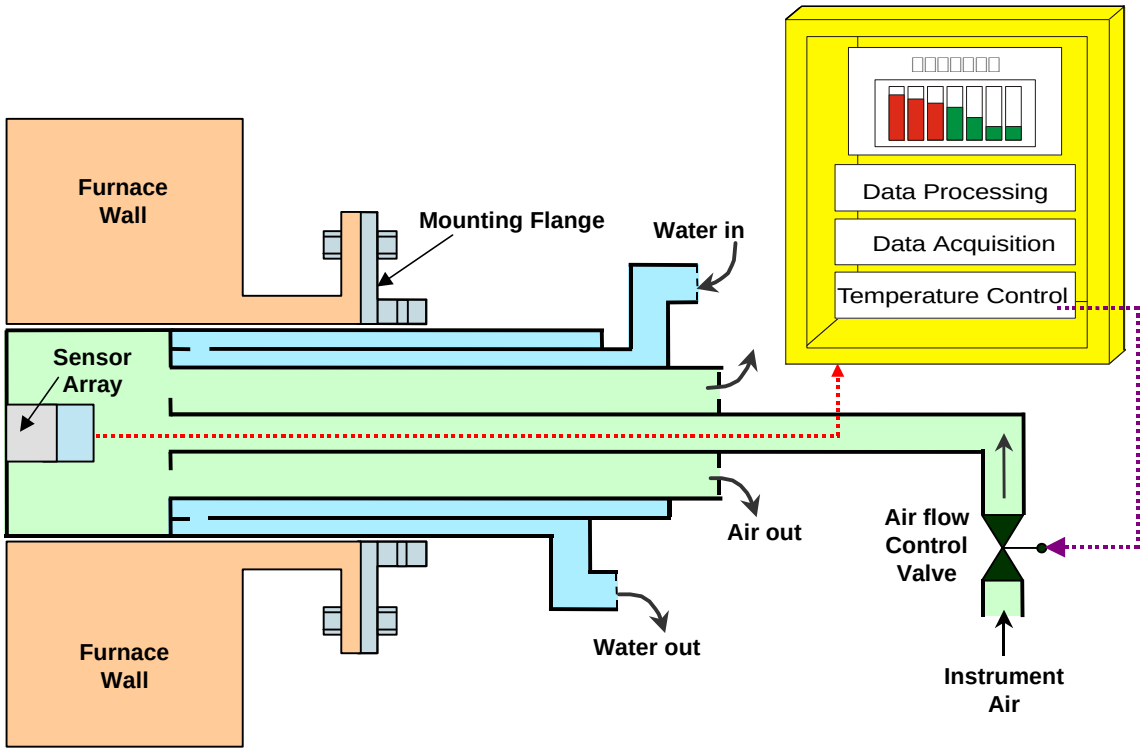

Figure 4.3. Corrosion probe schematic.

4.3.1 Results

Initial tests of the system have been performed in two facilities used by Reaction Engineering International at the University of Utah's Advanced Combustion Engineering Research Center: a nominal 15 MMBtu/hr pilot-scale furnace and a 150,000 Btu/hr laboratory furnace as discussed in Section 6. Initial tests were performed at pilot-scale as the system is designed for the higher heat fluxes and more stable conditions typical of full-scale units. Further testing was then continued in the laboratory in order to reduce costs during a more systematic and long-term series of tests to evaluate the impact of stoichiometry and sulfur concentration.

Pilot-scale Testing

Sets of tests were performed as an initial evaluation of the system under conditions typical of a coal-fired boiler. In order to roughly approximate the ash loading of a cyclone-fired plant, the furnace firing rate was achieved with approximately 10% coal and 90% natural gas. This results in an ash layer on the surface of the sensor array, which theoretically should not adversely effect the operation of the probe. This was verified during the testing. The arrangement of the equipment with respect to the furnace is shown in Figure 4.4. The sections of the furnace are clearly visible in this photograph. The burner is located well to the right of the test section (the third section from the right) to allow complete combustion and thorough mixing of the product gases. Burnout air is added downstream of the test section (the large hose looping down from the roof of the furnace entering the fourth section). Also visible in the photograph is the gas sample probe (the long pipe extending out from the third section), which passes a continuous sample to several analyzers including a UV analyzer setup for H_2S measurement.

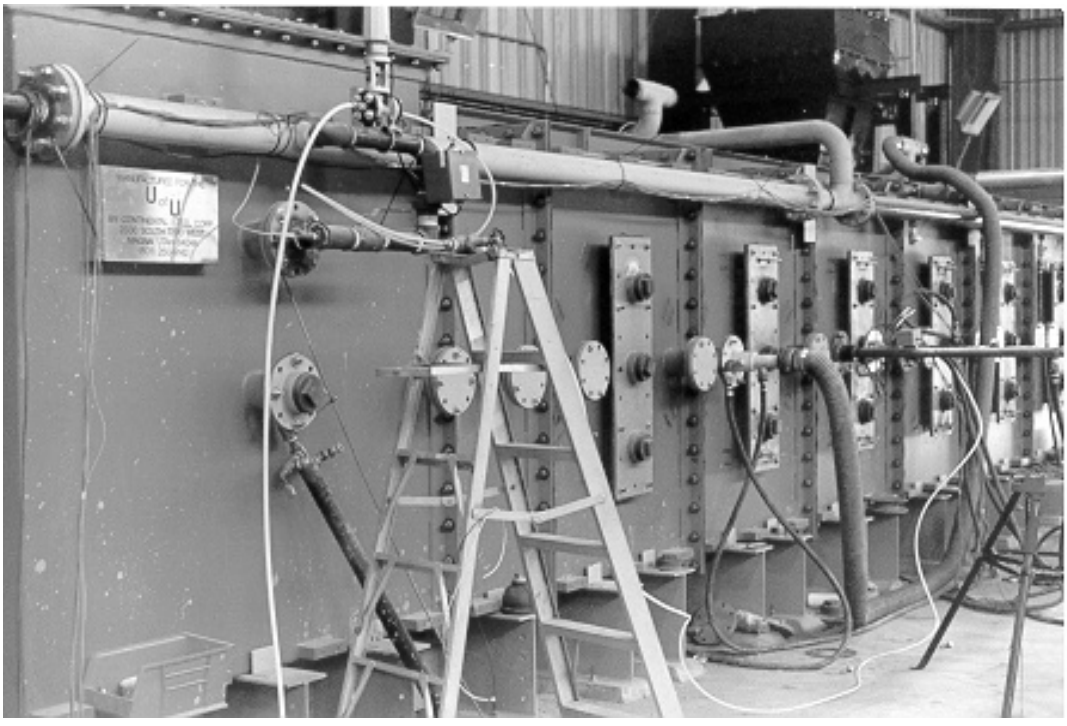

Figure 4.4. University of Utah pilot-scale experimental test facility.

The probe itself is also in the third section, just upstream from the sample probe. The control valve for the corrosion probe cooling air is at the top of the photograph above and to the left of the ladder. The probe was operated continuously in this furnace for a period of several days. During the last day of testing, the furnace stoichiometry was adjusted every four hours with the purpose of varying H_2S concentration. Average corrosion rates were then determined for each H_2S concentration. As Figure 4.5 shows, tests were run with no H_2S before and after tests at different H_2S levels.

These data suggest the following:

- Significant levels of corrosion exist even without H_2S.
- Corrosion increases as H_2S concentration increases
- The increase in corrosion is qualitatively similar to that predicted by the Kung correlation [1997].

The testing at this scale was remarkably trouble-free. Setup of the equipment involved less than two days, operation was relatively simple, and no maintenance was required during the test. The initial and final test periods, run with no H_2S, show that the corrosion rate is within an order of magnitude of corrosion rates observed at higher H_2S levels. In his work, Kung [1997] correlates corrosion rates with H_2S concentration, surface temperature and steel composition such that no corrosion would be indicated in the absence of H_2S. However, corrosion problems in boilers have long been tied to rich conditions even when sulfur species are not present. This is a concept that will be explored further in the laboratory tests.

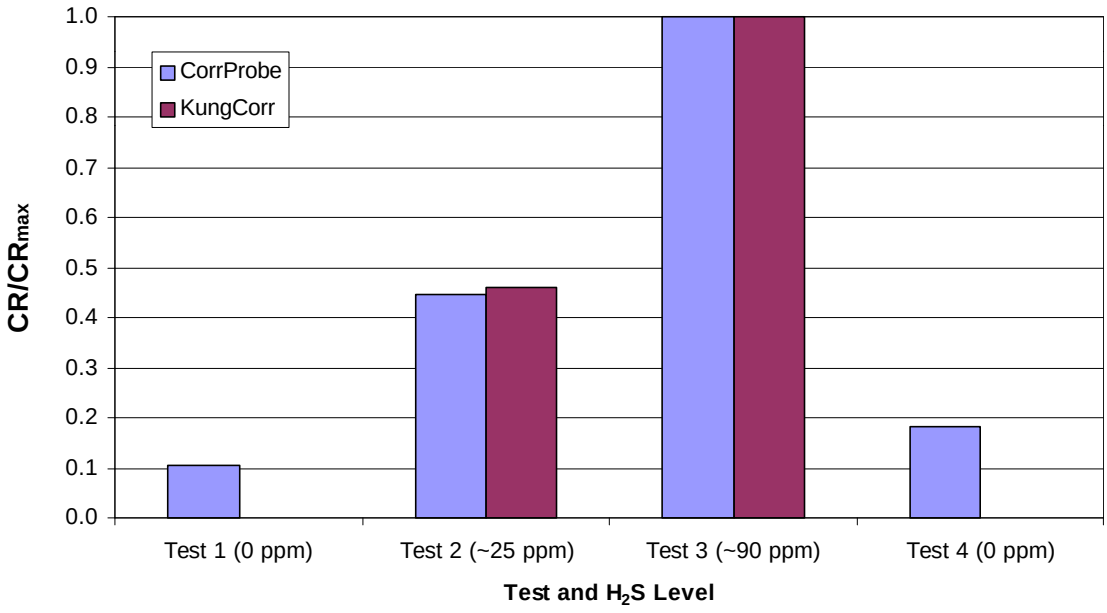

Figure 4.5. Pilot-scale results illustrating the effect of H_2S on corrosion rate.

Lab-scale Testing

In order to more cost effectively evaluate the behavior of the probe under conditions where stoichiometry and H_2S concentration could be independently controlled, the system was transferred to a second site containing a lab scale furnace. Operation of the corrosion probe at the laboratory scale was more problematic due to the significantly lower heat flux and generally less stable conditions. However, the scale (150,000 Btu/hr) made it practically convenient to continuously test over a period of several weeks. Again, as in the pilot scale tests, the probe was inserted well downstream of the burner such that mixing was complete. Although this test program is still in its early stages, a series of tests involving stoichiometry variations has been completed. The results presented here do not examine H_2S variations and rely solely on natural gas as a fuel. This natural gas does however contain sulfur species that result in approximately 10 ppm of H_2S in the combustion gases under fuel-rich conditions.

Figure 4.6 illustrates the nature of real-time data recorded over a period of about a day-and-a-half. The test period begins at a stoichiometric ratio (SR) of 0.90. The SR is then increased to 0.95, is set back to 0.90 again, and finally is lowered to 0.85. The fluctuations in the data are not unreasonable for a phenomenon such as corrosion. As a surface corrodes it is possible that pits and crevices can form abruptly thereby exposing fresh surfaces. Although the actual sampling frequency of the data from the sensor array is one Hz, the recorded data presented in this paper is the result of averaging over a period of approximately eight minutes. The physical mechanisms of metal loss can happen in an irregular manner, leading to variations in the corrosion rate on time scales shorter than that of the averaging period. Mean corrosion rates however still clearly show that the corrosion rate increases as fuel rich conditions become more extreme. Although the quantitative accuracy of these measurements is uncertain as this system is being extended to untested temperature regimes and fluid environments, the corrosion rates indicated are reasonable in both trend and magnitude.

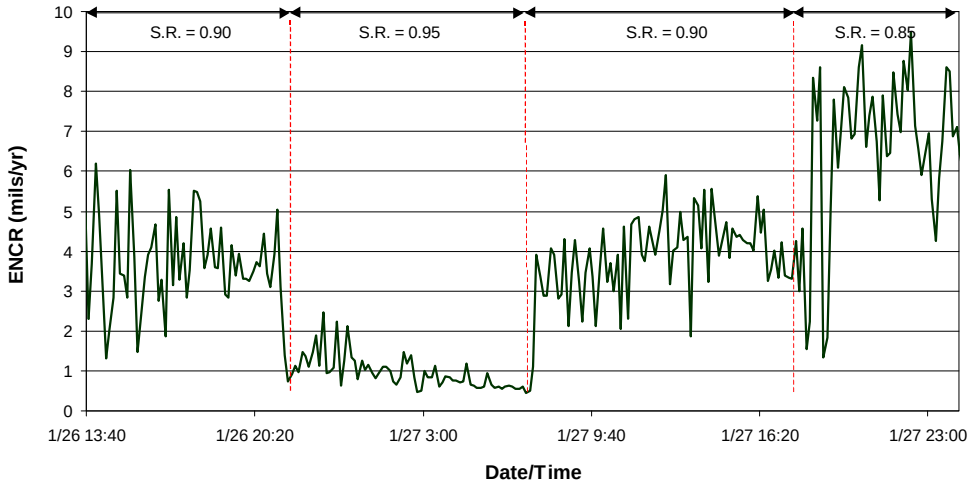

Figure 4.6. Corrosion rate data in a laboratory scale furnace over several stoichiometries.

Testing was performed over a range of stoichiometries and data and averages were calculated for each series of tests. The results of this effort are shown in Figure 4.7. The two different symbols are indicative of two series of tests performed at different times. Although the scatter in the data is noticeable, the trend of increasing corrosion with decreasing stoichiometry is clear. In addition, this trend appears to be non-linear such that lower stoichiometries become increasingly problematic. The data in this plot gives quantitative information; however, as mentioned previously the uncertainty in the data is still being investigated at this point.

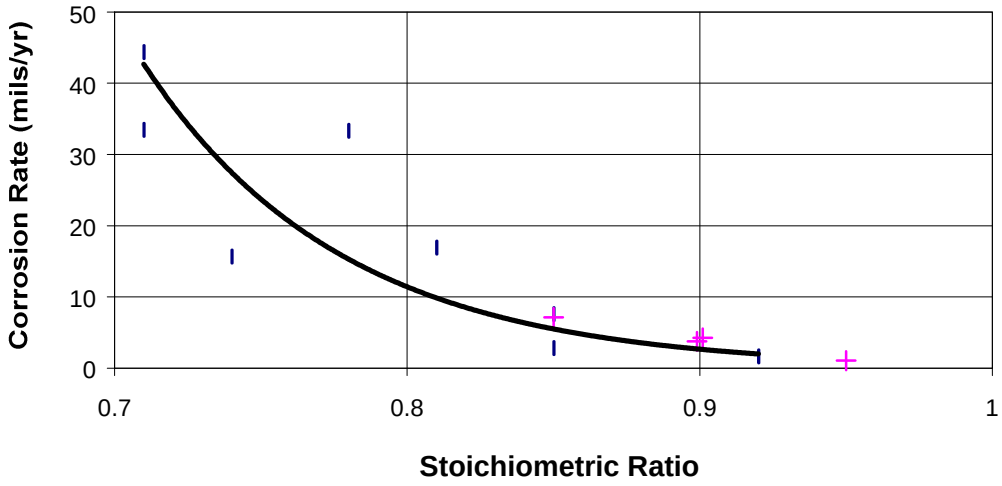

Figure 4.7. Lab-scale results illustrating the effect of stoichiometry on corrosion rate.

Additional tests were completed where the probe temperature was increased while holding all operating conditions constant to show the effect of corrosion on higher temperature waterwalls. These results are shown in Figure 4.8. The response from the corrosion probe mirrors the temperature increase confirming the fact that the higher the boiler waterwall tube temperature, the higher the corrosion rate at the same set of operating conditions. This becomes important from a practical standpoint as supercritical boilers, with higher waterwall temperatures will have higher corrosion rates than subcritical units. This has been shown to be the case in practice as well.

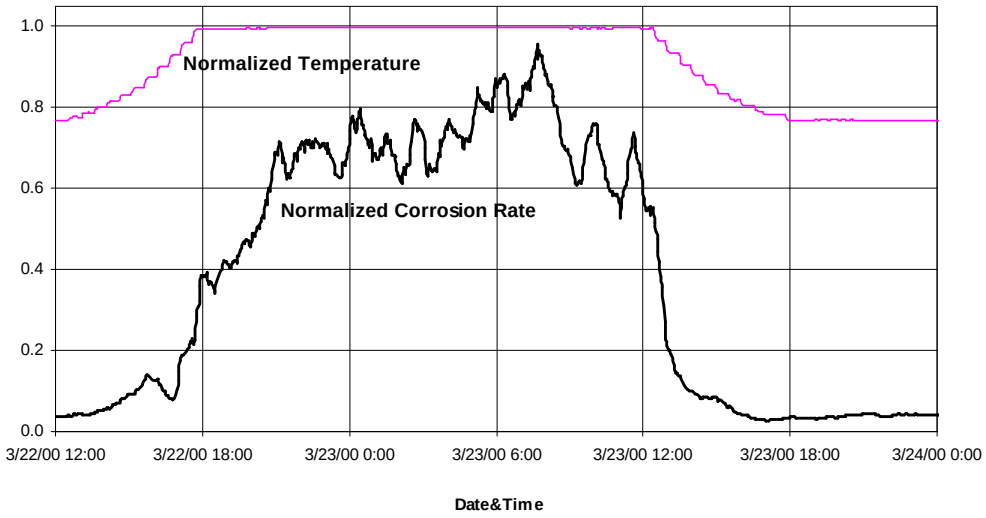

Figure 4.8. The effect of temperature on corrosion.

Boiler Installation

An opportunity arose near the completion of this program to take the corrosion probe and install it in a full-scale operating boiler. The unit selected was the NRG (Conectiv) B. L. England Station located outside Atlantic City, NJ. The boiler is a 135 MW cyclone-fired boiler with three barrels, 1 over 2. The location of the access port for the corrosion probe was in the lower furnace directly across from one of the barrels. Figure 4.9 shows the corrosion probe installed in the unit.

Figure 4.9. Corrosion probe installed in B.L.England Station

For this program, the corrosion probe was checked-out and initial testing was completed. Additional work with the corrosion probe is part of the follow-on DOE program entitled "NO_X Control Options and Integration for U.S. Coal-fired Boilers" (DOE Contract No.: DE-

FC26-00NT40753) and privately funded programs with the Ohio Coal Development Office and utility companies.

Figures 4.10 and 4.11 show the response of the corrosion probe in the boiler during a start-up sequence and some steady-state operation.

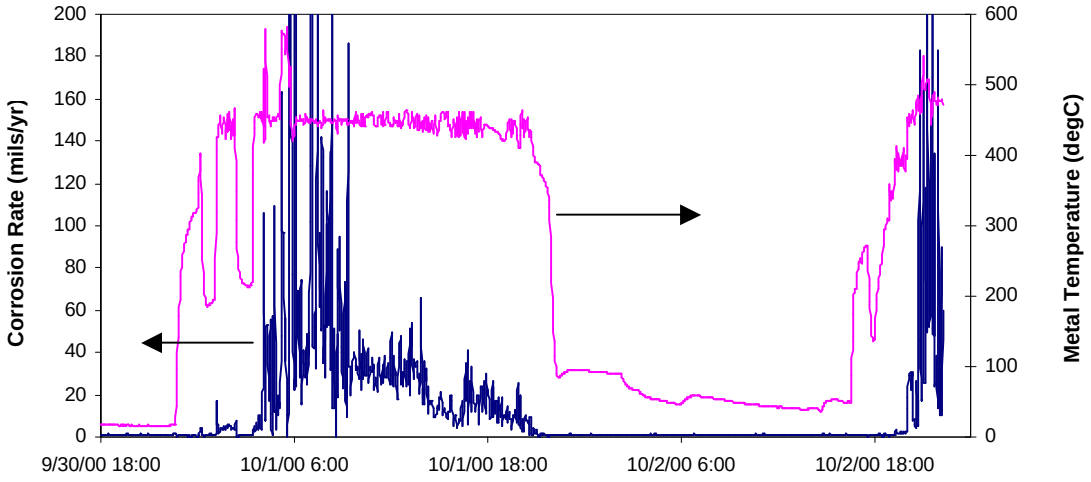

Figure 4.10. Corrosion probe response during start-up and shut down sequence.

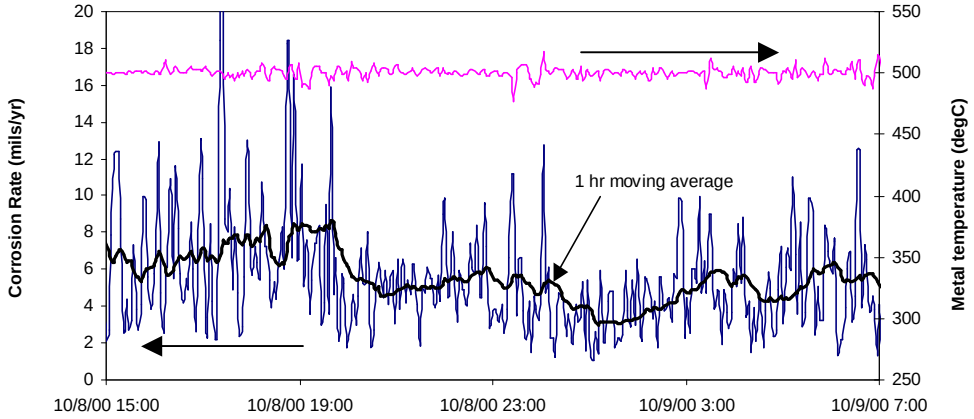

Figure 4.11. Corrosion probe response during steady-state operation.

The probe is now being further tested and calibrated against known corrosion rates. The current plans are then to install it in two different boilers, one a cyclone-fired unit and the other an opposed-wall-fired unit. Testing in each boiler will be approximately one month.

4.4 References

W. T. Bakker, S.C. Kung, M. Heap, J. Valentine, "Waterwall corrosion in low NO_X boilers: Root causes and remedies," EPRI-DOE-EPA Combined Utility Air Pollution Control Symposium: The MEGA Symposium, Atlanta, GA, August 16-20, 1999.

K. Davis, J. Valentine, E. Eddings, M. Heap, W. Bakker, A. Facchiano "Waterwall corrosion after combustion modifications for NO_X control," 24th International Technical Conference on Coal Utilization & Fuel Systems, Clearwater, FL, March 1999.

D. A. Eden, K. Hladky, D. G. John and J. L. Dawson, Corrosion 86, Paper 274, NACE, 1986.

EPRI, Effect of Iron Sulfide on Furnace Wall Corrosion, Palo Alto, CA: 1998. TR-111152.

S.C. Kung, "Prediction of corrosion rates for alloys exposed to reducing/sulfidizing combustion gases," *Materials Performance*, vol. 36, No. 12, pp. 36-40, December 1997.

F. Mansfeld and H. Xiao, *J. Electrochem. Soc*., vol. 140, p2205, 1986.

"Power Plant Diagnostics Go On Line," Mechanical Engineering, December, 1989.

J. C. Nava , A. L. Plumley, and R. Knodler, "Wastage control in low emission boiler systems," Proceedings: Third Int'l Conference on Boiler Tube Failures in Fossil Plants, Nov. 11-13, 1997.

B. C. Syrett and W. M. Cox, "A review of EPRI projects since 1984 that used electrochemical noise measurement instrumentation," Electrochemical Noise Measurements for Corrosion Applications, Electrochemical Noise Measurements for Corrosion Applications, pp. 173-185, ASTM, 1996.

Y. J. Tan, S. Bailey and B. Kinsella,, *Corr. Sci*., vol. 38, p1681, 1996.

5. CHAR REACTIVITY

This section discusses the work on char reactivity carried out at Brown University. This work was divided into three subtasks:

1. The development and testing of carbon burnout submodels;

2. An experimental study of the effect of combustion conditions on unburned carbon *properties* (rather than *amount*), with emphasis on those properties critical to practical ash utilization markets;

3. An experimental study of the nitric oxide and oxygen reactivity of chars as a function of fuel type and heat treatment conditions.

Detailed results from these three subtasks are described in separate sections below. The report emphasizes the specific work done in Phase II of the project, but also incorporates results from Phase I and other sources as appropriate to put the results into perspective and to point out their significance and practical implications.

5.1 Development and Testing of Carbon Burnout Submodels

Much progress has been made in recent years in our understanding of single particle coal combustion as it occurs in the high-temperature environment of pc-fired boilers. A variety of experimental studies have addressed in-flame heat treatment [Shim and Hurt, 2000], single-particle extinction [Essenhigh et al., 1999a,b], coal-to-coal differences in char reactivity [Hurt and Mitchell, 1992, Hurt et al., 1996], and the implications of each of these for burnout.

In this subtask we have drawn on this recent experimental data to develop a series of char combustion submodels specifically designed to model carbon burnout. During Phase I we completed the Carbon Burnout Kinetic Model (CBK) Version 6 and in Phase II have completed a major upgrade leading to the release of CBK8. The CBK8 development was co-funded by a separate DOE project (DE-FG22-96PC96249) and by the Electric Power Research Institute. In addition we have used the model to carry out parameter studies revealing the intrinsic sensitivity of carbon burnout to various fuel-related parameters. The development of CBK8 and the sensitivity studies are discussed in detail below.

5.1.1 CBK8 Development

Previous studies have documented large decreases in particle temperature in the late stages of carbon combustion [Froberg and Essenhigh, 1978; Mitchell, 1990; Hurt and Davis, 1994; Hurt et al., 1998], including several studies specifically focused on conditions found in pulverized fuel-fired boilers. Mitchell [1990] used *in situ* particle sizing micro-pyrometry to observe the sudden appearance of particles near the local gas temperature after long residence times in an optically accessible entrained flow reactor. The author attributed this observation to ash-rich particles in the final stages of burning. In a subsequent study [Hurt and Davis, 1994] the optical data were analyzed further to show that many of these particles

have emissivities indicative of a carbon-rich composition. Also, in separate experiments with captive particles, extinction-like events were directly observed by long-focal-length video microscopy [Hurt and Davis, 1994]. It is clear that pulverized char combustion occurs in two distinct stages: a rapid high temperature stage followed by an extinction-like event that greatly increases the time required to reach the very high conversions required in industrial practice (> 99%). In this original paper [Hurt and Davis, 1994], the mechanism responsible for the extinction-like events was not identified.

A number of mechanisms have been subsequently considered to explain the extinction phenomena, including reactivity loss by thermal annealing [Hurt et al., 1998], mineral/carbon interactions [Michell, 1990; Hurt et al., 1998; Lunden et al., 1998, Antxustegi et al., 1998] and the preferential consumption of more reactive carbon. A carbon burnout model was recently proposed that incorporates submodels of annealing, ash effects, and statistical kinetics [Hurt et al., 1998]. This model, CBK6, predicts extinction-like events under certain conditions, but only for ash-containing particles. In later work, Lunden et al. [1998] did not find well-developed ash films at a sufficiently low conversion to explain the extinction-like events for Pittsburgh seam coal chars. Also, further captive particle imaging experiments directly reveal extinction events even for particles with little or no ash [Hurt and Davis, 1999]. The same set of experiments showed extinction behavior at gas temperatures from 1150 - 1250 K to be precursor dependent, occurring for bituminous coal chars but not for lignite chars. The CBK6 model requires at least one additional extinction mechanism needed to predict the rank-dependent behavior and the extinction of ash-free particles.

Very recently, Essenhigh et al., [1999a,b] have carried out analyses of internal reaction and diffusion in char particles and concluded that the Zone I reaction mode (corresponding to complete oxygen penetration) can occur under pulverized coal combustion conditions. These authors also conclude that accounting for the Zone II to Zone I transition is key to modeling extinction behavior in the late stages of combustion [Essenhigh et al., 1999a,b]. Also relevant to this discussion on extinction mechanics is new information available on thermal annealing under flame conditions [Russel et al., 1997; Shim and Hurt, 2000].

In this project we re-examined the complete mass and energy transport processes that govern char particle temperature, and used the recent literature to consider a number of separate mechanisms that may lead to extinction and extinction-like phenomena. The result of this study has led to a new version of CBK (Version 8) that explains each of the observations related to extinction-like behavior in the experimental studies cited above. The model development focuses primarily on two sets of combustion conditions:

1. pulverized coal char combustion (PC) conditions defined here by: 20 $\mu m < d_p < 150$ μm; $1500 < T_g < 2000$ K; $3\% < [O_2] < 12\%$; $500\ K < T_w < T_p$.

2. captive particle imaging (CPI) conditions as used in the Sandia experiments defined by 100 $\mu m < d_p < 300$ μm; $900 < T_g < 1250$ K; $3\% < P < 19\%$; $T_w \sim 500$ K.

In addition, however, the CBK8 predictions will prove to be consistent with measured oxidation rates at much lower temperatures (500 ^oC) for a suite of U.S. coals of various rank [Jenkins et al., 1973].

Theory

Equations 5.1 – 5.4 represent the single particle energy balance in simple approximate form, assuming non-absorbing, non-emitting gases, no interparticle interactions (dilute solids limit), and omitting the correction for Stefan flow.

$$m_p C_p \, dT_p / dt = Q_{rxn} - Q_{rad} - Q_{conv} \tag{5.1}$$

where

$$Q_{rad} = A \, \sigma \, \varepsilon \, (T_p^4 - T_w^4) \tag{5.2}$$

$$Q_{conv} = A \, U \, (T_p - T_g) \tag{5.3}$$

$$Q_{rxn} = R \, (-\Delta H_{rxn}) / MW_C \tag{5.4}$$

The governing relations for oxygen transport have been presented previously [Hurt et al., 1998]. To ensure validity through complete burnout, this general theory must consider mineral matter, which necessarily becomes the principal component at some point late in the combustion process. Mineral inhibition is generally believed to be a secondary effect under most conditions, but has been shown to be important when ash is abundant and in a partially fused state [Hurt and Davis, 1994; Lin et al., 1994]. After three passes through the Sandia entrained flow reactor (total residence time 350 msec) the ash is observed to be partially fused, occurring in irregular geometries, and often in intimate contact with islands of remaining carbon. In these entrained flow reactor samples at high conversion, ash can be expected to influence both heat and mass transfer to the unreacted carbon islands. The present analysis therefore considers the effect of mineral matter on both heat and mass transfer, using an idealized geometry consisting of a spherical particle with an internal spherical carbon core. Note that adoption of this idealized geometry for modeling purposes is not meant to represent true ash encapsulation, which has been observed in at least one incident in the field, but is believed to be rare. The overall heat transfer coefficient, U, is now given by:

$$U = \frac{\left(\frac{d_p}{d_c}\right)^2}{\left(\frac{1}{h_{ext}} + \frac{1}{h_{int}}\right)} \tag{5.5}$$

where: $h_{ext} = \dfrac{\lambda_g \, Nu}{d_p}$ and $h_{int} = \dfrac{2 \, \lambda_a}{\delta} \dfrac{d_c}{d_p}$ (5.6)

Here d_p is the overall particle diameter, d_c is the diameter of the residual carbon island, and λ_a is the thermal conductivity of the porous ash, given as the volumetric average of the gas phase conductivity, λ_g , and the conductivity of the fully dense mineral phase, $\lambda_{a,true}$:

$$\lambda_a = (1- \theta)\, \lambda_{a,true} + \theta\, \lambda_g \qquad (5.7)$$

where θ is the porosity of the aggregated ash. Analysis of equations 4.5-4.7 reveals that ash can either increase or decrease heat transfer rate depending on the value of the Nusselt number for convective loss. In the small particle limit (Nu = 2) ash always enhances heat transfer, acting in the manner of a fin conducting heat from the carbon surface to a larger external area. It is surprising that a porous glassy component does not act as a net insulator, but this can be physically rationalized by considering that the ash replaces a gas phase, which in the small particle limit (Nu = 2) is effectively stagnant and is an even better insulator by virtue of its lower thermal conductivity.

Internal Reaction and Diffusion

This section presents a simple kinetic model for the overall burning rate, R, appearing in Equation 5.1. For this work, the single particle combustion rate, R (gm carbon/sec), is modeled by the simple expression:

$$R = \eta\, k_o S\, e^{-E/R\, T_p}\, P_s^n\, m_p \qquad (5.8)$$

where k_o is the preexponential factor for the surface rate constant (gm carbon/s-cm^2-atm^n), S is the total surface area/mass, (cm^2/gm), E is the intrinsic activation energy, P_S is the oxygen partial pressure at the outer particle surface (atm), n is the empirical apparent reaction order for the range of T and P_S examined, m_p is the carbon mass in the particle (gm), and η is the dimensionless effectiveness factor:

$$\eta = \frac{1}{\phi}\left[\coth(3\,\phi) - \frac{1}{3\phi}\right] \qquad (5.9)$$

where ϕ is a generalized Thiele modulus for spheres [Froment and Bischoff, 1990]:

$$\phi = \frac{d_p}{6}\left[\frac{(n+1)\;\; k_0 S\, \rho\, (P_s/RT)^{(n-1)}}{2\, D_{eff}}\right]^{1/2} \qquad (5.10)$$

A value of η near unity indicates a Zone I reaction mode, in which the observed rate is approximately equal to the intrinsic chemical rate. Values of h much less than unity indicate a Zone II reaction mode, in which the oxygen penetration depth is much less than the particle radius and observed rates are much less than intrinsic rates at the given particle temperature. Equations 5.9 and 5.10 yield good approximate values of η for all exponents $0 < n < 1$ in power law kinetics [Froment and Bischoff, 1990]. The oxygen partial pressure at the particle surface, P_S, is found by solution of mass transfer relations for boundary layer

diffusion and diffusion through porous ash in series, as described elsewhere [Hurt et al., 1998].

It has been noted previously that the parameters k_o and S appear together in this formalism and for some purposes can be advantageously treated as a single parameter, k_oS — a "mass specific intrinsic reactivity". The lumped parameter k_oS is a property of a carbon sample that can be directly measured (e.g. in TGA experiments). The subsequent decomposition into the individual parameters k_o and S requires choice of an appropriate surface area (subject to uncertainty for microporous chars or catalyst-containing chars) and, while often providing detailed insight into reaction behavior, offers no particular advantage for the specific analyses in this paper.

The major challenge in applying this formalism is the estimation of the effective diffusivity, D_{eff}, a property of the complex inhomogeneous pore structure of chars. Pore diameters span up to five orders of magnitude, from 4 Å micropores to 40 μm vesicles. Diffusion limitations may occur in pores that feed the particle interior or in microporous regions lying between the large feeder pores [Satterfield, 1981; Carberry, 1962]. Of primary interest here are the transport limitations to the particle interior, as these occur over the whole particle length scale and must be described explicitly to predict the influence of particle diameter on overall rate.

Transport to the particle interior is believed to occur primarily through large feeder pores [Simons, 1983] in which diffusion occurs in or near the molecular regime. Although a significant fraction of the porosity and almost all the surface area in chars lies on the surfaces of fine (micro- and meso-) pores, these pores are not believed to be primarily responsible for providing long-path-length transport to the particle interior [Simons, 1983]†. Simple calculations with the parallel path pore model confirm that the meso- and micro-pores contribute little to the long-path-length transport for pore size distributions typical of flame chars.

With this simplifying assumption, the effective diffusivity for transport to the particle interior will be modeled as $D_{eff} = D_M \theta f/\tau$, where D_M is the molecular diffusivity, θ the total porosity, f is the fraction of the total porosity in feeder pores, and τ is the tortuosity. The advantage of this simple approximate formulation is that D_M and θ are known at all points from T, P, d_p, and particle density, and the complex nature of the pore structure in char is embodied in the ratio f/τ or (τ f) which can be treated as a single empirical parameter. In practice the parameter (t/f) will absorb other factors neglected here, such as the influence of partial Knudsen diffusion in the smaller feeder pores. It will be seen later that a single, physically realistic value of the intraparticle transport parameter, (τ f), without adjustments for rank or temperature, allows the description of reactivity and extinction behavior over a wide range of fuels and conditions.

Pseudo Steady State Solutions: Extinction and Near Extinction

The features of the complex equation set (5.1 - 5.10) are best understood by examining certain simplified cases. In particular, if the term m_pC_p dT/dt (representing the particle

thermal mass) in Eq. 5.1 is small (as is often the case during near-isothermal burning), the differential equation is transformed into an algebraic equation which can be solved jointly with the remaining 9 equations to yield the instantaneous particle temperature, T_p.

Figure 5.1 depicts the basic relations in the form of two separate curves of heat flow, Q, vs. particle temperature for each of two sets of conditions in pseudo steady state in the form of the classical Semenov theory. The first curve gives the heat release rate, Q_{rxn}, by solving the reaction and mass transfer relations alone for known T_p. The second curve represents the energy balance and yields Q_{loss} (= Q_{rad} + Q_{conv}), while the intersection of the two curves gives the particle temperature in the limiting case of small $m_p C_p \, dT_p / dt$.

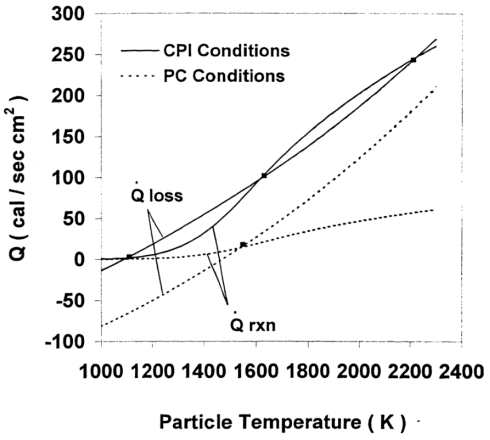

Figure 5.1 Analysis of the single particle energy balance under the pseudo-steady-state approximation for two sets of combustion conditions: (1) typical pulverized coal (PC) conditions (T_g = 1500 K, P_{ox} = 0.06, d_p = 23 μm); and (2) captive particle imaging (CPI) conditions (T_g = 1100 K, P_{ox} = 29%, d_p = 23 μm, T_w = 300 K). Note the existence of multiple steady states under CPI conditions, but not under PC conditions. Model parameters as in Table 5.1.

---

† This treatment adopts the view of Simons [1983], that a given fine pore is statistically unlikely to intersect the external surface of a char particle. The porosity in chars thus functions like a tree, in that large pores provide the long-path-length transport to the particle interior, feeding the fine pores acting as branches and leaves. Further scaling analysis yields the counter-intuitive result that as temperature is raised, diffusion limitations arise first in the larger pores and only thereafter in the fine microporous zones. For this reason, the present analysis focuses on the long-path-length transport to the particle interior through the largest pore class as the main mass transfer resistance. Even if some diffusion limitation does exist in microporous grains, it not materially affected by particle diameter, and its effects may be approximately absorbed into the intrinsic surface rate coefficient.

It is seen from Fig. 5.1 that there is only one steady state under PC conditions, while three steady states are possible under CPI conditions at lower gas temperatures. In the latter case the upper and lower steady states are stable with respect to small perturbations, while the middle steady state is unstable. As a result, the upper and lower are both observable in practice and the appearance of one or the other depends on previous particle history (initial conditions). Careful exploration of the entire range of PC conditions (stated in introduction) revealed multiple steady states only under very restricted conditions at the fringes of the regime ($[O_2]$ 12%, d_p 20 μm, cool walls, T_g 1500 K, low reaction order, and high activation energy). Specifically, when choosing PC conditions found to be most favorable for the existence of multiple steady states (12 mol-% oxygen, cool walls, 1500 K gas temperature, zero intrinsic reaction order, and 40 kcal/mol activation energy) multiple steady states were only observed for particles smaller than 20 μm. Under the conditions where extinction-like events were observed in the previous entrained flow reactor experiments [Hurt and Davis, 1994], no multiple steady states were found. Even in the CPI range, high oxygen concentrations are often required to bring about the phenomenon of multiple steady states.

Under CPI conditions in Fig. 5.1, a gradual decrease in gas temperature can cause a discontinuous change in the pseudo steady T_p due to loss of the upper point of intersection, as has been shown elsewhere [Essenhigh et al., 1999a,b]. Under most PC conditions, however, because multiple steady states are not observed, the particle temperature drops continuously, eventually reaching the inert particle limit when the reaction is too slow to significantly influence the energy balance. To distinguish these two phenomena, we will refer only to the first discontinuous change as an "extinction". The mathematically continuous change, if it occurs over a narrow time interval can lead to a rather abrupt transition and will be referred to as a "near-extinction". If the temperature drop occurs over an extended time interval, it deserves no special designation. In practice, the temperature drop during a true extinction event will be abrupt, but not instantaneous due to the thermal lag associated with the transient term, $m_p C_p \, dT_p/dt$. As a result, it is not always possible to distinguish a true extinction event from a near-extinction event based on data — it is a mathematical distinction that ultimately requires analysis for proper classification by these definitions.

Figure 5.2 shows the heat release and heat loss curves under CPI conditions with elevated oxygen in Arrhenius form. Also shown for comparison is the heat release curve predicted by a simple model based on constant Zone II reactivity, rather than solution of the internal reaction/diffusion equations. Only the full solution shows the lower unignited state, emphasizing the importance of the Zone I/II transition for the proper prediction of extinction behavior. Also note the absence of a clearly defined Zone II region in Fig. 5.3. Rate estimation *within* the Zone I/II transition region requires solution of the differential equation for internal reaction and diffusion, which in some treatments has been accomplished by splicing separate asymptotic solutions for Zone I and Zone II at a prescribed transition point. Figure 5.3 shows that this asymptotic solution technique can exhibit multiple steady states when the full solution does not. The calculations in Fig. 5.3 are based on a reaction order of 0.5, however, and the accuracy of the asymptotic approximation is observed to improve significantly at lower reaction orders.

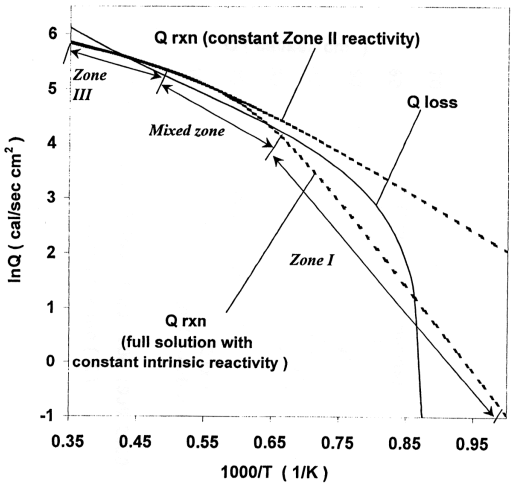

Figure 5.2 Arrhenius-form depiction of the single particle energy balance under the pseudo-steady-state approximation for CPI conditions chosen to be favorable for multiple steady state behavior (T_g = 1150 K, P_{OX} = 29%, d_p = 23 μm). Also shown for comparison is the heat release curve predicted by a simple model based on constant Zone II reactivity, rather than solution of the internal reaction / diffusion equations. Note that the full solution is required to observe the multiple steady states including the non-ignited solution at 1000/T = 0.85. Note also in the full solution that there is no identifiable zone II region, with a constant slope of -E/2R, but a continuous transition from Zone I to Zone III.

Numerical simulations

A large set of comprehensive single-particle simulations were carried out, accounting for internal reaction and diffusion, annealing, and ash effects. The goal of these simulations was to determine if a single set of coal-general parameters could describe the complete set of observations summarized in the introduction. The main parameters varied were τ/f, which establishes the effective diffusivity; and δ_m and θ_{taf} which give the ash grain size, and ash porosity respectively. A rank-dependent correlation for initial reactivity, k_oS_o, was derived by fitting the model to Sandia entrained flow reactor data on a suite of coals of various rank. Table 5.1 summarizes typical and recommended fuel-general values of these three parameters and gives other important constants that fully define the new model, CBK8.

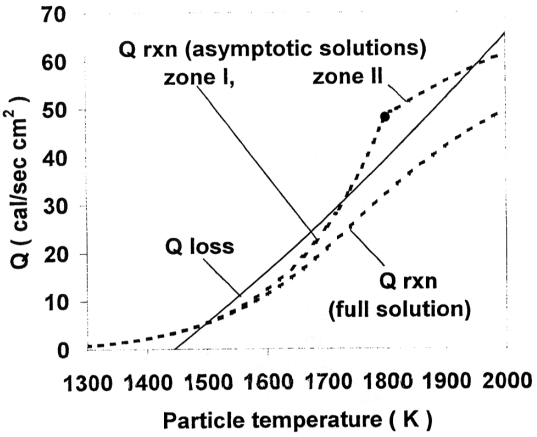

Figure 5.3 Comparison of full solution and Zone I/II asymptotic solution to the single particle energy balance under the pseudo-steady-state approximation. Combustion conditions and kinetic parameters are chosen to be favorable for multiple steady state behavior but to lie within the PC range: T_g = 1500 K, P_{ox} = 12 mol-%, d_p = 50 μm, E = 40 kcal/mol, n = 0, T_w = 300 K. The asymptotic solution consists of the Zone I curve and Zone II curve spliced together at a transition temperature reported in the literature, without explicit treatment of the transition zone. It is seen that the asymptotic approximation can exhibit multiple steady states that are not observed in the full solution.

Table 5.1
Recommended CBK8 Model Parameters for Fuel-General Estimates

Name	Symbol	Value
Adjusted parameters		
carbon pore structure parameter	τ / f	6
mineral grain size	δ_m	5 μm
porosity of final ash particle	θ_{taf}	0.17 (PC temperatures) >0.5 (CPI temperatures)
correlation for initial reactivity:	$\log_{10}(k_o S_o)$ = 14.97 - 0.0764 (wt-%C)	(daf in parent coal)
Additional parameters		
intrinsic reaction order	n	0.5
intrinsic activation energy	E	35 kcal / mol
empirical constants† for CO/CO_2 ratio	A_C	200
	E_C	9 kcal/mol

† derived from summary of literature kinetic data by Skokova [1997].

Figures 5.4 - 5.7 show example predictions generated with CBK8 and the above parameter set. Figure 5.4 compares the measured and predicted mass loss profiles for Illinois #6 and Wilcox lignite. The model correctly predicts the shape and magnitude of the mass loss curves at all times and conversions (to 99%). Also shown on Fig. 5.4 are the predictions for hypothetical chars with no mineral content. The two predictions for Illinois #6 are the same, indicating that mineral effects are not responsible for the near-extinction of this char. The two predictions for Wilcox lignite do show an effect of mineral matter on near-extinction. The different behavior of the two coals can be understood as follows. The much more reactive Wilcox lignite maintains high burning rates in Zone II reaction mode until high conversion (90 - 95%), at which point the abundant mineral matter is predicted to modify the heat and mass transfer and induce near-extinction. A similar effect is predicted for larger particles (~ 300 μm) that develop an ash film before they are small enough to approach the Zone I regime. In contrast, the less reactive Illinois #6 chars extinguish earlier by a mechanism that does not involve ash, and because the subsequent reaction occurs essentially in Zone I, transport processes are no longer limiting and the increasing ash content has no effect on the rate, even as burnout advances well into the ash-rich region.

More insight into the underlying cause of the near-extinction event for Illinois #6 coal chars is provided by Fig. 5.5. Particle temperature is seen to drop continuously after 30% conversion, and the drop becomes steep near 70 - 80% conversion, the point where the knee in the curve is observed in Fig. 5.4. This decreasing temperature is accompanied by a decrease in R/R_{max} to near zero, indicating the disappearance of boundary layer concentration gradients, and an increase in effectiveness factor, η, to near unity, indicating the disappearance of internal gradients. These particles begin their combustion lifetimes reacting in Zone II/III transition region, and fall to Zone I conditions during the near-extinction event. The underlying cause of the near-extinction in this case is a decreasing particle diameter (see Figure) with a lesser contribution from annealing-driven decreases in reactivity, k_oS, and from decreasing density. Accounting for the Zone II/I transition is found to be important for the proper prediction of many such near-extinction events, in agreement with the conclusions of Essenhigh et al., [1999a]. It is found in most simulations that annealing occurs early, causing k_oS to change rapidly at low conversion, but slowly thereafter. Recent direct measurements have shown char reactivity to be very sensitive to peak temperature, even for exposures on second- and sub-second time scales [Russel et al., 1997; Shim and Hurt, 2000]. Annealing is thus an important factor in coal flames, but its major influence is felt early and it is rarely predicted to be the primary cause of near-extinction events in the late stages of combustion (compare the shapes of the T_p and k_oS curves in Fig. 5.5).

The same parameter set successfully predicts rank-dependent extinction under CPI conditions (see Fig. 5.6). The lignite char maintains a high particle temperature late in burnout due its intrinsically high reactivity that maintains Zone II/III conditions even for smaller particles. Ash does not cause near-extinction in these simulations because a higher ash porosity was used (θ_{taf}, = 0.5), based on microscopic observations of unfused mineral grains which agglomerate into low-density, lacy structures at the lower particle temperatures of CPI experiments (1100 - 1300 K).

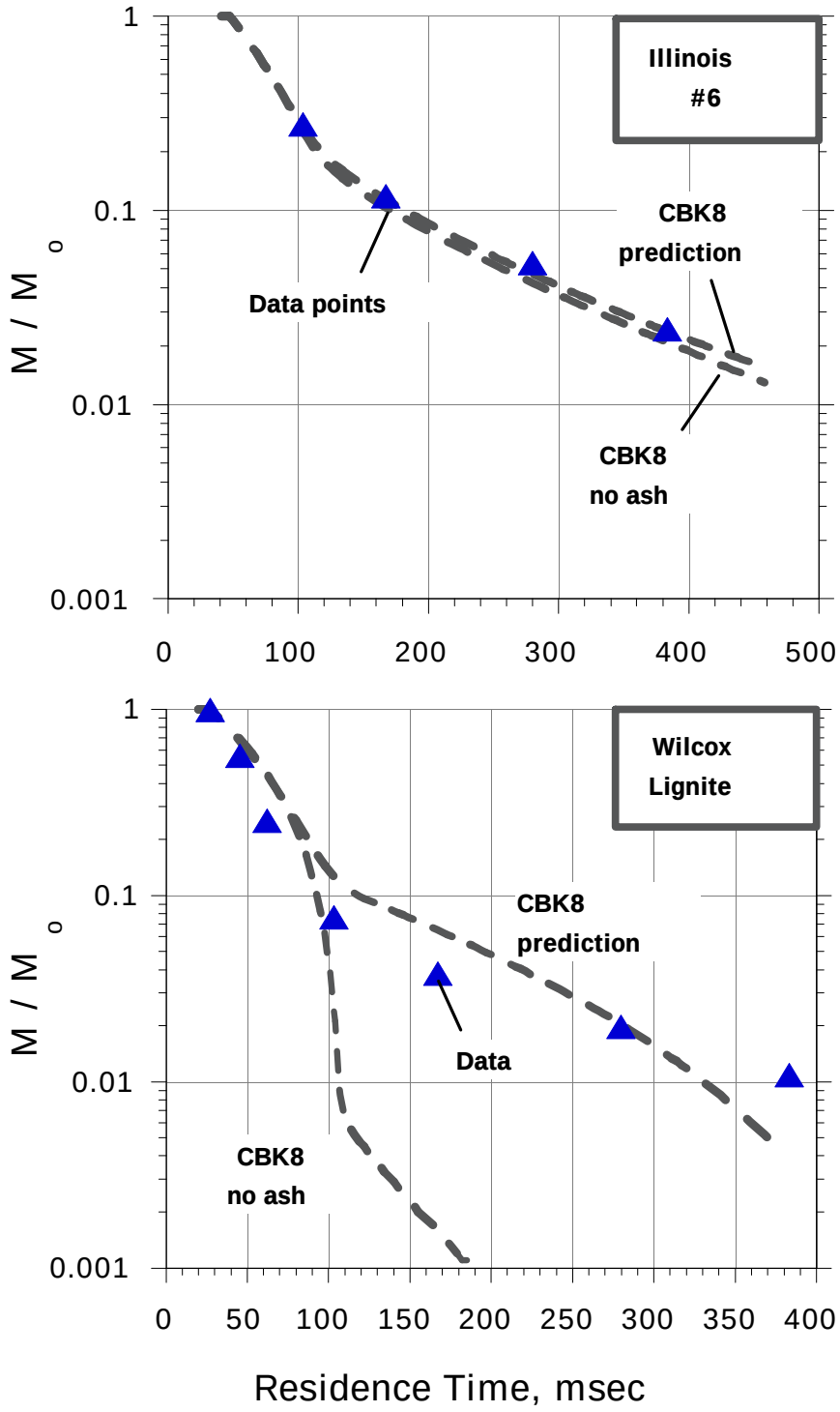

Figure 5.4 Overall carbon conversion as a function of time determined by extractive sampling in a hybrid flame-driven entrained flow reactor with supplementary electrical heating. Oxygen concentration is 12% and gas temperature is 1450 K.

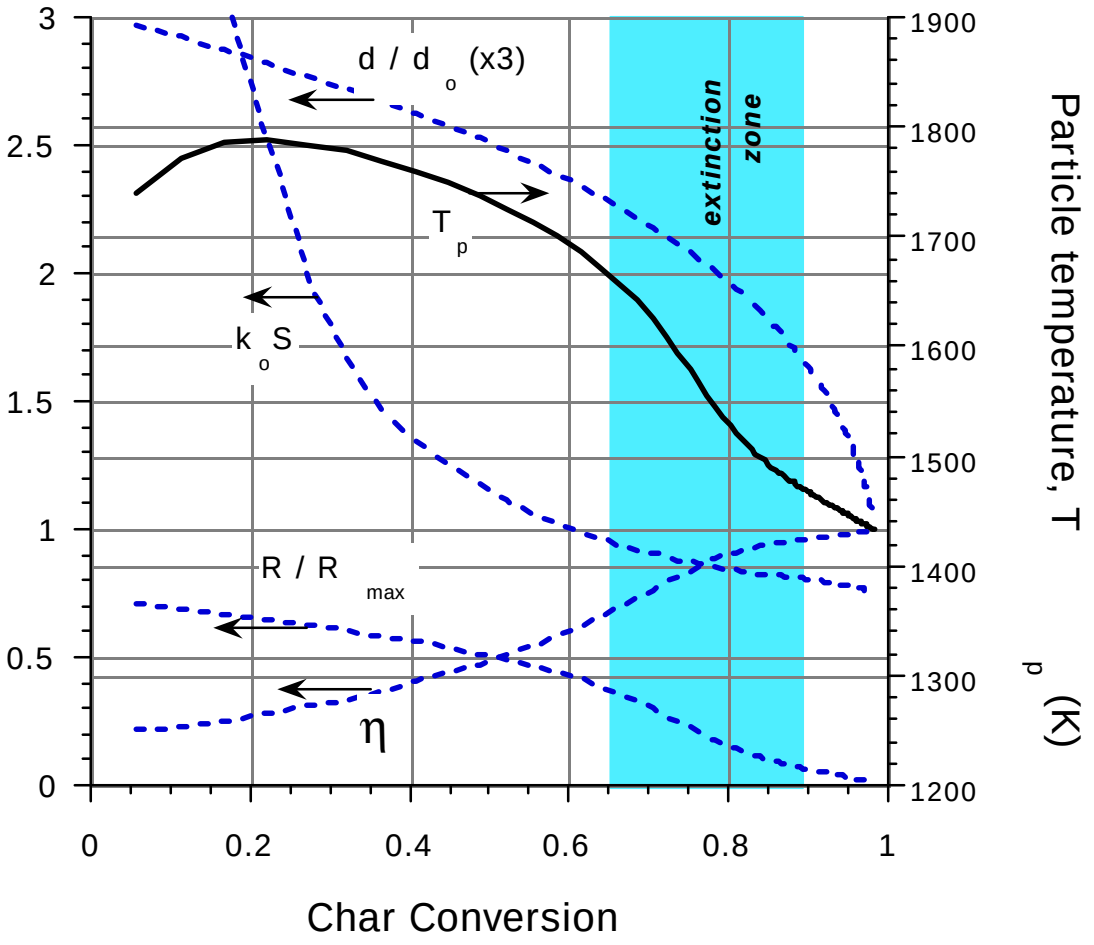

Figure 5.5 CBK8 predictions of Illinois char behavior giving insight into reaction zones and mechanisms of near-extinction. Conditions identical to those in Fig. 5.4. R_{max} is the theoretical diffusion limited rate, and R/R_{max} is a measure of the extent of approach to this limit (a measure of the severity of boundary layer diffusion limitations ranging from 0 to 1). k_oS is the mass-specific intrinsic reactivity and η is the effectiveness factor describing the extent of pore diffusion limitations.

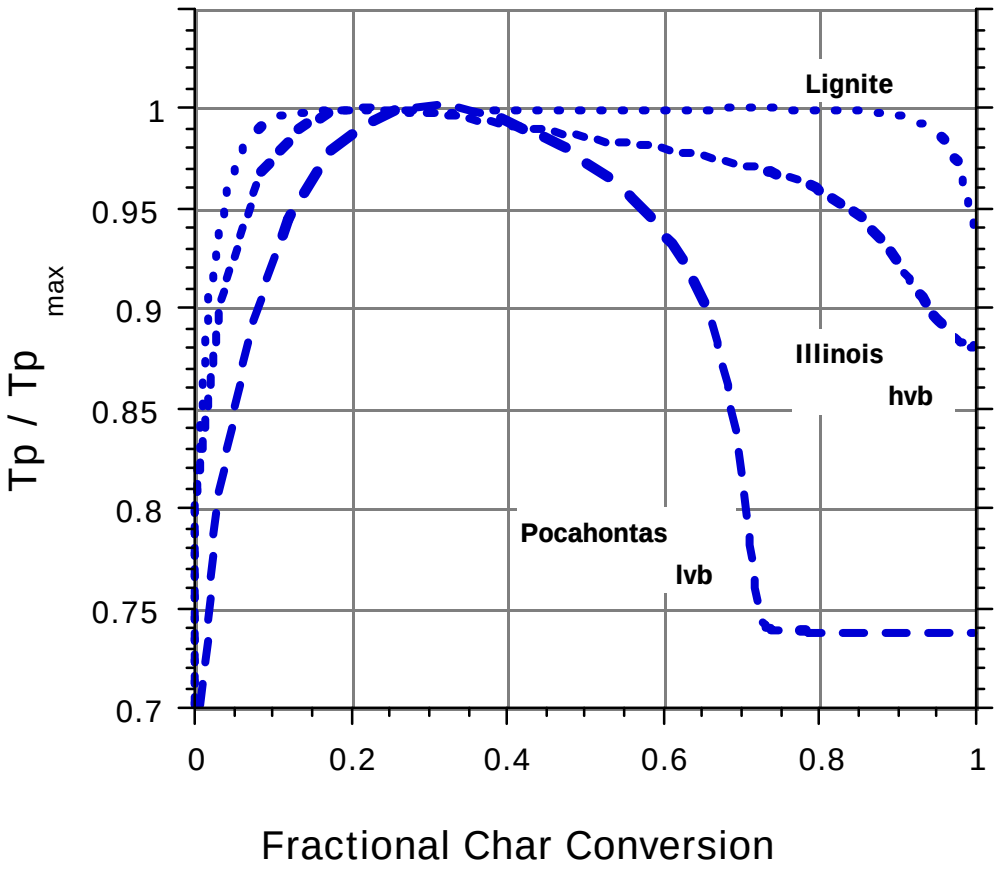

Figure 5.6 CBK8 predictions of particle temperature histories under CPI conditions, showing rank-dependent extinction behavior. Conditions: lignite: 3 mole-% oxygen, 1175 K gas temperature; Illinois #6: 6 mole-% oxygen, 1250 K gas temperature; Pocahontas: 19% oxygen, 1250 K gas temperature.

Finally, the model was compared to low-temperature oxidation data of Jenkins et al. [1973], who report Zone I reactivities at 500 ^{o}C in air for chars prepared by 2 hour heating at 1000 ^{o}C from a suite of U.S. coals of varying rank. While these conditions are far from those in pulverized coal combustion, the present model does have the essential features to make reasonable predictions of burning rates in this regime as well. Specifically, the intrinsic formulation is directly applicable to low-temperature oxidation, and the annealing submodel can correct for the large differences in heat treatment histories between flame chars and the chars of Jenkins et al. [1973]. A useful test of CBK8, therefore, is its ability to describe the Jenkins et al. data with the same parameter set used to describe the high temperature Sandia data.

Fig. 5.7 shows CBK8 predictions of absolute burning rates for a range of coals of various rank under two sets of conditions: PC conditions in the Sandia entrained flow reactor and very low temperature conditions (500 ^{o}C) in TGA data of Jenkins et al. The successful fit of the Sandia data at high temperature is not significant in itself, as this data was used to

develop the reactivity correlation in CBK8 (see Table 5.1). In contrast, the successful prediction of the TGA data is very encouraging, as the same parameter set was used with no adjustments (see Table 5.1), tantamount to an extrapolation of 1000 ^{o}C in particle temperature and 4 to 5 orders of magnitude in reaction rate. Note that both the annealing model and the explicit description of internal reaction/diffusion were needed to achieve this unification over such a wide temperature range.

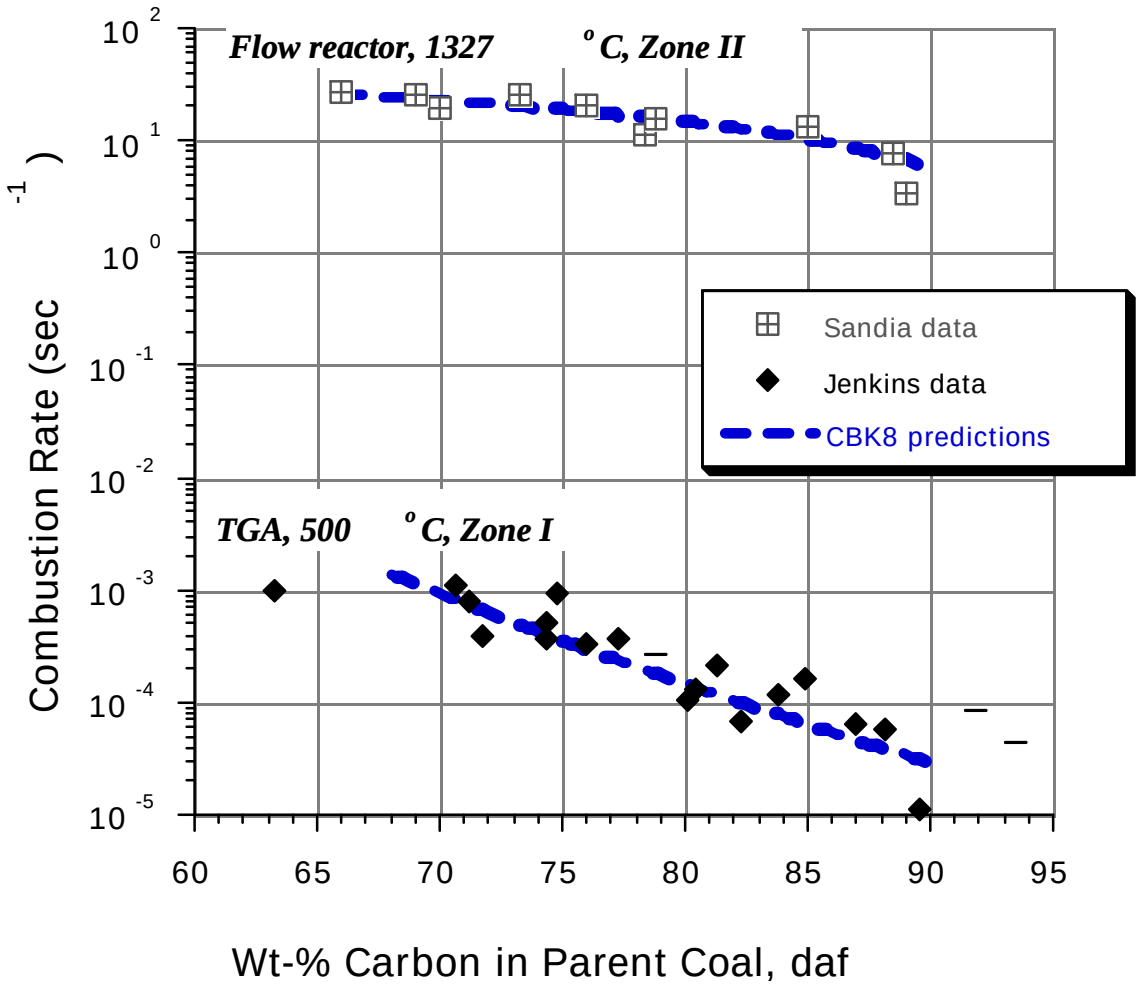

Figure 5.7 CBK8 predictions of absolute char reactivities and their rank dependencies under two sets of conditions. The upper points are maximum burning rates measured by sampling in the Sandia flame supported flow reactor, with gas temperature 1600 K, oxygen concentration 12 mol-%, nominal particle diameter 100 μm, using U.S. coals from lignites to low-volatile bituminous. The TGA data are from Jenkins et al. [1973] in air at 500 ^{o}C, on chars prepared by 2-hr heat treatment in inert gas from U.S. of various rank.

All of the results in Figs. 5.4-5.7 were generated using the common parameter set presented in Table 5.1. Critical examination of these parameters shows them to be physically realistic. The ash grain size is 5 microns and the ash porosities are reasonable for the partially fused material seen in at high temperature ($\theta = 0.17$) and the lacy ash observed in CPI experiments ($\theta = 0.5$). The intraparticle transport parameter, $\tau / f = 6$ lies in the expected range, as τ values for heterogeneous catalysts typically lie between 2 to 6 [Satterfield, 1981], while f must be less than unity. The unification of Zone I and Zone II data requires proper decoupling of intrinsic reaction and pore diffusion, so the successful result in Fig. 5.8 also suggests that τ/f has been appropriately estimated.

5.1.2 Burnout parameter studies

One subgoal within this study is to identify the most important fuel-related factors influencing carbon burnout. CBK8 with the fuel input correlations used in the NOxLOI PREDICTOR has been seen to reproduce the fuel trends seen in laboratory, pilot, and commercial scale combustors [Niksa et al., 1999], and thus is an ideal tool for exploring the inherent sensitivity of the burnout process to various coal properties. In this section, the simple one-dimensional numerical model used in the NOxLOI PREDICTOR is used in a series of parameter studies designed to improve our understanding of fuel effects in carbon burnout.

The approach is to carry out a baseline simulation under a chosen set of typical conditions and then to vary the input parameters individually and record the changes in burnout from the baseline value. Table 5.1 lists the fuel properties and combustion conditions used in the baseline simulation. The fuel properties are typical of a high-volatile bituminous steam coal (e.g. Pittsburgh #8) and the combustion environment was chosen to be in the range of relevance for pc-fired boilers and to give an unburned carbon content of approximately 5wt-% for the baseline coal.

Figures 5.8 and 5.9 show the main results of the parameter studies. In each case, only the parameter plotted on the abscissa was varied — all others retain the values in baseline condition shown in Table 5.1. The most important results from Figure 5.8 are the following. The mode of burning parameter, α, which relates the diameter change to carbon conversion:

$$r_c / r_{c,o} = (m_c / m_{c,o})^a \qquad (5.11)$$

shows only a modest effect on LOI when varied from 0 (constant density or shrinking core behavior) to 1 (combustion at constant diameter). The mode of burning parameter is thus of secondary significance in the accurate prediction of carbon burnout.

Coal ash content has a strong influence on LOI as seen in top right hand panel of Fig. 5.8 Although the CBK model includes a description of ash inhibition, this effect is small under pc conditions and the net effect of increasing coal ash content is always to *decrease* LOI due to the dilution of the unburned carbon with mineral matter. Figure 5.8 shows that LOI decreases sharply and almost linearly with high temperature volatile loss, HTVL. This is not surprising, as char yield dictates the total mass of carbon to be consumed in the burnout

process, and is equal to 1 - HTVL on an ash-free basis. Swelling factor is also seen to be a first order effect. At constant volatile loss and coal density, the swelling factor increases particle diameter and reduces char density simultaneously. The effect of swelling factor is particularly pronounced at values much less than one (implying net shrinkage), values that have been seen for some biomass fuels that undergo solid state carbonization.

Intrinsic reactivity, k_oS, has a lesser effect on LOI around the value for the baseline bituminous coal, but strongly effects LOI in the range of much lower reactivities (i.e. for anthracites). This extreme non-linearity arises from boundary layer diffusion effects — beyond a critical reactivity, further increase of k_oS affects LOI little, as much of the burning process takes place under Zone III conditions, where the reaction rate is limited by diffusion and is independent of surface reactivity.

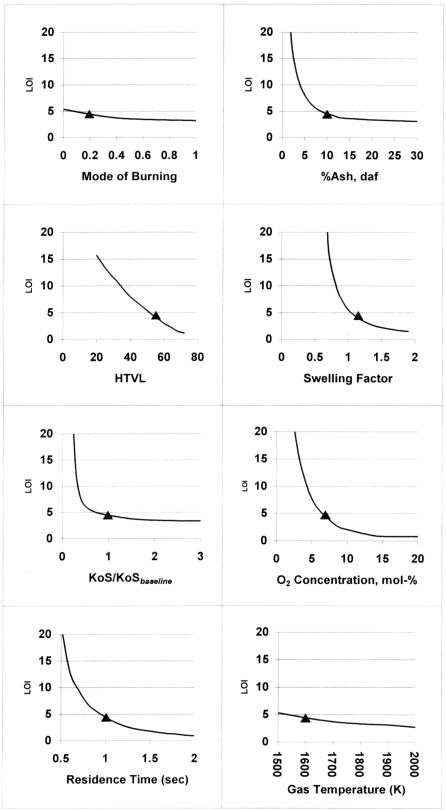

Figure 5. 8. Sensitivity of LOI to various coal properties and basic furnace characteristics. Solid triangles represent the baseline case defined in Table 5.1, for which LOI=4.4%. The various panels indicate the effect of varying the single parameter cited from its baseline value, holding all other parameters constant.

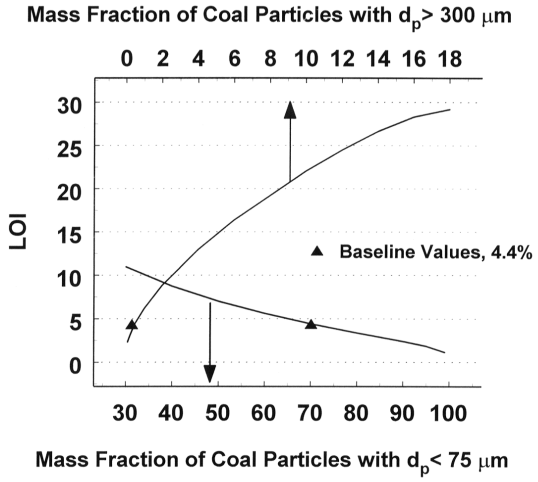

Figure 5.9. Sensitivity of LOI to coal particle size distribution. All calculations use the Rosin-Rammler distribution with the fuel properties and conditions listed in Table I, except particle size. Solid triangles represent the baseline case with the following two-point fineness specification: 70 wt-% <75 μm, and 0.5 wt-% > 300 μm. Curves show the effect of systematically varying one of these percentages (either 70 or 0.5), while keeping the other fixed and maintaining the Rosin-Rammler functional form.

Figure 5.8 also contains some information on the effect of oxygen concentration, residence time, and gas temperature on the burnout process. Increasing gas temperature always causes small but significant decreases in LOI due the intrinsic temperature dependence of the reaction and diffusion processes.

Figure 5.9 explores the role of coal particle size distribution using the Rosin-Rammler function to represent a typical utility grinds:

$$\frac{100 - F}{100} = \exp\left(-(d / d_o)^n\right) \qquad (5.12)$$

where F is the mass percentage of particles with diameter less than d (μm), and d_0 (μm) and n are the two distribution parameters. In utility practice fineness is commonly specified by two points in the distribution: the wt-% of particles with diameters less than 75 μm (200 mesh), and the wt-% of particles with diameters greater than 300 μm (50 mesh). As an example, a typical utility grind might have 70% below 75 μm and 0.5 % above 300 μm. Here we assume the Rosin-Rammler functional form and use the two-point fineness specification to determine the two Rosin-Rammler parameters (d_O and n) by rearrangement of Eq. 5.12.

For these sensitivity studies, 8 size bins were selected ranging from 15 to 350 μm, and the mass in each bin determined from the complete Rosin-Rammler distribution as described above. If one of the two fineness specifications is now altered while leaving the other

constant, a new Rosin-Rammler distribution results, whose parameters can be re-calculated by rearrangement of Equation 5.12. Figure 5.9 uses this technique to explore the sensitivity of LOI to each of the two fineness specifications (% < 75 μm; % > 300 μm) varied independently. Figure 5.9 shows LOI to be sensitive to these fineness values as expected. The sensitivity is particularly acute for the upper size specification: the wt-% larger than 300 μm. Increasing this fraction from 0.5 to 2 wt-% increases LOI from under 5% to about 10%, underscoring the widely recognized critical role of larger particles in carbon burnout. While all the calculations presented in this paper were obtained with the reduced furnace model, a number of parameter studies were also carried out using large sets of temperature/ oxygen trajectories for particles from three dimensional CFD simulations. Where direct comparisons were made, these multidimensional studies gave similar trends for the sensitivity to fuel properties.

5.1.3 Subtask 5.1 Conclusions

1. The nonlinear equations describing heterogeneous reaction and transport predict extinction-like events during combustion of single pulverized char particles under some conditions, in agreement with data and previous analyses. The extinction-like events greatly increase the time required to achieve the high conversion desired in combustion practice.

2. This work confirms the conclusions reached by Essenhigh et al., [1999a,b] that a transition from Zone II to Zone I can occur under pulverized coal combustion conditions, and that this transition must be described explicitly to correctly model extinction behavior.

3. Only some of the observed extinction-like events are associated with multiple pseudo-steady-state solutions to the single-particle energy balance as described in the classical Semenov theory. The existence of multiple steady states is favored by low gas temperature, high oxygen concentration, cool radiation surfaces, small particles, and the use of Zone I/II asymptotic curves as an approximate solution technique. Under most conditions of direct relevance to pulverized fuel combustion, the temperature drops are continuous transitions defined as near-extinction events.

4. The most common cause of extinction-like events under pulverized coal combustion conditions is predicted to be reductions in particle diameter and gas temperature, accompanied by a transition from Zone II to Zone I burning. In high reactivity materials extinction can be delayed to very high conversion (>95%), where the primary cause may be transport modification by mineral matter under conditions when the ash is partially fused. Annealing influences char reactivity, but is rarely predicted to be the primary cause of extinction in the late stages of combustion.

5. A kinetic model accounting for internal reaction/diffusion, annealing, and ash effects is capable of describing a large set of data on extinction-like events. The model (CBK8) with the same parameter set also successfully describes the TGA data of Jenkins et al. at 500 ^{o}C for a wide range of U.S. coals, thus unifying reactivity measurements

spanning over 1000 ^{O}C in particle temperature and 4 - 5 orders of magnitude in reaction rate.

6. Parameter studies with the validated model indicate that a number of coal-related factors exert a significant influence on carbon burnout and LOI. The burnout propensity of a fuel is not governed by a single dominant fuel property. LOI is particularly sensitive to the char yield (flame volatile loss), swelling factor, coal particle size distribution, and coal ash content. Despite the inclusion of a modest ash inhibition effect in the combustion model, *increases* in ash content are predicted always to lead to *decreases* in LOI by diluting of the unburned effect with inorganic matter. Lesser sensitivities are observed for intrinsic reactivity, gas temperature profiles, and the mode of burning parameter that describes the particle diameter evolution during combustion. The sensitivity to intrinsic reactivity increases with decreasing char reactivity.

5.2 Characterization of unburned carbon properties

This subtask takes a very first look at the *properties* of unburned carbon in ash as a supplement to the work on the *amount* of carbon, which has been the traditional focus. Unburned carbon properties have been found to be critical for ash behavior in construction applications, which is the most important utilization market. The work described below has led to the first real understanding of the factors that lead to poor concrete performance in some ash samples, and has also led to a spin-off technology that employs ozone for the reactive surface modification of unburned carbon. This process has the potential to make higher carbon ash samples usable in concrete and is currently under development and scale-up at Brown in collaboration with EPRI and several industrial partners.

5.2.1 Technical Introduction to Subtask 5.2

Pulverized coal combustion produces over 75 million tons of fly ash and bottom ash in the U.S. every year [Ghafoori and Buchole, 1997]. The most widespread and economically attractive option for utilizing fly ash is in concrete manufacture (see Fig. 4.10), where the fly ash serves as a partial replacement for Portland cement [Helmuth, 1987; Malhotra and Mehta, 1996], thereby saving cement costs, improving certain concrete properties (such as long term strength and permeability [Helmuth, 1987]), and slowing the heat release of hydration, which can be a beneficial effect in large pours [Helmuth, 1987].

In most concrete mixtures, specialty surfactants, or "air entraining admixtures," are added to stabilize sub-millimeter air bubbles, which improve resistance to freeze/thaw cycles [Lea, 1970; Ramachandran, 1995; Helmuth, 1987; Rixom and Mailvaganam, 1986]. The bubbles are believed to provide excess volume to accommodate the expansion of residual water upon freezing in the set concrete [Ramachandran, 1995]. Solid carbon residues, if present in fly ash in high concentration, can adsorb these surfactants and render them unable to fulfill their intended function. As a result the stable air volume is too low or the mean bubble separation (spacing factor) is too high to impart the desired freeze/thaw resistance [Helmuth, 1987; Rixom and Mailvaganam, 1986; Freeman et al., 1997]. Although increasing surfactant dose may compensate for the adsorption loss, large surfactant doses in practice lead to large and intolerable variations in entrained air when normal variations in ash properties are encountered in the field.

Current regulations in the U.S. limit the carbon content in ash streams for concrete applications to 1 to 6 weight-%, depending on region and regulatory body. The need for carbon levels below these regulatory thresholds is a major motivation for improving and controlling the fuel conversion efficiency in commercial pulverized-fuel fired power plants. Almost without exception, the combustion experiments carried out to date have focused on the *amount* of char consumed as a function of fuel type and combustion history. Recent studies, however [Freeman et al., 1997; Gao et al., 1997; Hill et al., 1997] have observed variations in the surfactant adsorptivity of commercial ash samples that cannot be fully explained by variations in the amount of carbon present, but are related to variations in specific carbon *properties* such as surface area, surface chemistry, and particle size. Very little is known about the effect of combustion conditions, coal type, and post-combustion treatment on carbon adsorptive properties. Several recent studies have measured the

relevant adsorptive properties of commercial ash samples [Freeman et al., 1997; Gao et al., 1997; Hill et al., 1997], but these samples come from complex and incompletely characterized combustion environments, and, as a result, it has not yet been possible to link surfactant adsorptivity to specific combustion conditions or fuel type.

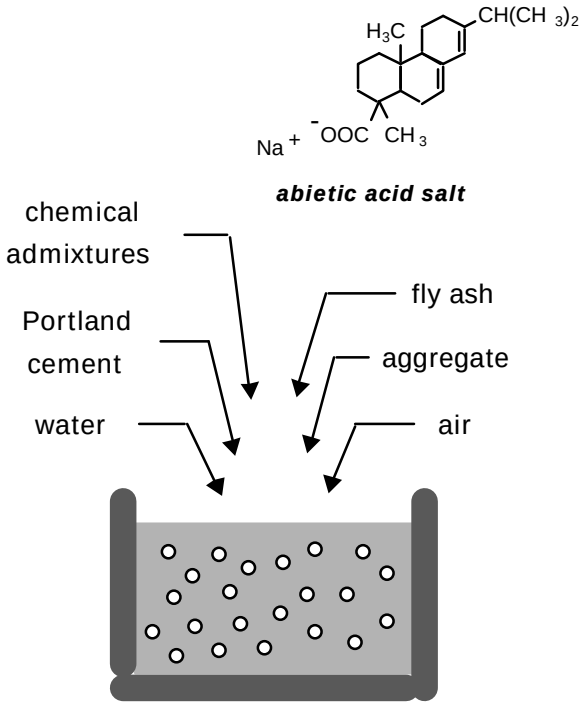

Figure 5.10 Components of fly ash concrete. In a typical formulation, fly ash replaces about 20% of the Portland cement. A variety of chemical admixtures are in common use for the reduction of water demand, the enhancement of workability, and the promotion of air entrainment. Most air entraining admixtures are complex mixtures derived from natural sources such as wood resins or tall oil. Abietic acid (structure shown) is a pure compound exemplifying the chemical structure of the active agents in resin-derived admixtures.

The goal of this subtask is to make the first set of measurements of surfactant adsorptivity for partially combusted coal char samples generated under carefully controlled and characterized laboratory and pilot-scale conditions simulating high temperature pulverized coal combustors. The first set of experiments, described below, was carried out in the laboratory at Brown on two coals in a flame-supported, high-temperature flow reactor with rapid-quench sampling. These experiments were supplemented by additional experiments in which a commercial high-carbon ash sample was subjected to controlled low temperature oxidation. The pilot-scale experiments were carried out at the University of Utah and are described in a later section.

5.2.2 Laboratory Experiments

Experiments were carried out on size-classified samples of Pittsburgh #8 and Beulah lignite coals (75 - 106 μm in diameter) and on a commercial fly ash sample. Sample properties are given in Table 5.2. Partially combusted chars were generated from the two raw coals in a high-temperature flow reactor by rapid-quench extractive sampling at residence times from 15 to 160 msec. The reactor is fed by a Hencken burner (Research Technologies, Pleasanton, CA) fueled with a $CH_4/O_2/Ar$ mixture, producing a hot gas stream with post-flame oxygen concentration of 14 mole-% for Pittsburgh seam coal and 12 mole-% for Beulah lignite. The oxygen concentrations were selected to cover the entire range of conversion for each coal in the residence time available. Centerline temperatures varied from 1650 K at a residence time of 15 msec to 1280 K at a residence time of 140 msec. Particle temperatures are estimated to range from 1800 - 1950 K (peak values at short residence times), or 1650-1800 K (time-averaged values). The solids feed rate was limited to less than 1 gm/hr, yielding dilute phase conditions in which particle-to-particle interaction is minimal and the temperature/oxygen history of each particle is nearly identical. The reactor design and operation are similar to those described by Mitchell et al. [1992].

Table 5.2
Sample Properties

Raw coals:	Pittsburgh #8	Beulah lignite
ASTM Volatile matter, % daf	39.9	46.6
ash content, % db	13.9	8.0
%C, daf	80.1	67.1
%H, daf	5.3	4.2
%N, daf	1.6	.95
%S, daf	1.6	1.63
%O, daf (diff)	11.4	26.2

Commercial ash sample:

Carbon-rich fraction from electrostatic separation, courtesy of P. Calvert, New England Power. Loss-on-ignition: 66 wt-%.

An additional series of experiments was carried out in which a commercial ash sample was oxidized in air in a bench-top tube furnace for two hours at a series of temperatures from 20 ^oC to 900 ^oC. Combustible matter contents for all the partially reacted samples were determined by the ASTM Loss-on-Ignition (LOI) test modified for small samples, and the results used to determine conversions from a total ash tracer analysis. (The LOI test is a gravimetric measurement of combustible matter loss during prolonged air oxidation at 700 ^oC.) Weight fractions of C, H, O, and ash were also determined for the partially combusted coal chars by Huffman Laboratories. Oxygen contents were determined directly by a modified Unterzaucher (pyrolysis) technique, and also estimated by difference. Both techniques for oxygen become increasingly inaccurate as conversion proceeds, due to

increasing ash content. Trends in the data suggest that the direct measurement is especially biased by contributions from inorganic oxide decomposition for samples with ash contents greater than about 50%.

The specific surfactant adsorptivity of the partially oxidized samples was determined by a standard laboratory titration procedure [Helmuth, 1987; Gao et al., 1997] in which 2 grams of fly ash are placed in a 70 ml cylindrical weighing bottle along with 25 ml of distilled water. The sample is ultrasonically dispersed for 5 minutes, after which 8 grams of Portland cement is added. The weighing bottle is then capped and thoroughly shaken for one minute to completely wet the cement and fly ash. A 10 vol-% aqueous solution of surfactant (Darex II from W.R. Grace) is then added one drop at a time from a 2 ml microburet. After each addition the bottle is capped and shaken vigorously for 15 seconds, after which the lid is removed and the liquid surface observed. Prior to the endpoint of the test, the foam on the liquid surface is extremely unstable, the bubbles bursting within a few seconds. The endpoint is realized when a constant foam is maintained on the surface for at least 45 seconds. The volume of diluted Darex II required to produce this stable foam minus the amount required in a reference experiment using Portland cement alone is referred to as the specific adsorptivity of the ash or carbon sample. In addition, total surface areas of the partially oxidized samples were measured by multi-point BET analysis of nitrogen vapor adsorption isotherms at 77 K, and pore size distributions were computed from the nitrogen isotherms by the Barrett, Joyner, and Halenda method [Barrett et al., 1951] and the HK method [Horvath and Kawazoe 1983].

5.2.3 Results and Discussion

Figure 5.11 shows the evolution of specific surfactant adsorptivity during high-temperature combustion of the two coals. The adsorptivity is presented per total gram of solid sample (comprising inorganic and carbonaceous parts), and is thus a direct measure of the activity per unit weight of ash relevant to concrete applications. This activity is very low for the parent coal and the partially devolatilized chars, but rises sharply near the end of devolatilization and then falls in the early-to-intermediate stages of char combustion. Removal of all carbon by low temperature oxidation is observed to reduce the specific adsorptivity to a very low value, as seen previously [Freeman et al., 1997], so the adsorption is occurring almost exclusively on the carbonaceous portion of the sample. The falling values during char combustion are therefore in part due to the decreasing carbon mass fraction in these samples. Figure 5.12 plots the same data normalized per unit mass of carbonaceous (combustible) matter, and compares the trend observed to carbonaceous surface areas measured by nitrogen vapor adsorption.† Plotted in this way, both adsorptivity and area can be regarded as properties of the carbonaceous portion of the sample. Even on this basis, the specific adsorptivity rises and falls sharply during combustion, indicating significant changes in the char *properties*.

† The surface areas of the inorganic portion of the samples were also measured and lie between 0.6 and 1 m^2/gm inorganic matter. They are a negligible fraction of the total surface are in most cases, and even where they are not, they do not make an important contribution to the surfactant adsorptivity [Freeman et al., 1997].

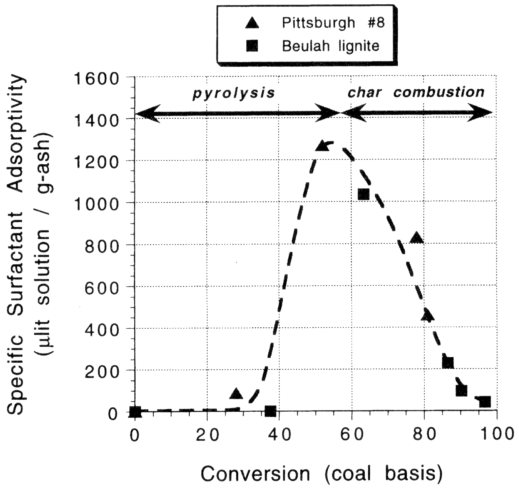

Figure 5.11 Specific surfactant adsorptivity as a function of conversion during the high-temperature combustion of a high-rank and a low-rank coal. Specific adsorptivity is expressed per gram of sample (comprising inorganic and carbonaceous portions), and thus serves as an ash property directly relevant to behavior in air-entrained concrete.

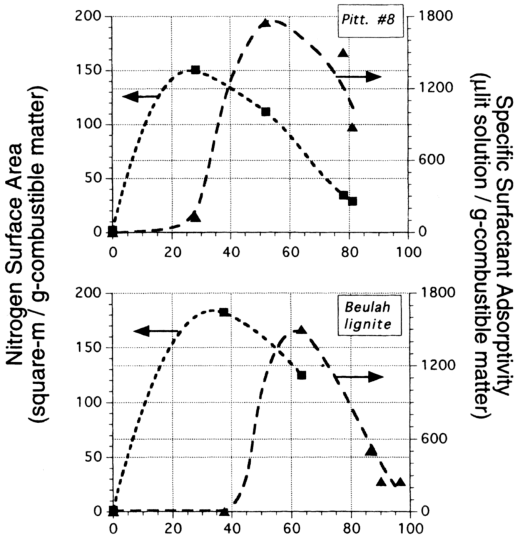

Figure 5.12 The effect of conversion on specific surfactant adsorptivity and nitrogen BET surface area, both per gram of combustible material. (The contribution of the inorganic portion of these samples both to surface area and to surfactant adsorptivity is very small.) Top: Pittsburgh #8 bituminous coal; bottom: Beulah lignite.

The evolution of surface area shows a similar trend, but with a clear and significant lag relative to the adsorptivity curve. The initial increase in surface area can be easily rationalized as pore opening associated with the loss of material from the solid phase during devolatilization and early char combustion.

The subsequent decrease in surface area is believed to be caused by rearrangements and pore collapse associated with the thermal treatment of the young char. The oxidation process itself is not a likely cause of the decrease; surface areas calculated on this basis (per gram of combustible matter remaining) would show monotonic increases for any plausible model of the porous structure, including spherical, cylindrical, or sheet-like grains, or random cylindrical pores [Hurt et al., 1988; Gavalas, 1980]. Indeed, sharp decreases in surface area in the early stages of heterogeneous combustion are not observed in low temperature oxidation experiments conducted on chars that have been pre-stabilized by heat treatment at temperatures above the reaction temperature. The sharp decreases seen in Figure 5.12 after 30 - 40 % conversion must be caused by annealing of the young flame-generated char.

Similar arguments explain the sharp rise and fall in surfactant adsorptivity, but the pronounced lag relative to the surface area curve is noteworthy and may provide insight into the special features of the surfactant adsorption process. Specifically, it is remarkable that the samples obtained in the devolatilization zone process show high surfaces area (> 150 m^2/gm) but almost no measurable surfactant activity. In general, adsorption phenomena are affected by surface area, the accessibility of this area (transport and size exclusion effects), and the chemical nature of the surface. The effects of surface chemistry and accessibility are specific to a given adsorbate, and we therefore expect that changes in surface chemistry and accessibility will affect the nitrogen and surfactant adsorptivities in different ways. These two factors therefore have the potential to explain the trends in Fig. 5.12.

Specifically, two hypotheses can be considered to explain the lag between surfactant and nitrogen adsorptivities in Fig. 5.12. First, the standard surfactant adsorptivity test is carried out over a time interval limited by the hydration reaction of the cement present in the test mixture, and thus is not necessarily an equilibrium measurement. Even nitrogen adsorption suffers from long equilibration times in certain cases, and it is likely that the larger size of the surfactant molecules and the requirement of diffusion in the liquid phase make transport and size exclusion effects more pronounced for the surfactant than for nitrogen vapor. In particular, some of the smaller micropores accessed by N_2 may not be accessible to the larger surfactant molecules. Abietic acid (see Fig. 5.10), cited as a model compound for the amphiphilic molecules in resin-derived air entraining admixtures [Rixom and Mailvaganam, 1986] has a molecular size of approximately 8 Å (estimated from the molecular volume calculated from the Schroeder formula [Reid et al., 1987]) compared to 3.8 Å for N_2. Calculation of micropore and mesopore size distributions from the N_2 isotherms indicate significant widening between 30% and 50% conversion for the Pittsburgh samples, consistent with the greatly increasing surfactant adsorptivity relative to nitrogen.

There was no clear evidence of micropore and mesopore widening in this conversion range for Beulah, however. Solid samples extracted under similar flames show a greatly increasing number of surface-accessible macropores by SEM [Hurt and Hardesty, 1994], especially for bituminous coals, as oxidation attacks the external surface in Zone II burning

mode. In conclusion, low effective diffusivities prior to the onset of oxidation may explain in part the low adsorptivity of the aqueous phase surfactant relative to nitrogen vapor. As with most adsorption and reaction phenomena of carbons, the true effective surface area is not easily identified or measured, and more work is needed to fully understand the role of pore size distribution on the adsorption of concrete surfactants.

Secondly, previous measurements of the surfactant adsorptivity of surface treated carbon blacks [Gao et al., 1997] suggests that the adsorption is sensitive to surface chemistry, and that the introduction of polar oxygen functionalities suppress surfactant uptake. Changes in surface oxygen functionalities may help explain the late development of surfactant adsorptivity in Fig. 5.13. To explore this second hypothesis, Fig. 5.14 plots the adsorptivity per unit surface area vs. conversion for Pittsburgh #8 and compares the trend to the evolution of elemental organic oxygen content. The area-normalized adsorptivity increases greatly with conversion, showing a maximum between 70 and 80%. The organic oxygen content is seen to decrease greatly during devolatilization and to maintain low values during most of char combustion. The overall trend of decreasing oxygen content provides a plausible if not unique explanation for the increasing area-normalized adsorptivity. A similar trend is seen for Beulah (Fig. 5.14), but with a more pronounced maximum in adsorptivity and generally higher oxygen contents. The increase of surfactant adsorptivity in the late stages of pyrolysis may be related to the loss of surface hydroxyl groups that have been shown to occur relatively late in the pyrolysis process [Solomon et al., 1990]. Comparing Figs. 5.13 and 5.14 it can be seen that the area-normalized adsorptivity in the char combustion regime is much higher for Pittsburgh than Beulah. The higher activity of the Pittsburgh char surfaces is consistent with the lower oxygen content of these chars in Fig. 5.13. It is possible that the Pittsburgh char with its much lower combustion reactivity [Hurt and Mitchell, 1992] has a smaller number of active sites for the oxidation reaction, and thus fewer sites with the potential to chemisorb oxygen from the gas phase and render the surfaces hydrophilic.

Low-temperature oxidation experiments

The possible effect of surface chemistry was explored further by controlled low-temperature oxidation experiments. Figure 5.15 shows the effect of two-hour air oxidation at a series of increasing temperatures on the adsorptivity and mass of a commercial, high-carbon ash sample. At temperatures below 200 ^{o}C, two-hour exposure to air has no measurable effect. At higher temperatures, oxidation leads to decreases in adsorptivity and decreases in sample mass as carbon is consumed. Note that adsorptivity reaches a very low value after the complete removal of carbon, as discussed previously. The most interesting feature in this data set is the offset between the mass and adsorptivity curves — adsorptivity begins to decrease before significant mass loss by oxidation occurs.

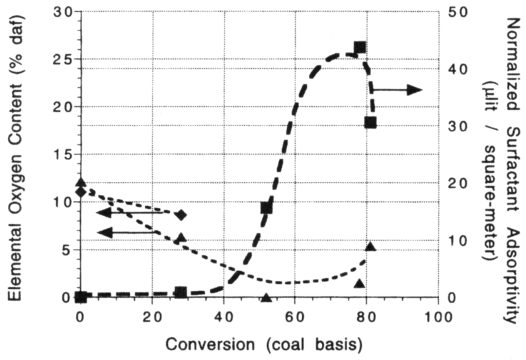

Figure 5.13
Evolution of specific surfactant adsorptivity per unit area and weight-percent organic oxygen in the Pittsburgh #8 char (daf basis). Oxygen contents are measured by the Unterzaucher technique (diamonds) and calculated by difference (triangles).

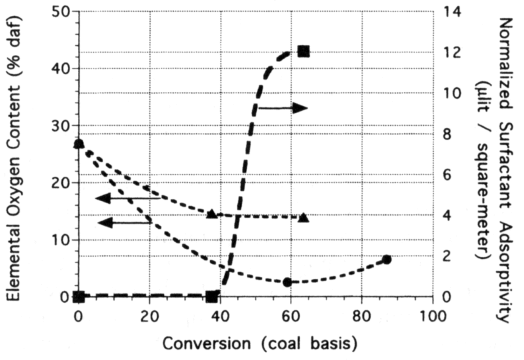

Figure 5.14
Evolution of specific surfactant adsorptivity per unit area and weight-percent organic oxygen in the Beulah lignite char (daf basis). The plot shows oxygen contents from this study calculated by difference (triangles) and from an earlier study of the same coal under similar combustion conditions (circles) [Mitchell et al., 1992].

Differences between the mass and adsorptivity curves are most clearly seen in Fig. 5.16, which replots the data from Fig. 5.15 as specific adsorptivity per gram of remaining carbon vs. degree of conversion of the combustible matter. The adsorptivity drops to approximately half its initial value before a measurable conversion has occurred. A reference back to Fig. 5.15 shows that this decrease occurs between 300 and 450 ^{o}C. Oxygen chemisorption is widely accepted as the first step in carbon oxidation [Laine et al., 1963; Lizzio et al., 1990] and the formation of a significant stable oxide layer has been observed in the early stages of low temperature oxidation [Lizzio et al., 1988; Floess et al., 1988]. Under these conditions it is believed that initial oxygen chemisorption occurs in the temperature range 300 - 450 ^{o}C prior to significant weight loss, leading to an increase in surface polarity and corresponding decreases in specific surfactant adsorptivity. This conclusion is consistent with the prior observation of the effect of surface oxidation on carbon black surfactant adsorptivity [Gao et al., 1997].

Also shown on Figs. 5.15 and 5.16 is a single measurement of surfactant adsorptivity after 900 ^{o}C treatment in argon. This heat treatment *increases* the surfactant adsorptivity significantly, presumably by cleaning the surface of existing oxygen functionalities. The range of points at zero conversion on Fig. 5.16 illustrates the range of activities achieved in this study by surface treatment alone, from the most active surface cleaned of oxides at 900 ^{o}C in argon to the least active containing an inventory of chemisorbed oxygen at the point of incipient combustion.

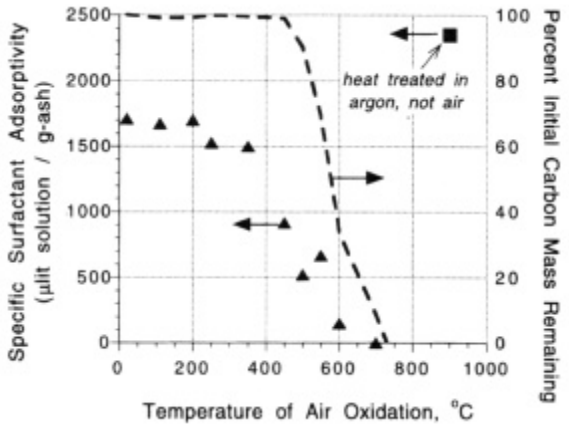

Figure 5.15 Effect of low temperature air oxidation on the mass and specific surfactant adsorptivity of a commercial high carbon ash sample. Also shown is a single data point indicating the effect of heat treatment in inert (argon) at 900 °C.

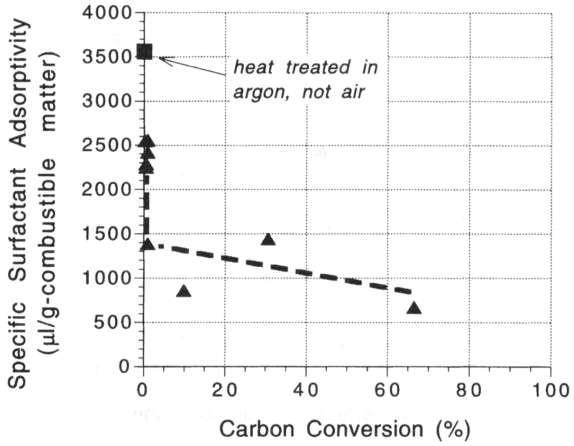

Figure 5.16 Effect of low temperature air oxidation on the specific surfactant adsorptivity of a commercial high carbon ash sample. Data from Fig. 5.16 are replotted as specific adsorptivity vs. conversion. Note the initial drop in adsorptivity before significant conversion occurs.

Figure 5.17 illustrates a proposed mechanism for competitive surfactant adsorption in concrete mixtures, based on the results in Figs 5.11 – 5.16. The amphiphilic molecules in air entraining admixtures are depicted with their nonpolar parts as light-colored tails and the polar or ionic group as dark spherical heads. The results in Figs. 5.13 – 5.16 suggest that the most active adsorption sites on carbon are nonpolar (hydrophobic) sites, and it is therefore expected that the dominant interaction involves the nonpolar portions of the surfactant molecules (as shown). This is not surprising, as polar functionalities are already abundant in the system: in the solvent, on the cement particle surfaces, and on the surfaces of the inorganic fly ash particles, which are primarily glassy inorganic oxides. The only hydrophobic surfaces in the system are the air / water interface and the nonpolar fraction of the total carbon surface area. Based on the results in this work, it is believed that these two surfaces are in direct competition for the nonpolar portions of the surfactant molecules.

The observed sensitivity to surface oxide population raises a number of important issues for combustion processes. Multi-step (adsorption/desorption) models of the carbon/oxygen surface reaction predict the steady-state inventory of chemisorbed oxygen to increase with increasing oxygen concentration and decreasing temperature in the flame. Further, carbon samples heat treated in inert environments have been observed to chemisorb oxygen gradually from air at room temperature, an effect which can be largely avoided by heat treatment in hydrogen to cap the active nascent sites created by thermal surface cleaning [Menendez et al., 1996]. Based on these observations it is likely that the population of surface oxides and thus the surfactant adsorptivity of unburned carbon will significantly depend on flame temperature, furnace oxygen concentrations, quenching rate, and post-combustion history (encompassing capture, storage, and handling).

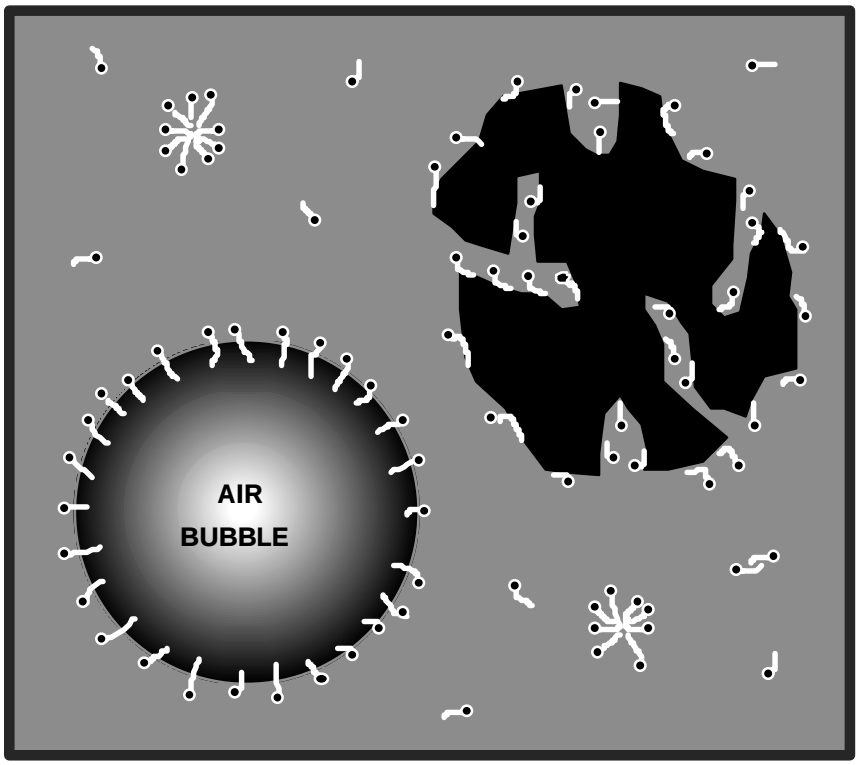

Figure 5.17 Proposed mechanism for competitive adsorption of amphiphilic compounds in concrete mixtures. Polar or ionic head groups are denoted by dark circles and the nonpolar parts by white, irregular lines. Note: surfactant molecules and carbon micropores are order 10^7 smaller than the carbon particles and air bubbles and are therefore not shown to scale.

Pilot-scale Experiments

It is well documented that installation of low-NO_X systems in commercial boilers can lead to poor ash quality in concrete applications, and this effect is often ascribed to increases in the *amount* of carbon. However, the analysis of more than 80 commercial ash samples at Brown has clearly shown ash quality to be related not only to amount, but also to the specific properties of the carbon fraction in ash. What is not clear is the possible role of low-NO_X firing on these specific carbon properties. Are the carbon residues from low-NOx flames intrinsically more active than those from conventional flames? It is difficult to answer this question using commercial samples, as they are not often available in appropriate matching pairs — i.e. from a given unit burning a given coal before and after a low-NOx retrofit. Pilot-scale studies provide the best opportunity for investigating this important question, as pilot furnaces can be operated in different firing modes on a single coal.

This task, therefore, has undertaken the analysis of ash samples from the "U-furnace" at the University of Utah, operated by Dr. John Veranth in a variety of low- and high-NO_X firing configurations on two selected coals. The facility is a 30 kW, down-fired, U-shaped furnace with an inside diameter of 0.17 meters and an overall length of 7.3 meters [Veranth et al., 1998]. Combustion conditions included a base case (high-NO_X) and a staged (low-NO_X) case with nominal 1.5 seconds of residence time in the reducing zone. Exit temperatures

were measured using a ceramic-sheathed type B thermocouple, and the oxygen, carbon dioxide, and NO_X concentrations in the flue gas were recorded using continuous monitors. The ash and carbon particles were collected by drawing the entire exit gas flow through a one-bag fabric filter. About 20% of the ash from this unit is collected as fly ash, with 80% remaining in the furnace, analogous to bottom ash in a larger scale facility [Veranth et al., 1998].

Table 5.3 gives a summary of the ash samples and their properties. For the second campaign samples, the NO_X levels were reported as 1180 ppm for the high-NO_X case, and ranged from 65 ppm to 198 ppm for the various low-NO_X firing conditions. There was evidence of soot in the low NO_X sample with the highest LOI value, as reported in detail elsewhere [Veranth et al., 1998]. This sample was fractionated to recover gram amounts of the soot and char fractions by procedures described previously [Veranth et al., 1998] and the fractions were added to a carbon-free ash (prepared by air oxidation) to make "synthetic" ashes enriched in the soot and char fractions respectively. These samples were also studied and the results summarized in Table 5.3.

Table 5.3
Properties of Pilot Scale and References Commercial Scale Ash Samples

Samples	LOI	Specific Adsorptivity (ml/g-carbon)	Adsorptivity (ml/g-ash)
Pilot-scale	10.8	4.5	0.49
Utah, high NOx	10.8	4.5	0.49
Utah, low NOx	25.7	17.4	4.5
Illinois, high NOx	7.7	0	0
Illinois, low NOx	24	9.2	2.2
Utah, low NOx (decarburized)	0	0	0
Utah, low-Nox soot fraction	25.7	21	5.4
Utah, low-Nox char fraction	25.7	16	4.1
Second campaign (all Utah coal)			
High-NOx	0.85	0	0
LNB, no staging	1.8	0	0
staging	0.92	2.2	0.020
Deep staging	0.78	1.9	0.015
Commercial scale reference samples			
Powder River Basin, Class C, marginal ash	0.41	8.8	0.036
Power River Basin, Class C, "bad" ash	1.31	5.4	0.071
Bituminous coal, class F	6.7	3.4	0.23

Table 5.3 shows that the LOI and surfactant adsorptivity of the ashes varied greatly. Their physical appearance is seen in the optical photograph of Fig. 5.18. Note the light color of the "UT Char" sample, which is the char fraction from the Utah low NOx condition in campaign one, and the dark color of the "UT Soot" sample, which is the soot fraction from the same sample. These two samples have equal carbon contents (10 wt-%), and the difference reflects the high optical activity of the fine soot particles. In the other samples (presumably all dominated by char carbon) darkness correlates well with carbon content (LOI).

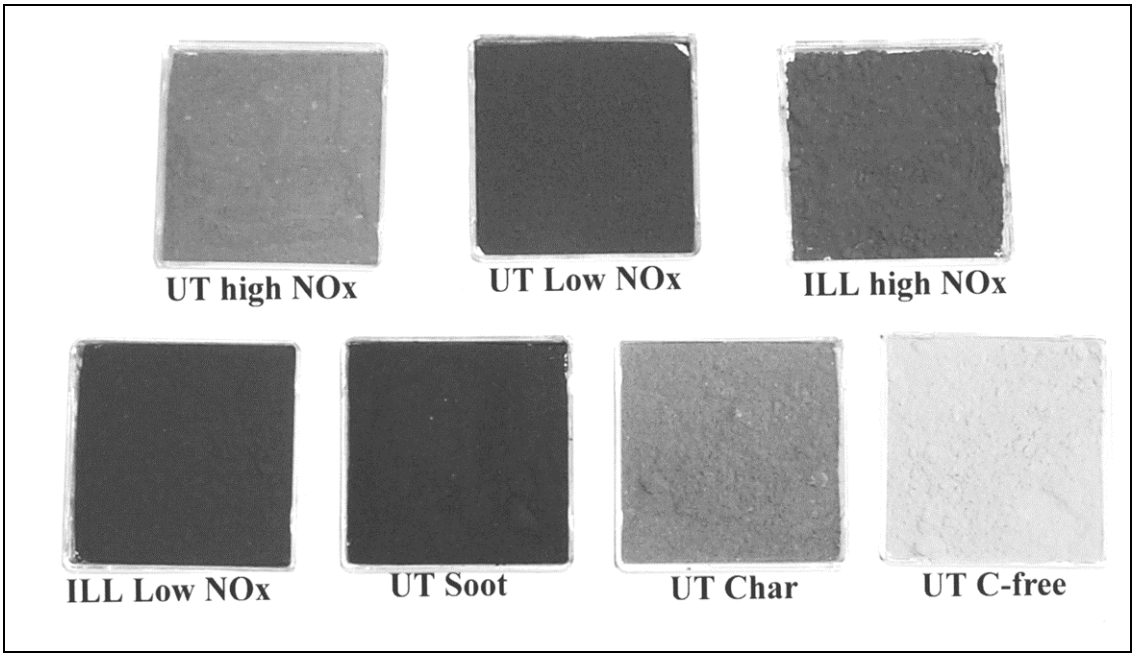

Figure 5.18 Photograph of pilot-scale ash samples from the University of Utah "U-furnace".

Figure 5.19 plots the data from Table 5.3 as the total surfactant adsorptivity (ml/gm-ash) vs. carbon content expressed as %LOI. The trend is highly non-linear — the surfactant adsorptivity is low for all samples with LOI values up to about 10%, and then rises sharply. A similar trend with LOI has been noticed in field samples, especially when examining subsets of data for bituminous steam coals only.

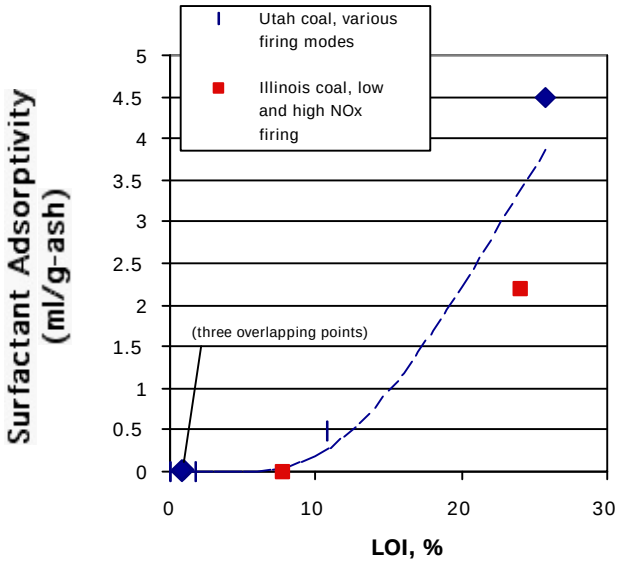

Figure 5.19 Surfactant adsorptivity of ash samples generated in the pilot-scale "U-furnace" at the University of Utah. The effect of unburned carbon amount (or LOI) is highly non-linear, as shown by the dashed trend line.

Figure 5.20 shows the specific surfactant adsorptivity (ml/gm-carbon) as a function of LOI for the pilot samples together with some commercial ash samples for reference. This plot also shows the specific adsorptivity of the soot and char enriched fractions from the Utah low-NOx sample in campaign one. This presentation clearly shows that the carbon is more active in higher LOI ashes (which is the origin of the non-linear effect in the previous graph). There is also some noticeable dependence on fuel type with the class C ashes (from sub-bituminous coals) lying higher than class F ashes (from bituminous coals) at the same LOI. The soot fraction is also observed to be somewhat more active than the char fraction in the very high LOI ash that was subject to fractionation. This latter result is in qualitative agreement with the higher activity of soot reported previously [Gao et al., 1997].

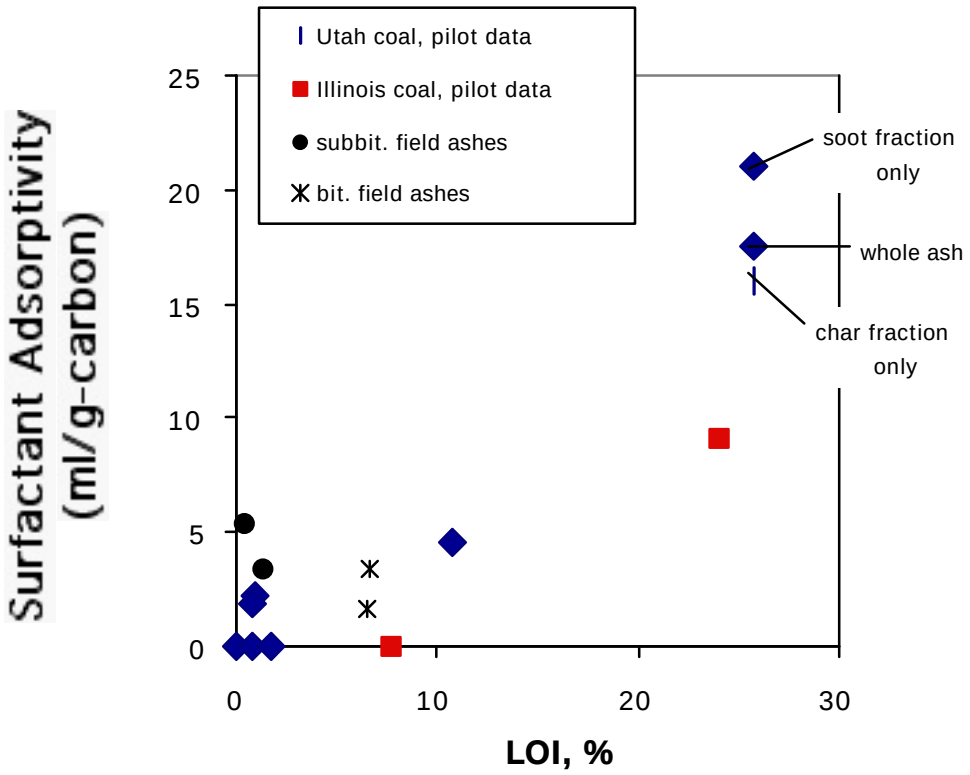

Figure 5.20 Specific surfactant adsorptivity (ml surfactant/gm-carbon) of ash samples generated in the pilot-scale "U-furnace" at the University of Utah. The adsorptivity of the carbon generally increases with the amount of carbon present, as measured by the LOI test. At a given LOI value there is very little difference between different flame types.

Figure 4.21 displays the same data (without the reference ashes) with symbols that facilitate distinction of the high and low-NO_X firing conditions. There is an obvious relation between carbon adsorptivity and LOI, but at a given LOI no obvious connection between carbon adsorptivity and flame type. This data suggests that low-NO_X flames do not necessarily produce chars that are intrinsically more adsorptive. Thus if a low-NO_X flame can be designed to control carbon amount, it should be able to achieve high ash quality as well.

The origin of the correlation between LOI and carbon activity is not at present understood. The laboratory studies presented earlier showed decreasing surface areas in the late stages of combustion, accompanied by decreasing surfactant adsorptivity. Since increasing conversion corresponds to decreasing LOI, this trend suggests that decreases in surface area in the late stages of pilot and full-scale combustion could be the main underlying cause of the non-linear relationship in Fig. 5.19. Other factors may also contribute, such as changes in particle size with conversion, and more work is needed on the underlying mechanisms. The pilot-scale studies begun in this project will be continued in a new NETL-sponsored project involving Brown, the University of Utah, and Southern Company, beginning in the fall of 2000.

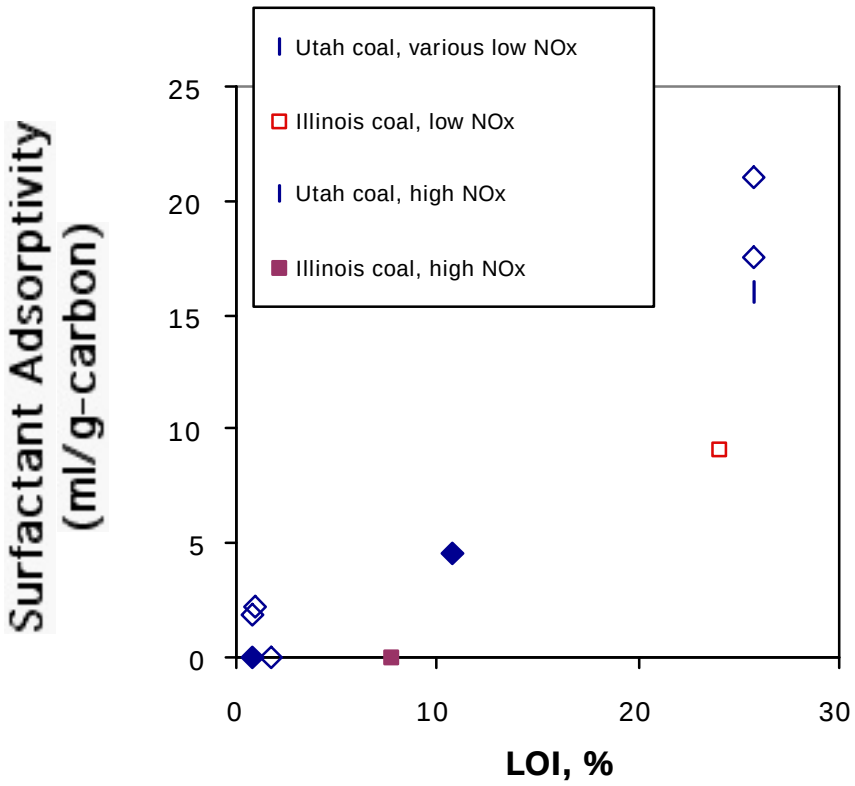

Figure 5.21 Specific surfactant adsorptivity (ml surfactant/gm-carbon) of ash samples generated in the pilot-scale U-furnace at the University of Utah. The adsorptivity of the carbon generally increases with the amount of carbon present, as measured by the LOI test. At a given LOI value there is very little difference between different flame types.

5.2.4 Subtask 5.2 Conclusions

1. These first experiments under controlled combustion conditions confirm the conclusion from earlier studies that the adsorption of concrete surfactants on fly ash is a complex process that cannot be simply related to the *amount* of unburned carbon present. It also depends on the carbon surface area, its accessibility, and the chemical nature of the carbon surface.

2. Partially combusted coal chars from well-characterized uniform combustion environments show large variations in specific surfactant adsorptivity over the course of conversion. The adsorptivity is low throughout most of devolatilization, rises sharply in the late stages of devolatilization, and then decreases sharply throughout char combustion. The main features of this evolution can be explained by considering the concurrent evolution of total surface area, oxygen content, and surface-accessible macroporosity. It has also been shown that surfactant adsorptivity can be greatly altered by post-combustion surface modification in the form of air oxidation at

temperatures above about 300 ^{o}C (reduced activity) or heat treatment at 900 ^{o}C in argon (increased activity).

3. Analysis of pilot-scale samples from the University of Utah provides further proof that carbon properties vary with combustion conditions and fuel type. Further, the specific adsorptivity of unburned carbon increases with its amount in ash, yielding a highly non-linear relationship in which increased unburned carbon levels lead to dramatic increases in adsorptivity. Evidence of this behavior has also been seen in field ash samples.

4. Analysis of pilot-scale samples suggest that carbon adsorptivity is less sensitive to flame structure (high vs. low NOx) than to the absolute carbon burnout. Thus low-NO_X flames can produce high quality ash if the unburned carbon levels can be controlled.

5. The experimental results suggest a mechanism for the detrimental action of carbon in concrete mixtures: the nonpolar fraction of the total carbon surface area competes directly with the air/water interface for the nonpolar portions of amphiphilic molecules in air entraining admixtures. The ultimate outcome of this competition determines the number and size of air bubbles, and is strongly dependent on the amount and properties of the carbon, which in turn depend significantly on combustion conditions.

6. The above mechanism and the data on air oxidation suggests that other forms of surface oxidation may also be effective at passivating carbon. This idea was pursued under separate funding and has led to a patent at Brown (issued fall 2000) on the use of ozone for the room temperature beneficiation of problem carbon-containing ash steams.

7. More work is needed before the variations in surfactant adsorptivity among field samples can be fully understood and the most favorable combustion and post-treatment conditions can be identified. There is strong motivation to expand the scope of many experimental programs in pulverized fuel combustion to include the characterization of unburned carbon adsorptive properties.

5.3 Char reactivity in NO and oxygen as a function of fuel type and heat treatment conditions

In this third subtask we have conducted a study of the intrinsic reactivity of chars to oxygen and NO as a function of heat treatment and fuel type. Work on NO has emphasized the role of rapid heat treatment, in order to test the hypothesis that young chars in flames have much higher activities for NO reduction than indicated by previous kinetic studies. For the O_2 reaction we have carried out measurements of intrinsic reactivity for a variety of coals and alternative solid fuels of interest in co-firing applications. For many of these materials there is no kinetic data available, and the work presented here is an important first step in the development of fuel-general predictive capabilities for combustion and burnout.

5.3.1 NOx Reduction On Char

The goal of this work is to identify the effect of char age on the NO/carbon reaction, which plays an important role in a variety of low-NOx combustion systems including those involving reburning. The kinetic expressions previously in use at REI had suggested that the heterogeneous reaction is too slow to contribute to NO reduction, but most prior kinetic studies employed chars that were pre-stabilized by long-time heat treatment, and may be relatively unreactive as a consequence. This study has focused therefore on the measurement of NO reduction activity for very young chars, both in the entrained phase and as captive powders, and the quantification of the effect of char age (heat treatment history).

Entrained Flow Reactor Experiments

The first set of experiments were carried out using a flame-supported entrained flow reactor equipped with an extractive sampling system and NO_X analysis instrumentation, as described in detail in the Phase I report. In brief, methane, oxygen, and an argon/NO mixture were fed to a Henken honeycomb flat-flame burner, yielding approximately 30 slpm of hot gas downstream of the primary flame containing about 1000 ppm of NO and 1 volume-% oxygen. A variety of solid fuels were entrained in a small secondary flow (1 slpm) and metered to the reactor at a uniform mass flow over the course of each 2-minute experiment. The gases downstream of the secondary flame are sampled by a small diameter, stainless steel, water-cooled probe, are then passed through a ice bath, a silica gel dryer, and then to a chemiluminescent NO_X analyzer. The NO concentration is continuously monitored on a strip chart recorder, and a steady baseline value established prior to the introduction of secondary solid fuel. The secondary solid fuel is added quickly at constant, preset, volumetric flow, using a modified syringe pump feeder. The solid fuel is added over the course of 1 - 2 minutes, and the extent of NO reduction determined by integrating the area under the strip chart recorder between the actual and extrapolated baseline NO concentrations. The young chars were prepared in the same flow reactor, but in a separate experiment.

Table 5.4 and Fig. 5.22 summarize the results of the NO reduction experiments for 11 different solid fuels. This study addresses possible heterogeneous effects, and thus chars and low-volatile fuels were the main focus of study with two raw coals included for reference. Table 5.4 shows the large variations in the percentage NO reduced, from 0% for a heat-

treated petroleum coke to 40% for the raw bituminous coal. The two highest amounts both derive from experiments with high-volatile fuels (Illinois #6 coal and Beulah lignite). The chars from these materials had activities that were lower, and were a pronounced function of preparation conditions, most notably heat treatment temperature and time.

Table 5.4
Results of NO Reduction Experiments

Sample #	Description	Solids feed rate, g/min	%NO Reduction
1.	raw lignite	1.54	13
2.	lignite char 600 ^{o}C in Ar, 2hr	1.55	6
3.	lignite char 950 ^{o}C in Ar, 2 hr	1.55	4
4.	lignite char 1200 ^{o}C in N_2, 2 hr	1.55	1.5
5.	lignite char 1400 ^{o}C, 50 msec, 1% O_2 (in flame reactor)	0.92	9
6.	lignite char #3 after exposure to ozone / air mixture	1.55	5.5
7.	Illinois #6 raw coal	1.09	40.
8.	Illinois #6 char 950 ^{o}C in Ar, 10 min	2.0	2.5
9.	Illinois #6 char 1400 ^{o}C, 50 msec, 1% O_2 (in flame reactor)	0.75	0.8
10.	raw petroleum coke	2.01	5.6
11.	pet. coke, heat treated 950 ^{o}C in Ar, 10 min	2.1	<0.5

Apparent Heterogeneous Kinetics

For all but the two raw coals, the NO reduction activities in Table 5.4 were converted to apparent heterogeneous rates and compared to a large set of literature values compiled in the recent review by Aarna and Suuberg [1997]. The kinetic analysis is based on the first-order rate expression for NO reduction:

$$d M_{NO} /dt = - k_S P_{NO} M_C \qquad (5.13)$$

with k_S in g-NO/g-carbon-atm-sec. A preexponential factor was calculated for each material assuming a typical activation energy of 133 kJ/mol [Aarna and Suuberg, 1997]. For purposes of comparison with the literature kinetics, an apparent heterogeneous rate constant is also reported at a standard reference temperature, 1250 K. The results of the kinetic analysis are shown in the Arrhenius plot of Figure 5.22. Figure 5.22 also shows three lines from the Aarna and Suuberg review [1997] representing the mean kinetic law for a wide variety of materials, and lines representing the highest and lowest reported values (considering only those data sets with measurements at temperatures above 1100 K). The rates measured in this study are much higher than the mean line, and most samples are more reactive than the most reactive material in the high-temperature literature data. The wide range of lignite activities caused by different heat treatment conditions is easily seen. The apparent high reactivities of the coke and Illinois #6 may in fact be due to homogeneous effects related to the residual volatile matter. The high activity of the lignite char, however, is primarily a true heterogeneous effect.

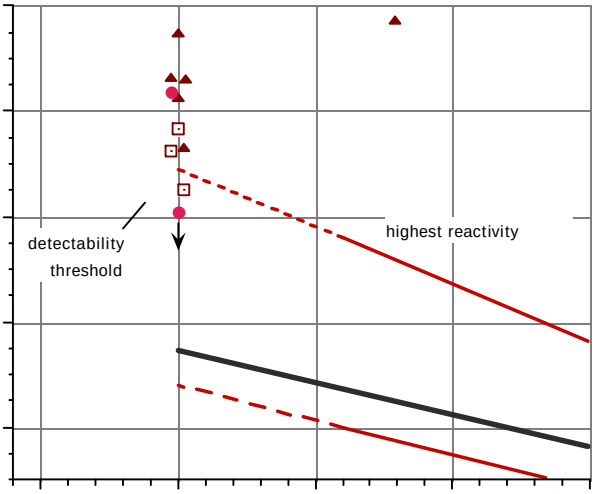

Figure 5.22 NO reduction reactivities for a variety of solid fuels expressed as apparent heterogeneous rate constants at 1250 K. Measured points are compared to literature values reviewed by Aarna and Suuberg [1997].

This experiment clearly demonstrates the effect of heat treatment on NO reduction activity under reburning conditions, either through changes in char reactivity, and/or through reduction in residual volatile matter in some cases. Because of the high reactivity of the very young chars, heterogeneous effects should indeed be important in reburning environments, at least for some coal types.

Captive Particle Measurements

Additional experiments were performed on captive char samples heat treated in an all-graphite transient heat treatment apparatus developed at Brown (see Fig. 5.23). This device was designed to study thermal annealing of chars under flame-like temperature histories in the absence of oxidizing gases. The device is capable of maximum temperatures above 2700°C and heating rates about 10^3 °C/sec. The device employs two thin graphite sheets held at the ends by brass electrodes connected to a DC power supply. Powdered char samples are sandwiched between the graphite sheets, which act as an electrical resistance heater in direct contact with the sample. The electrode chamber is purged to prevent oxidation while the center section is at high temperature. Current is fed to the electrodes according to a pre-established program, designed to achieve a target peak heating rate, peak temperature, and hold time at peak temperature. The temperature of the lower graphite sheet is monitored in real time with a Luxtron high-speed one-color pyrometer with 2 mm target diameter.

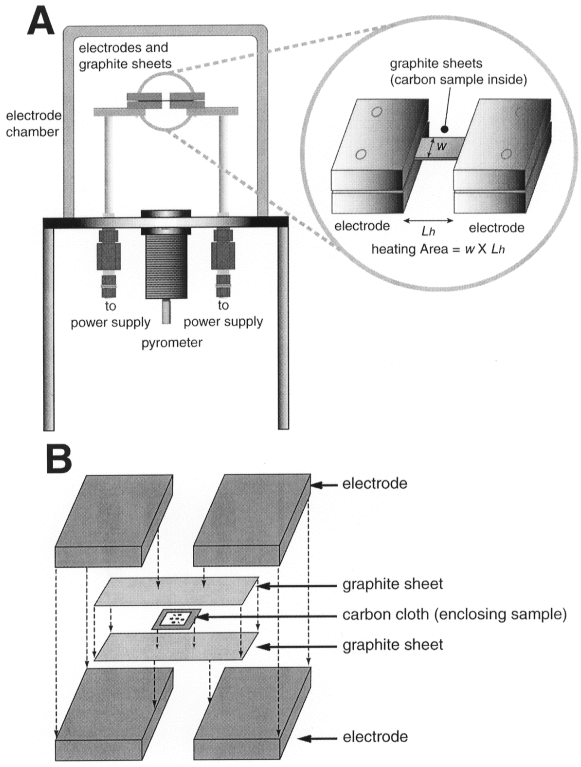

Figure 5.23 Sketch of the all-graphite transient heat treatment apparatus used in the captive particle experiments. The apparatus is described in detail elsewhere [Shim and Hurt, 2000].

In these experiments, Beulah lignite and Illinois #6 coal were subjected to mild pyrolysis at 700 ^{O}C in a tube furnace to remove the bulk of the volatile matter. Then 6-10 mg of size graded char were charged to the transient heat treatment device and brought to 2000 ^{O}C for a hold time of 2 second. Isothermal thermogravimetry was used to measure the loss in activity in a stream of 2% NO in UHP helium at 900 ^{O}C. The normalized rate of mass loss, (1/m)(dm/dt), was measured in the early stages of conversion and the baseline drift (due to the presence of residual oxygen in helium) is subtracted. The resulting normalized mass loss is reported in Fig. 5.24 as a measure of the NO reduction activity of the heat-treated char.

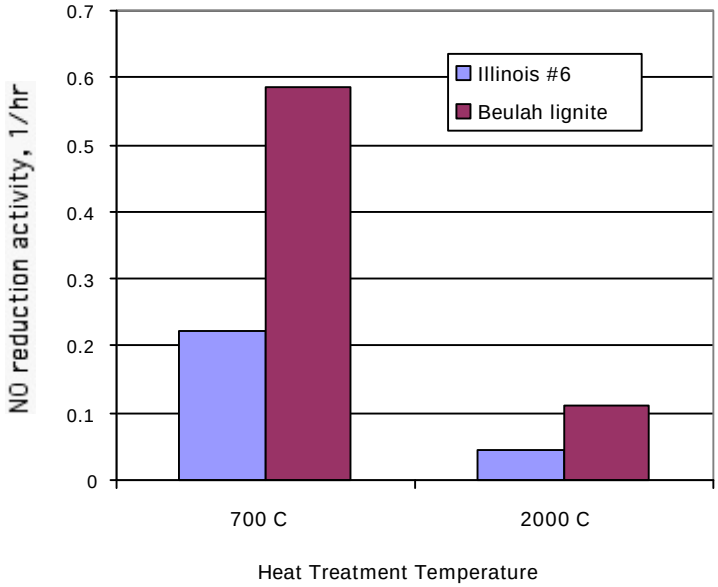

Figure 5.24 NO reduction activity of chars as a function of captive sample heat treatment for two parent coals. Heat treatment for 2 seconds; NO reduction in 2 % NO at 900 ^{O}C.

The results indicate that char reactivity toward NO is indeed sensitive to rapid heat treatment (~ 2 sec) at flame temperatures. The results provide direct support for the conclusions drawn in the entrained flow reactor studies (above) that loss of char reactivity is at least in part responsible for the difference in reburn activities between mature chars and partially devolatilized coals.

5.3.2 Oxygen Reactivities of Diverse Solid Fuels

A selected set of experiments was performed in this subtask to provide information on the relative reactivity of diverse solid fuels. Most kinetic studies have focused on one or at most several fuels, and as a result it is very difficult to extract from the literature relative burning rates or kinetics needed to make predictions of fuel-specific effects. It is often desirable to use relative kinetics or relative burning rates measured in a single laboratory to derive practical kinetic laws for new fuels as corrections to the existing kinetic laws used for common reference coals. This technique is often more accurate than assembling reactivity information on diverse fuels from diverse sources. In the latter case, the differences between

laboratory techniques, analysis methods, and even reactivity definitions, can far exceed the real fuel-to-fuel differences that are key to the combustion calculation. For this reason, simple experiments were designed in this subtask to provide data on relative intrinsic reactivity that can be used to in combustion simulations on a variety of coals and alternate fuels. For most of these materials, the existing literature contains no combustion data in the form of kinetics or burning rates relative to known reference coal chars.

For the reactivity experiments, a series of chars were prepared by 700 ^{o}C pyrolysis of a wide variety of practical solid fuels, including international coals, petroleum cokes, and diverse biomass samples. The fuels and their properties are listed in Table 5.5. Reactivity measurements were conducted by nonisothermal TGA, yielding a rapid and efficient single measure of mass-specific intrinsic reactivity.

Table 5.5
Oxidation Reactivity of Coals and Alternate Fuels

Material ID		Proximate Analysis (wt%)				Ultimate Analysis (wt%, daf)					Reactivity
name	type	ash	volatile matter	fixed carbon	moisture	C	H	O	N	S	$\log_{10} k_o$
Beulah (ligA)	coal	6.37%	37.36%	22.89%	33.38%	73.14%	4.46%	20.59%	1.00%	0.82%	7.46
Illinois #6 (hvCb)	coal	14.47%	34.16%	40.93%	10.43%	78.11%	5.44%	9.73%	1.32%	5.39%	6.31
Koonfontain (mvb)	coal	12.20%	25.54%	58.74%	3.52%	78.72%	4.78%	13.79%	1.99%	0.71%	5.82
Lei Yang (an)	coal	21.90%	5.53%	70.54%	2.03%	90.47%	2.01%	5.86%	0.72%	0.93%	4.89
Lykens Valley #2 (an)	coal	10.71%	4.33%	80.97%	3.99%	90.33%	4.01%	4.30%	0.80%	0.56%	5.02
Pocahontas #3 (lvb)	coal	4.55%	18.13%	76.31%	1.01%	89.87%	4.90%	3.31%	1.14%	0.78%	4.96
Rosebud (subB)	coal	9.85%	32.68%	35.89%	21.58%	78.19%	4.22%	15.21%	1.05%	1.33%	7.00
Conoco Delayed Coke	coke	<0.05%	10.97%	88.44%	0.59%	87.80%	3.96%	1.41%	1.43%	5.40%	5.51
Tosco Fluid Coke	coke	<0.05%	6.00%	91.31%	2.69%	87.38%	2.41%	5.14%	2.57%	2.50%	5.24
Graphite Powder	graphite	0.28%	-	-	-	96.30%	0.38%	<0.10%	0.87%	2.44%	4.36
Graphite Rods	graphite	-	-	-	-	100.00%	0.00%	0.00%	0.00%	0.00%	3.51
Bagasse Sachurum	biomass	3.55%	72.85%	16.48%	7.12%	45.92%	6.26%	47.60%	0.17%	0.05%	5.92
Corn Stalk	biomass	2.84%	65.52%	22.10%	9.54%	43.99%	6.28%	48.93%	0.70%	0.09%	8.20
Dried Sludge	biomass	<0.05%	64.59%	20.00%	15.41%	42.37%	6.54%	48.01%	3.05%	0.03%	6.42
Microcrystalline Cellulose	biomass	<0.05%	85.75%	8.78%	5.47%	41.86%	6.42%	51.68%	0.02%	0.02%	5.55
Rice Hulls	biomass	14.99%	59.04%	18.74%	7.23%	44.59%	6.36%	48.70%	0.29%	0.05%	7.21
Wheat Straw	biomass	8.59%	62.65%	19.88%	8.88%	44.23%	6.39%	48.63%	0.60%	0.15%	7.78
Hardwood	wood	0.52%	73.50%	17.64%	8.34%	45.80%	6.20%	47.82%	0.15%	0.03%	6.83
Pinus Radiata	wood	0.20%	72.29%	18.51%	9.00%	46.05%	6.31%	47.58%	0.04%	0.02%	6.10
Populus Deltoides	wood	0.58%	74.58%	17.53%	7.31%	46.43%	6.11%	47.32%	0.08%	0.06%	7.08
Softwood	wood	0.42%	70.15%	21.56%	7.87%	46.14%	6.32%	46.01%	1.48%	0.05%	6.82
Refuse-Derived Fuel	waste fuel	18.99%	68.26%	8.46%	4.29%	41.95%	6.46%	51.55%	0.02%	0.02%	5.49
Tire Bits	waste fuel	5.77%	-	-	-	87.63%	7.57%	2.55%	0.39%	1.87%	5.37

The reactivity measurement proceeds as follows. From 3 - 11 mg of char were loaded in the TGA and heated to 100 ^{o}C for 1 hr in air to stabilize the balance. The oven was then programmed for a linear ramp at 7 ^{o}C/min followed by a hold at 950 ^{o}C. When the sample reached 20% conversion (daf), the temperature and reaction rate were recorded. The raw temperatures are reported as an index of reactivity, as well as preexponential factors calculated using a typical activation energy for Zone I oxidation (35 kcal/mol). Note that measured activation energies for the reaction between oxygen and impure, disordered chars are observed to fall in a relatively narrow range in Zone I, from about 33 - 40 kcal/mol.

Adjusting E within this range does change the absolute values of the preexponential factors but affects only slightly the relative reactivities, which are the focus of this study.

The resulting relative char reactivities, expressed as preexponential factors, are listed in the last column of Table 5.5 and plotted in Fig. 5.25 as a function of the carbon content in the parent fuel. The measured reactivities span about 4.5 orders of magnitude, from graphite (lowest) to corn stalk char (highest). The biomass materials alone have reactivities spanning 3 orders of magnitude. The coals and cokes as a group span 2.5 orders of magnitude in reactivity.

For coals, the carbon content is an approximate indicator of rank, and has been used to correlate the reactivities of chars prepared under standard conditions [Hurt and Mitchell, 1992; Jenkins et al., 1973]. Indeed, such a rank-dependent correlation is used in CBK8 along with a second-order correction for inertinite content, and has been used as the basis for estimating burnout behavior of various coals in full-scale furnaces in EPRI's NOxLOI PREDICTOR. The empirical correlation between reactivity and percent carbon is seen again for the coals in the new data of Fig. 5.25, and it also provides a reasonable description of the petroleum cokes and the tire-derived fuel. It bears no resemblance, however, to the biomass data.

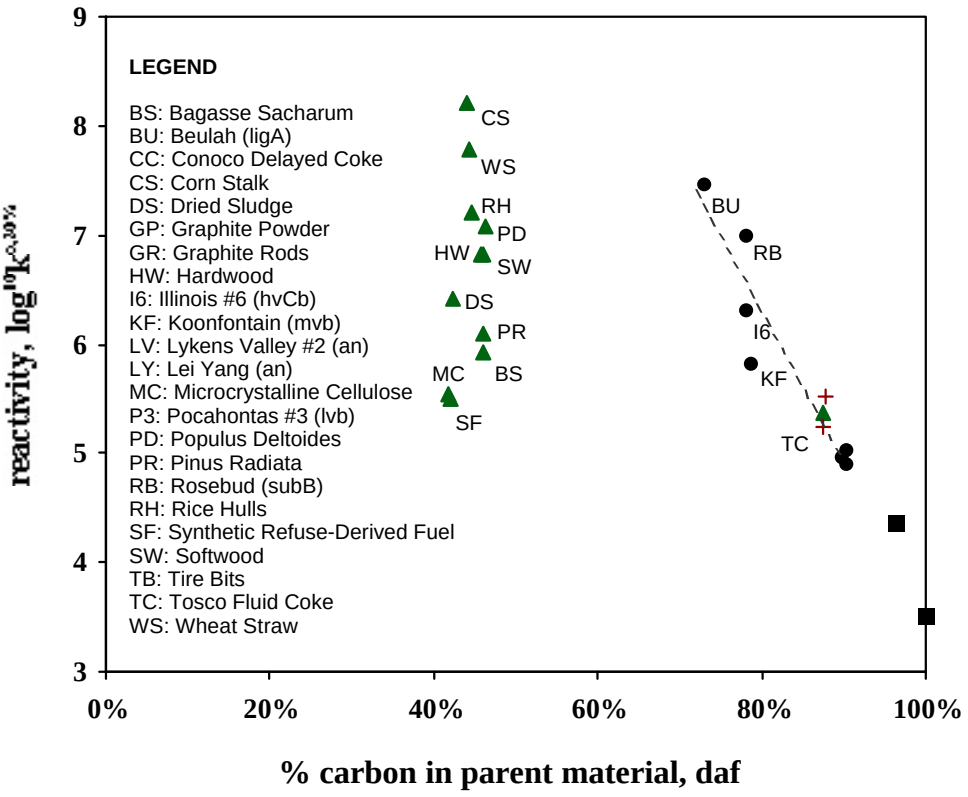

Figure 5.25 Intrinsic oxygen reactivities under standard conditions for a wide range of coals and alternative solid fuels. Circles: coals; Triangles: biomass fuels; Crosses: petroleum cokes; Squares: graphites. (Note: the three coal points with lowest reactivities are anthracites from China and the U.S.) The dashed line gives a simple linear trend in the coal data (reactivity vs. rank) as often used in coal-based combustion reactivity correlations.

The biomass materials have similar organic elemental compositions (see Table 5.5) and fall in a narrow range of carbon contents on Fig. 5.25. Despite this, their reactivities vary by 3 orders of magnitude. It is likely that inorganic catalysis is playing a key role in the reactivity of these materials, accompanied perhaps by physical differences in the chars (surface area and pore structure) that are only poorly correlated with the starting organic composition.

The data in Fig. 5.25 provide some of the first information on char reactivities for many alternate fuels that are candidates for co-firing applications with coal. We can further conclude that the simple correlations used in the past for coal chars have no utility for alternate fuels. It is not possible at this time to rationalize the observed differences in a way that could serve as a general predictive tool for all fuels. More work is needed on the identification and understanding of the physical and chemical phenomena that dictate the reactivity differences. Work is also needed on chars prepared at higher (flame-like) temperatures. A longer-term goal is the development of new rationale correlations or models for predicting or estimating high temperature char reactivity from the properties of arbitrary organic precursors. Work is underway in pursuit of this goal.

5.3.3 Subtask 5.3 Conclusions

1. Two independent experimental techniques indicate that the reactivity of chars in NO reduction is quite sensitive to the extent of rapid heat treatment under flame-like conditions. The high reactivities of partially devolatilized coals and young chars suggests the importance of heterogeneous NO reduction routes in a variety of low-NO_X combustion systems, including those incorporating reburning.

2. A first set of data has been acquired on the relative intrinsic combustion reactivities of chars from a diverse set of coals, biomass materials, and other alternative fuels. The alternative solid fuel chars have a wide range of intrinsic combustion reactivities that do not follow the simple trends observed for coal chars. The data are useful for combustion calculations on specific fuels, but more work is needed to develop generalized estimation techniques such as those currently available for coal.

5.4 References

Aarna, I. and Suuberg, E.M., *Fuel*, 76(6) 475-491 (1997).

Antxustegi, M.M., Calo, J.M. Hurt, R.H. and Shim, H.-S. *Proc. Eurocarbon '98, Science and Technology of Carbon,* Strasbourg, France, p. 737, 1998.

Barrett, E.P., Joyner, L.G., Halenda, P.H., *J.Am.Chem.Soc.* 73 373 (1951).

Carberry, J.J., *A.I.Ch.E. J.* 8 557 (1962).

Essenhigh, R.H., Klimesh, H.E., and Förtsch, D. *Energy and Fuels*, 13 826-831 (1999a).

Essenhigh, R.H., Förtsch, D., and Klimesh, H.E. *Energy and Fuels*, 13 5 (1999b).

Floess, J.K., Longwell, J.P., Sarofim, A.F., *Energy and Fuels*, 2 18 (1988).

Freeman, E., Gao, Y.M., Hurt, R.H., Suuberg, E.S. *Fuel*, 76 (8) 761-765 (1997).

Froberg, R.W., Essenhigh , R. *Proc. Combust. Inst.* 27: 179 - 187 (1978).

Froment, G.F., Bischoff, K.B., *Chemical Reactor Analysis and Design*, p. 162, John Wiley and Sons, New York, 1990.

Gao, Y.; Shim, H.; Hurt, R.H.; Suuberg, E.M.; Yang, N.Y.C. *Energy and Fuels*, 11, 457-462 (1997).

Gavalas, G.R., *AIChE Journal* 26 (4) 577 (1980).

Ghafoori, N., Buchole, J., *ACI Materials Journal*, March-April, 1997.

Helmuth, R. *Fly Ash in Cement and Concrete*, Portland Cement Association, 1987.

Hill, R.L., Sarkar, S.L., Rathbone, R.F., Hower, J.C., *Proceedings; 12th International Symposium on Coal Combustion By-Product (CCB) Management and Use*, Vol. 1 p. 23-1, American Coal Ash Association, Alexandria, VA, 1997.

Horvath, G. and Kawazoe, K., *J. Chem. Eng. Japan*, 5 470 (1983).

Hurt, R. H., D. R. Dudek, J. P. Longwell, and A. F. Sarofim. *Carbon* 26:4, 433 (1988).

Hurt, R.H., Hardesty, D.R., in *Coal Combustion Science Quarterly Progress Report, January - March 1993*, Sandia Technical Report, SAND94-8215, 1994.

Hurt, R. H. and R. E. Mitchell. *Twenty-Fourth Symposium (International)on Combustion*, The Combustion Institute, Pittsburgh, PA, pp. 1243 - 1250 (1992).

Hurt, R. H. and Davis, K. A., *Proc. Combust. Inst.* 25: 561-568 (1994).

Hurt, R.H., Davis, K.D., *Combustion and Flame*, 116 662-670 (1999).

Hurt, R.H., Sun, J-K, and Lunden, M., *Combustion and Flame*, 113 181-197 (1998).

Hurt, R. H. and R. E. Mitchell. *Proc. Combust. Inst.* 24: 1243 - 1250 (1992).

Jenkins, R.G., Nandi, S.P., Walker, P.L.Jr., *Fuel* 52 288 - 293 (1973).

Laine, N.R., Vastola, F.J., Walker, P.L.Jr., *J. Phys. Chem*. 67 2030 (1963).

Lea, F.M., *The Chemistry of Cement and Concrete: Third Edition*, Chemical Publishing Co., Inc., New York, 1970.

Lin, S.Y., Hirato, M., Horio, M., *Energy and Fuels*, 8 598-606 (1994).

Lizzio, A.A., Jiang, H., Radovic, L.R., *Carbon* 28 (1) 7 - 19 (1990).

Lizzio, A.A., Piotrowski, A., Radovic, L.R., *Fuel* 67 1691 (1988).

Lunden, M.M., Yang, N.Y.C., Headley, T.J., Shaddix, C., *Proc. Combust. Inst.* 27: 1695-1702 (1998).

Malhotra, V.M., Mehta, P.K., *Pozzolanic and Cementitious Materials*, Gordon and Breach, Amsterdam, 1996.

Menendez, J.A., Phillips, J., Xia, B., Radovic, L.R., *Langmuir* 12 4404-4410 (1996).

Mitchell, R.E., *Proc. Combust. Inst.* 23: 1297-1304 (1990).

Mitchell, R. E., R. H. Hurt, L. L. Baxter, and D. R. Hardesty "Compilation of Sandia Coal Char Combustion Data and Kinetic Analyses: Milestone Report" SAND92-8208, June 1992.

Niksa, S., Muzio, L., Fang, T., Hurt, R.H., Sun J., Kornfeld, A., Stallings, J., Mehta, A. "Assess Coal Quality Impacts on Nox and LOI with EPRI's NOx LOI PREDICTOR," presented at the *Fifth International Conference on Technologies and Combustion for a Clean Environment*, Lisbon, 1999.

Ramachandran, V.S., *Concrete Admixtures Handbook*, Noyes Publications, Park Ridge, N.J., 1995.

Reid, R.C., Prausnitz, J.M., Poling, B.E. *Properties of Gases and Liquids, Fourth Edition*, McGraw-Hill, New York, 1987.

Rixom, M.R., and Mailvaganam, N.P., *Chemical Admixtures for Concrete, Second Edition*, E.&F.N. Spon Ltd., London, 1986.

Russell, N.V., Beeley, T.J., Gibbins, J.R., Man, C.K., Williamson, J. *Proceedings International Conference on Coal Science*, DGMK, Hamburg, pp. 995-998 (1997).

Satterield, C.N., *Mass Transfer in Heterogeneous Catalysis*, Robert Krieger, Huntington, New York, 1981.

Shim, H., Hurt, R.H. *Energy and Fuels*, 14 340-348 (2000).

Simons, G.A, *Prog. Energy Combust. Sci.* 9 269-290 (1983).

Skokova, K.A. Ph.D. Thesis, The Pennsylvania State University, 1997.

Solomon, P.R., Serio, M.A., Carangelo, R.M., Bassilakis, R., Gravel, D., Baillargeon, M., Baudais, F., Vail, G., *Energy and Fuels*, 4 (3) 319 (1990).

Veranth, J.M., Pershing, D.W., Sarofim, A.F., Shield, J.E., Twenty-Seventh Symposium (International) on Combustion, The Combustion Institute, Pittsburgh,1998, pp. 1737-1744.

6.0 COMBUSTION INVESTIGATIONS

One area of major focus for Reaction Engineering International and the University of Utah was in continuing the combustion studies to determine the maximum possible NO_x reduction that might be achieved within a burner. This work combined the fundamental studies on bench-scale combustion testing and pilot-scale testing in the University of Utah's 5 MMBtu/hr L-1500 furnace. Each of these subprograms will be presented in detail.

As a result of these combustion efforts, it was determined that there appeared little one could do from a burner retrofit scenario to reduce NO emissions to meet proposed EPA standards. However, from these low-NO_X studies, it became apparent that one of the potential problems that would be encountered by boiler operators would be the potential for waterwall wastage or corrosion. Therefore, an effort was undertaken to investigate waterwall wastage and to try and develop a "real-time" measurement technique. This is described in an earlier portion of this report (Section 4.0).

6.1 Bench-scale Studies

6.1.1 Introduction

The level of nitrogen oxides (NO_X) produced by pulverized coal combustion can be reduced by staged combustion, low-NO_X burners, low excess air operation, and reburning [Chen et al., 1982]. Creation of oxygen-deficient furnace regions minimizes the conversion of fuel nitrogen to NO_X but also inhibits the oxidation of carbon species, resulting in high carbon content in the fly ash [Storm, 1993 and Maier et al., 1994]. Carbon in the fly ash is undesirable because the carbon represents wasted fuel and prevents using the ash for cement production. The mutagenicity of coal fly ash has been associated with the organic content [Chuang et al., 1992, Morris et al., 1995 and Mumford et al., 1990].

When a pulverized coal particle is injected into a flame it decomposes into char and volatiles, and the volatiles further decompose to produce soot that creates a luminous zone surrounding the source particles [Mitra et al., 1987 and Fletcher et al., 1997]. Char refers to porous, carbon-rich particles that remain in a solid or liquid phase while soot refers to carbon-rich solid material produced from gas-phase precursors.

Soot formation in pulverized coal flames has been extensively studied since it affects both nitrogen evolution [Chen and Niksa 1992] and radiative heat transfer. Most studies of residual carbon in coal fly ash, however, have focused on the unburned char [Hurt and Davis, 1994 and Walsh et al., 1994]. Soot was assumed to make a negligible contribution to carbon in the ash because soot particles, although less reactive than char, are also orders of magnitude smaller [Unsworth et al., 1991]. The sooting tendency of coal varies with rank [Mitra et al., 1987], and soot aggregates have been reported to form in the wake of coal particles burning in a laminar flow laboratory furnace [Seeker et al., 1981 and McLean et al., 1981]. At least one study [Seeker et al., 1981] speculated that staged combustion would enhance the tendency to form large soot aggregates in full-scale furnaces.

A previous study of pilot-scale coal combustion at the University of Utah [Veranth, 1998] showed that the unburned carbon in the fly ash produced from low- NO_X pulverized coal

combustion consisted of a mixture of soot and coal char. The soot was identified by the presence of chains or aggregates of 10—50 nm diameter primary particles in electron microscope images of both laboratory samples and a sample of fly ash from a power plant operating low-NO_X burners. Laboratory samples showed increasing carbon content with decreasing NO_X concentration. The experiments included a high-NO_X base case and four low-NO_X cases consisting of 1) staged combustion with short (0.5 s) residence time 2) staged combustion with long (1.5 s) residence time, 3) a low-NO_X burner with slow mixing, and 4) reburning using coal as the reburning fuel. Comparison of the base case which used premixed coal and air with the long residence time staged combustion case shows a decrease in the NO_X from over 900 ppm to below 200 ppm and an increase in the carbon in the ash from 4% to over 30%. The fly ash from staged combustion was a mixture of large soot aggregates, porous char, and spherical particles of mineral ash, while the ash from reburning lacked the large soot aggregates. For all laboratory conditions the carbon content in the particle fraction with an aerodynamic diameter over 10 μm was higher than in the 1—2.5 μm diameter fraction. Both soot aggregates and char contributed to the high carbon in the large particle fraction. The difference in carbon burnout between the two staging conditions was consistent with published soot oxidation rates.

Laboratory furnace data for bituminous coals show that the unburned carbon increases when staged combustion is used to reduce NO_X emissions but the unburned carbon in lignite fly ash is low for both high- NO_X and low- NO_X combustion conditions. The carbon in the fly ash shows a bimodal distribution with the carbon concentration reaching a minimum in the 1—3 μm aerodynamic diameter fraction. Electron microscope images confirm that the unburned carbon found in the fly ash over 10 μm aerodynamic diameter is a mixture of soot aggregates and porous coal char particles. A method for quantitatively estimating the relative mass of soot and char in coal fly ash samples was developed and validated [Veranth et al., 2000]. Previous data from the University of Utah showed that for the extreme low-NO_X laboratory combustion conditions the furnace exit ash contains about 10% soot, and this exit soot represents 0.2 to 0.6% of the fuel carbon [Veranth et al., 2000].

The dependence of furnace exit NO_X on furnace stoichiometry has been extensively investigated and is documented in both reviews [Beer et al., 1990] and in recent project reports [Eddings et al., 1999]. However, only one stage combustion condition, 0.85 stoichiometric ratio in the reducing zone, was used in the previous study which concluded that both char burnout and soot formation need to be considered in studies of the carbon content of pulverized coal fly ash. There was therefore an interest in obtaining data on the variation of carbon content over a practical range of stoichiometric ratios.

6.1.2 Methods

This section describes the methods used for the experimental series that was conducted at the University of Utah during the summer of 2000 to obtain data on unburned carbon as a function of particle size and combustion stoichiometry for a range of low- NO_X combustion conditions. Due to operational problems and delays, the planned experimental matrix was reduced to emphasize measurement of the carbon in the submicron ash fraction upstream of the staging air and at the furnace exit.

A 30 KW laboratory furnace, which simulates the time and gas temperature history of a full-scale coal-fired boiler, was used for this study. The experimental methods were based on previous work on coal combustion and particle formation at the University of Utah [Veranth et al., 1998a, Veranth et al., 2000, Spinti et al., 1997 and Veranth et al., 1998b]. Appendix A includes dimensional drawings and a text description of the research furnace, the burner, and the control room instrumentation.

6.1.3 Combustion Equipment

The laboratory samples were produced in a down-fired, U-shaped furnace. The furnace shell is 0.56 m square, and the combustion zone has a 0.17 m inside diameter by 6.7 m from the burner to the exhaust. Ports along the length of the furnace are available for injecting fuel or air and for extracting samples. The furnace has a Reynolds number, based on furnace diameter, of 1000—2000 depending on stoichiometric ratio and temperature. A premixed combustion burner in which the pulverized coal and air are combined before entering the furnace was used. The premix burner was used with combustion air preheated to 400 °F. This burner, when operated without staging, produces high NO_X levels comparable to those obtained with high swirl burners in full-scale power plants.

The fuel was a Utah high-volatile, bituminous-b from the Wasatch Plateau field, Huntington Mine, Emery County, Utah. This coal is representative of a commercially important United States coal producing region and is a member of a suite of research coals that have been used in numerous investigations of coal chemistry and coal combustion as reviewed by [Smith et al., 1994]. The coal was pulverized to 70% less than 200 mesh and had been stored at the University Combustion Research Facility at 870 South 500 West, Salt Lake City prior to use. The coal heating value was 29 MJ/kg and the ASTM volatiles were 40% on a dry basis with 9% ash. The coal analysis for the shipment is provided in Table 6.1.

The combustion conditions were a base case at 1.15 stoichiometric ration (SR), and staged combustion with SR of 1.05, 0.95, 0.85 and 0.75 SR in the reducing zone and with the staging air injected at port 2-2. Final SR downstream of the staging air injection was 1.15 for all conditions. A listing of the port locations and the calculated time from the burner to the indicated port is listed in Table 6.2. These times were calculated from the molar combustion product flow rate assuming plug flow and using radiation-corrected thermocouple measurements for the temperature distribution along the length of the furnace.

Table 6.1 Coal Analyses*

	As Received	Dry
Proximate Analysis %		
Moisture	4.68	0.00
Ash	10.44	10.95
Volatile	39.42	41.36
Fixed Carbon	45.46	47.69
BTU/lb (HHV)	12303	12907
MAF BTU/lb		14653
Ultimate Analysis %		
Moisture	4.68	0.00
Carbon	69.65	73.07
Hydrogen	4.42	4.63
Nitrogen	1.25	1.31
Sulfur	0.40	0.42
Ash	10.44	10.95
Oxygen (By Diff.)	9.16	9.62
Ash Analysis %		
SiO_2		54.61
Al_2O_3		16.36
TiO_2		0.61
Fe_2O_3		4.98
CaO		10.50
MgO		1.87
Na_2O		3.12
K_2O		1.08
P_2O_5		0.22
SO_3		5.70

*Coal Analysis for the Summer 2000 University of Utah experiments. Data from Hazen Research, Inc. Golden, Colorado. Report dated January 24, 2000. Sample L1500-UT-HS-03.

Table 6.2 Gas Residence Time and Flow*

Gas Residence Time and Flow vs. Furnace Location Calculation Results

Transport time calculated from molar flow, temperature, and diameter.

Temperature linearly interpolated from measurement points.

Residence time from burner to indicated port in seconds

Port	Distance, m	BASE	STG@0.5S
Burner	0	0	0
1-1	0.502	0.16	0.19
1-2	0.756	0.23	0.28
2-1	1.060	0.32	0.40
2-2	1.365	0.41	0.52
3-1	1.975	0.61	0.72
4-1	2.896	1.02	1.13
4-2	3.175	1.15	1.26
4-4	3.734	1.43	1.54
6-1	5.010	2.10	2.22
6-3	5.721	2.51	2.63
6-4	6.153	2.78	2.90
Outlet	6.636	3.10	3.24

*U-furnace port locations and calculated gas residence time from the burner to the indicated port for two combustion conditions.

The exit temperature and oxygen and NO_x (sum of nitrogen oxide and nitrogen dioxide) concentrations were continuously logged during the experiments. The furnace temperature was measured using a ceramic-sheathed type B thermocouple which was able to operate for extended periods, even with the high ash loading produced in the core of a pulverized coal flame. A previous study documented the difference between the type B thermocouple reading and suction pyrometer readings [Spinti et al., 1997]. Stoichiometric calculations were performed using the target thermal input, the fuel ultimate analysis, and the target excess air to determine the furnace air flow meter setting. The air flow was held constant and the coal feeder speed was adjusted throughout the run to control the exit oxygen concentration.

6.1.4 Test Conditions

The test conditions were a base case with all air added at the burner as either primary or secondary air and a series of staged combustion conditions with the burner primary and secondary air being 1.05, 0.95, 0.85, and 0.75 of theoretical air. The staging air was always added at Port 2-2 and the overall SR after staging air addition was 1.15. The stoichiometric ratio was calculated as the measured moles of oxygen supplied in the combustion air divided

by the calculated oxygen for complete combustion to CO_2 and H_2O based on the coal ultimate analysis. The nominal residence time in the reducing zone was about 0.5 second but varied with the air flow and gas temperature. The measured gas analysis for the various test runs is summarized in Table 6.3. Data from the first three runs were rejected due to errors in the data logging so the sequence starts with Run #4.

Table 6.3. Gas analysis for the Summer 2000 test runs

Run	Port	SR	Mean	stdev	max	min	Mean	stdev	max	min	Mean	stdev	max	min
				Oxygen				NOx				Carbon Dioxide		
4	6,4	0.95a	2.57	0.34	3.64	1.79	643	24	702	579	16.43	0.3	17.14	15.38
5	6,4	0.95b	2.59	0.32	3.38	1.83	643	20.9	688	586	16.48	0.28	17.15	15.77
6	6,4	0.75a	2.41	0.86	3.64	0	444	76	549	231	16.6	0.68	18.24	15.62
7	6,4	0.75b	2	0.31	2.71	0.89	416	27	478	310	16.86	0.26	17.68	16.29
8	6,4	1.15b	3.16	0.71	4.43	1.3	805	26.9	841	705	15.6	0.66	17.28	14.29
9	2,1	1.15a	3.16	0.35	3.76	2.04	769	19	793	707	15.28	0.31	16.25	14.72
10	2,1	1.15b	3.25	0.59	4.22	1.62	809	20	831	747	15.61	0.56	17.13	14.58
11	2,1	0.85a	3.48	0.51	4.38	2.14	410	40	474	295	15.04	0.48	16.22	14.11
12	2,1	0.85b	2.91	0.88	4.44	2.06	385.7	89.55	527	287	13.67	1.48	15.8	10.95
13	2,1	1.05a	2.38	0.31	2.93	1.72	578	26	627	516	16.16	0.34	16.78	15.46
14	2,1	1.05b	3.07	0.38	3.84	2.29	633	22.6	674	582	15.49	0.39	16.27	14.51
15	2,1	0.75a	2.76	0.46	3.89	1.97	340	36	416	269	15.7	0.41	16.45	14.75
16	2,1	0.95a	2.97	0.63	4.68	1.76	612	38.5	691	519	15.57	0.6	16.7	13.87

6.1.5 Sample Collection

A water-cooled probe shown schematically in Figure 6.1 was used to collect the furnace gas and particles. Dilution nitrogen at a flow of 20 CFH was added to the sample flow for an overall flow rate into the cascade impactor of 60 actual CFH (1 acfm). Prior experiments indicated that the probe and selected gas flow conditions produced acceptable samples of the particles smaller than 10 µm aerodynamic diameter [Veranth et al., 1998b]. Larger particles settle along the horizontal portion of the furnace and cannot be collected quantitatively regardless of the probe design. This is analogous to the bottom ash in coal-fired boilers. However, the lower gas velocity at the laboratory-scale results in more of the total ash remaining in the furnace than is typical observed for full-scale pulverized coal combustion. The dilution was sufficient to keep the mixture dew point for water condensation lower the furnace room air temperature. Rapid dilution at the probe tip was not used since the transport time inside the probe was small compared to the time from the burner to the sampling port.

For the summer 2000 experiments the carbon samples were collected using a water-cooled probe installed in port 2-1 for samples upstream of staging air injection and at port 6-4 for furnace exit samples. Preliminary samples (analysis not reported) were collected using a total filter. Either 90 mm glass fiber (Whatman 934-AH) or 0.22 µm polyvinyldiene fluoride membrane (Millipore GVHP) filters in a preheated holder were used to collect bulk samples.

To obtain data on the carbon content as a function of particle size an Andersen 8-stage 1-acfm cascade impactor and preseparator were used with methods that were originally

developed to produce large samples of oil-free particles for toxicology studies [Veranth, 1998a, Veranth et al., 1998b, Smith et al., 1997 and Veranth et al., 2000b]. A fraction enriched in particles larger than 10 µm aerodynamic diameter was collected in the preseparator. The deposits collected on impactor stages 1, 2 and 3 were combined to make a sample enriched in particles between 2.5 and 10 µm. Stage 5 produced a sample enriched in particles between 1 and 2.5 µm. Stage 7 plus the final filter were combined to produce a sample of submicron particles. Oiled substrates were used on impactor stages 1, 4, and 6 to provide a separation. The impactor setup and composite sample collection is shown in Figure 6.2.

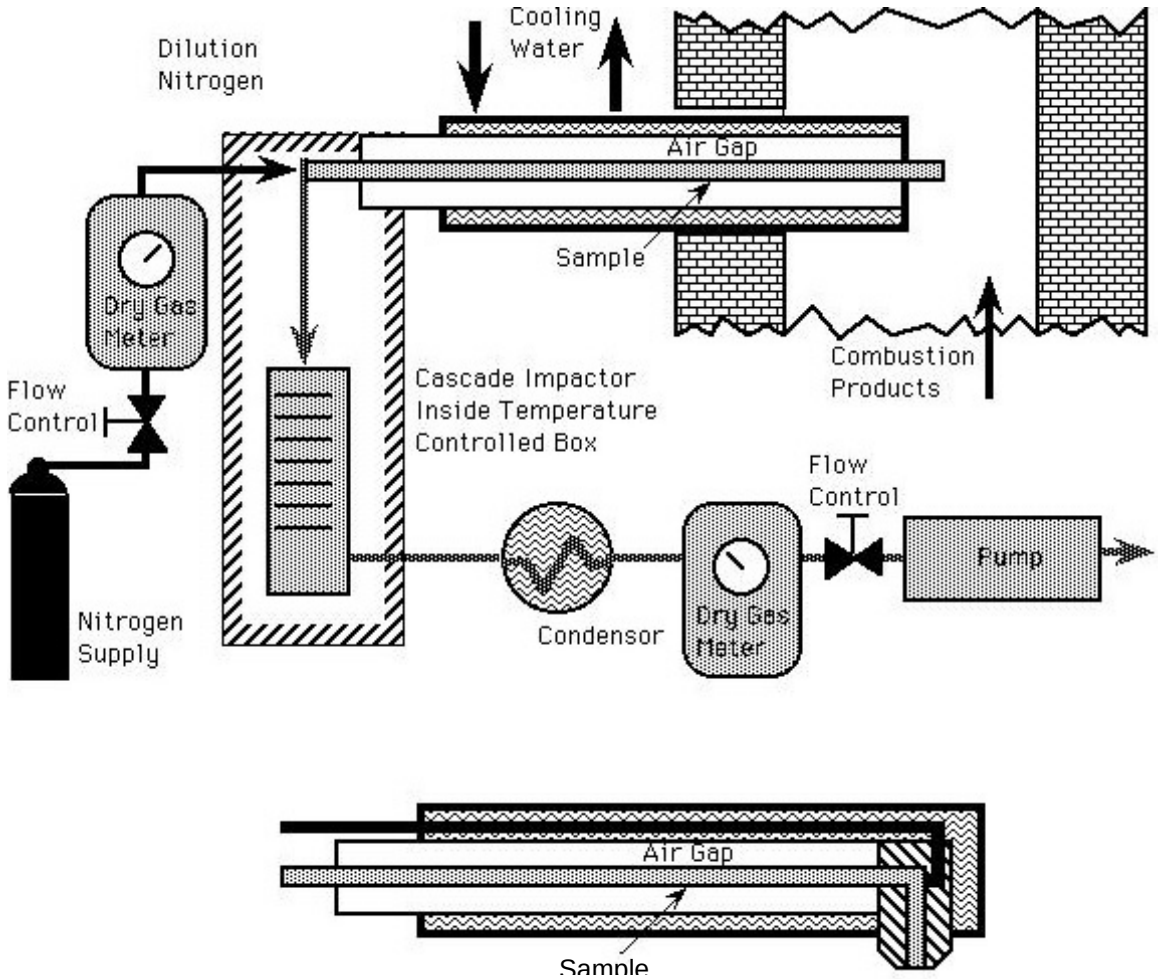

Figure 6.1. Water-cooled sample probe used to collect furnace gas and particle samples.

Due to schedule delays the sampling procedure was simplified to allow collecting data on a full range of staging conditions. An abbreviated Andersen cascade impactor consisting of a preseparator, stage 7 and the final filter was used to collect fractions nominally d >10 µm, 1 - 10 µm, and d < 1 µm respectively. Whatman #42 ashless filter paper was used in the final

filter assembly. This simplified procedure reduced the time needed to collect sufficient mass for carbon analysis to 15 minutes for the Port 6-4 samples and to 5 minutes for the Port 2-1 samples. Sampling was conducted at only one port during each furnace run due to difficulties with simultaneous sampling.

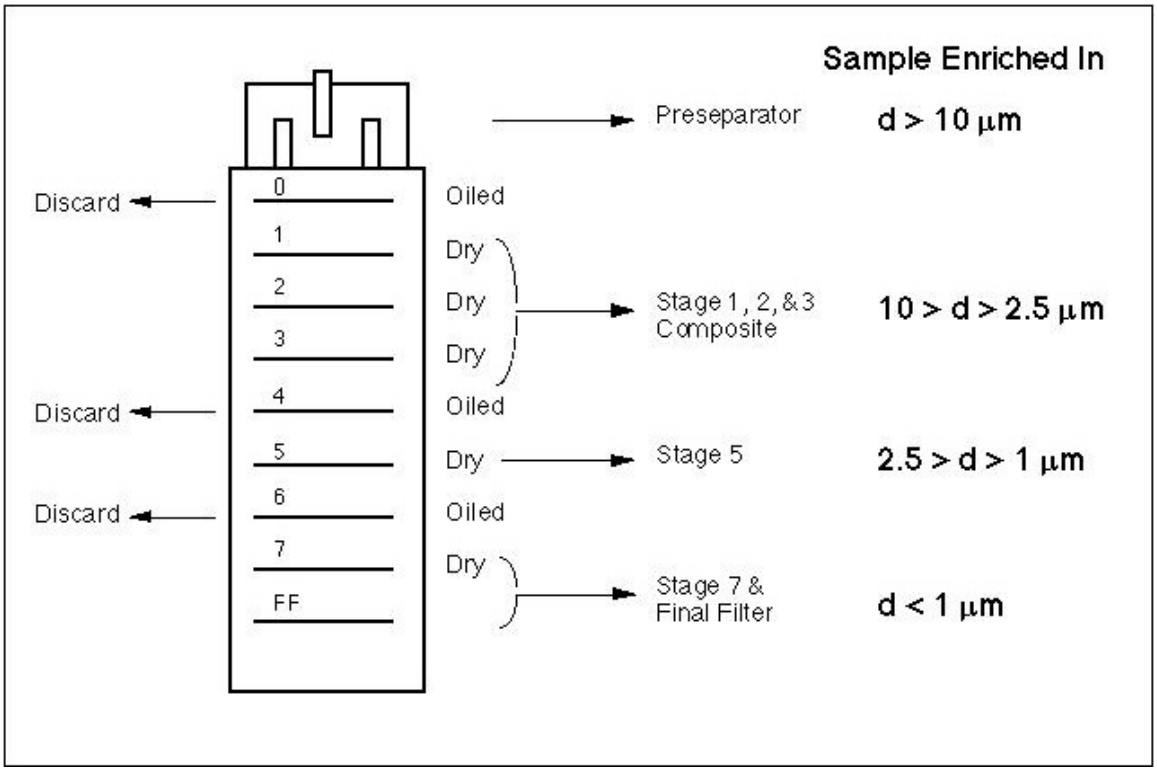

Figure 6.2. Use of the Andersen cascade impactor to produce oil-free composite samples approximating the size ranged discussed in the toxicology literature. The combinations of stages that were used to produce samples evolved during the course of the study.

6.1.6 Sample Analysis

The ash deposits from stage 7 and the final filter were removed from the final filter using ethanol and ultrasonic agitation and the material was composited and transferred to ceramic crucibles for oven drying and followed by weighing of the recovered fly ash. The samples were analyzed for carbon by the Leco method by Western Analysis, Salt Lake City, Utah. Samples of a standard ash were used to verify reproducibility with the low sample mass available for the submicron particles.

6.1.7 Testing of Thermal Optical Reflectance Carbon Analysis

The typical size distribution of coal fly ash results in overloading of the large particle collection stages of a cascade impactor before sufficient mass is collected to allow accurate carbon analysis of the submicron fly ash fraction. The thermal optical reflectance method (TOR) [Chow et al., 1993] is able to analyze elemental carbon and organic carbon in sub milligram-sized samples of ambient particulate. A preliminary test of this method was

conducted to evaluate the feasibility of using it to characterize the carbon in the submicron fly ash from pulverized coal combustion.

Sealed cassette filters, obtained from Data Chem Laboratory, Salt Lake City, Utah, were connected to the exit of a full Andersen cascade impactor that served to remove supermicron particles. Flow rate was 0.34 ACFM due to pressure drop in the cassette filter and sampling time was 10 minutes. The samples were analyzed in accordance with NIOSH Method 5040.

6.1.8 Results

Figure 6.3 shows the carbon versus SR for the reducing zone and furnace exit samples. As expected, the carbon decreased with increasing oxygen supplied to the reducing zone and the carbon in the submicron ash is much higher at the exit of the reducing zone than at the furnace exit. Individual measurements are shown as points and a linear fit to the data is indicated. Replicates within the summer 2000 experimental series collected at the same stoichiometric ratio show good agreement as indicated by the data points in Figure 6.3. A comparison was made for the one condition that was common to both the summer 2000 set and the Veranth 1998 data [Veranth, 1998]. For staging at 0.85 SR, the carbon content on the final filter at the furnace exit was 2.59 and 5.59% for the 1998 data while the summer 2000 measurement was 11.0% carbon. The good agreement within the current data set and the poor agreement with prior data indicate that the results may be very sensitive to details of furnace setup and operation.

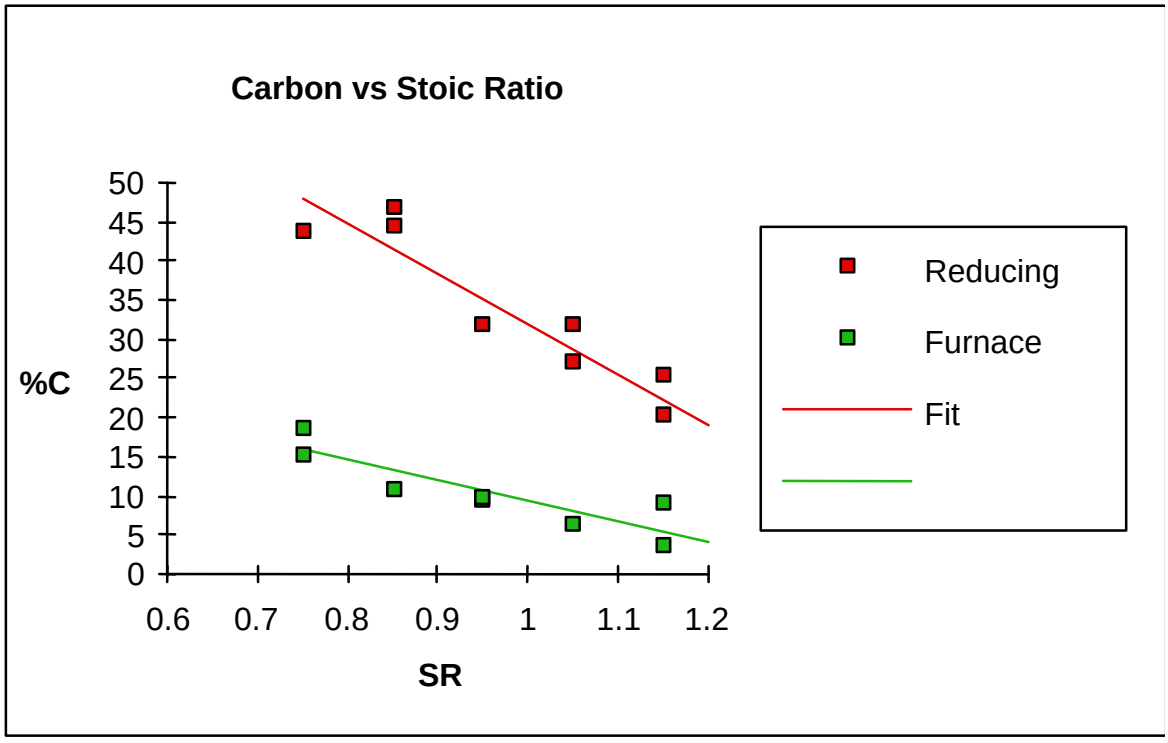

Figure 6.3. Percent carbon as measured upstream and downstream of burnout air injection as a function of burner Stoichiometric Ratio.

Figure 6.4 shows the NOx versus SR for the summer 2000 experiments. Due to data logging errors it was not possible to match gas analysis for NOx with some of the samples. As expected, the NOx decreased with lower SR in the reducing zone. The data in Table 6.3 show large swings in the oxygen during the sampling period. Oxygen standard deviation was reasonable but the recorded minimum and maximum values indicate periods of unstable coal feed that would affect ash carbon content.

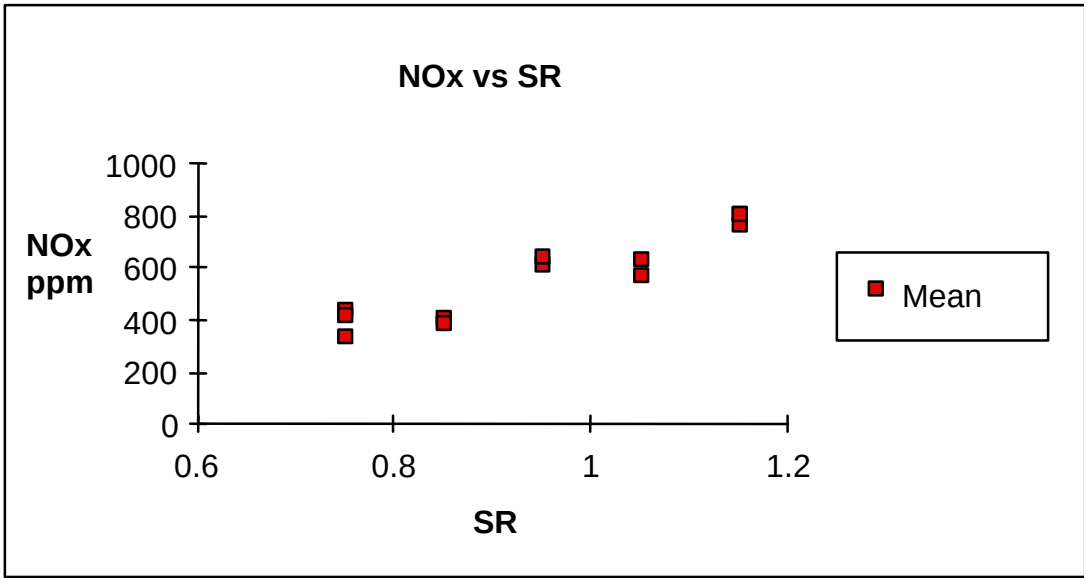

Figure 6.4. NOx versus stoichiometric ratio. Mean of 5-second readings for 20-30 minute sample period.

Table 6.4. Carbon analysis data for the furnace samples and standards; data provided by Western Analysis, Inc. Salt Lake City, Utah

Run	Port	Leco C
1	6,4	9.32
2	6,4	11
3	6,4	6.59
4	6,4	9.46
5	6,4	9.93
6	6,4	15.3
7	6,4	18.8
8	6,4	3.72
9	2,1	25.6
10	2,1	20.3
11	2,1	44.4
12	2,1	46.9
13	2,1	27.3
14	2,1	32
15	2,1	44
16	2,1	31.8
17	Nixon standard (white crucible)	0.25
18	Nixon standard (green crucible)	0.37

Figure 6.5 shows the carbon in the submicron fly ash versus NO_X. There is a great deal of scatter in the data for the reducing zone and a limited number of points for the furnace exit due to lost sampling runs. The ash samples show the expected trend of increasing carbon with decreasing NO_X.

The results of the preliminary testing of the TOR method are listed in Table 6.5. Due to the developmental nature of the experiments and the lack of replication the results should be considered preliminary. However, this appears to be the first reported use of TOR to measure carbon in the submicron ash fraction from pulverized coal combustion. The method appears to be promising for future studies.

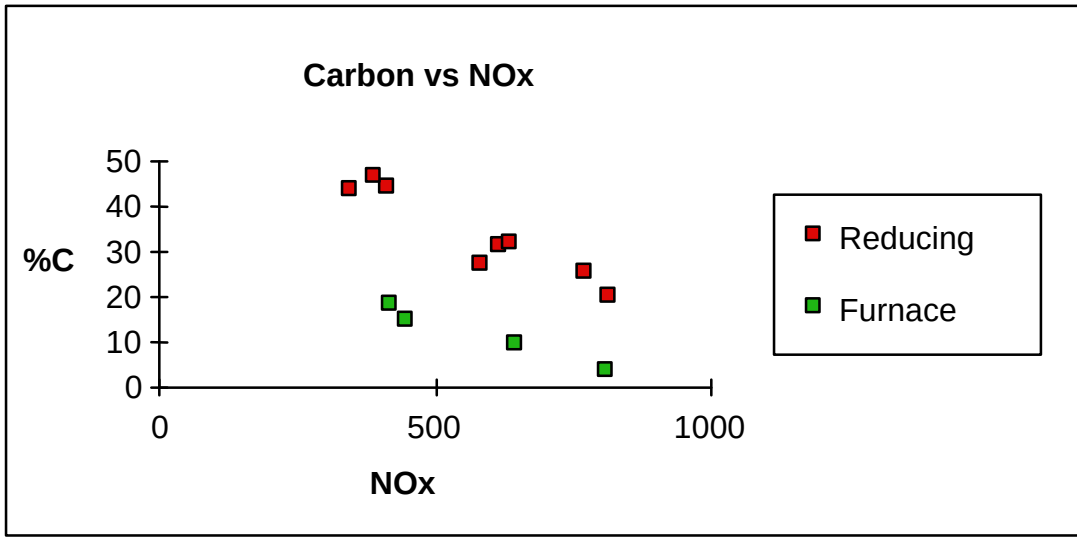

Figure 6.5 Percent carbon as measured upstream and downstream of burnout air injection as a function of the NOx concentration measured at the furnace outlet.

Table 6.5. Thermal Optical Reflectance (TOR) determination of the carbon on quartz filters which collected submicron ash from coal combustion

Sample ID	Combustion Condition	Organic C µg / cm^2	Elemental C µg / cm^2
#1	1.15 SR, Port 6-4	19.95	32.3
#1 Dup	1.15 SR, Port 6-4	20.85	33.6
#2	1.15 SR, Port 6-4	ND	4.0
#3	1.15 SR, Port 6-4	ND	5.1
#4	1.15 SR, Port 6-4	ND	7.8

6.1.9 Discussion

The summer 2000 experiments provide new data that confirms expectations regarding the variation of carbon in ash under staged pulverized coal combustion conditions.

The experiments were adversely affected by problems with uneven coal feed from the screw feeder to the conveying eductor and by difficulty in closing a material balance. Subsequent to the experiments, it was discovered that the air compressor supply was cycling from 80-105 psi that caused fluctuations in the air flow with period of about 6 minutes. The problems with coal feed and with air supply lead to large swings in the stoichiometric ratio even though the average was near target. Since residence time in the furnace is less that 4 seconds the short term SR, not the one-minute average is the relevant value for carbon burnout. Previous work suggests that most of the carbon in ash is generated during excursions to low oxygen. Considerable time was consumed in diagnosing the problem with material balance closure including work fixing leaks in the gas analysis train and verifying rotameter calibrations. The above problems compromised the data quality but the experiments are still useful. The expected trends were confirmed and data is now available on the magnitude of the variations.

6.2 PILOT-SCALE STUDIES

6.2.1 Introduction

In recent years, tighter restrictions on NO_X emissions have resulted in significant efforts to control NO_X levels in pulverized-coal-fired utility boilers. While low emissions can be achieved using expensive post-combustion control such as Selective Catalytic Reduction (SCR), the search continues for more effective in-furnace control techniques. This section describes a series of tests to evaluate a potential new idea for in-furnace NO_X control: In-Situ Gas Reburning. The idea is straightforward: can selective amounts of natural gas be injected into the core of the pulverized coal flame to provide "in-situ" reburning of NO_X formed early in the flame? There were various parameters that required investigation including determination of the appropriate amount of gas, the most effective momentum for the gas jet, effect of initial NO level and the interplay with other burner operating parameters such as combustion air swirl. These parameters were systematically evaluated and the results of these evaluations will be described below. In addition, the effectiveness of in-situ gas reburning was contrasted with NO_X reduction obtained using conventional downstream gas reburning, to provide a comparison with an existing technology.

6.2.2 Experimental Facilities

The pilot scale L-1500 is capable of firing natural gas and/or pulverized coal at a nominal rate of 5 million Btu/h. The facility is designed to simulate low emissions, pulverized coal-fired, wet bottom boilers and is used to investigate full-scale commercial electric power generating unit design and operation.

The L-1500, shown in Figure 6.6, consists of a horizontal combustion chamber with a total length of about 50 ft and a square cross section. The chamber is made of 12 sections. The sections are numbered 1 to 12 beginning at the burner. The first ten sections are of the same length; section 11 is shorter, section 12 longer. Section 12 contains a water-tube heat exchanger. The cross section of sections 1 - 4 is little larger than sections 5 - 12. The sections are illustrated in Figure 6.7. The chamber is lined with refractory. After leaving the heat exchanger in section 12, the flue gas is cooled down to 530 F in an attached downstream heat exchanger. The flue gas leaves the exhaust line after it has passed through a wet caustic scrubber.

The combustion chamber is equipped with several ports in every section. Sampling probes, pyrometers, and other devices can be inserted in different positions through the ports and mounted on a flange. The burner is equipped with special features. It is a Low- NO_X burner built using design parameters similar to the DB Riley CCVIIA burner. Figure 6.8 shows the design of the burner.

Pulverized coal is blown in with primary air in an annular tube with a central bluff body. This central bluff body was replaced with a gas injector for the in-situ reburning tests of this study. Secondary and tertiary air is added through coaxial gaps. Secondary and tertiary air swirl can be separately set from 0% to 100%. These, together with adjustable air preheat and

secondary to tertiary air velocity ratio enables L-1500 to operate from strong mixing close to a diffusion flame mode. High swirl and velocity ratios secondary to tertiary air cause coal and air to mix quickly. Setting a low swirl and the velocity ratio close to unity causes a delay of mixing and allows for substoichiometric conditions in the flame. This concept is similar to the concept of staging.

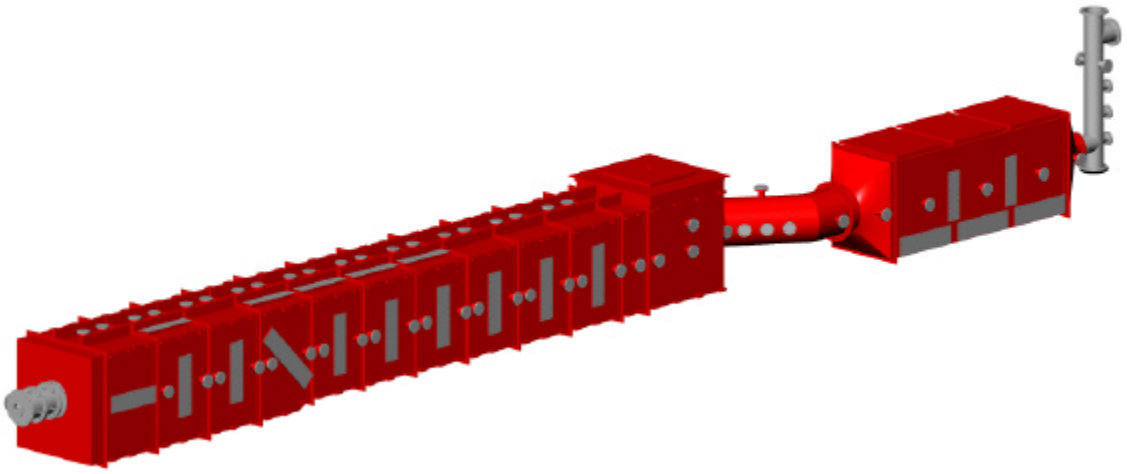

Figure 6.6. L-1500 pilot-scale furnace.

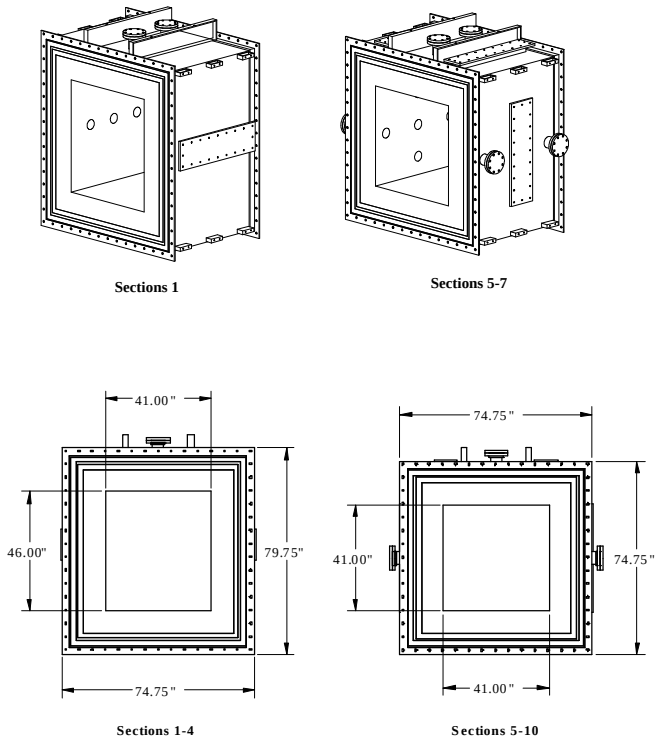

Figure 6.7. Design of L-1500 furnace sections.

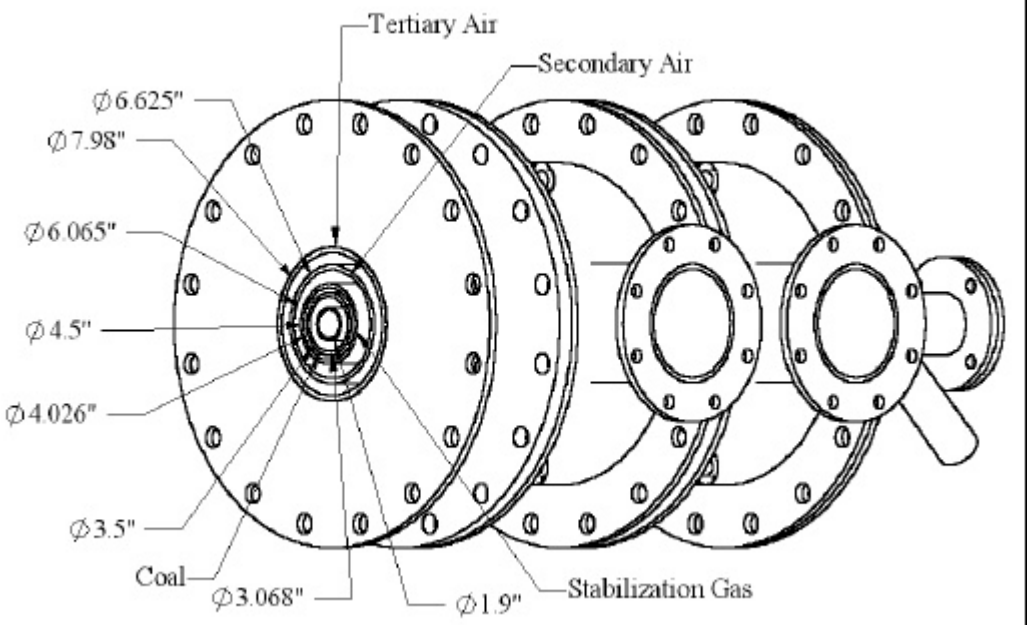

Figure 6.8. Dual register low-NOx burner installed on the L-1500.

For the observation and control of the conditions flue gas is sampled and analyzed in continuous emission monitors (CEMs) including the measurement of CO_2, CO, NO, NO_2, and O_2. The gas is sampled at the transition between the combustion chamber and the heat exchanger through a straight, water-cooled probe. After the flue gas passed a particle filter, it is cooled down and dehumidified before analysis. Analyzers produce a signal proportional to the concentration of measured species, but calibration with gases of known composition is necessary prior to each experiment.

6.2.3 Results and Discussion

Low Initial NO_x Operation

The concept of in-situ gas reburning was applied initially to a burner that had been previously optimized for low NO_X operation. Natural gas was injected through a pipe inserted down the center of the annular coal pipe. A plate was welded onto the end of the gas pipe and a small hole was drilled in the plate to allow for high gas injection velocities. Varying amounts of natural gas were added through the central gas pipe, while the coal feed rate was simultaneously decreased to preserve a constant overall firing rate. Gas addition varied from 0 to 25% of the total firing rate.

In addition to the core gas addition, natural gas was added in an annular ring on the periphery of the coal jet to assist in stabilization of the coal flame. This stabilization gas was used for all tests and all conditions listed under the Low Initial NO_X Operation heading. The burner was originally designed for optimal combustion air velocities in the absence of air

preheat, as the capability for preheating the combustion air was not available when the L-1500 was originally constructed. Thus, these tests consist of no air preheat and natural gas stabilization (at 5% of the overall firing rate) to achieve an anchored flame and to provide Low Initial NO_X Operation. Combustion air was split 1/3 and 2/3 between secondary and tertiary air annuli for all tests corresponding to Low Initial NO_X Operation.

Effect of Swirl

In-situ gas injection was varied from 5 to 25% and the combustion air swirl settings were varied from 0 to 100% as shown in Figure 6.9. The burner was operated under optimal low NOx conditions, with the burner staged to a stoichiometry of 0.9 and with burnout air addition introduced in section 3. As shown, the effect of in-situ gas reburning is most evident under conditions of no swirl. At higher levels of swirl, the effectiveness of the in-situ gas reburning goes down because the flame is quite stable and we have achieved what has been identified to be a minimum NOx level for this burner in this facility with the specified staged residence time [Eddings et al. 2000, Eddings et al. 2001].

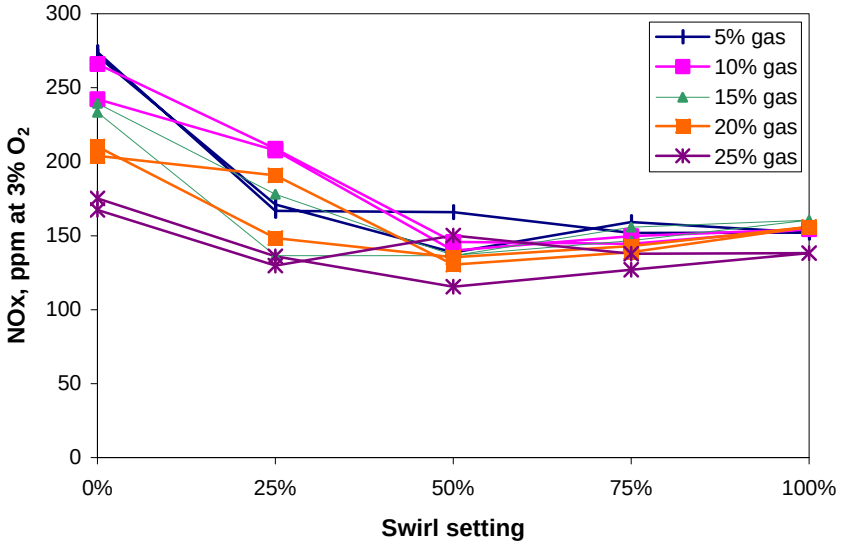

Figure 6.9. Internal gas addition as a function of burner swirl. (Utah coal; 4 MMBtu/h; sec:tert air ratio 33:66; air not preheated; burner SR 0.90; staging in section 3; overall stoichiometric ratio 1.15).

Effect of Burner SR

The effectiveness of in-situ or internal gas reburning as a function of burner stoichiometric ratio is shown in Figure 6.10. The staging was carried out at one set of burner swirl settings; that of 25% of full swirl capability or theoretical swirl numbers of approximately 0.5. As can be seen, at conditions of deep staging, there is little benefit of using more and more natural gas, as the 5 and 10% gas addition results are essentially the same.

The Low Initial NO_X Operation tests confirmed what has been observed for other Low NO_X technologies: there is a minimum achievable NOx level for a given configuration that can be obtained by many different approaches, including air staging and conventional gas reburning. This minimum NOx level is attributed to the presence of nitrogen in the unburned char, which is later converted to NO with the addition of burnout air downstream of the primary reducing zone. The conversion of char N to NO is inversely proportional to the concentration of NO in the gas phase, and thus higher levels of NO reduction in the primary reduction zone will result in greater conversions of char N to NO in the char burnout zone [Molina et al., 2000]. The overall effect of this phenomenon is an apparent minimum achievable NO for a given configuration. One can achieve this minimum in a variety of ways, but will be always be limited in reductions achieved because of the char N contribution that acts like an NO "buffer" to counteract NO reductions gained early in the flame [Eddings et al., 2001].

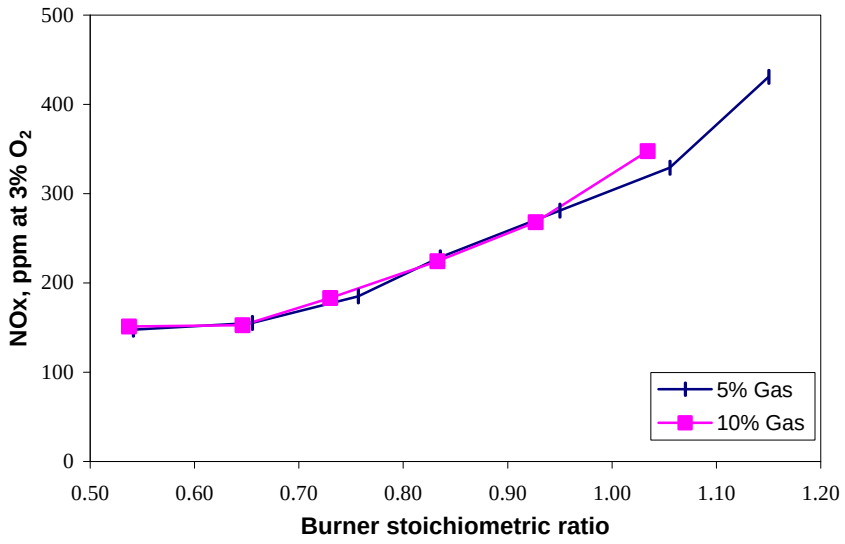

Figure 6.10. Internal gas addition as a function of burner stoichiometric ratio. (Utah coal; 4 MMBtu/h; secondary:tertiary air ratio 33:66; air not preheated; 25 % swirl; staging in section 3; overall stoichiometric ratio 1.15)

High Initial NOx Operation

The poor performance of in-situ gas reburning appeared to be a result of operation near the minimum achievable NO. Thus, the burner parameters were set such that High Initial NOx Operation was possible. High NOx conditions were achieved by using 600 F air preheat and no burner swirl. This regime of operation would be more applicable to boilers that have yet to undergo a low NOx retrofit.

No Burnout Air Addition

The results obtained when starting with a higher level of initial NOx are illustrated in Figure 6.11, where the impact of adding increasing amounts of internal gas is shown for two different injection momentums. Recall that the internal gas addition is performed through a capped-off pipe down the center of the coal pipe annulus, and various-sized holes are drilled in the cap to allow different gas injection velocities. The results are shown in Figure 6.11 for two different hole sizes; 0.5 inches and 1.05 inches. The results showed little benefit to internal gas reburning under unstaged conditions; in other words, all burnout air required for combustion of both the in-situ gas and the coal is introduced at the burner. Also, very little benefit was observed when going to a higher momentum jet.

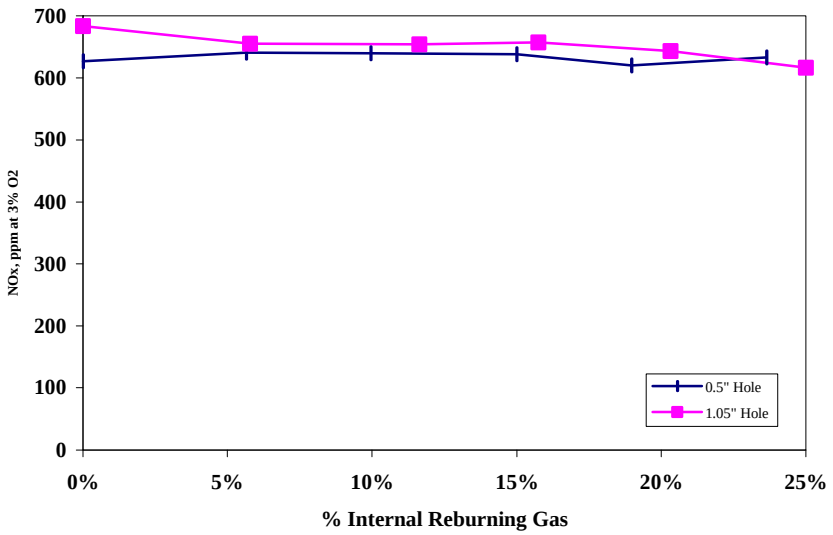

Figure 6.11. Internal gas addition under high initial NO conditions with no overfire air addition. Different gas injection velocities achieved using different injector hole sizes. (Utah coal; 4.25 MMBtu/h total firing rate; secondary:tertiary air ratio 33:66; air preheated to 600 F; no swirl; burner stoichiometric ratio 1.15).

Use of Burnout or Staging Air

The tests were repeated using a scenario more similar to conventional reburning, with internal natural gas addition at the burner, and subsequent overfire air addition downstream to compensate for the gas addition in the burner. This overfire air was introduced in Section 6 to allow subsequent comparison of results with conventional reburning. In addition, the coal feed rate was held constant. In these tests, shown in Figure 6.12, a notable effect was seen with increased internal gas addition. Also, the higher momentum with the smaller hole size appears to give greater reductions, and both hole sizes show increasing reductions with an increase in the amount of gas addition. Nearly 50% reduction is achieved when very high levels of gas addition are utilized.

The results can also be plotted as a function of burner stoichiometric ratio, where the addition of gas resulted in increasingly staged burner operation subsequently offset by downstream air addition. These results, shown in Figure 6.13, illustrate a decrease in outlet NO_X with an increase in gas addition or a decrease in burner stoichiometry. Such an effect is to be expected due to typical air staging behavior in coal systems; however, this effect was evaluated by running a comparison test without the use of internal gas reburning and this result is also plotted in Figure 6.13. As shown, the condition with no gas injection is similar to the case with a 1.05 inch injector; however, the 0.5 inch injector provided greater NO_X reductions than either the no gas case or the 1.05 inch injector case under all burner stoichiometries tested.

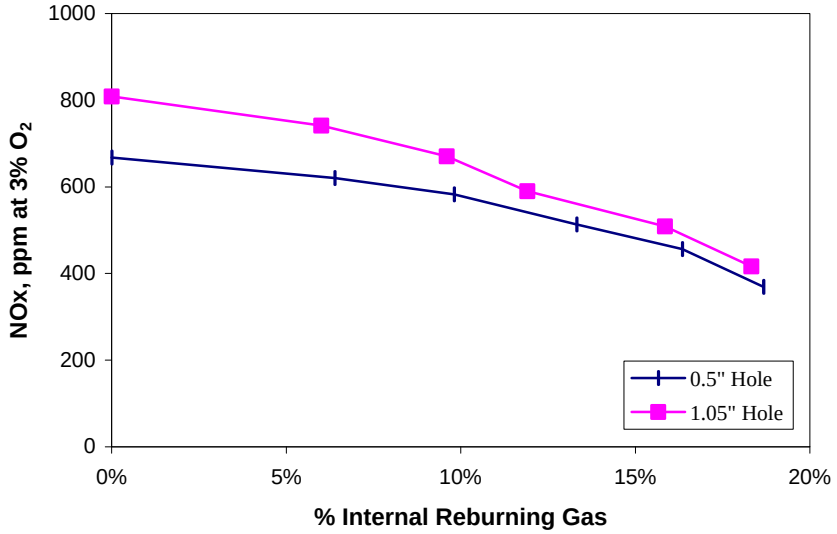

Figure 6.12. Internal gas addition under high initial NO conditions with overfire air addition. Different gas injection velocities achieved using different injector hole sizes. (Utah coal; 4.25 MMBtu/h total firing rate; secondary:tertiary air ratio 33:66; air preheated to 600 F; no swirl; burner stoichiometric ratio 1.15).

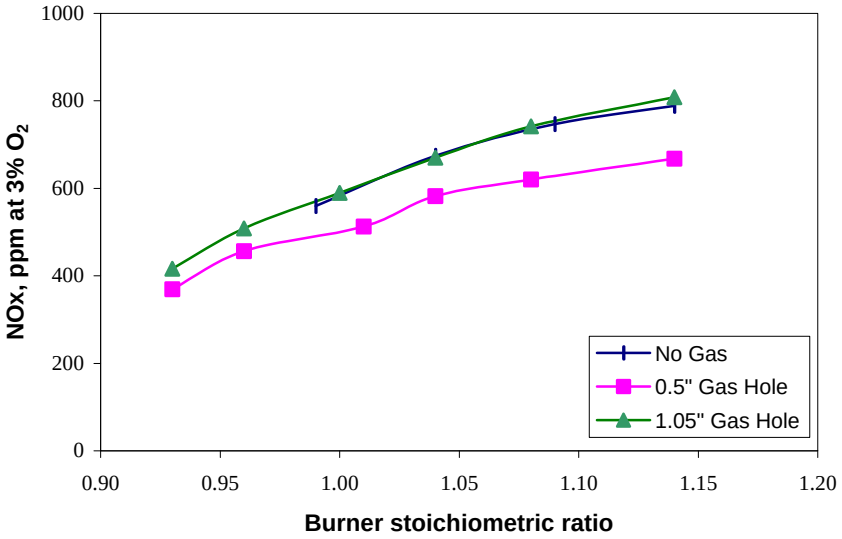

Figure 6.13. Internal gas addition vs. burner SR under high initial NO conditions with overfire air addition. Different gas injection velocities achieved using different injector hole sizes. (Utah coal; 4.25 MMBtu/h total firing rate; secondary:tertiary air ratio 33:66; air preheated to 600 F; no swirl; OFA added in Section 6; overall stoichiometric ratio 1.15).

Comparison with Conventional Reburning

As there appeared to be some increase in NO_X reduction when using internal gas addition, a complete evaluation of the technology requires comparison with natural gas reburning when injection occurs in more of a conventional mode. To this end, natural gas reburning was also performed by addition of gas in Section 3 by opposed gas injectors, followed by burnout air addition in Section 6. The coal feed rate was held constant as before, and the results are shown in Figure 6.14 as a function of burner stoichiometry. As shown, the internal gas reburning with the higher momentum jet and the conventional gas reburning results are similar over the range of stoichiometries investigated.

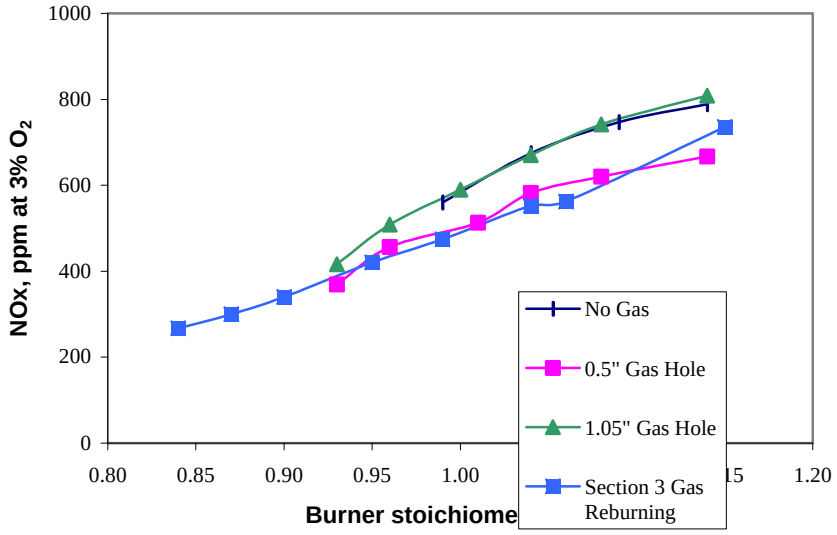

Figure 6.14. Internal gas addition vs. conventional reburning for high initial NO conditions with overfire air addition. Different gas injection velocities achieved using different injector hole sizes. (Utah coal; 4.25 MMBtu/h total firing rate; secondary:tertiary air ratio 33:66; air preheated to 600 F; no swirl; OFA added in Section 6; overall stoichiometric ratio 1.15).

6.2.4 Conclusions

The most effective use of in-situ gas reburning appears to be when applied under high initial NO_X conditions. Use of in-situ reburning at low initial NO_X levels is likely to be ineffective due to apparent limitations on NOx reductions achievable in pulverized coal fired systems.

Injection momentum has a clear effect on efficiency of internal gas addition, and higher jet momentums result in increased reduction efficiencies. Use of internal gas addition shows an effect not attributable to simple decrease in burner stoichiometry, as reductions were achieved in excess of those observed when simply staging the burner firing without internal gas addition.

Comparison with a conventional reburning scenario indicated similar reduction efficiencies for an optimized in-situ gas injector and downstream gas addition indicating that either approach would be acceptable when applied under initially high NO_X conditions. Thus, while there was no clear benefit to using in-situ gas addition over conventional reburning from a NO_X reduction perspective, there may be advantages to using the in-situ technique from an installation perspective.

6.3 References

Beér, J.M.; Bowman, C.T.; Chen, S.L.; Corley, T.L.; DeSoete, G.G.; Folsom, B.A.; Haynes, B.S.; Heap, M.P.; Kramlich, J.C.; Lanier, W.S.; Lester, T.W.; Martin, G.B.; Pershing, D.W.; Prado, G.P.; Samuelsen, G.S.; Sarofim, A.F.; Seeker, W.R.; Solomon, P.R.; Smith, I.W., Pulverized Coal Combustion: Pollutant Formation and Control, 1970-1980, U.S. Environmental Protection Agency, EPA/600/8-90/049, 1990.

Chen, J.C.; Niksa, S., "Suppressed Nitrogen Evolution from Coal-Derived Soot and Low-Volatility Coal Chars," in *Twenty-Fourth Symposium (International) on Combustion*, The Combustion Institute, 1992 pp. 1269-1276.

Chen, S.L.; Heap, M.P.; Pershing, D.W.; Martin, G.B., "Influence of Coal Composition on the Fate of Volatile and Char Nitrogen During Combustion," in *Nineteenth Symposium (International) on Combustion*, Pittsburgh, PA: The Combustion Institute, 1982 pp. 1271-1280.

Chow, J.C.; Watson, J.G.; Pritchett, L.C.; Pierson, W.R.; Frazier, C.A.; Purcell, R.G. The DRI Thermal/Optical Reflectance Carbon Analysis System: Description, Evaluation and Application in U.S. Air Quality Studies, *Atmos. Environ.*, 1993, 27A(8), 1185-1201.

Chuang, J.C.; Wise, S.A.; Cao, S.; Mumford, J.L. Chemical characterization of Mutagenic Fractions of Particles from Indoor Coal Combustion: A study of Lung Cancer in Xuan Wei, China, *Environ. Sci. Technol.*, 1992, 26, 999-1004.

Eddings, E.G.; Pershing, D.W.; Molina, A.; Sarofim, A.F.; Spinti, J.P.; Veranth, J., Advanced Combustor Design Concept to Control NOx and Air Toxics, University of Utah, Department of Chemical and Fuels Engineering, DOE Project No. DE-FG22-94PC94223, 1999.

Eddings, E.G., Z.M. Djurisic, R. Okerlund, M. Wachenhausen, D.W. Pershing, K.A. Davis and M. P. Heap, "DOE Combustion 2000 Low Emission Boiler System (LEBS): Interim Technical Report," Project Number DE-AC22-92PC92158, June 2000.

Eddings, E.G., Z.M. Djurisic, A.F. Sarofim and D.W. Pershing, "Limitations to NOx Reduction in Pulverized Coal Fired Utility Boilers," to be submitted to *Combustion Science and Technology*, 2001.

Fletcher, T.H.; Ma, J.; Rigby, J.R.; Brown, A.L.; Webb, B.W. Soot in Coal Combustion Systems, *Prog. Energy Combust. Sci.*, 1997, 23, 283-301.

Hurt, R.H.; Davis, K.A., "Near-Extinction and Final Burnout in Coal Combustion," in *Twenty-fifth Symposium (International) on Combustion*, Pittsburgh, PA: The Combustion Institute, 1994 pp. 561-568.

Maier, H.; Spliethoff, H.; Kicherer, A.; Fingerle, A.; Hein, K.R.G. Effect of coal blending and particle size on NOx emission and burnout, *Fuel*, 1994, 73(9), 1447-1452.

McLean, W.J.; Hardesty, D.R.; Pohl, J.H., "Direct Observations of Devolatilizing Pulverized Coal Particles in a Combustion Environment," in *18th Symposium (International) on Combustion,* Pittsburgh, PA: The Combustion Institute, 1981 pp. 1239-1248.

Mitra, A.; Sarofim, A.F.; Bar-Ziv, E. The Influence of Coal Type on the Evolution and Polycyclic Aromatic Hydrocarbons During Coal Devolatilization, *Aerosol Sci. Technol.,* 1987, 6, 261-271.

Molina, A., A.F. Sarofim, E.G. Eddings and D.W. Pershing, "A General Review of NO-Char Behavior," *Progress in Energy and Combustion Science*, Vol. 26, pages 507-531 (2000).

Morris, W.A.; Versteeg, J.K.; Bryant, D.W.; Legzdins, A.E.; McCarry, B.E.; Marvin, C.H. Preliminary Comparisons between Mutagenicity and Magnetic Susceptibility of Respirable Airborne Particulate, *Atmos. Environ.,* 1995, 29(23), 3441-3450.

Mumford, J.L.; Helmes, C.T.; Lee, X.; Seidenberg, J.; Nesnow, S. Mouse skin tumorigenicity studies of indoor coal and wood combustion emissions from homes for residents in Xuan Wei, China with high lung cancer mortality, *Carcinogenesis,* 1990, 11(3), 397-404.

Seeker, W.R.; Samuelsen, G.S.; Heap, M.P.; Trolinger, J.D., "The Thermal Decomposition of Pulverized Coal Particles," in *18th Symposium (International) on Combustion,* Pittsburgh, PA: The Combustion Institute, 1981 pp. 1213-1226.

Shibaoka, M. Carbon Content of Fly Ash and Size Distribution of Unburned Char Particles in Fly Ash, *Fuel,* 1986, 65, 449-450.

Smith, K.L.; Smoot, L.D.; Fletcher, T.H.; Pugmire, R.J., *Structure and Reaction Processes of Coal*, Plenum Press: New York, 1994.

Smith, K.R.; Aust, A.E. Mobilization of Iron from Urban Particulates Leads to Generation of Reactive Oxygen Species *in Vitro* and Induction of Ferritin Synthesis in Human Lung Epithelial Cells, *Chem. Res. Toxicol.,* 1997, 10(7), 828-834.

Spinti, J.P., "An Experimental Study of the Fate of Char Nitrogen in Pulverized Coal Flames," Ph.D. Dissertation, University of Utah, Salt Lake City, Utah, 1997.

Spinti, J.P.; Pershing, D.W.; Brouwer, J.; Heap, M.P. Influence of Near Burner Combustion Modifications on NOx Formation from an All-Axial Multifuel Burner, *Combust. Sci. Technol.,* 1997, 126, 1-21.

Storm, R.F. Optimizing combustion in boilers with low-NOx burners, *Power,* 1993, (October), 53-62.

Unsworth, J.F.; Barratt, D.J.; Roberts, P.T., *Coal Quality and Combustion Performance*, Coal Science and Technology, ed. L.L. Anderson. Vol. 19, Elsevier: Amsterdam, 1991.

Veranth, J.M.; Pershing, D.W.; Sarofim, A.F.; Shield, J.E., "Sources of Unburned Carbon in the Fly Ash Produced from Low-NOx Pulverized Coal Combustion," in *27th Symposium (International) on Combustion*, Boulder, Colorado: The Combustion Institute, 1998 pp. 1737-1744.

Veranth, J.M., "Particle Emissions from Practical Combustion Systems," Ph.D. Dissertation, University of Utah, Salt Lake City, Utah, 1998.

Veranth, J.M.; Fletcher, T.H.; Pershing, D.W.; Sarofim, A.F. Measurement of Soot and Char in Pulverized Coal Fly Ash, *Fuel*, 2000, 79(9), 1067-1075.

Veranth, J.M.; Smith, K.R.; Aust, A.E.; Dansie, S.L.; Griffith, J.B.; Hu, A.A.; Huggins, M.L.; Lighty, J.S. Coal fly ash and mineral dust for toxicology and particle characterization studies: Equipment and methods for PM2.5- and PM1-enriched samples, *Aerosol Sci. Technol.*, 2000, 32(2), 127-141.

Walsh, P.M.; Xie, J.; Douglas, R.E.; Battista, J.J.; Zawadzki, E.A. Unburned Carbon Loss from Pulverized Coal Combustors, *Fuel*, 1994, 73(7), 1074-1081.

7. TWO-PHASE MIXING STUDIES

7.1 Introduction

The purpose of this report section is to document the progress and results of the two-phase mixing studies performed in connection with the DOE PRDA entitled, "Optimized Fuel Injector Design for Maximum In-Furnace NO_x Reduction and Minimum Unburned Carbon." This research was conducted in the Physical Fluid Dynamics (PFD) laboratory, University of Utah. The goal of these studies is to gain a better understanding of the flow field mechanisms underlying the dispersion of particles in the near-field of the injector jet flow. In the present experiments, the basic injector geometry was modeled as a coaxial jet, with the interior (primary) jet being loaded with particles. The particular objectives of the research focused on 1) obtaining accurate descriptions of the fluid velocity and velocity gradient field, and 2) correlating these descriptions with injector nozzle characteristics and the dispersion of the suspended phase. These studies are motivated by the broader PRDA goals. These include aiding in the validation and development of the computational models being employed to predict boiler performance and to provide data bases that quantify the influences of injector geometry and operating parameters (e.g., secondary-to-primary jet velocity ratio).

The remainder of this Introduction contains a brief discussion of how fundamental studies of particle dispersion can have a long-term benefit regarding the development of rational (i.e., physically informed) strategies for the design and modification of coal-fired furnace injectors. These ideas were previously discussed in the Phase I final report, and are reiterated here. The remainder of this report provides a brief recapitulation of the results and recommendations from the Phase I portion of the project. This is followed by a discussion of the research steps and experiment modifications taken during the Phase II portion, and a presentation of the results from the Phase II portion.

7.2 Fundamental Understanding and Better Injector Designs

It is widely held that perhaps the most important parameter describing particle dispersion is the Stokes number, $St = t_p/t_f$, where t_p is the aerodynamic response time and t_f is a characteristic time scale of the fluid turbulence. Physically, the magnitude of the Stokes number indicates the how well the particles follow the flow. For $St << 1$ the particle are nearly in equilibrium with the fluid motions, and thus will essentially follow the flow. Conversely, for $St >> 1$ the particle inertia is high and the trajectory of the particle is nearly unaffected by the turbulence. Owing to the fact that at any instant a turbulent flow field is comprised of a range of scales of motion, the Stokes number is a stochastic parameter. In addition, in the present case of coaxial jets the flow is developing in the axial direction. Thus, even in an average sense, the Stokes number will vary with position. Based upon computations of the near-field of typical coal-fired furnace injectors [P.J. Smith, private communication), a typical Stokes number is O(1). For St O(1), there is significant interaction between the particles and the turbulence. That is, for this condition there exists a range of turbulent motions that are capable of changing the particle trajectories. There is a body of evidence [Kamalu et al. 1989, Longmire and Eaton 1992, Wicker and Eaton 1994] that the nature of the large-scale coherent motions within a flow can significantly influence

the time-averaged rate of particle dispersion. A knowledge of how the scale and intensity of the coherent motions relate to the time averaged particle dispersion allows one to think about the effect of a given design modification relative to fluid motion/particle interactions.

Particularly relevant to this idea are the studies by Fan et al. [1992], Wicker and Eaton [1994], and Fan et al. [1996]. These experiments explored the dynamics and control of particle-laden coaxial jets with and without swirl. These experiments, along with numerous others [see, Sadr 2000], indicate that the characteristics of the shear layers between the primary and secondary jets and between the secondary jet and the ambient fluid, play predominant roles in determining the net rate of particle dispersion. As will be mentioned further below, modifying the flow structure and development in the so-called intermediate zone of the coaxial jet holds perhaps the greatest promise for controlling the net dispersion.

An important notion underlying the strategy undertaken in the present work is the fact that any modification of the time-averaged particle dispersion results from the cumulative effect of the instantaneous coherent motions acting within the flow. For the case of Stokes number near unity, this issue is complicated by two facts. The first is that only a subset of the turbulent motions is responsible for the bulk of the particle transport. The second is that the presence of particles changes the structure of the turbulence. Given these, a promising method for attaining the project goals is to determine the connections between the net changes in particle dispersion (for a given set of flow parameters), and the coherent structure of the turbulence. This can be done by acquiring information relating to both the instantaneous and time averaged spatial distributions of the fluid velocity and particle density fields. Such information will allow the connections between the instantaneous flow features and the time averaged dispersion to be identified. Arguably then, this information can then be used as a broad basis for the development of better injector designs. This is the goal of the present work.

7.3 Summary of Phase I Results

The results of the Phase I portion of this work were presented in the final report for that part of the project [Heap et al. 1998]. In this section of this report these results are reiterated and summarized so to provide a context for the subsequent work performed. The primary elements of the Phase I work were to construct a particle laden coaxial jet flow facility, and to obtain measurements of the fluid turbulence and the particle dispersion for a range of velocity ratios. As is described further in Section 7.5, laser-based optical methods were used for both of these measurements. In what follows, representative results from Phase I are presented, and the main conclusions restated.

7.3.1 Development of the Experimental Facility

An important accomplishment of the initial part of the project was the development of a flow facility capable of attaining Reynolds numbers close to those encountered in industrial boilers, while simultaneously allowing optical-based fluid velocity and particle dispersion measurement techniques to be employed. The coaxial jet facility was developed from an existing water tunnel. The baseline facility was manufactured by Engineering Laboratory Design, and was originally configured as a 0.15m x 0.15m cross section channel flow. Extensive modifications, however, were required for the present work. As shown in Figure

7.1, the main components of the current facility consist of a large rectangular test section, a particle filtration tank, a particle feed system, and pumps for both the primary and secondary jets. The configuration of the facility now and its configuration during the Phase I studies are similar. Extensive modifications to the particle feed system, however, have been made. As described in Section 7.4 below, this has resulted in a dramatic improvement in the control and repeatability of the particle injection rate. A more detailed description of the facility, and its calibration, is also given below.

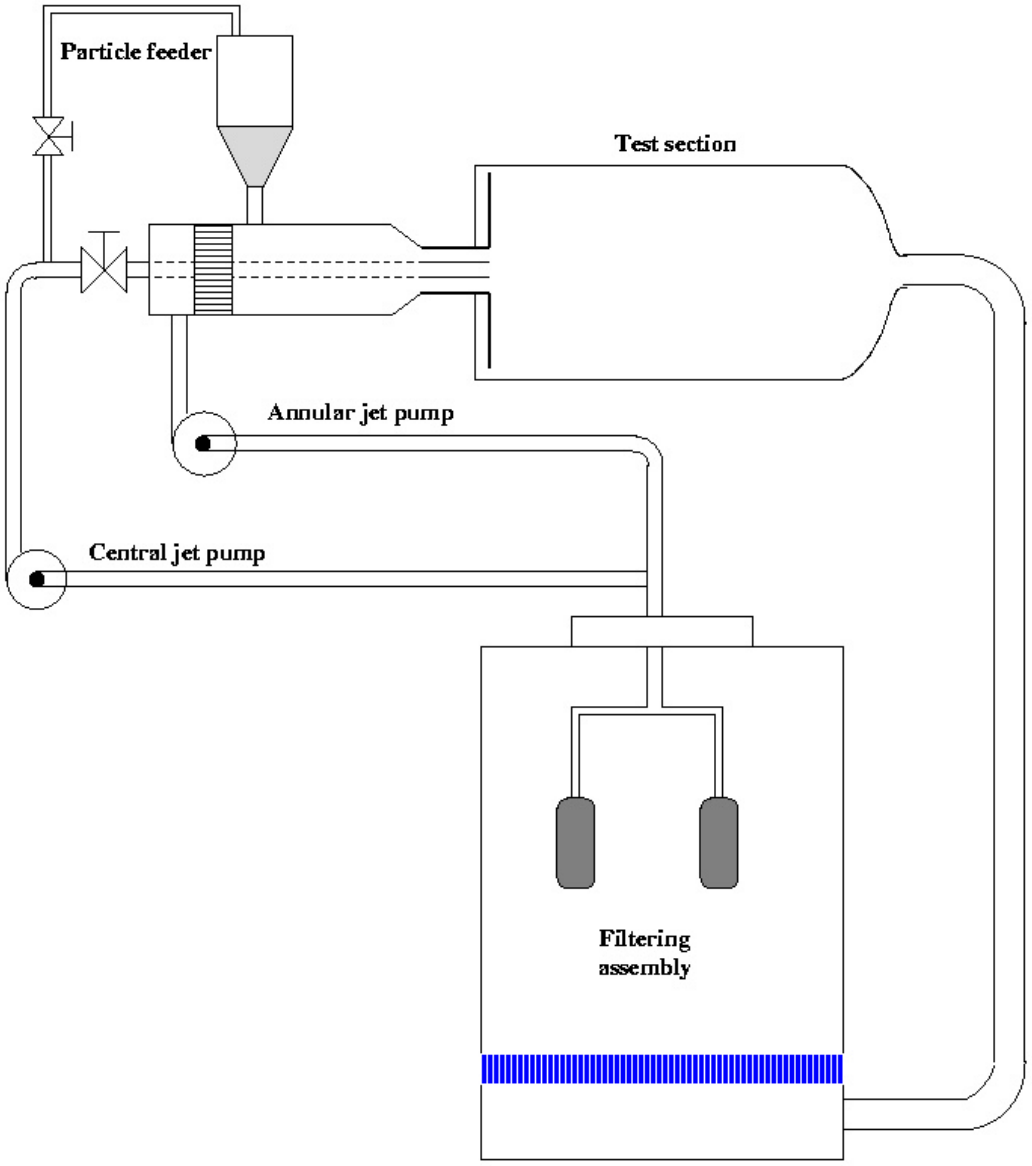

Figure 7.1. Schematic of the coaxial jet facility.

7.3.2 Phase I Experiment Parameters

The experiments conducted during the first phase of the project were at a Reynolds number of 1.2 x 10^5 based on the annular jet diameter. Two velocity ratio conditions were examined, $\lambda = U_o/U_i = 0.5$ and 1.0, where U_o is the outer annular jet mean velocity and U_i is the central jet mean velocity. Measurements were taken at axial positions ranging from the jet exit to 7.5 central jet diameters downstream. High quality crown glass particles having a specific gravity of 2.5 and a diameter of 0.1 mm (as given by the manufacturer) were used as the solid phase. These were injected at an estimated mass loading of about 5%. As described in the Phase I final report, the particle time scale, t_p, was estimated to be 0.0017 seconds, while the typical turbulent time scale, t_f was estimated to be 0.014 seconds. These resulted in a Stokes number estimate of 0.12. Note that as described in more detail below, during Phase II, a number of these parameter settings were re-examined and/or more precisely calculated.

7.3.3 Velocity Field Statistical Profiles

Pure Fluid Case

Initial velocity measurements were for a fluid phase flow only. As described in the Phase I report, and as further discussed in Section 7.4 below, the velocity field measurements were acquired using Molecular Tagging Velocimetry (MTV). Mean and RMS axial component velocity profiles, U(r) and u'(r) respectively, for positions x/d = 2.5, 5.0 and 7.5 were acquired for velocity ratios $\lambda = 0.5$ and 1.0. Example results from these experiments at x/d = 2.5 are given in Figures 7.2 and 7.3 respectively.

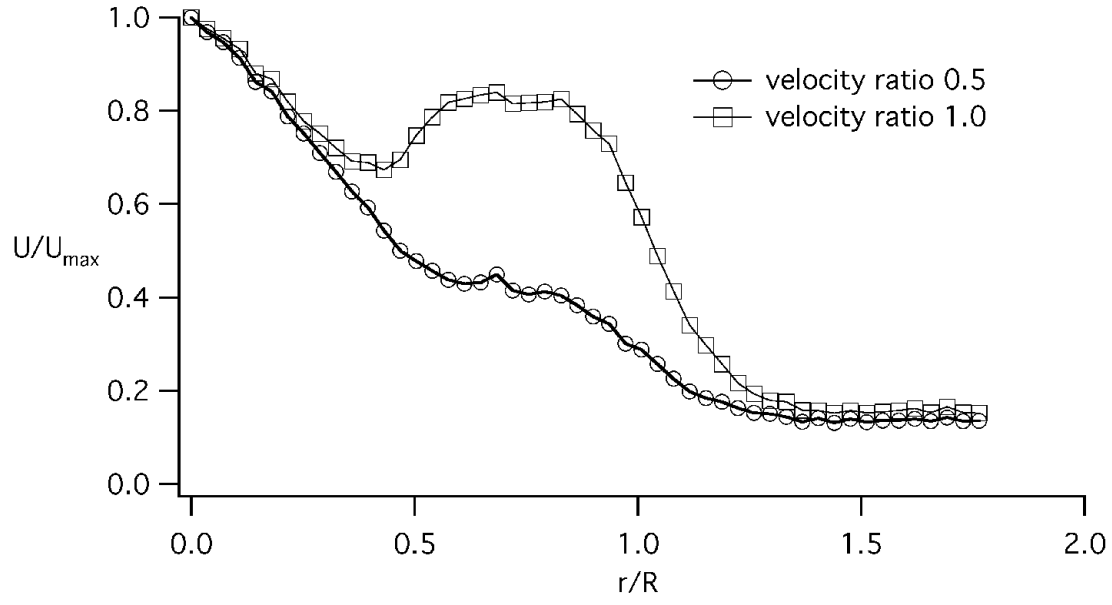

Figure 7.2. Mean axial velocity profiles at x/d = 2.5, pure fluid case.

Apart from the expected spreading behavior indicated, one can also see that in Figure 7.2 the central jet has undergone acceleration. This phenomenon has been seen previously [e.g.,

Ribero and Whitelaw 1980], and is essentially due to the confinement of the central jet by the annular jet. This effect diminishes with decreasing velocity ratio. As can be clearly seen in Figure 7.2, for the case of $\lambda = 1.0$ there exists a significant wake-like region between the central and annular jets. Recent results by Buresti et al. [1998] indicate that a previously overlooked parameter determining the structure of coaxial jets is the thickness of the tube wall separating the central and annular jets. That is, given a fixed velocity ratio, this wall thickness determines the Strouhal number of the vortices being shed from the inside and outside surfaces of this wall. The nature of the interaction between the two sheets of opposing vorticity being shed from the wall strongly determine the subsequent merging and mixing between the central and annular jets.

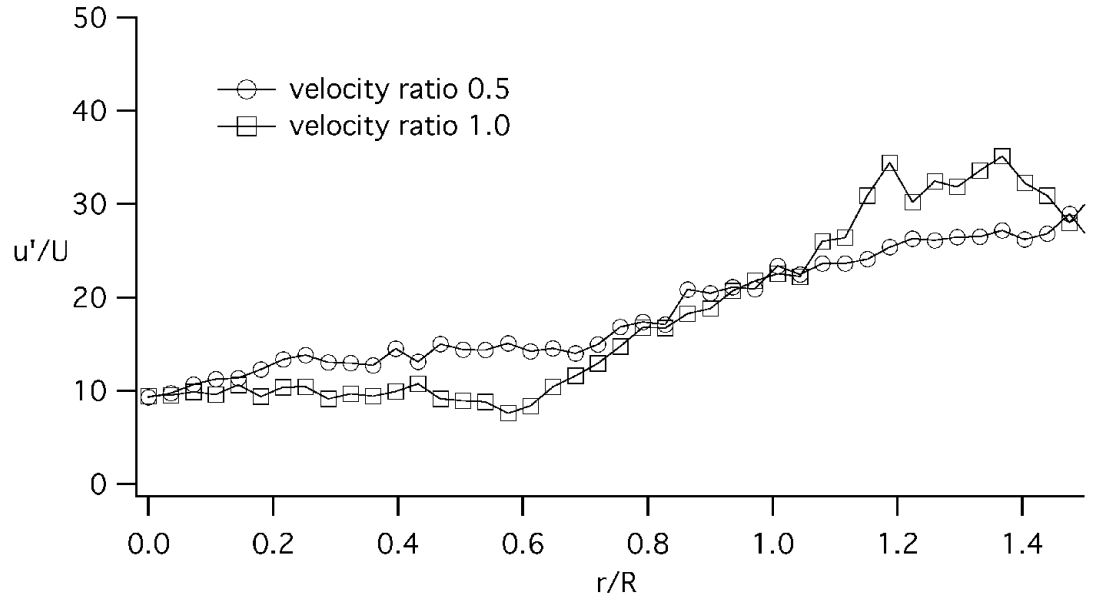

Figure 7.3. RMS axial velocity profiles at x/d = 2.5, pure fluid case.

Owing to the fact that the production term in the turbulence kinetic energy equation contains the mean gradient, dU/dr, the axial velocity RMS profiles align with the regions of strong shear in the mean profiles. Because the location of the strongest shear is a function of velocity ratio, the position of maximum RMS may either be located in the shear region between the two jets, or in the shear layer between the annular jet and the ambient fluid. This is seen by comparing the $\lambda = 0.5$ and $\lambda = 1.0$ profiles of Figure 7.3. Similar and/or related phenomena were observed for the other parameter conditions explored.

Flow with Particles

Mean and RMS axial component velocity profiles, U(r) and u'(r) respectively, for positions x/d = 2.5, 5.0 and 7.5 were acquired for velocity ratios $\lambda = 0.5$ and 1.0. For comparison with Figures 7.2 and 7.3, example results from these experiments at x/d = 2.5 are given in Figures 7.4 and 7.5, respectively. In total, comparison of results such as these indicates that for the mean flow the particle laden jet cores attain higher velocities, and the jets spread more

slowly. This observation is in good agreement with the results of Fan et al. [1992, 1996]. The RMS profile results for the particle laden case show, however, mixed agreement with previously reported results that the addition of particles unambiguously leads to a reduction in the turbulence intensity. That is, when compared with the pure fluid case, the results in Figure 7.5 indicate that depending on the velocity ratio, the magnitude of the intensity may either decrease ($\lambda = 1.0$) or increase ($\lambda = 0.5$). As discussed more below, the resolution of these subtle differences lead us to take measures to more precisely define our exact flow conditions.

7.3.4 Passive Scalar and Particle Concentration Distributions

The initial mixing and dispersion experiments in the facility involved comparisons between the mixing of a passive scalar (sodium fluorescein dye) and the dispersion of particles. The primary reason for these experiments was to determine the relationship between the spread of a purely passive scalar (the fluorescein dye) and the particle-laden case in which the turbulence is modulated through an interaction with the particles. Example results from these studies are shown in Figures 7.6 through 7.9. Figures 7.6 and 7.7 show the dye results for x/d = 5.0 and l = 1.0 and 0.5 respectively. Figures 7.8 and 7.9 show the particle laden flow results under nominally the same conditions. The contour results in Figures 7.8 and 7.9 are presented as average particle number densities (ratio of the total number of particles found to occupy a given pixel location to the total number of particles in all the frames analyzed).

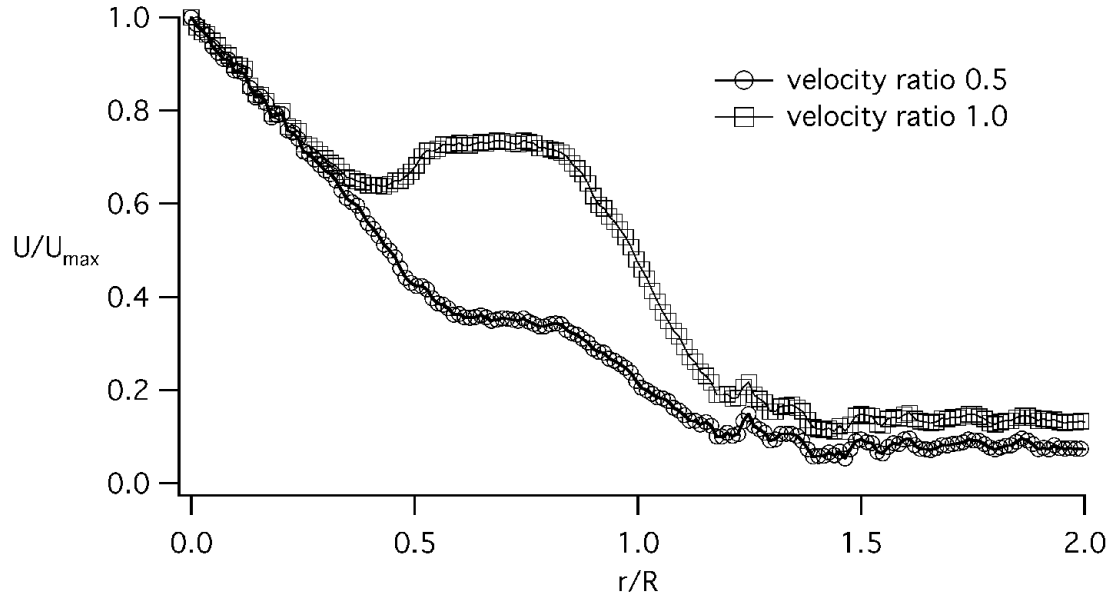

Figure 7.4. Mean axial velocity profiles at x/d = 2.5, 5% mass particle loading.

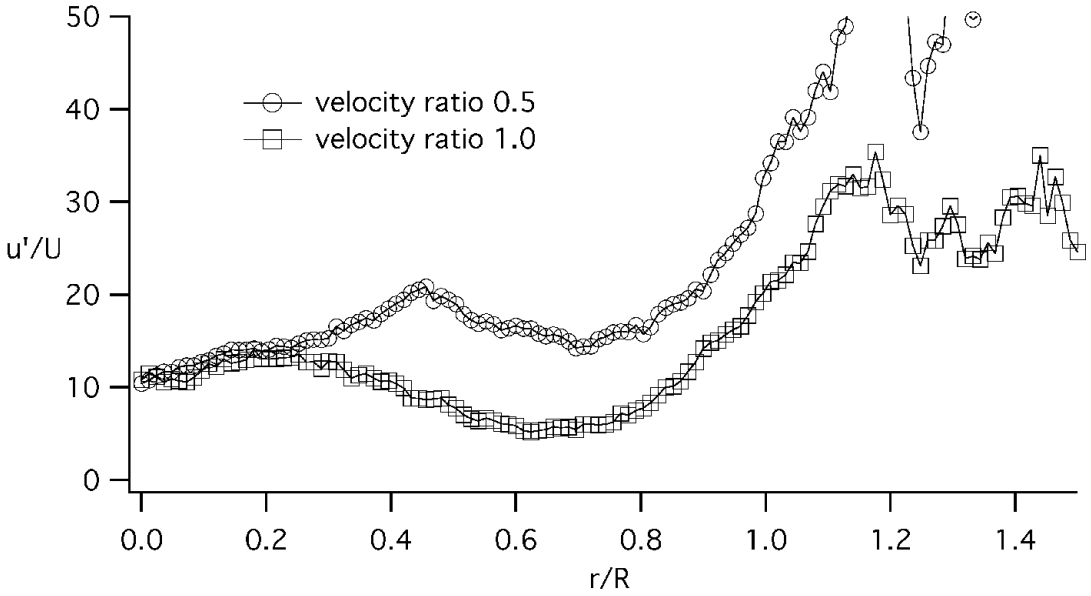

Figure 7.5. RMS axial velocity profiles at x/d = 2.5, 5% mass particle loading.

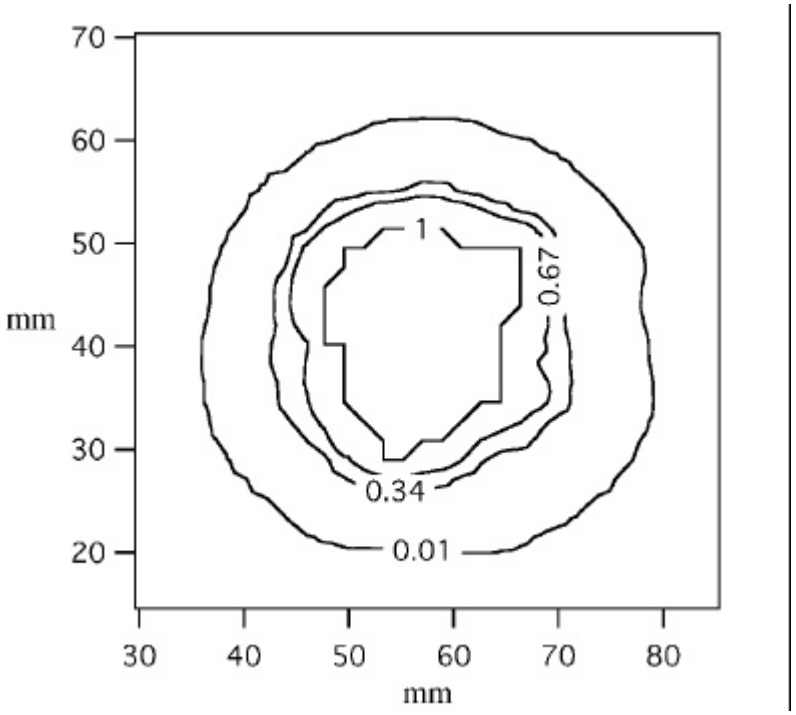

Figure 7.6. Fluorescein concentration contours at x/d = 5.0, velocity ratio = 1.0.

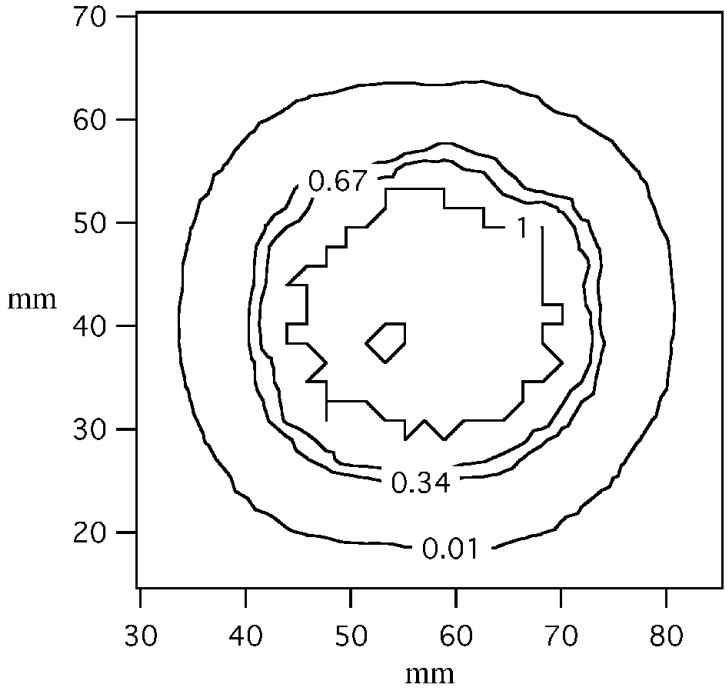

Figure 7.7. Fluorescein concentration contours at x/d = 5.0, velocity ratio = 0.5.

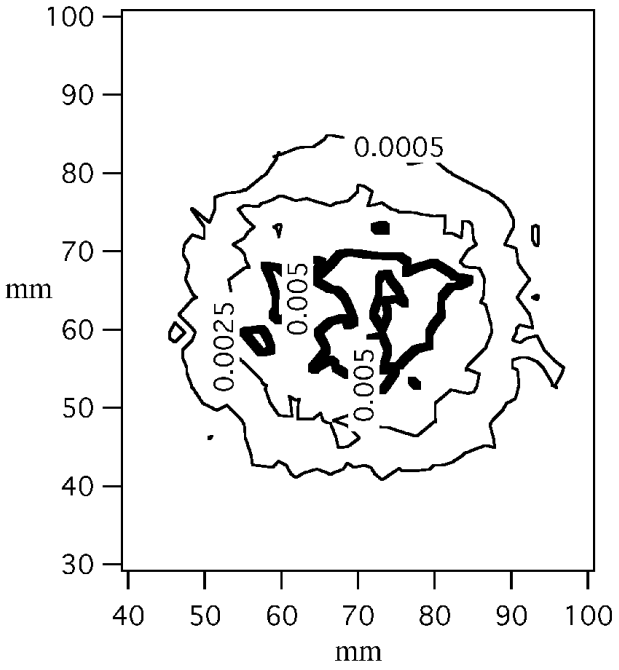

Figure 7.8. Particle concentration contours at x/d = 5.0, velocity ratio = 1.0.

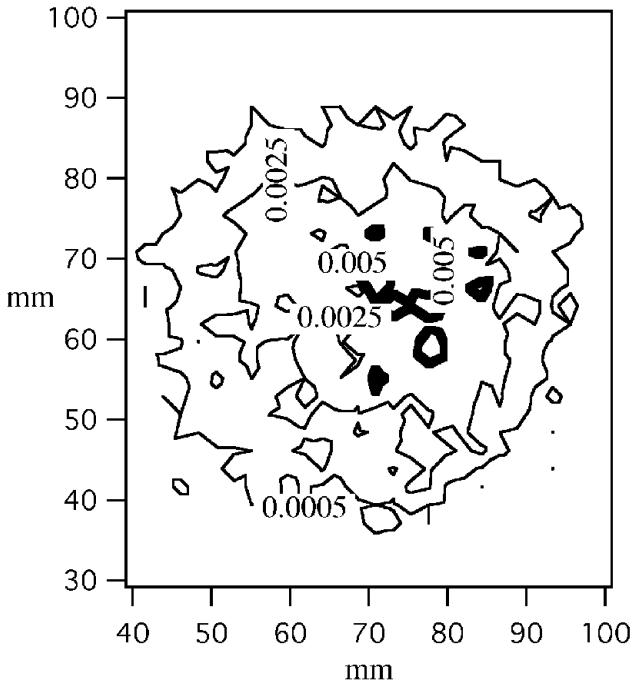

Figure 7.9. Particle concentration contours at x/d = 5.0, velocity ratio = 0.5.

Briefly, the results in Figures 7.6 and 7.7 indicate that the passive dye spreads significantly more in the case of $\lambda = 1.0$ than for $\lambda = 0.5$. This is attributed to two factors: 1) the counter-rotating vortical structure of the wake-like flow between the central and annular jets is more effective in transporting central jet fluid radially to the annular jet, and 2) the higher shear created at the outer edge of the annular jet (in the $\lambda = 1.0$ case) is more effective in transporting annular jet fluid radially. On the other hand, it is significant to note that the particle results in Figures 7.8 and 7.9 (and in general) exhibit trends that are opposite those of the dye. That is, the particle results indicate that the $\lambda = 0.5$ case is more effective at spreading the particle cloud radially. This phenomenon is attributable to particle inertia effects and has been alluded to previously by Lilly [1973] and Hinze [1975]. Physically, the apparent mechanism is the erosion of the annular core owing to a much more single-signed vorticity distribution (for the $\lambda = 0.5$ case) in the region between the central and annular jets. Conversely, the wake-like nature of this region for the $\lambda = 1.0$ case apparently either suppresses radial particle motion, or the presence of particles in this region changes the turbulence structure such that there is a reduced communication between the inner and outer shear layers. As mentioned previously, the overall spreading characteristics of the near-field of the annular jet are strongly connected to the development of the shear region between the annular and central jets in the so-called intermediate zone.

7.3.5 Spatial Velocity Correlation Measurements

A particular strength of the Molecular Tagging Velocimetry Technique is that, at a minimum it provides instantaneous velocity information along a line. Thus, unlike point measurements (e.g., LDA), MTV naturally provides data relevant to computing spatial

velocity correlations. These correlations are felt to be particularly useful in the present program since they provide direct information relating to the length scales over which the turbulent motions interact.

Figures 7.10 through 7.13 present spatial correlations (represented as a correlation coefficient) of the axial velocity fluctuations as a function of radial separation. For comparison, Figures 7.10 and 7.11 show the pure fluid case (x/d = 7.5, λ = 1.0) for reference locations near the center of the interior and outer shear layers (r/R = 0.72 and r/R = 1.44) respectively. (In these figures, R is the radius of the annular jet, and Δr is the radial distance from the reference location.) Figures 7.12 and 7.13 show the same correlations for the case of a particle laden central jet. Comparison of the pure fluid and particle laden flow correlations indicates the following. The pure fluid results (for either reference position) maintain much larger correlation coefficient values for large Δr/R than the particle-laden case. Furthermore, for the pure fluid case and r/R = 0.72 reference location there is an indication of strong communication between the inner and outer shear layer eddies, while in the particle-laden case no such correlation exists. These results clearly indicate that the effect of the particles is significant with regard to the scales over which the turbulent eddies interact. They also provide a clear explanation as to why the passive scalar (fluorescein dye) and particle clouds spread differently under nominally the same flow conditions.

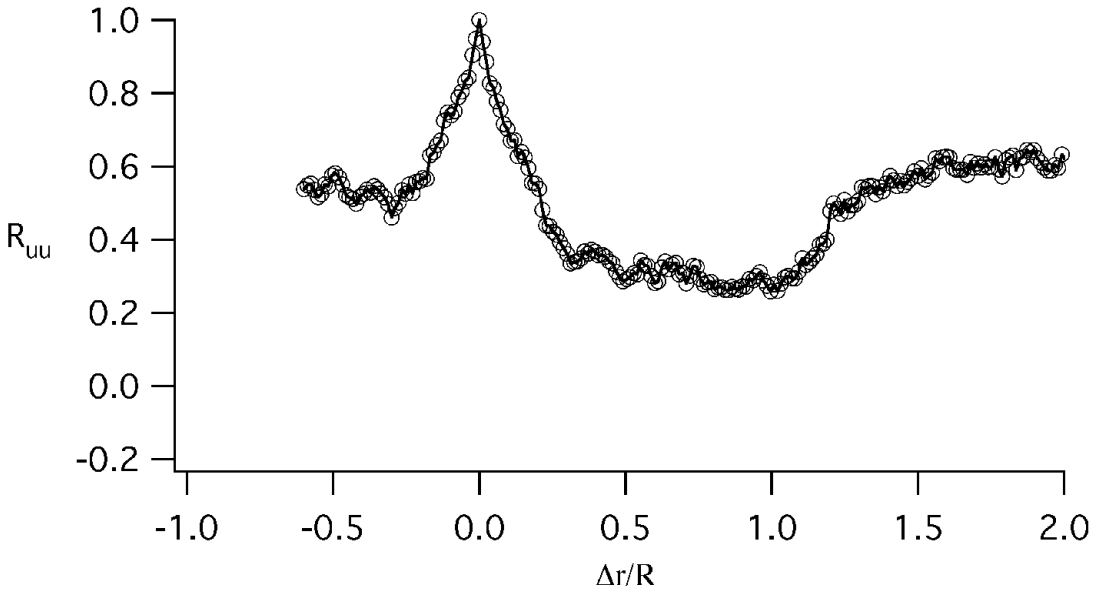

Figure 7.10. Two point spatial correlation of the axial velocity fluctuations at x/d = 7.5, velocity ratio of 1.0, and reference point at r/R = 0.72, pure fluid case.

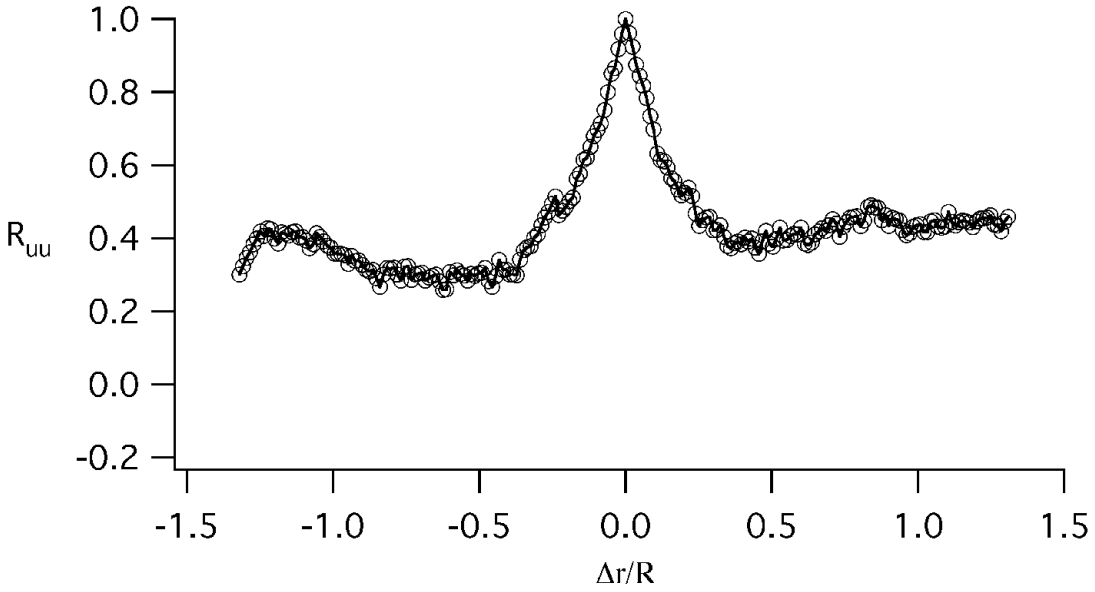

Figure 7.11. Two point spatial correlation of the axial velocity fluctuations at x/d = 7.5, velocity ratio of 1.0, and reference point at r/R = 1.44, pure fluid case.

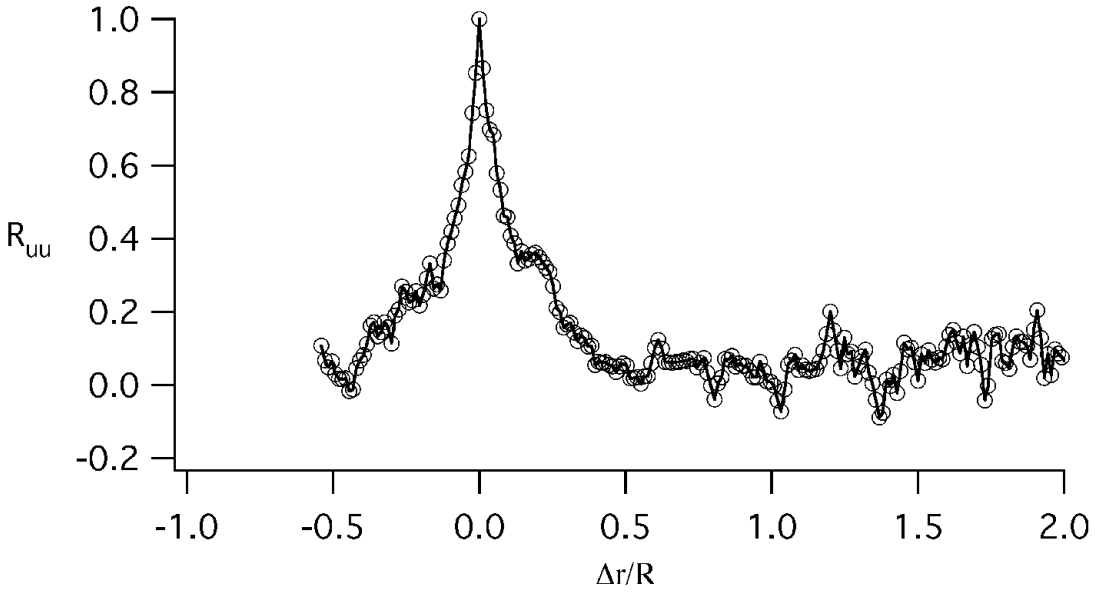

Figure 7.12. Two point spatial correlation of the axial velocity fluctuations at x/d = 7.5, velocity ratio of 1.0, and reference point at r/R = 0.72, 5% mass particle loading.

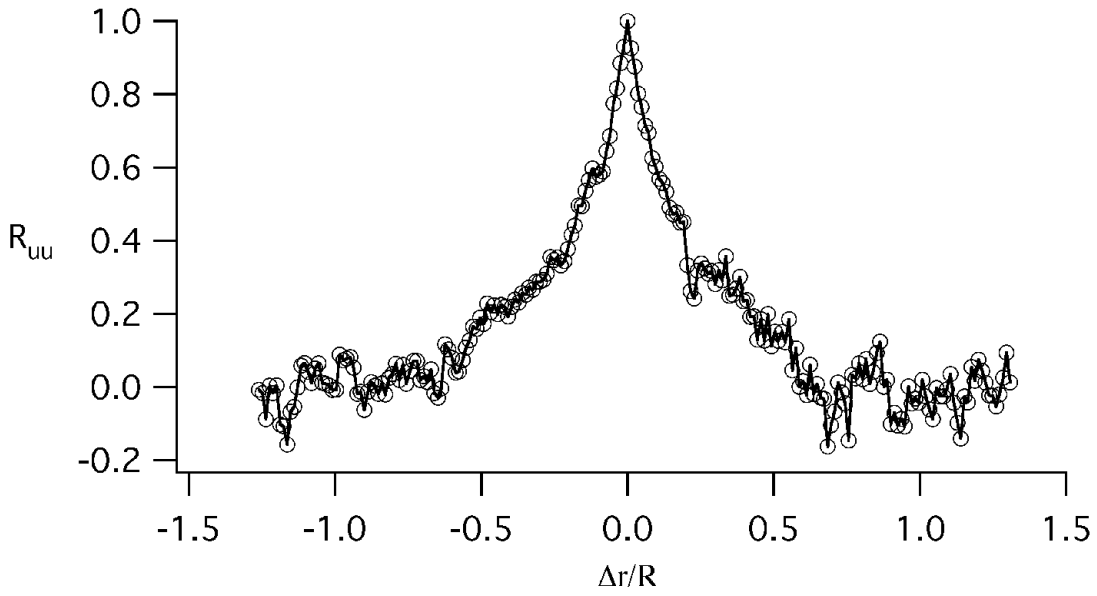

Figure 7.13. Two point spatial correlation of the axial velocity fluctuations at x/d = 7.5, velocity ratio of 1.0, and reference point at r/R = 1.44, 5% mass particle loading.

7.3.6 Summary and Recommendations from the Phase I Studies

Since they provide a context for the Phase II work, the main results from the Phase I portion of the project as stated in the final report for Phase I are reiterated here.

An experimental system was developed and tested at the University of Utah to study two-phase mixing for the model development and provide information on the performance of different coal injection devices. The conclusions from these studies may be divided into two categories:

1) The development and demonstration of significant new capabilities regarding the detailed study of particle dispersion, and

2) The application of the capabilities supporting the overall goals of developing improved low-NO_x burners.

Regarding item 1), the following are concluded:

- A coaxial annular jet facility has been designed and constructed. This facility allows detailed and controlled study of a variety of factors affecting two-phase

dispersion phenomena in a geometry, and over a range of parameters, having broad relevance to coal-fired furnace injectors.

- A variation of Molecular Tagging Velocimetry (MTV) has been developed and demonstrated in the present two-phase flow applications. This technique allows instantaneous velocity profile information to be measured to within about 8% uncertainty for mass particle loadings up to about 10%. A powerful outcome of this development is that the spatial structure of particle-laden flow may be studied without having to resort to "surrogate" measures such as the single point temporal autocorrelation.

- A simple yet effective method of determining particle concentration information that employs an image processing based particle counting technique has been developed and applied.

Regarding item 2), the following are felt to be the main results from the coaxial jet studies.

- Changes in the central-to-annular jet velocity ratio can have dramatic (and at what at first seemed to be contradictory) effects on the net momentum, passive scalar and particle transport produced by the coaxial annular jet.

- For the mass particle loading of 5% examined, the effects of particles on the annular jet (at any given axial location), and on its downstream development, produced only very subtle feature variations in the mean and root mean square (RMS) axial velocity statistics.

- Comparison of two point axial velocity correlation data for radial separations revealed that important underlying structural changes occurred in the turbulence. These changes occurred between both the $\lambda = 0.5$ and 1.0 cases, and perhaps more significantly, between the pure fluid and particle laden cases. In particular, by an axial location of $x/d = 7.5$ the correlations indicated that both the pure fluid and particle laden jets ($\lambda = 0.5$) contain a single dominant turbulent structure having a radial scale that nearly spans the entire jet half-width. In contrast, the pure fluid results for $\lambda = 1.0$ suggest the existence of two smaller scale but highly interacting structures. The addition of particles to slightly increase the turbulence length scales, but more significantly, for the $\lambda = 1.0$ case dramatically diminished communication (and presumably transport) between the inner and outer structures. The correlation results provided clear indications as to why the comparisons between the passive scalar and particle dispersion measurements produced apparently contradictory results.

- An initial study of the effects of a primary jet coal spreader geometry qualitatively validated *GLACIER* code simulations of a similar geometry.

7.4 PHASE II STUDIES

The results of Phase I were used to generate a course of action regarding the Phase II studies. Overall, the goals of Phase II were to:

1) Continue to map out the flow features and basic underlying mechanisms of particle dispersion in the coaxial jet, and

2) Add and explore modifications to the coaxial jet that contain features having specific and direct relevance to low-NO_x burners.

The results of Phase I also generally indicated that the effects of parameter variations (e.g., velocity ratio and particle size) and the effect of particles often produced only subtle (but potentially significant) variations in the velocity and particle concentration fields. This prompted a re-examination of both the experimental techniques and the precision to which the flow facility could attain specific parameter values (i.e., velocity ratios and particle mass flow rates). These re-examinations eventually lead to modifications to the MTV and particle density measurement techniques, as well as the development of a novel particle injection system. In addition, the results from Phase I also indicated that the downstream development and spreading rate of the coaxial jet is largely determined by the development of the shear layers between the central and annular jets. This prompted us to expand our literature survey from mainly particle-laden jets to the pure fluid jet literature in hopes of attaining a better understanding the basic physical mechanisms. The outcomes of all of these efforts are described below.

7.4.1 Brief Re-Examination of the Coaxial Jet Literature

A reasonably complete survey of both the pure fluid and particle-laden coaxial jet literature has been conducted [Sadr, 2000]. A specific purpose of this re-examination of the literature, in light of the results of our Phase I studies, was to better understand the flow dynamics in the shear zone between the central and annular jets. In what follows, the results from only a few of the most relevant and most recent studies are discussed.

Pure Fluid Coaxial Jets

The turbulent coaxial jet literature is extensive. Owing to its importance to industrial applications, however, this flow field continues to be a subject of intense study. Of particular relevance to coal injector applications are the factors that affect the spread of the jet, or conversely the erosion of the potential cores of the central and annular jets. A schematic of the coaxial jet configuration along with the relevant flow regions is given in Figure 7.14 [adapted from Ko and Kwan 1976]. An emerging result from recent studies of both pure fluid and particle-laden jets is the importance of the intermediate zone development.

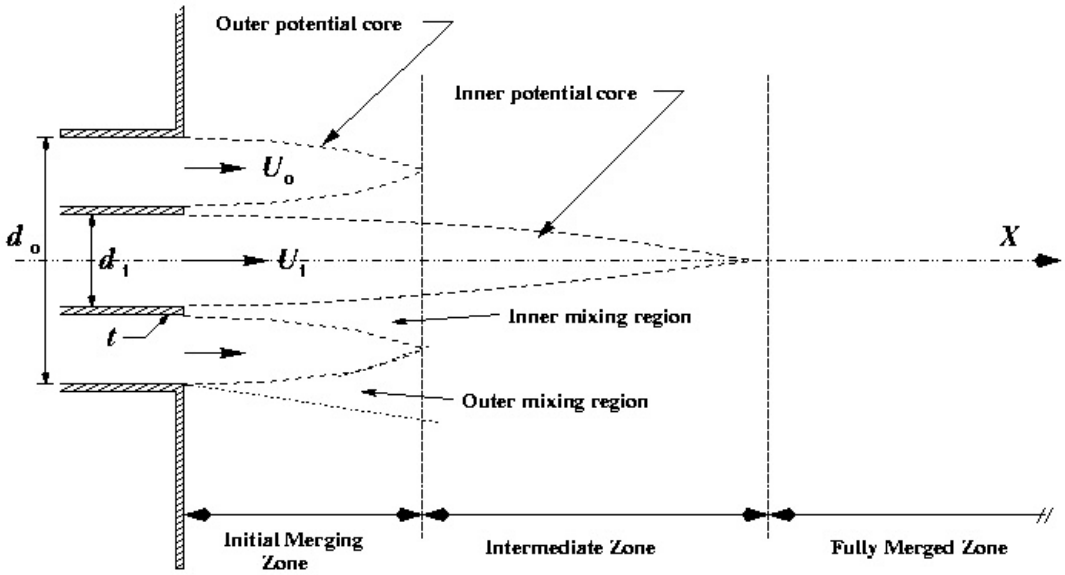

Figure 7.14. Coaxial jet flow features and parameters.

It is generally understood [e.g., Hinze 1975] that the spread of a turbulent jet is linear with x (the longitudinal coordinate) for short distances from the jet exit, and that the jet velocity decreases in inverse proportion to x. Very recently, however, Warda et al. [1999] indicate that the core length of even a single jet also depends on the turbulence intensity of the flow at the exit plane, as well as the exit profiles of the mean velocity. They showed that the uniformity of the mean velocity and low turbulence intensity serve to increase the core length. In the case of the coaxial jet, Warda et al. also confirmed earlier observations that the inner potential core length strongly depends on velocity ratio, while the outer potential core for a jet having velocity ratios less than unity seems to be insensitive to velocity ratio. Their results demonstrate that even for large differences between the inner and outer mean velocities, the wake region behind the wall of the inner nozzle still exists but with a reduced influence compared with the case of velocity ratio more than one. They also conclude that coaxial jets with a velocity ratio more than unity ($\lambda = 1.56$) develop faster than that with $\lambda < 1.0$.

The importance of the inner jet wall thickness and its subsequent effect on the intermediate zone development has recently received increasing attention. Dahm et al. [1992] performed comprehensive flow visualizations of the vortex patterns and dynamics of their interactions in the near field of a round coaxial jet. They state that between each pair of streams, there is a velocity jump resulting from the difference in stream velocities together with a velocity defect imparted by the viscous boundary layers on either side of each nozzle lip. It is useful to conceptually view the profile as being composed of a wake component and a shear layer component resulting, respectively, from the symmetric and asymmetric parts of the profile. Dahm et al. conclude that even over the limited range of parameters they considered, a wide

variety of dramatically differing near field vortex patterns can arise. These different patterns result in very different interaction dynamics that can depend both on the velocity ratio and on the absolute velocities of the two coaxial streams. The changes on potential core length also depend strongly on the differing near field vortex dynamics. These variations in core length are not simply, or even monotonically, dependent on the velocity ratio of the two jets, as has been suggested previously, but instead show a nonlinear dependence on the stream velocities. They mention that the vortex patterns and dynamics observed in their work are very different from the picture proposed by Ko and Kwan [1976] and Kwan and Ko [1977]. In particular they found no way to usefully reconcile their direct observations with the conclusion that the vortex structure of the coaxial jet near field can be considered simply as a combination of several single jets.

Buresti et al. [1994] examined the effect of a coaxial jet with an outer to inner diameter ratio of 0.485 and velocity ratio of $\lambda = 1.5$. Their results indicate that two sheets of alternating vortices are shed with a well defined frequency from the two sides of the inner duct wall, and that within an axial distance between one and two inner jet diameters these two sheets merge. This phenomenon was shown to exist over a range of velocity ratios with a constant Strouhal number, St= 0.24, based on the thickness of the wall and on the average velocity of the two streams. In the near exit region, their data suggest that the influence of the wake of the wall between the jets persists at least up to one inner jet diameter downstream. They also pointed out that the quantities defining the configuration, and thus potentially influencing the characteristics of the various flow regions of a coaxial jet are numerous; the inner and outer exit velocities, the inner and outer areas, the thickness of the inner nozzle wall, the momentum thickness of the boundary layers at the exit, as well as their state (laminar or turbulent), and the turbulence level of the exit jets.
Regarding the present application, the dependence of the intermediate zone development on the inner jet wall thickness (and/or exit lip geometry), appears to provide a promising avenue for coal injector design modifications. In connection with this, further investigations wer made with coaxial jets with velocity ratios of $\lambda = 1.5$ and 3.33 at two different central jet wall thicknesses, 5 mm and sharp. They confirmed the results of Tang and Ko [1994] that the highest turbulence intensity occurs in the intermediate merging zone. They mentioned this is probably due to the fact that the intermediate merging zone is always the one in which the largest momentum transfer between the two streams takes place. They also show the important role of the inner jet wall thickness on the occurrence and characteristics of the vortex shedding phenomena. If this thickness is decreased, the wake-like behavior in the near field is progressively reduced and shear-layer instabilities may become dominant, even at low velocity ratios. This thickness seems to produce a moderately quicker mixing of the streams only at lower velocity ratio, at which regular vortex shedding is present. The distribution of skewness also reveals the larger and stronger effect of the wake of the inner jet wall at a velocity ratio of 1.5.

Overall, the results of the pure fluid coaxial jet literature indicate that promising avenues for predictable injector design improvements are likely by modifying the intermediate zone development through changes in the central jet wall and/or exit lip characteristics.

Particle Laden Coaxial Jets

In a set of particularly relevant studies, Fan et al. [1992, 1996] examined the effect of velocity ratio, particle mass loading ratio, and particle diameter on the flow structure in the fully merged zone of axisymmetric turbulent coaxial jets. The central air jet was laden with silica particles having a specific gravity of 1.25, diameters ranging from 50 to 200 microns, and mass flow rates of γ_m = 0.5, 1, and 1.5. Data were taken at four velocity ratios of λ = 1.5, 2, 2.5, and 3. The most important findings of their study are:

- The fully merged zone for a two-phase turbulent coaxial jet exhibits similarity for mean velocity and particle concentration.
- The development of both mean and turbulent velocities is strongly correlated with the particle loading ratio, particle diameter, and velocity ratio.
- The centerline velocity of the two-phase coaxial jet decays more slowly than that of a single-phase coaxial jet. Other parameters being the same, an increase in particle loading ratio reduces the rate of decay of the fluid centerline velocity. This can be a result of augmentation of the momentum sources of the carrier fluid as a result of an increase in the inter-phase surface area.
- The spreading rate of the two-phase coaxial jet is smaller than that of the single-phase coaxial jet. The spreading rate of the two-phase coaxial jet decreases when the particle-loading ratio increases. This is because the particles weaken the turbulent fluctuations of the jet. The spreading rate of the two-phase coaxial jet decreases when the velocity ratio decreases at the same particle-loading ratio.
- While the profiles of turbulent intensity for the single-phase and two-phase are similar, there is a consistent reduction in the turbulence intensities for the two-phase flow case. The turbulent intensity levels are slightly lower for the jet having a higher loading ratio. For the cases of fix particle-loading ratio, the turbulence intensity appears to increase with an increase in the velocity ratio.
- The gas phase disperses much more rapidly than the particles. This indicates that the particles do not move with the gas but lag significantly, owing to particle inertia. Smaller particles disperse more rapidly than larger ones.
- With increasing velocity ratio, the gas dispersion is also increased. An increase in the annular velocity, when the central jet velocity remains constant, causes an increase in the gas dispersion and a slight increase in the particle dispersion.
- An increase in particle loading causes a slight decrease in the gas and particle dispersion. The reason is that the turbulent intensity of the gas is reduced as the particle mass loading increases.
- The larger particles disperse slower than the smaller particles, since dispersion is caused by drag forces of the gas on particles that vary strongly with particle size.

Wicker and Eaton [1994] further studied the dynamics of the particle-laden coaxial jet (with and without swirl) with a particular emphasis on obtaining a better understanding of the

instantaneous mechanisms leading to the time averaged dispersion characteristics. Their observations indicated that the coherent motions characteristic of the shear layers between the central and annular jets, as well as between the annular jet and the ambient fluid, have a dominant influence on the particle dispersion. Consistent with the above review of pure fluid coaxial jets, they also found that dramatic changes in the dispersion may be achieved by modifying the central jet lip (in their case by adding swirl generators). Such modifications ultimately change the net particle dispersion by altering the coherent motion dynamics in the inner and outer shear layers. This is consistent with our Phase I correlation results indicating that altering the characteristic scales of the inner shear layer structures (even though gross measures of the turbulence undergo only subtle changes) can have significant influences on the net particle dispersion.

Summary

The important conclusions most relevant to the present objectives study may be summarized as follows:

- For single-phase coaxial jets, velocity ratio, geometry and flow condition at the nozzle exit are the most important parameters affecting coaxial jet flows.
- The intermediate zone is the most important region within the near-field of a coaxial jet flow since most of the mixing between the central and annular flow happens in this region.
- Regarding two-phase flows, the most important parameters are the Stokes number, particle diameter to turbulent length scale, and the density of particles in the flow.
- Two-phase flows decay at a slower rate compared with single-phase case and the presence of particles reduces dispersion.
- The presence of particles modulates the level of turbulent fluctuations depending on Stokes number and particle diameter to turbulent length scale.

7.4.2 Experimental Facility and Experiment Parameters

As mentioned previously, the subtle yet significant results of Phase I prompted efforts to more precisely control of the experimental facility, and more accurately measure the velocity fluctuations (both the axial and transverse components). The efforts regarding the former are described immediately below, while the latter are described in Section 7.5.

Experimental Facility

The experimental facility originally developed by Sefcik [1997] has been modified. Figure 7.1 shows a schematic of the experiment facility with its major system components.

The test section measures 0.5 meters in height and width and 0.6 meters in length. The coaxial jet orifice, located in the center of the upstream wall of the test section, issues fluid horizontally into the test section. The test section is configured such that the flow experiences a sudden expansion immediately downstream of the jet exit. The top and one

sidewall of the test section are made of 9.5 mm thick quartz plate to allow passage of an ultraviolet laser beams used in MTV method.

The central (primary) and annular (secondary) jets are d_i = 30 mm and d_o = 75 mm in diameter, respectively. The wall thickness of the central jet nozzle, t, is 1.5 mm. The central and the annular jets are driven by 1.12 kW centrifugal pumps. These pumps are operated through separate motor controllers to obtain the variable pump speeds needed to control the jet velocities. Both jets were calibrated to obtain the jet velocity as a function of pump speed. Figure 7.15 shows the calibration results for jet speeds as a function of pump speed. Since the system is closed with part of the piping in common, a change of velocity in one jet can affect the other jet. (This effect was noted in the Phase I final report.) Experiments were performed to document this effect. Figure 7.16 shows the typical variation of velocity in the central jet with a change of annular jet velocity. According to this figure the central jet velocity may vary up to 20% as the annular jet speed changes.

Particle selection was made based on the required physical properties (corrosion resistance, size, density, optical properties), availability, and cost. The particles used in this study are clear glass beads (MS-XH manufactured by Cataphote Inc.), and have a specific gravity of 2.46. The beads are spherical, made from high quality optical crown glass with no more than 15% irregularly shaped particles. For each set of particles used in the experiments, a particle size distribution was obtained according to ASTM standard test sieves. Figure 7.17 shows the size distribution for the particles used in this study.

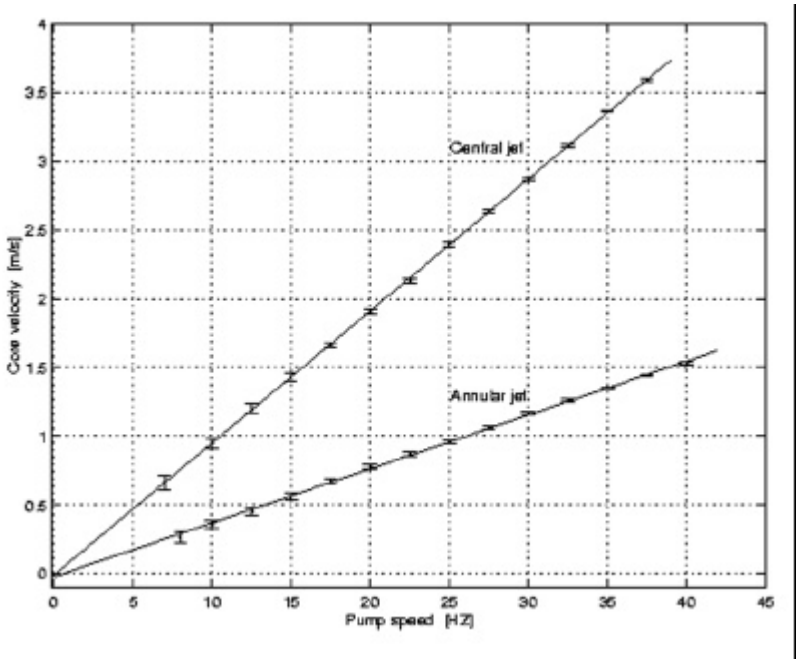

Figure 7.15. Calibration of the central and annular jets as a function of pump speed.

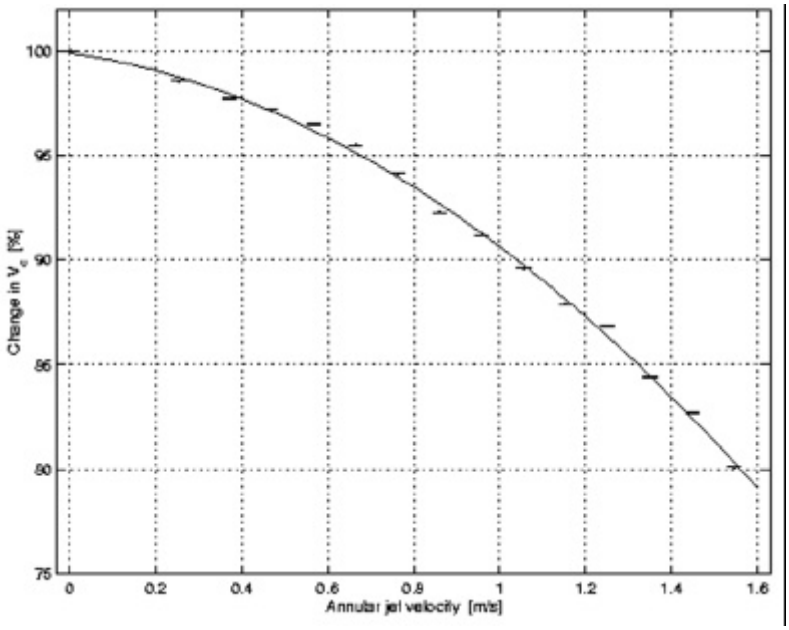

Figure 7.16. Effect of the annular jet flow on the central jet.

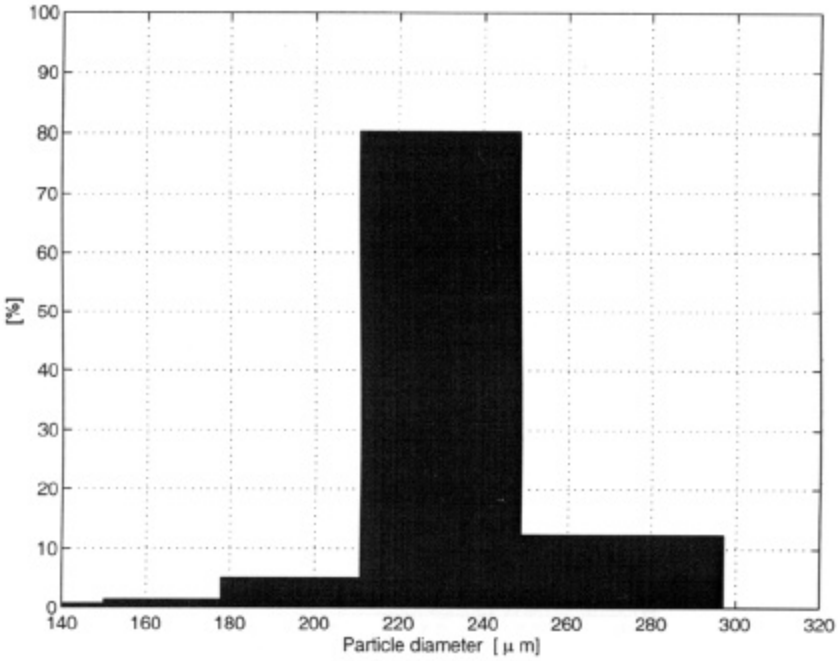

Figure 7.17. Particle size distribution.

A particle injection system is used to introduce particles into the central flow line approximately 40 pipe diameters upstream of the jet orifice. Different methods for feeding the particles into the flow were considered and tried. A new method has been devised to inject a small quantity of particles into the flow at a steady rate. Unlike our previous

particle injection system, this method enables a wide range of mass loading ratios with different particle sizes. A brief description of the system is as follows: A small vessel is filled with particles. The bottom of the vessel is connected to the central flow stream via an orifice with small diameter. The particles pass through the orifice and enter the flow stream. For a given fluid and particle properties, the mass flow rate of the particles is a function of the orifice diameter and the pressure difference across the orifice. In order to control the pressure difference, a small bypass line is connected to the vessel from upstream. A regulating ball valve is located between this point and the orifice. This valve regulates the pressure difference, which in turn regulates the particle mass flow rate. Figures 7.18 a and b show a sample calibration plot for the particle feed system.

The error-bars in Figures 7.18 are the measurement uncertainty and do not account for the particle size distribution. The error-bars are only shown for part of the data points to avoid congestion. The uncertainties associated with the rest of data points are similar. In Figure 7.18b both the pressure difference and mass flow rate are normalized using their maximum values for each experiment. It is observed that, using this method of normalization, the system shows a self-similar characteristic, i.e., all the curves in Figure 7.18a lie on a single line in Figure 7.18b.

Figure 7.18 show that the amount of particles injected into the system is a function of the applied pressure difference. This pressure difference is created through the use of a ball valve in the central jet flow. Since the system is using centrifugal pumps to drive the jets, the central jet velocity is not independent of the pressure drop caused by the ball valve. This effect is illustrated in Figure 7.19. As expected, the fluid flow rate is a function of both the pump speed and the pressure drop. Similar to Figures 7.18, the change in fluid flow rate can be normalized to obtain one single function for all pump speeds, Figure 7.19b. In this figure, V_{max} is the maximum velocity obtained for the ball valve fully opened, and P_{max} is the maximum pressure drop (for the ball valve closed).

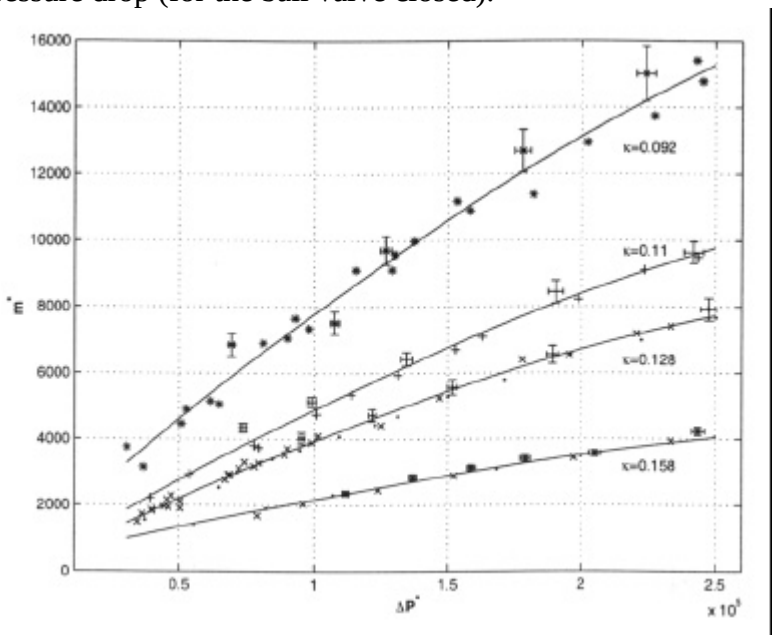

Figure 7.18a. Calibration curve for the particle injection system.

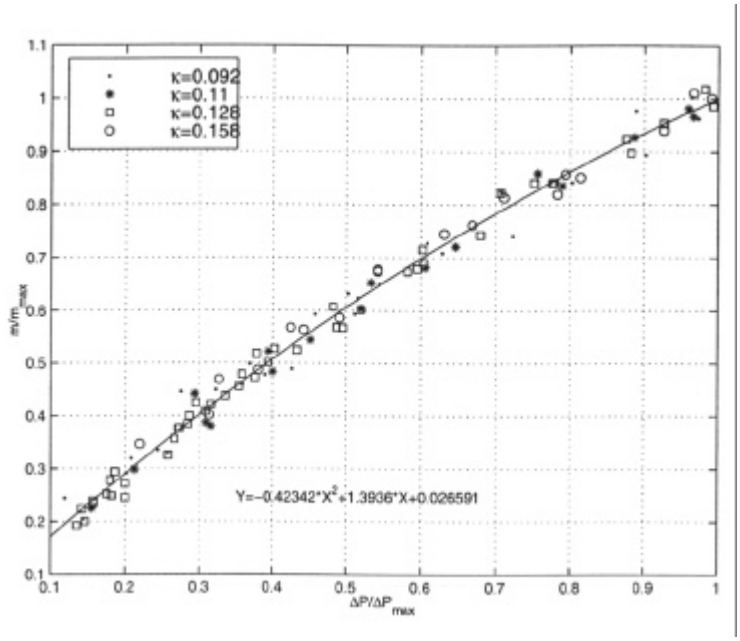

Figure 7.18b. Universal calibration curve for the particle injection system.

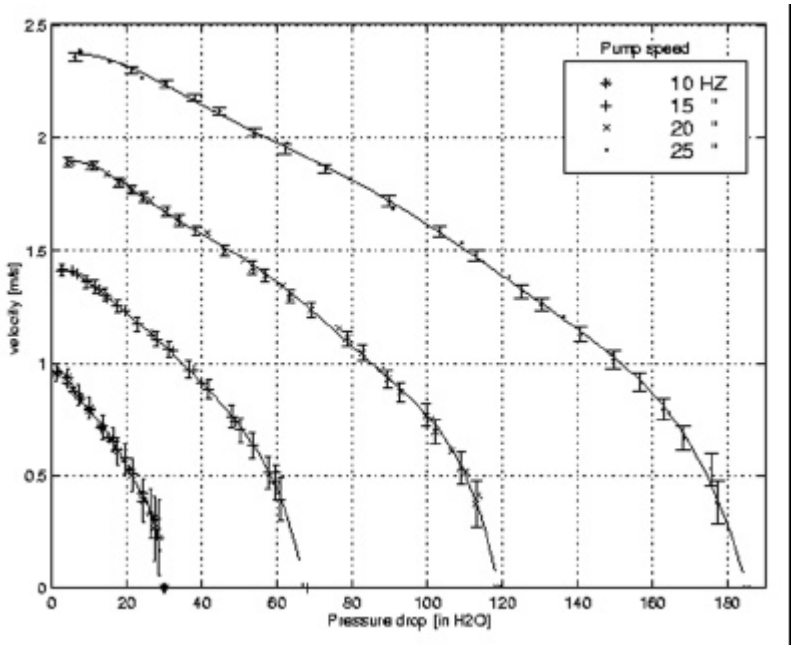

Figure 7.19a. Effect of pressure drop on the central jet velocity at different pump speeds.

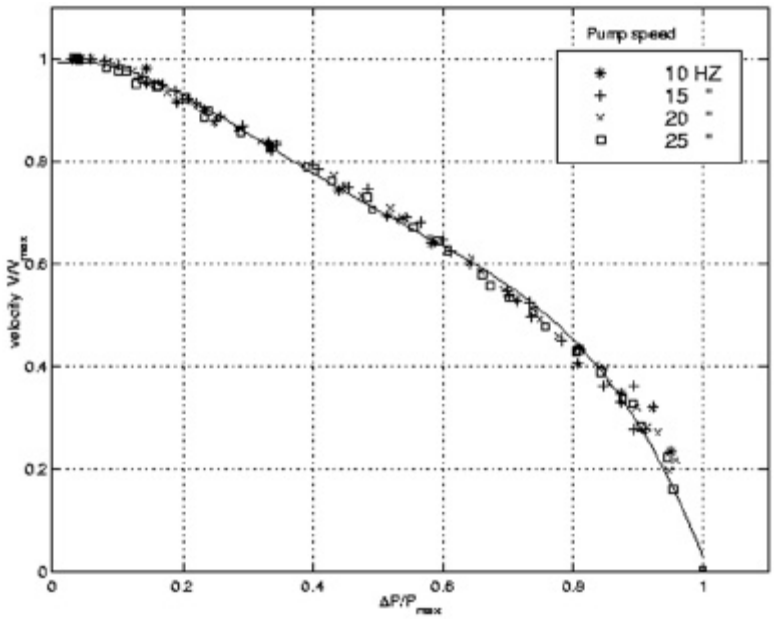

Figure 7.19b. Universal normalization of pressure drop effects on the central jet velocity.

Since the experimental facility circulates, a particle filtration system is required. The particle filtration component, consisting of a 0.568 m^3 stainless steel tank containing several baffle elements and 75 micron stainless steel mesh filters, is located in the return flow line down stream of the test section. The particle filtration component can be isolated from the test section via two large union ball valves. The major benefit of this is that the tank can be isolated for cleaning without draining of the entire facility. The fluid volume capacity of the whole system is about 1.03 m^3.

Experimental parameters

Throughout the course of any experiment, the central jet velocity is kept constant. The corresponding Reynolds number, based on central jet diameter and velocity, is Re=43,500. Other major parameters in particle-laden coaxial jets are jet velocity ratio, particle flow ratio, and Stokes number.

Velocity Ratio

As mentioned above, the velocity ratio, U_0/U_i, in coaxial jets strongly influences the characteristics of the flow field. Based on the above calibrations for the annular and central flow jets, 4 velocity ratios, 1, 0.75, 0.5, and 0.25, were chosen for present study. For any given experiment, the exact value for the velocity ratios will be obtained after obtaining velocity profiles for both the annular and central jets using the MTV method.

Particle Flow Ratio

Particle mass flow ratio for a particle-laden jet denoted γ_m and is the ratio of the particle and fluid mass flow rates. A typical mass flow ratio for a low NO_x emission pulverized coal utility boiler is about 12%. Considering a specific density of 1.2 for coal and air at standard conditions this yields a volume flow rate of γ_v =0.012 %. In the present study the particle-laden flow consists of glass particles (Sg=2.5) in water. In this case a volume flow rate of 0.012 % equals a mass flow rate of 0.03%. The effect of solid particles on the fluid flow is believed to primarily be due to particle interaction with the turbulent motions in the flow. This seems to be most affected by the volume of the solid phase in the flow. As discussed in Sadr [2000], the inter-phase surface area, which is more closely dictated by volume flow rate, is an important parameter in two-phase flow studies [e.g., Fan et al. 1992]. Given this, it was decided to consider volume flow rate as the main particle density parameter in this study. Three volume flow rates of about 0.02%, 0.04%, and 0.07% are chosen for the present work. As with the velocity ratios, the exact value for the volume ratios will be obtained after obtaining velocity profiles of the central jet using the MTV method and measuring the amount of discharged particles for each test.

Stokes Number

As discussed previously, the Stokes number is defined as the ratio of the particle time scale to an appropriate fluid time scale. Thus, in a turbulent flow the Stokes number is a local and statistically based parameter. For the given particles and carrier fluid the particle time scale estimate is 0.008 seconds. To analyze the behavior of a particle-laden jet in terms of Stokes number, appropriate scales for length and velocity of the fluid phase must be estimated, i.e., $t_f = \delta/U$. Longmire and Eaton [1992] argued that, in a single jet, either a vortex propagation velocity or the tangential velocity at the outer edge of a vortex could be chosen for the velocity scale. The vortex propagation velocity in the jet near field is assumed to be half of the nozzle exit velocity. For the present study, a coaxial jet, the appropriate velocity scale is approximated by the average of the central and annular jet velocities. The upper limit for the length scale of the energy containing eddies can be considered to be the thickness of the mixing region. For the coaxial jet this may be approximated by the diameter of the inner jet. The resulting Stokes numbers calculated for each test case range from 0.47 to 0.8, and thus are all 0(1).

7.4.3 Measurement Techniques

A significant effort has been dedicated to the further development of the velocity and particle density measurement techniques. In the case of the velocity measurements, three important factors motivated this extra effort. The first is that the results from Phase I indicated that often times only subtle changes in the velocity field structure resulted in significant changes in the particle field. The second is that we wished to accurately measure velocity gradients and spatial correlations of these gradients. The third is that we wished to measure both the axial and radial velocities simultaneously and subsequently compute spatial correlations. Given these considerations, an effort to reduce the uncertainty of the MTV technique was deemed necessary. In the case of the particle measurements, we wished

to have a more robust technique that could handle the situations in which a single particle occupies multiple pixels, and could distinguish between closely spaced particles. As it turned out, this more robust technique followed directly from the efforts to improve the MTV technique in particle-laden flow.

Fluid Velocity Measurements

Fluid velocity measurements are performed using Molecular Tagging Velocimetry (MTV). This non-intrusive technique has been successfully applied by a number of researchers in recent years to obtain accurate instantaneous fluid velocities, in both liquid and gases, e.g. Hill and Klewicki [1995], Gendrich and Koochesfahani [1996] and Thurlow [1998].

The MTV technique relies on simple principles. First, the flow field is non-intrusively tagged. Then after a short time delay, relative to the flow physics, the displacement of the tagged region is measured. Using the Lagrangian formula, e.g., $u = \Delta x/\Delta t$, the instantaneous velocity vector of the tagged region is determined. The two aspects of this method are thus the tagging process and the algorithm used to find the displacement of the tagged region.

To tag the flow, a small amount of a phosphorescent chemical is mixed into the fluid. The present experiments use 1-BR-NP*Gβ-CD*ROH Ternary Complex developed by Ponce et. al. [1993]. This chemical has two important properties: 1) it emits visible light when excited by an ultraviolet (UV) light source, and 2) it remains in its excited state for about 12 ms after the UV light source is removed. To excite the chemical, the flow is exposed to ultra-violet (λ = 308nm) laser light. This light is typically configured into a series of lines or a grid. The part of fluid exposed to the laser is excited and the phosphor illuminates for some time. A CCD camera images this tagged region, e.g., lines or grid. After some short time delay another image of the tagged area is acquired. A data reduction program is then used to process the two sets of the images and find the displacement vector for the tagged region.

In many MTV applications a single camera can be used to take undeformed and deformed images. In this case the undeformed set of images are taken immediately after the laser is fired (usually within a microsecond). The data obtained from these images are then averaged to obtain a highly accurate statistically based estimate of the undeformed pattern. Then the camera is set to acquire images some time delay, Δt, after the laser has fired. Each of these images is then compared with the undeformed data to obtain instantaneous displacements. This method relies on the assumption that there is no difference in the undeformed images at different times. In this case then, the deformed image can be compared with a single undeformed pattern. In some cases, however, this assumption may not be sufficiently accurate. In particular, the presence of solid particles in the flow may result in the situation where at one instant a particle blocks the laser beam at some location. For single component measurements, this issue is not too critical since one obtains data at every pixel along a material line. For multiple component measurements, however, such data dropouts are unacceptable.

To implement the MTV method in this case there is a need to obtain the unique undeformed image corresponding to each deformed image. This requires the use of a two-camera system, one for undeformed and one for deformed image. Since the two cameras do not have

identical fields of view, a protocol is required to map the image from each camera into the same coordinate system. In the present work this is done via an affine warping method as described by Sadr [2000].

1-D and 2-D Data Reduction Algorithms

The basic goal of the data reduction program is to accurately determine the displacement vector by comparing the deformed and undeformed images. Presently two approaches are used to find the displacement vector. One method for finding the displacement of MTV lines relies on finding the best fit to the laser line intensity near its peak. This can be done, for example, by Gaussian or second order polynomial curve fits, see Hill and Klewicki [1995]. A second approach is based on a spatial correlation technique, Gendrich and Koochesfahani [1996]. This technique has similarities to the methods by which particle image velocimetry (PIV) data are reduced.

After reviewing the different methods of data reduction it was decided that the estimation of the location of the brightest point in each tagged region would be used to find the displacement vector. In the one-dimensional case the goal is to find the brightest location across the line, whereas in the two dimensional case the goal is to find the brightest point in the intersection region of two photochemical lines. To find the brightest point, and to avoid the drawbacks associated to the first method, a spline fit is used instead of a single function for the whole tagged region. After a spline function is fitted to the data, a minimization algorithm is used to find the coordinate of the brightest point. Since this method is applied for the first time here, it is felt necessary to briefly explain the basic method in more detail. A more complete discussion is given by Sadr [2000].

Figures 7.20 and 7.21 illustrate examples of 1-D and 2-D MTV image data respectively. The first step in the one-dimensional program is to fit a smooth cubic spline to the image along one direction. In the two dimensional case, the first step is to fit a two-dimensional smooth rational function to the tagged region of the image. In either case, the subsequent step is to find the brightest point using a conjugate gradient minimization procedure [see Polak 1971]. The minima found by the programs are local, and thus, have to be filtered appropriately. This is especially important due to the presence of particles in the flow, and their possible interference with the tagged region. The final results of the program are saved as files containing the locations of the maximum light intensity in the image coordinate system. Figure 7.21 includes these points on the images shown.

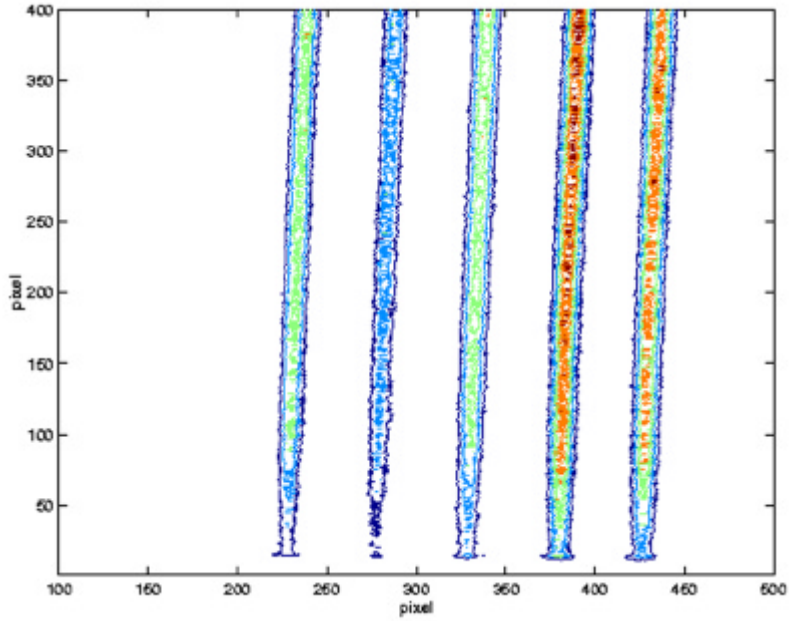

Figure 7.20a. Undeformed MTV lines.

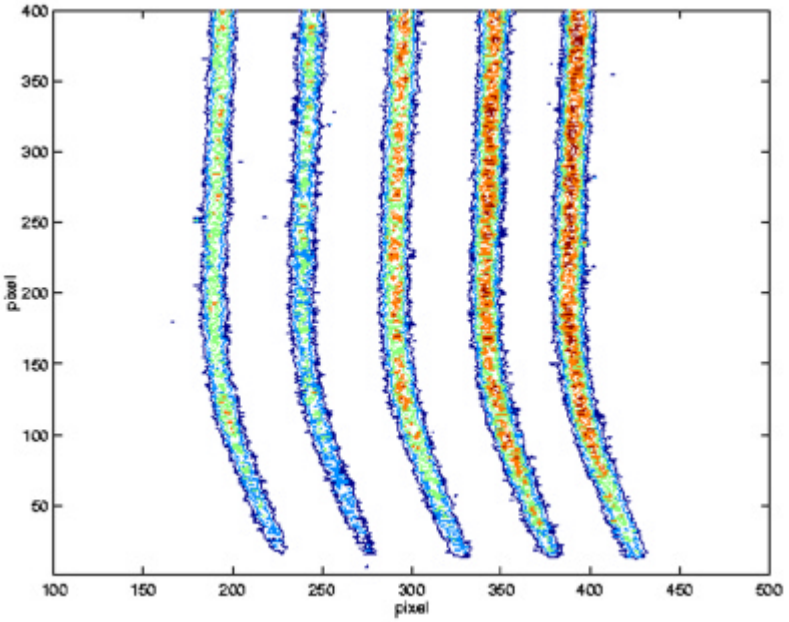

Figure 7.20b. Deformed MTV lines.

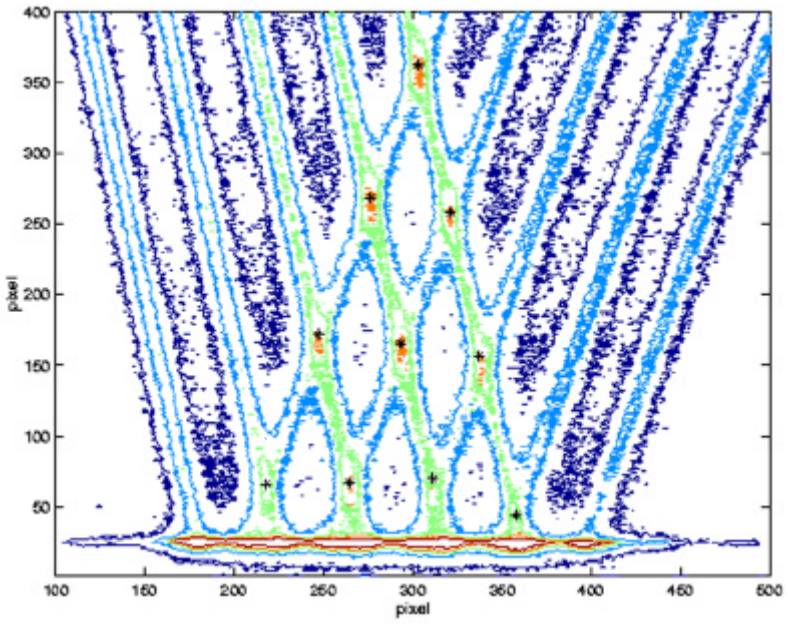

Figure 7.21a. Undeformed MTV grid.

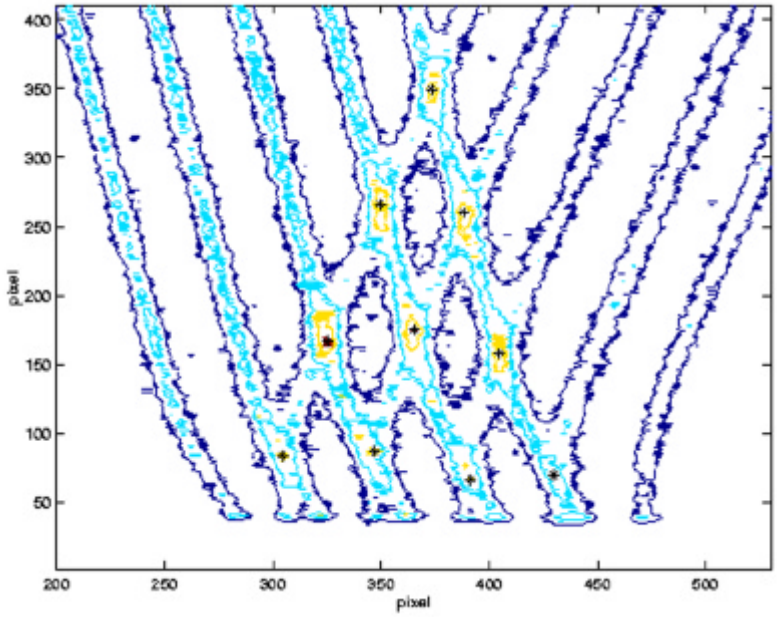

Figure 7.21b. Deformed MTV grid, depicting intersection centers.

Particle Concentration Measurements

Particle number density measurements are acquired by directing a sheet of visible laser light into the test section, and recording the light reflections from the particles on digital images. These images are then processed using a data reduction program that locates the particles, and subsequently maps them on the physical coordinate system attached to the facility. Figure 7.22 shows a sample image file. This figure also identifies the estimated location of the particles. If one pixel of the image file were occupied by the reflection of one particle then a simple algorithm could be applied to locate the particles in each image. In reality, however, several complicating factors must be considered in the image-processing algorithm. Some of these are:

- Particle reflections almost always occupy more than one pixel. The size of the reflected light region varies from one image to another, and is not constant in the same image.
- The magnitude of the reflected light is not constant. This magnitude also varies from one image to another, and is not constant in the same image.
- Particles that are in close proximity to each other can create an effect similar to that of a single particle.
- Distortion and blockage of the reflected light by other particles.

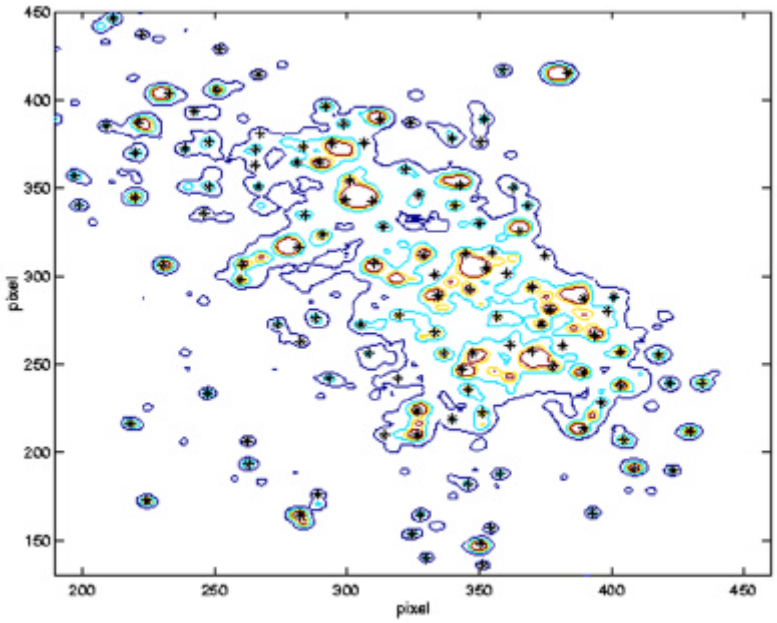

Figure 7.22. Example instantaneous particle distribution, with estimated location of the particles.

A computer code adapted from the MTV data reduction method has been developed to locate the particle centers. The algorithm involves first applying the smoothing routine to reduce the noise in the image. Next, a rational spline function is fitted to the image. Then the minimization algorithm is used to find the location of each particle. Finally a filtering subroutine is used to identify the true locations of the particles. This computer code has been tested extensively, and an example result is shown in Figure 7.22. The particle dispersion data are presented in the next section as a number density function. This is defined as the number of particles per unit volume for each point in the plane, normalized by the average density of particles in the view. In this way, a contour level of 1.0 reflects the average particle density of the entire image.

7.4.4 Particle Concentration Results

A comprehensive set of particle dispersion experiments have been performed. These measurements were acquired at six axial locations (x/d = 1, 2, 3, 4, 5, 6) from the jet exit, at four velocity ratios (l = 1.0, 0.75, 0.5, 0.25), and three volume flow ratios (γ_v = 0.024, 0.046, 0.075). Only a subset of these measurements are presented below. A complete reporting of these results will be presented in the forth-coming dissertation by Sadr [2001]. Regarding the choice of volume flow ratios, some comment is appropriate. The mass flow rate for a typical coal burner is about 12%. Considering a specific weight of 1.25 for coal and air at standard conditions this yields a volume flow rate of about 0.012%. Since in the present facility the fluid phase is water and the solid phase is glass beads, it is not possible to simultaneously match the same mass and volumetric flow rates. Several factors were considered in choosing the appropriate solid phase flow rate for this work. For glass beads in water, a mass flow rate of 12% will lead to a volume flow rate of 4.8%. Aside from the fact that this magnitude of particle injection is not accurately attainable in the present facility, owing to the volume occupied by the particles, it also results in a strong interaction between particles – an effect clearly not present in actual coal-fired furnaces. As previously mentioned, the effect of the solid phase on the turbulence is largely determined by the Stokes number and the inter-phase surface area in the flow field. Based on this, the present volume flow ratios are felt to reflect an appropriate fluid/particle interaction regime.

In these experiments the velocity of the central jet is kept constant. The corresponding central jet Reynolds number is Re = 43,500, based on the centerline velocity and central jet diameter. Changes in velocity ratio are attained by increasing or decreasing the flow rate of the annular jet. A velocity ratio of one equates to a Reynolds number of Re=108,000, based on the annular jet average velocity and annular jet diameter. Particle dispersion data are presented in the form of contour plots of normalized particle number densities. This is defined as the ratio of the local number density of the particles to the average particle number density. Therefore, a value of 1.0 corresponds to the average particle number density of the whole image.

Figures 7.23 and 7.24 present contour plots showing particle dispersion in a plane normal to the jet axis at a distance of x/d = 2.0 from the jet exit for two different volume flow ratios. These figures show that at a given velocity ratio, an increase in volume flow rate results in a more uniform particle distribution. Also, as the velocity ratio decreases, the extent of the particle cloud increases in the radial direction. This obviously indicates a larger particle diffusion, and is consistent our Phase I results and with the aforementioned dynamics within

the inner shear region. That is, as the velocity ratio decreases, the flow in this shear region loses its wake-type character (an effect resulting from the inner wall of the jet for $\lambda = 1$), and becomes more like a mixing layer type of flow. As previously discussed, this can lead to a change in the turbulent characteristics in the intermediate mixing region and consequently greater particle mixing in the inner region.

Figures 7.25 and 7.26 at x/d = 4 show that the particles are dispersed more uniformly and cover a larger area compared to the results at x/d = 2. The centroid of the contour plot is shifted more toward negative y/d as a result of gravity. Also the shape of contour at a velocity ratio of 0.25 is not circular. This may be due to the possible differences in the velocity profiles at the jet exit. It is believed, however, that these differences will not affect this study since the main objective of the research is to study the net effect of solid particles on the flow field.

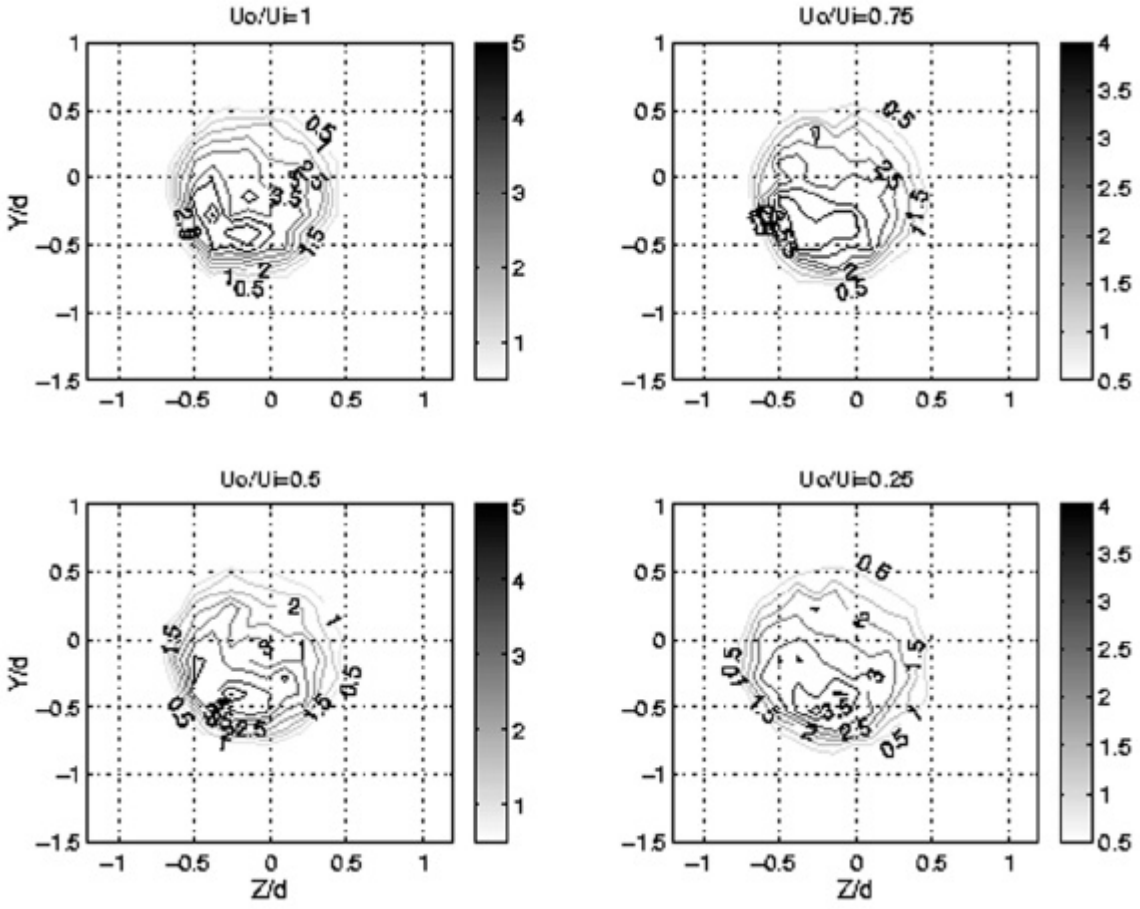

Figure 7.23. Particle dispersion results at x/d = 2, and volume flow rate of 0.024%.

Figures 7.27 and 7.28 show the spread of particles continues at larger x. The centroid of the contour plot has also shifted more toward negative y/d compared to the x/d = 2 and 4 results.

Furthermore, the confinement effect at velocity ratio = 1.0 on particle dispersion is observed more clearly at these downstream locations.

7.4.5 Summary

From the data presented, the effects of the flow field on particle dispersion are made evident by the changes in the particle density distribution at different velocity ratios. The effect of presence of the particles on the flow field is also implied by change of normalized particle number density as the particle flow rate is varied. The ultimate objective of this research is to explore the fluid dynamics that underlie the mechanisms responsible for these effects. At the time of the writing of this final report, MTV measurements of the associated velocity and velocity gradient fields are being acquired. A comprehensive reporting of these results will be made in the dissertation of Sadr.

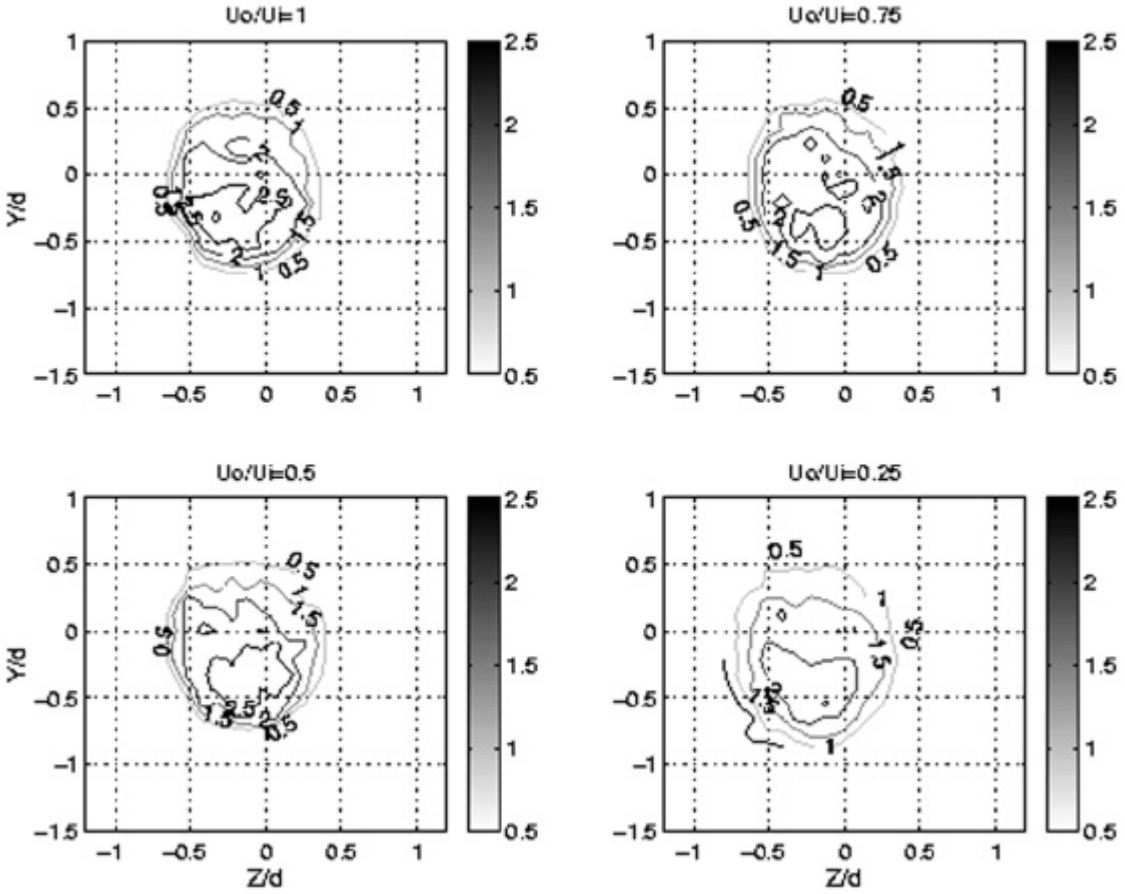

Figure 7.24. Particle dispersion results at x/d = 2, and volume flow rate of 0.075%.

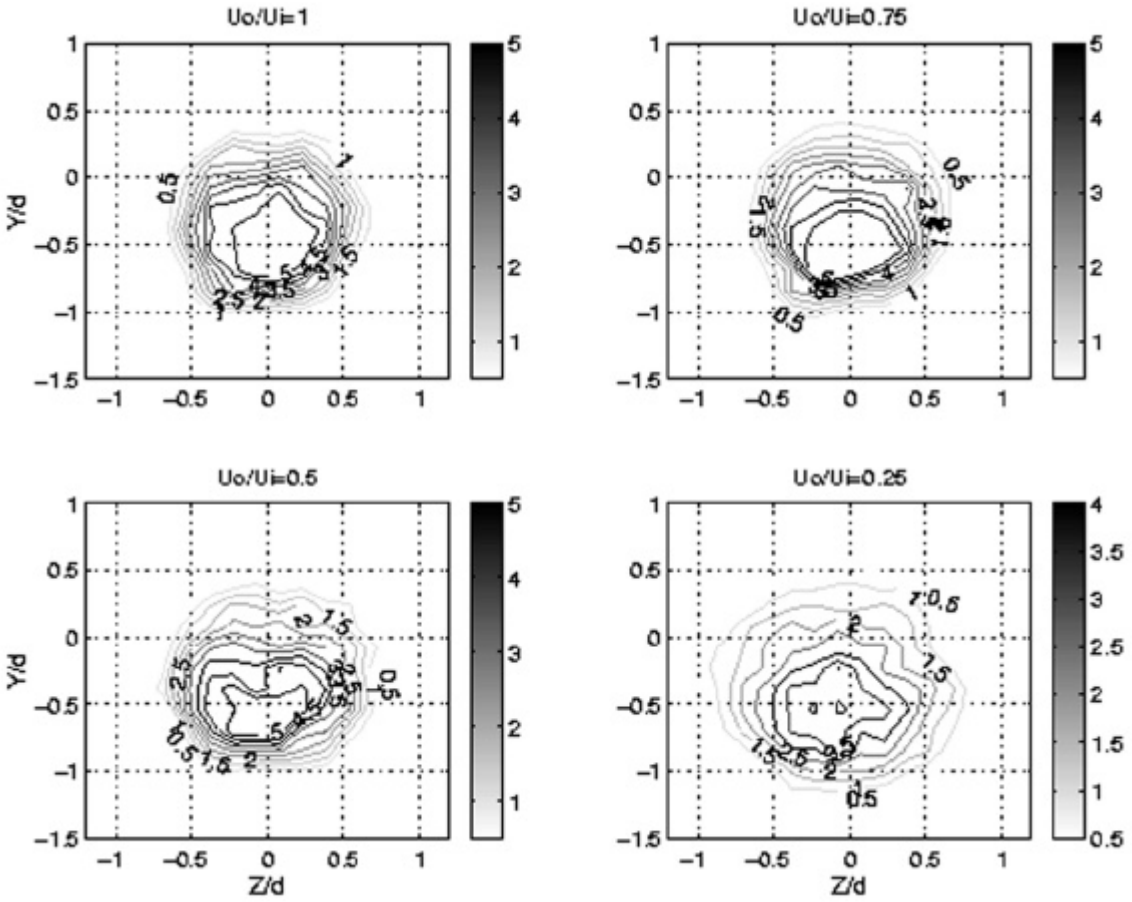

Figure 7.25. Particle dispersion results at x/d = 4, and volume flow rate of 0.024%.

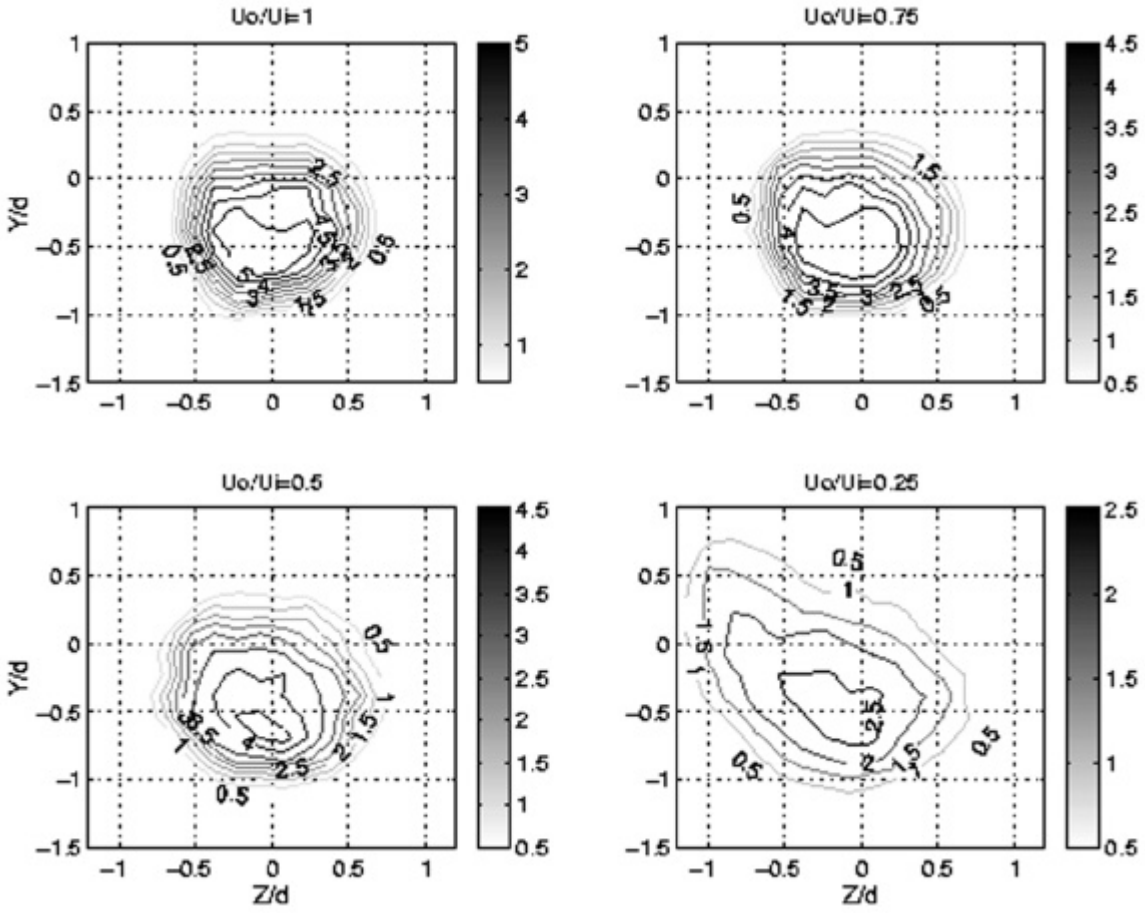

Figure 7.26. Particle dispersion results at x/d = 4, and volume flow rate of 0.075%.

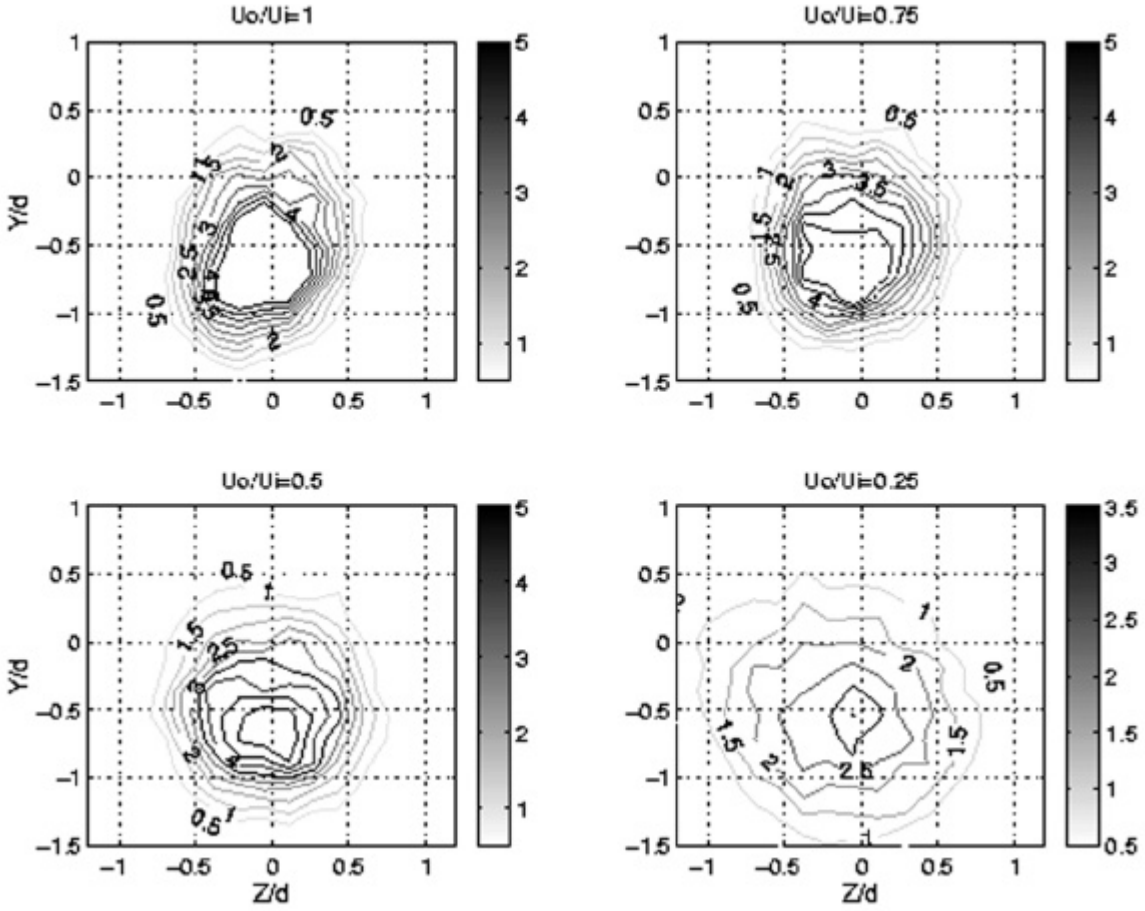

Figure 7.27. Particle dispersion results at x/d = 6, and volume flow rate of 0.024%.

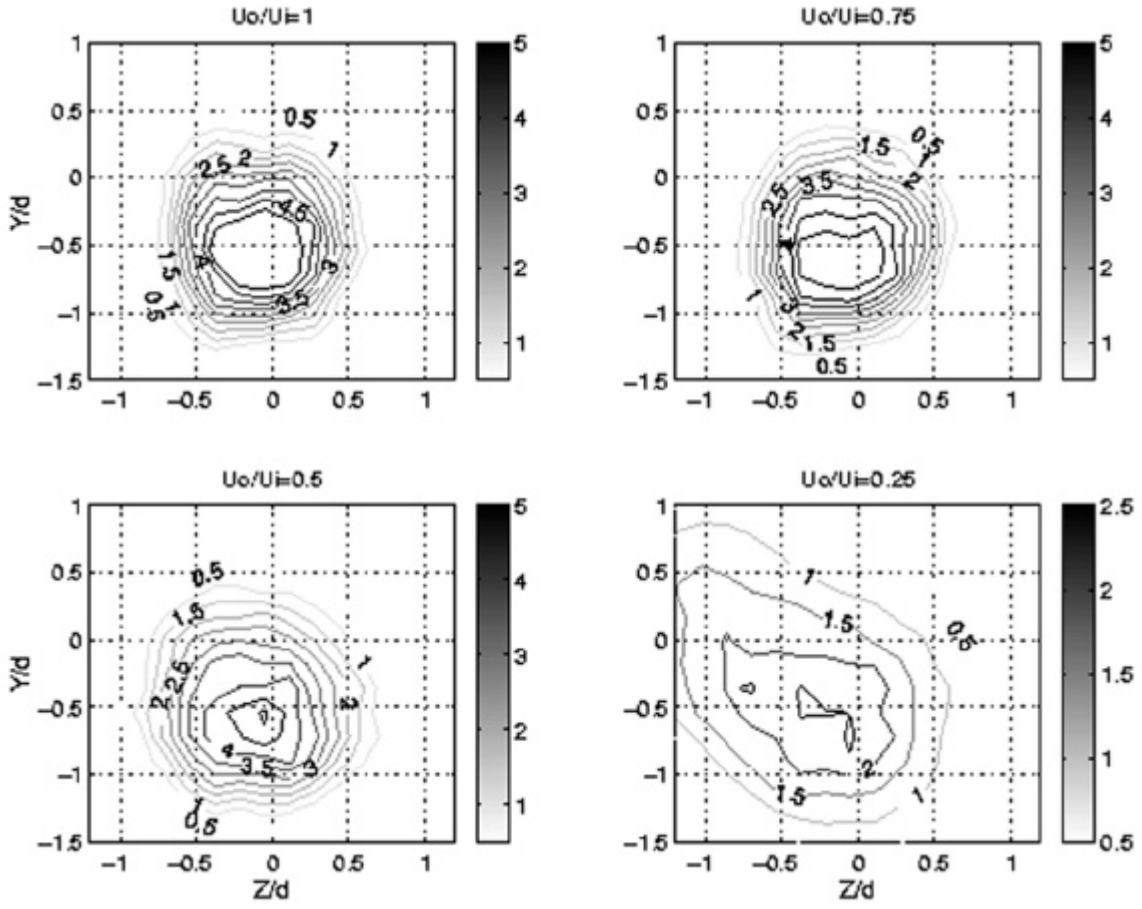

Figure 7.28. Particle dispersion results at x/d = 6, and volume flow rate of 0.075%.

7.5 References

Buresti, G., A. Talamelli, P. Petagna, "Experimental characterization of the velocity field of a coaxial jet configuration", *Exp. Thermal and Fluid Sci*., **9**, 1994, 135.

Buresti, G., P. Petagna, A. Talamelli, "Experimental investigation on the turbulent near-field of coaxial jets", *Exp. Thermal and Fluid Sci*., **17**, 1998,18.

Dahm, W.J.A., C.E.Frieler, G. Tryggvason, "Vortex structure and dynamics in the near field of a coaxial jet", *J. Fluid Mech*., **241**, 1992, 371.

Fan, J., H. Zhao, K. Chen, "An experimental study of two-phase turbulent coaxial jets", *Experiments in Fluids*, **13**, 1992, 279.

Fan, J., H. Zhao, J. Jin, "Two-phase velocity measurements in particle-laden coaxial jets", *The Chemical Eng. J*., **63**, 1996, 11.

Gendrich, C.P., M. M. Koochesfahani, "A spatial correlation technique for estimating velocity fields using molecular tagging velocimetry (MTV)", *Exp. in Fluids* **22**, 1996, 67.

Heap, M.P., J. Brouwer, K.A. Davis, A.F. Sarofim, M.J. Bockelie, E.G. Eddings, D.W. Pershing, J.C. Klewicki, R.H. Hurt and R.A. Lisauskas, "Optimized fuel injector design for maximum in-furnace NO_x reduction and minimum unburned carbon", Phase I Final Report, DOE-PRDA contract no. DE-AC22-95PC95103, 1998.

Hill, R.B., J. C. Klewicki, "Data reduction methods for flow tagging velocity measurements", *Experiments in Fluids*, **19**, 1995, 142.

Hinze, J.O., *Turbulence* 2nd ed, McGraw-Hill,New York, 1975.

Kamalu, N., L. Tang, T.R. Troutt, J.N. Chung and C.T. Crowe, "Particle dispersion in developing shear layers", in *Mechanics of Two-Phase Flow* (edited by S.L. Lee and F. Durst), Institute of Applied Mechanics, National Taiwan University, Taipei, ROC, 1989, 199.

Ko, N.W.M., A.S.H. Kwan, "The initial region of subsonic coaxial jets", *J. Fluid Mech*., **73**, 1976, 305.

Kwan, A.S.H., N.W.M. Ko, "The initial region of subsonic coaxial jets. Part 2", *J. Fluid Mech*., **82**, 1977, 273.

Lilly, G.P., "Effect of particle size on particle diffusivity", *Industrial and Engineering Chemistry Fundamentals*, **12**, 1973, 268.

Longmire, E.K., J.K. Eaton, "Structure of a particle-laden round jet", *J. Fluid Mech*., 1992, **236**, 217.

Polak, E., *Computational Methods in Optimization*, NewYork: Academic Press, 1971.

Ponce, P., P. A. Wong, J. J. Way and D. G. Nocera "Intense phosphorescence triggered by alcohols upon formation of a cyclodextrin ternary complex", *J. Physical Chem*., **97**, 1993, 11137.

Sadr, R., "Experimental study of particle-fluid interactions in the near field of a particle-laden coaxial jet", Ph.D. research proposal, University of Utah, 2000.

Sefcik, P., "An Experimental study of particle dispersion and particle-fluid interactions in the near field of a particle-laden coaxial confined jet", Ph.D. research proposal, University of Utah, 1997.

Tang, S.K., N.W.M. Ko, "Coherent structure interactions in an unexcited coaxial jet", *Exp. Fluids*, **17**, 1994, 147.

Thurlow, E.M., "Experimental study of turbulent Poiseuille-Couette flow", PhD dissertation, University of Utah, 1998.

Warda, H.A., S.Z. Kassab, K.A. Elshorbagy, E.A. Elsaadawy, "An experimental investigation of the near-field region of free turbulent round central and annular jets", *Flow Meas. Inst*., **10**, 1999, 1.

Wicker, R.B., J.K. Eaton, "Near field of a coaxial jet with and without axial excitation", *AIAA J*., **32**(3), 1994, 542.

APPENDIX A

EXPERIMENTAL APPARATUS

All equipment used in the University of Utah experiments will be described in detail in this appendix. Detailed information will be provided on the physical facilities (combustor, burner, etc.) as well as instrumentation, sampling systems, and temperature measurement.

The description of the facility was provided in a previous DOE report. The following text has been updated to incorporate recent changes to the facility and to describe specifics of the way the furnace was configured for the carbon in ash experiments conducted during the summer of 2000.

A.1 U Furnace

A bench scale test facility was previously designed and built at the University of Utah for DOE and related combustion research projects. This multifuel combustion research facility, shown in Figure A.1, has a U configuration and is down-fired; it will hereafter be referred to as the U furnace. Its nominal firing rate is 30 kW. The combustion chamber is approximately 0.16 m in diameter and the overall length is 7.3 m. The composite walls of the furnace include both refractory and insulation board layers to minimize heat loss as described in below.

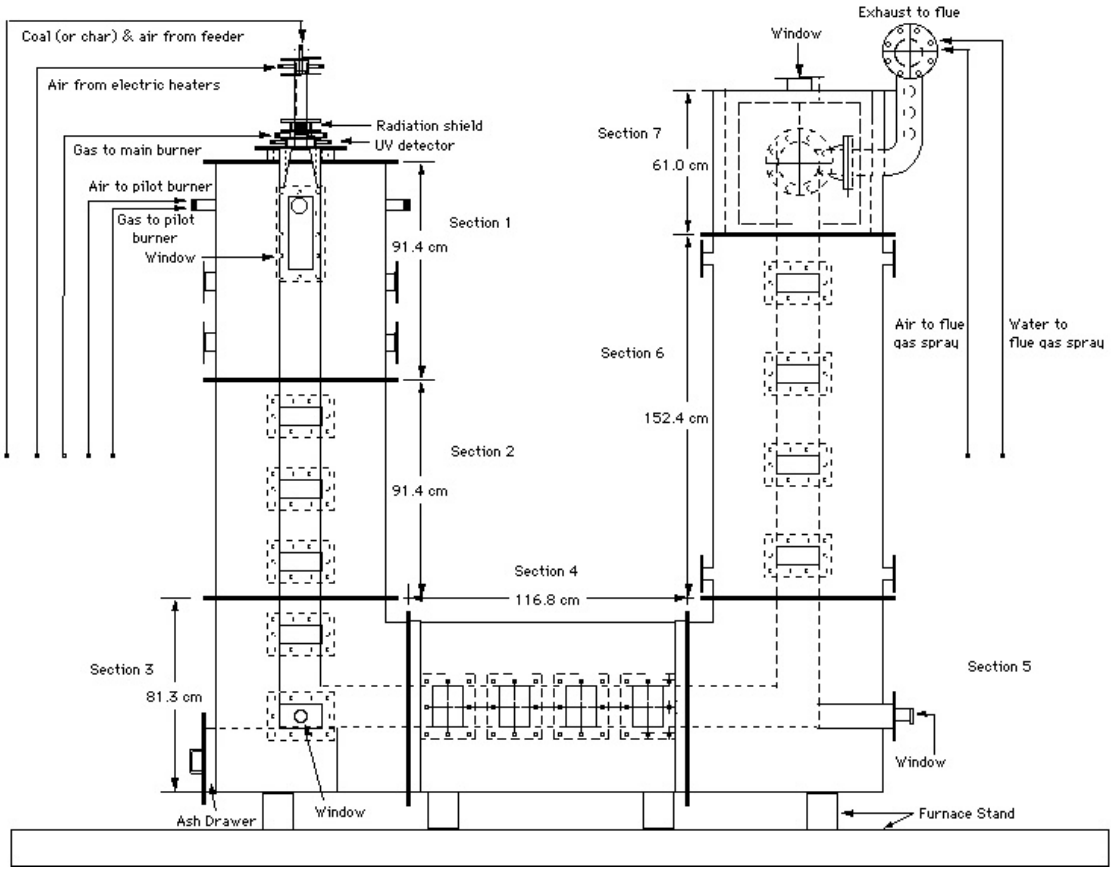

Figure A.1. Multi-Fuel combustion research facility ("U" furnace).

A1.1 Design of the U Furnace

The U furnace is made up of seven sections. Each section will be discussed in detail in the following paragraphs. All sections were fabricated from carbon steel unless otherwise indicated on the design drawing.

The burner is mounted to the top of Section 1. Section 1 also has a large, water-cooled window port for viewing the flame (quartz glass is used for the window), three-5.25 cm diameter ports located at the same level as the top of the window, and two sets of opposing ports located below the window. Although the window was important for flame observation, radiant heat losses to the window were large and a refractory plug was inserted into the window opening. The three ports are used for flame ignition and detection. A pilot burner is located in one of the two opposing ports. A UV flame detector (also called a "peeper") is located at the end of the port that directly opposes the port containing the pilot burner. A small flow of purge air is provided to keep the UV sensor window free of soot and ash deposits. The third port, located at 90° to the other two, also has a peeper located at its end. The pilot burner is used to ignite the main burner, and the peepers detect UV radiation from the flame once it is ignited. The two sets of opposing ports are used for inserting sample probes, thermocouples, etc. into the combustion chamber. Sampling ports are numbered by section in the direction of gas flow. In addition, the designations N, S, E, and W are included to indicate on which side of the furnace the port is located. Hence, the opposing ports just below the level of the window are ports 1-1N and 1-1S, and the opposing ports at the very bottom of Section 1 are ports 1-2N and 1-2S. This numbering system will be used subsequently to describe where sample probes and thermocouples were inserted.

Section 2 has three sets of opposing sampling ports, numbered in order according to the direction of gas flow as ports 2-1E and 2-1W, ports 2-2E and 2-2W, and ports 2-3E and 2-3W. There are no other special features of Section 2. Furnace flow changes direction by 90° in Section 3; furnace flow is vertical entering the section and horizontal leaving it. This sudden change in flow direction required special design considerations for the burning of solid fuels because larger particles would have enough momentum to deposit in the corner. In order to avoid a buildup of particles that could potentially plug the furnace and be difficult to clean out, a removable drawer was designed into Section 3. This drawer, known as the ash drawer, is lined with both refractory and insulation board. It sits directly below the combustion chamber, so any solids that aren't carried around the corner with the flow are deposited in this drawer. The drawer is removed from the furnace at frequent intervals and any collected solids are disposed of. Section 3 also has one set of opposing sampling ports (ports 3-1E and 3-1W) and a window port. The window consists of a threaded pipe welded onto a plate that is bolted onto the window port's flange. A screw cap with quartz glass recessed in the cap is then screwed onto the threaded pipe. The window diameter is approximately 5 cm. This Section 3 view port was replaced by a solid cover plate for the staging experiments during the summer of 2000.

Section 4, positioned horizontally, has four sets of opposing sampling ports. A gas sampling probe was inserted into port 4-1W for the summer 2000 experiments. Section 5 is similar to Section 3 in that the furnace flow changes direction again- from horizontal to vertical. Section 5 has one window port that is exactly the same as the one described on Section 3. Section 5 has no sampling ports or ash drawer. When solids do build up in the corner,

cleaning is done through the window port. Section 6 is the longest of all the sections. It has four sets of opposing sampling ports (east and west sides), again numbered in order in the direction of gas flow. There are also ports located at the top and the bottom of Section 6 (north and south sides).

The last section, Section 7, has one window port located on top and no sampling ports. The window is much larger than either the Section 3 or 5 windows. It consists of a 18 cm by 7.5 cm rectangle of quartz glass recessed in a metal box that is bolted to the flange on the window port. The furnace flow again changes direction by 90° as it exhausts through the rear of Section 7. Upon exiting the furnace, the flue gas enters a series of insulated, flanged elbows and tees that redirect the flow up and over the furnace. The flue gas then enters a long section of bare pipe where significant heat loss occurs; this section ends in a tee. The cooled flue gas then enters a flue duct in the laboratory that is maintained at a negative pressure by an evacuation fan on the roof of the building. By exhausting the furnace flue gas into this duct, the furnace can be maintained at slightly sub atmospheric pressures at all times.

A structural support was fabricated for the furnace in order to distribute the weight of the furnace as evenly as possible over the H-beams in the floor of the laboratory. The stand was constructed from 10 cm I-beams and is sketched in Figure A.1. Angle iron welded to the shell of the U furnace in eight locations is bolted to four of the beams running crosswise.

A1.2 Piping and Flow Metering

The furnace is equipped with piping for various natural gas and air streams including pilot burner air and gas lines, a main combustion air line from which a primary air line and a secondary air line tee off, a main burner gas line, and additional lines that were employed for various purposes during the experiments. Two electrically-heated tube heaters mounted in series are located in the secondary air line. These heaters are used to heat the secondary air prior to its entering the burner.

All air and natural gas flows into the furnace are metered using rotameters equipped with valves and pressure gauges. Actual flow rate is determined by the position of the float in the rotameter, the specific gravity of the fluid flowing through the rotameter (most rotameters are calibrated for air), and the pressure of the fluid in the rotameter according to the equation

$$Q_2 = Q_1 \sqrt{\frac{P_2}{P_1 \cdot SG}} \qquad \text{(A.1)}$$

where

Q_1 = Observed flow meter reading

Q_2 = Actual flow corrected for pressure and specific gravity

P_1 = Atmospheric pressure at sea level

P_2 = Actual pressure inside flow meter (local atmospheric pressure + pressure inside flow meter)

1.0 = Specific gravity of air

SG = Specific gravity relative to air of the gas being used in flow meter originally calibrated for air.

All flows except the main combustion air flow are metered using Dwyer rotameters. The pilot air and gas flows use Dwyer Series RMB rotameters which have a guaranteed accuracy of +/- 3% of full scale. All other air and natural gas flows (except main combustion air) are metered with Dwyer Series RMC rotameters that are accurate to +/-2% of full scale (Dwyer, 1993). The main combustion air is metered with a Brooks Model No. 1110-09K3G1A rotameter, which according to product literature is accurate to +/-2% of full scale.

The main combustion air line tees off to provide air to both the primary and secondary air lines. There are no flow constrictions in the secondary air line from the tee to the burner. The flow constrictions in the primary air line are a rotameter (Dwyer Series RMC) and a valve located just downstream of the tee. Flow rate in the secondary air line is determined by subtracting the flow rate through the primary air rotameter from the flow rate of main combustion air through the Brooks rotameter.

A1.3 Water cooling

Water cooling was originally installed at several furnace locations. Over time most of this cooling was found to be unnecessary and was removed from service.

A1.4 Refractory

As mentioned previously, the walls of the U furnace are a composite of castable refractory and insulation board. The materials in the composite wall were obtained from the A. P. Green Company. Table A.1 lists those materials along with some of their properties. Figure A.2 and Figure A.3 show how the refractory and insulation board are layered in each section of the U furnace.

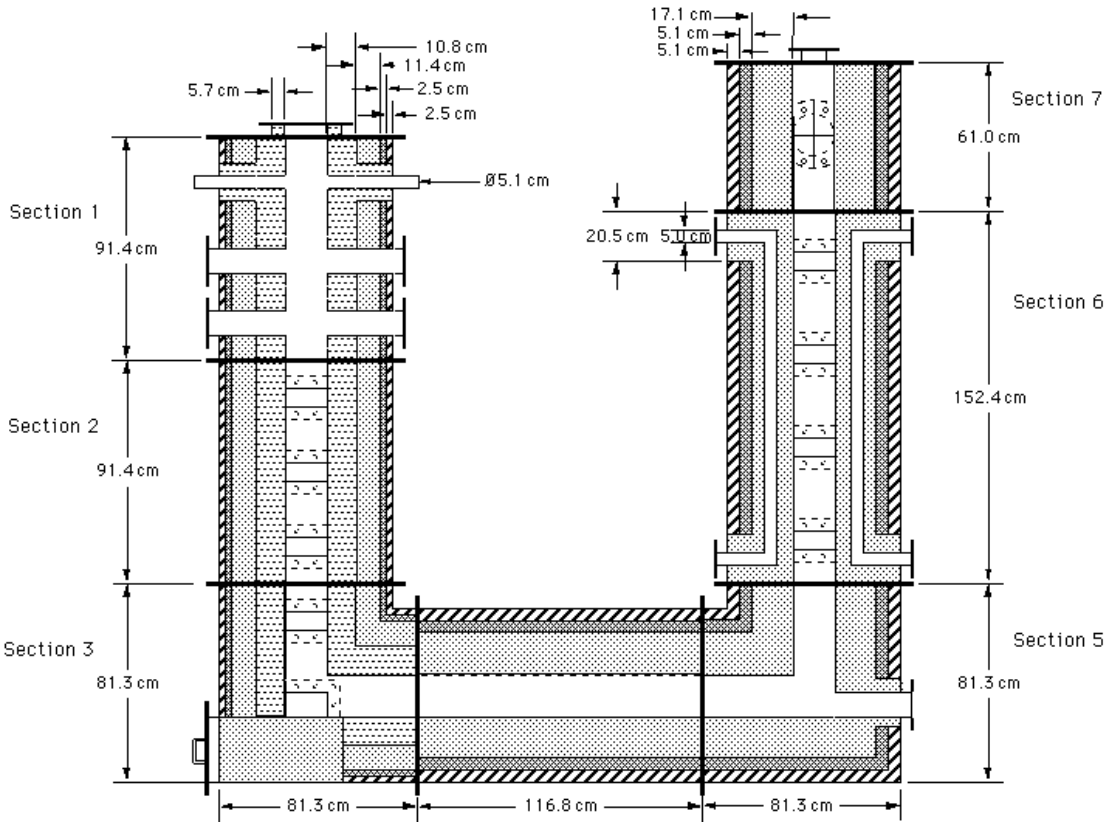

Figure A.2. Front view of refractory layers inside of U furnace.

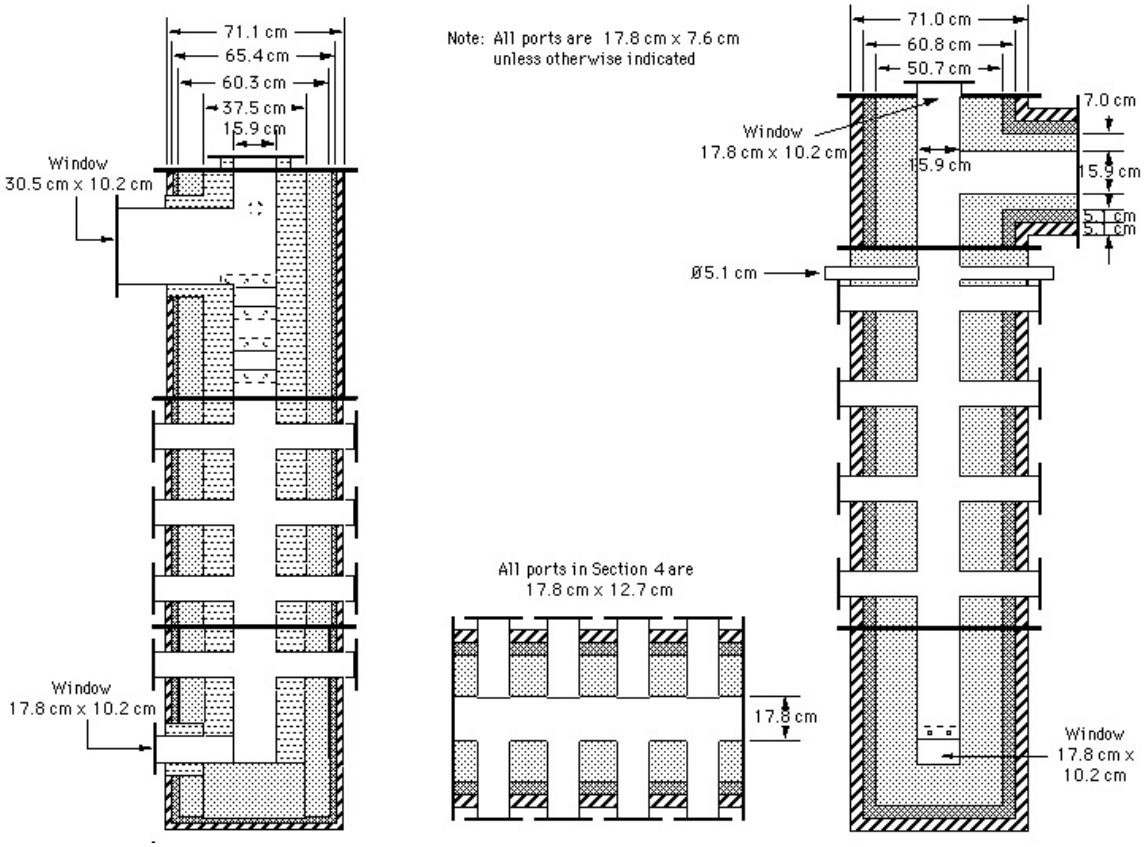

Figure A.3. Side view of refractory layers inside of U furnace.

Heat transfer calculations by the A. P. Green Company were used to estimate the temperature drop across the composite layer and to approximate the surface temperature of the furnace shell. Safety considerations required that the shell temperature not exceed 420 K. Performing the calculations with the composite layer in Section 1 and with a hot face temperature of 2035 K, the temperature drops across the different layers are as follows: Greencast 94 Plus layer = 228 K, Kast-o-lite 30 Plus layer = 462 K, Insboard 2300 layer = 271 K, and Insblok-19 layer = 683 K. These temperature drops yield an estimated shell temperature of 389 K. Actual shell temperatures measured after the furnace had been fired continuously for a period of several weeks indicate that Section 1 shell temperatures do reach 410 K in some locations.

Each section of the U furnace was poured separately. The refractory was firmly fixed to the steel shell of the furnace by steel anchors which were welded to the shell. The anchors extended into the innermost layer of refractory and were located on 15 cm centers. In Sections 1, 2, and 3, wooden forms were used to shape the outermost refractory layer (Kast-o-lite 30 Plus). With the exception of the horizontal component of Section 3, the innermost refractory layer (Greencast 94 Plus) was poured around a PVC pipe with an outside diameter of 15.9 cm. For all horizontal sections of the furnace, the innermost refractory layer was poured around a wooden form with a cross sectional area of 17.8 cm x 17.8 cm. In Sections

6, 7, and the vertical component of Section 5, the innermost refractory layer (Kast-o-lite 30 Plus) was poured around the 15.9 cm PVC pipe. The channels cast in the refractory layer of Section 6 (see Figure A.2) were formed by pouring refractory around channel forms made from foam core board. These channels, whose original purpose was to provide auxiliary heating in Section 6, were not required for this program. The 5.1 cm diameter ducts in Sections 1 and 6 were formed using PVC pipe as the mold. Wooden forms were used in all other locations where refractory shaping was required.

Table A.1 Insulating materials used in the U furnace

Trade Name	Type	Density kg/m^3	Mean Temp. K	Literature k value $W/m^2/K/cm$
Greencast-94 Plus	Castable refractory	2561	700	29.49
			955	26.58
			1145	24.57
			1365	23.90
			1590	24.13
Kast-o-lite 30 Plus	Insulating castable	n/a	700	6.48
			955	6.90
			1145	7.33
			1365	7.73
Insboard 2300	Ceramic fiber	28.8	1055	2.02
			1205	2.26
Insblock 19	Ceramic fiber		640	1.41
			730	1.67
			790	1.86

A1.5 Electronics and Safety System

The main control panel of the U furnace contains rotameters, pressure gauges, regulators, and the flame safety electronics. The "Main" button, when pulled out, turns on power to the furnace electronics. Power to each subsystem is controlled by its respective push/pull button. Once power to a subsystem has been turned on, the on/off push button switches can be used. For example, in order to turn on the coal/char feeder, the Coal Feeder System push/pull button must be pulled out and then the Coal Feeder on/off push button switch must be pushed on. At this point, a switch on the feeder can be flipped on and the augers will begin to feed coal. There is some redundancy in this system, but this redundancy ensures that the operator thinks through the process before turning anything on.

The Pilot sparker switch allows the sparker to be used to light the pilot burner. The U furnace is designed to be run continuously in a safe operating mode. Four safety parameters are constantly monitored: air supply pressure, water supply pressure, flue (evacuation) duct vacuum pressure, and flue duct temperature. An out-of-range reading for any one of these parameters indicates a dangerous operating condition. When an out-of-range reading occurs, solenoid valves, installed in all natural gas lines between the gas supply line and the combustor, are closed. Also, the electric heaters mounted in the secondary air line are shut off as is the coal/char feeder. Out-of-range readings do not cause the air supply to the combustor to be shut off unless the cause of the shutdown is lack of air supply pressure. In addition to these four parameters, the flame is continuously monitored by three peepers installed in parallel. If none of the peepers picks up a sufficient UV signal, the natural gas solenoid valves are closed.

There are several additional safety features. First, a pressure switch in the secondary air line monitors pressure in that line downstream of the rotameter. If the pressure drops too low, the electric heaters are shut off. This switch was added in the event that the secondary air is turned down too low (or even turned off) because the electric heaters can easily be damaged with little or no air flow through them. The three on/off push button switches that control the opening and closing of the natural gas solenoid valves (Pilot, and Main Gas) can only be turned on if two conditions are met. One, as mentioned above, the appropriate subsystem push/pull button must be pulled out. Two, the peepers must be able to detect a UV signal from the flame. The sparker is needed to light the pilot since the Main Pilot solenoid will not open and allow natural gas to flow until the peepers "see" a flame. A peeper located in the duct that directly opposes the pilot burner duct "sees" the spark produced by the spark plug and detects a flame. The Main Pilot solenoid can then be opened, and gas flows to the pilot burner where pilot air is already flowing. The spark ignites the fuel/air mixture and the peepers pick up this pilot flame. At this point, assuming main combustion air is already flowing, the Main Gas solenoid can be opened. The pilot flame, located directly beneath the main burner quarl, then ignites the main burner.

A1.6 Coal/Char Feeding System

All coals and chars tested in this thesis were fed using the coal/char feeding system sketched in Figure A.4 The major components of this system include a Ktron Model T20 Twin Screw Volumetric feeder, a pressure equilibration regulator, two sizes of eductors, and a primary air stream. Coal or char in the hopper is fed into the twin screws. The solid moves down the

screws until it drops off the end of the screws into a short stainless steel coupling. A bellows is attached to the bottom edge of the coupling. The solid falls through the bellows and into a funnel which narrows to the inlet diameter of the eductor. Primary air being fed through the eductor picks up the solid and carries it to the burner. The pressure equilibration regulator is used to balance primary air pressure upstream and downstream of the nozzle in the eductor. In order to prevent solids buildup in the eductor inlet, a slight vacuum, measured by the Magnehelic, is maintained on the downstream side of the eductor nozzle. Two sizes of eductors are needed because high moisture coals tend to cake up in the inlet of the smaller eductor, necessitating the use of the larger eductor. Details about the calibration of the Ktron feeder are found in Appendix A of Spinti (1997).

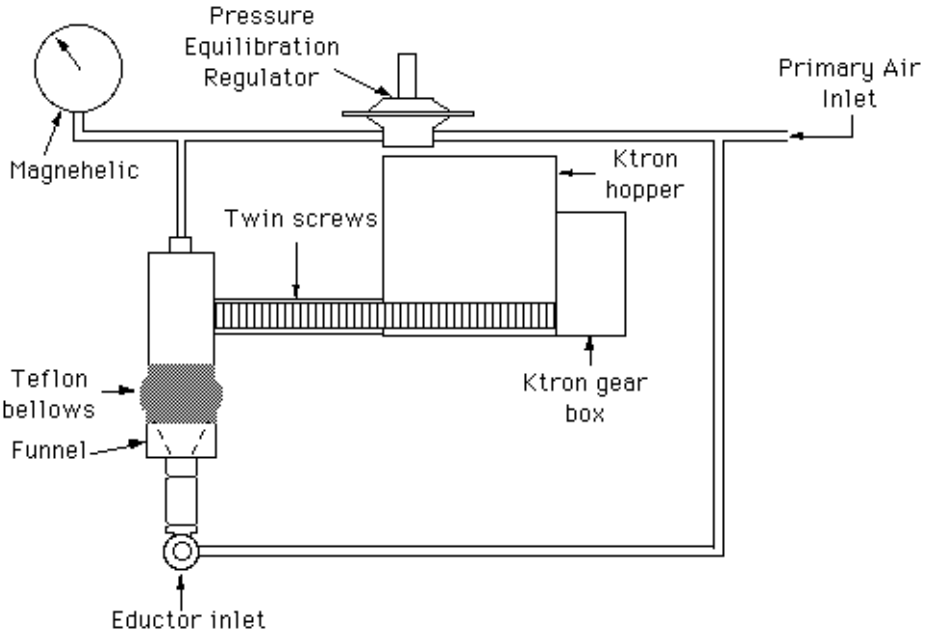

Figure A.4. Coal/char feeding system.

A.2 Premixed Burner

The burner used for all experiments described in this thesis is a premixed burner that was specially designed and built for the present work. Figure A.5 is an assembly drawing of the burner. The burner is fabricated from all stainless steel parts.

A.2.1 Premixed Burner Design

The burner consists of five main sections. The first section includes inlets for the secondary air and the primary air/coal mixture and a mixing plate. This mixing plate is designed to produce a well-mixed coal/air mixture in the second section, known as the mixing chamber. The primary air/ coal inlet pipe is welded to the mixing plate. The air/ coal mixture entering the burner is forced through six-3.6 mm holes equally spaced around a 0.86 cm circle on the mixing plate and drilled at an angle of -20° off the vertical. The secondary air enters the burner through two inlets and is forced through six-6.9 mm holes equally spaced around a

5.3 cm circle on the same mixing plate and drilled at an angle of + 15° off the vertical. The two streams (primary/coal and secondary) impinge on each other approximately 2.5 cm below the mixing plate. Based on a typical run where primary air makes up 15% of the total combustion air, primary jet velocity exiting the holes is 22.8 m/s and secondary jet velocity is 35.4 m/s.

The second section of the burner, the mixing chamber, is where the two impinging streams are allowed to fully mix before entering the third section of the burner, the radiation shield. The purpose of the radiation shield is to prevent premature ignition of the fuel/oxidant mixture in the premixing chamber. The radiation shield consists of three rows of staggered stainless steel tubes (OD = 0.64 cm) that extend across the burner cross section. The staggered configuration prevents any direct line of sight from the combustor up into the mixing chamber. Water runs continuously from a manifold-type configuration through the bank of tubes. The estimated velocity of the fuel + air mixture through the radiation shield, assuming the combustion air is preheated to 530 K and the natural gas firing rate is 29.3 kW, is 12.0 m/s.

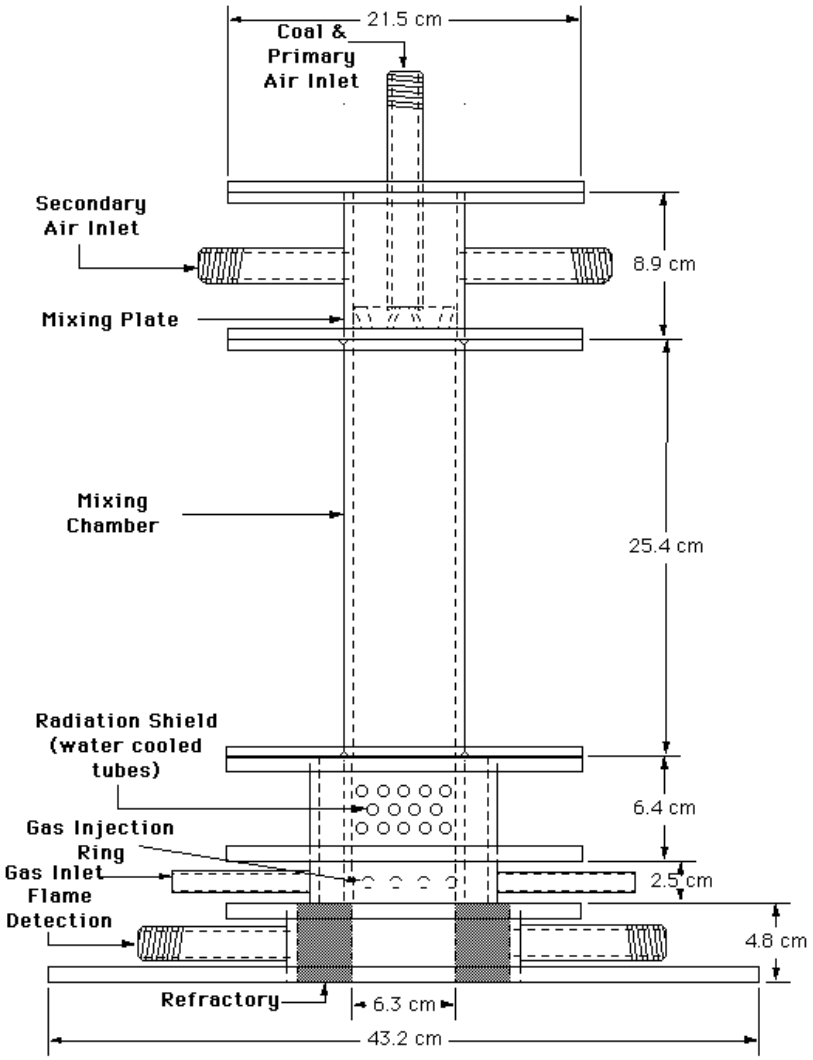

Figure A.5. Assembly drawing of premixed burner.

A water recirculation system was devised for the radiation shield in the event of an unexpected loss of supply water. If supply water pressure drops to zero, the pressure switch that monitors supply water pressure as part of the U furnace safety system will trip. This tripping will open two solenoid valves and close two others in the water lines feeding the radiation shield. The net effect is that water from a tank located above the furnace will be recirculated through the radiation shield, thus preventing any damage to the shield from furnace radiation.

Natural gas injection occurs just below the radiation shield in the fourth section of the burner. Natural gas enters the burner through two-1.3 cm OD tubes into an annular ring. The gas is then forced through eighteen-2.4 mm holes equally spaced around the diameter of the inner ring of the annulus into the flow of fuel + air coming through the radiation shield. For the summer 2000 experiments natural gas was used only for preheating of the furnace. Supplemental (stabilization) gas was not used with the coal combustion experiments.

The fifth and final burner section is refractory-lined with Greencast-94 Plus as shown in Figure A.6. The refractory layer is 3.3 cm thick. This section also has two-1.3 cm ducts that extend horizontally from the threaded pipe through the refractory layer to the burner interior. Peepers are mounted to the threaded pipe with a direct line of sight to the burner interior in case ignition occurs at this location and not down below the quarl where the other peepers are located. A quarl, although not shown in Figure A.6, extends from the bottom of the burner down into the combustor. The quarl has an ID of 6.3 cm at the top and opens to the diameter of the combustor (15.9 cm) over a length of 20.3 cm.

A.3 Instrumentation/Data Collection

Data from the U furnace were collected in the control room.

A.3.1 Control Room Instrumentation

Three instruments are located in the control room: the O_2 analyzer, the NO_x analyzer, and the CO/CO_2 analyzer. Output signals from these instruments are interfaced to the control room computer. In addition, four type B thermocouple lines from the U furnace were brought into the control room and interfaced to the computer. Opto-22 software was used to collect and record both analyzer signals and thermocouple readings.

A.3.2 O_2 and CO/CO_2 Analyzers

The O_2 analyzer used in these experiments was a Yokogawa Zirconia Oxygen Analyzer with an averaging converter system. This instrument was calibrated with a 2.5% O_2 calibration gas as the zero (low concentration) gas and room air as the span gas. It holds its zero (low concentration) gas calibration for at least a week, but if high O_2 concentrations are being measured (>15%), span gas calibration is necessary on a daily basis.

CO and CO_2 gas concentrations were measured by a Nova Model 4280RM Dual Range CO and CO_2 Analyzer. This instrument uses NDIR (nondispersive infrared spectroscopy) technology. The two ranges for CO are 0-1% and 0-10%; the two ranges for CO_2 are 0-3%

and 0-30%. The instrument was run with CO set on the 0-10% range and CO_2 set on the 0-30% range. It would have been preferable to run with CO set on the 0-1% range, but no calibration gas was available for that range. The instrument was calibrated with nitrogen as the zero gas and with a 5% CO/12% CO_2 calibration gas as the span gas. The calibration had to be checked on a daily basis (sometimes several times a day) because this analyzer did not hold its calibration very well.

A.3.3. Chemiluminescent NO_x Analyzer

Control room NO_X measurements were made with the Thermo Environmental Model 10A Chemiluminescent NO- NO_X Gas Analyzer, also known as the TECO. When NO reacts with O_3 , light emission occurs at a specific wavelength. This chemiluminescence is monitored through an optical filter by a high-sensitivity photomultiplier located inside the instrument. The output from the photomultiplier is linearly proportional to the NO concentration. To measure NOx concentrations (NO + NO_2), the sample gas is first diverted through an NO_2 -to-NO converter before it is reacted with O_3 (Model 10AR Instruction Manual). This NO_X analyzer has multiple linear, full-scale ranges. Depending on the NO concentration in the sample being measured, either the 0-1000 ppm or the 0-2500 ppm scale was used. The instrument was calibrated with nitrogen as the zero gas and three appropriate NO calibration gases.